CONTENTS

GENERALIZED METHODS OF ESTIMATIONS OF LUBRICANTS' INFLUENCE ON THE TRIBOTECHNICAL CHARACTERISTICS OF FRICTION PAIR "STEEL-STEEL" ON THE FOUR-BALL MACHINE

Sergey G. CHULKIN[*], **Aleksandr D. BREKI**[*], **Irina V. SOLOVIOVA**[*], **Roman KACZYŃSKI**[**]

[*] Department of Machine Science and machine Components, Faculty of Mechanical Engineering,
Sankt-Petersburg State Polytechnic University, Polytechnical 29, 125251 Sankt-Petersburg
[**]Department Of Machine Design, Faculty of Mechanical Engineering,
Bialystok University of Technology, Wiejska 45 C, 15-351 Białystok

uwc99@mail.ru, albreki@yandex.ru, solov`jeva_irina_@list.ru, rkgraf@pb.edu.pl

Abstract: This article is devoted to the development of generalized methods of estimations of lubricants influence on the tribotechnical characteristics of friction pair "steel-steel" and its usage for selection of the best lubricating material out of set of materials "Litol-24"produced by different manufacturers.

1. INTRODUCTION

To the main raw materials for manufacture plastic lubricants of various purpose serve:
1. mineral oils of various viscosity and a degree of clearing;
2. hydrocarbonic thickeners (petrolatums, cherezins, paraffins);
3. soaps of the fat acids allocated from natural fats, and natural fats of an animal and a phytogenesis;
4. soaps of synthetic fat acids;
5. various products of chemical synthesis (silicon-organic liquids, complex ethers, dyes, etc.).

Besides the additives improving their separate properties or some of different properties (multipurpose), and also inhibitors of oxidation are entered into plastic lubricants (PL), inhibitors of corrosion and other components.

In this connection plastic lubricants have the complex chemical compound defining their operational properties.

During the production process of any lubricant S, its manufacturer follows the requirements of the state standard. As any lubricant can be produced by a different manufacturer, that is why in a number of cases, it is necessary to compare the influence of different grades of lubricant S on tribotechnical characteristics of friction pair. Thus, the Department of Machine Science and machine Components of Saint-Petersburg State Polytechnic University carried out estimation of the influence of different grades of lubricant "Litol-24" on the tribotechnical characteristics of friction pair "steel-steel".

Complexity of chemical compound PL is one of the major factors influencing distinction of properties of same products at different manufacturers.

2. RESEARCH METHODOLOGY

The research of the influence of the lubricating materials from the set $\{Sm_i \,|1, 2, ..., p\}$ (S – name of the lubricant material, m_i – grade of the lubricating material S, p – quantity of grades (manufacturers) of the lubricating material S) on tribotechnical characteristics of the friction pair "steel-steel" is carried on the basis of grades numbering scheme according to the following algorithm:
1. Wearing test of the lubricant S of the manufacturer "p" is carried out on the friction test machine CH_SH_M 3,2 (GOST 9490-88).
2. Microhardness measurement of the sample friction surfaces is conducted using microhardness-meter PMT-3 (GOST 9450-76).
3. Two best lubricants from p are selected and then tear index test is carried out (GOST 9490-88).
4. Selection of the best lubricating material in the examined set is performed.

Friction pair elements, which are used in the wearing tests and tear index tests, are balls of the bearings GOST 3722. These balls are made of material "steel SHKH15", with diameter $d_m = (12,70 +/- 0,01)$mm. Normal ball loading at wearing tests is $P = 196$ N. Time for one test operation is $\Delta t = (60,00 =/- 0,50)$ min.

Length $l_j(m_i)$ and width $h_j(m_i)$ of the wear spot # j ($j = 1, 2, 3$), which was formed at lubricant Sm_i tests, were measured with the microscope "Prima-expert". The diameter of wear spot # j corresponding to Sm_i is defined as follows:

$$d_j(m_i) = \frac{l_j(m_i) + h_j(m_i)}{2}. \tag{1}$$

Mean diameter of the wear spot for lubricating material Sm_i is calculated by the following formula:

$$D_H(m_i) = \frac{1}{3} \cdot \sum_{j=1}^{3} \frac{l_j(m_i) + h_j(m_i)}{2}. \tag{2}$$

Initial data, measurement and calculation results are given in Table 1.

Tab. 1. Wear test results

No (i)	P		$d_j(m_i)$ mm	$D_H(m_i)$ mm	Limiting wear $d_r + 0,15$ mm
	N	k			
			Sm_1		
1	196	20	$d_1(m_1), d_2(m_1), d_3(m_1)$	$D_H(m_1)$	0,39
			...		
...	...	...	...	...	...
			Sm_p		
p	196	20	$d_1(m_p), d_2(m_p), d_3(m_p)$	$D_H(m_p)$	0,39

Microhardness measurement of the sample friction surfaces is conducted according to "restored dent method" (GOST 9450-76) using microhardness-meter PMT-3. Three (3) surface areas of the sample are tested: initial surface; friction surface without mass transfer section that is typical of abrasive wear; friction surface with mass transfer sections that is typical adhesive wear. The "q" (q – quantity of the dents) dents are marked in each area of the test sample subject to established distance between their centers.

Indentor diamond point is lowered by the counter-clockwise turn of the loading unit rod handle till its contact of the test sample surface during $t_K = 10 \ldots 15$ s. Then the indentor is held down during $t_{y\partial} = 30$ s under the load. Measuring of indentor dent parameters (Fig. 1) is carried out by the microscope with 100 x magnification [1-7].
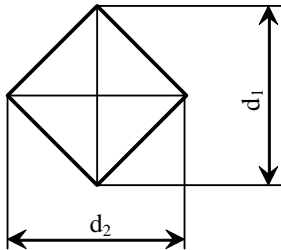
Fig. 1. Indenter dent parameters

Tab. 2. The results of microhardness measurements (i = 1, 2, ..., p, this complex symbol means the availability of p tables of reduced type)

	Lubricating material · Sm_i								
	Abrasive wear			Adhesive wear			Initial surface		
k	$d_{1,k}$	$d_{2,k}$	d_k	$d_{1,k}$	$d_{2,k}$	d_k	$d_{1,k}$	$d_{2,k}$	d_k
1	$d_{1,1}$	$d_{2,1}$	d_1	$d_{1,1}$	$d_{2,1}$	d_1	$d_{1,1}$	$d_{2,1}$	d_1
...	...	...	...	...	...	...	...	...	...
q	$d_{1,q}$	$d_{2,q}$	d_q	$d_{1,q}$	$d_{2,q}$	d_q	$d_{1,q}$	$d_{2,q}$	d_q
			d			d			d
Microhardness $HV_{a\partial}$				$HV_{a\partial z}$			HV		

The results of the measurements and calculations are listed in Table 2.

The diagonal length of k (k = 1, 2, ..., q) indentor dent in the selected area is defined by the formula:

$$d_k = \frac{d_{1,k} + d_{2,k}}{2}. \tag{3}$$

Mean length of the indentor dent diagonal in the same area:

$$d = \frac{1}{q} \cdot \sum_{k=1}^{q} \frac{d_{1,k} + d_{2,k}}{2}. \tag{4}$$

After the measurement of obtained dents parameters and calculations using of relations (3) and (4), microhardness is defined by the formula (Glazov and Vigdorovich, 1969):

$$HV = 1854 \cdot \frac{F}{d^2}, \tag{5}$$

where F gf – force, acting on indentor, $F = 50gf = const$, d – mean length of the indentor dent diagonal (μm), HV – microhardness value (kgf/mm^2).

By comparing the results, listed in the Tables above, the selection of the two best lubricating materials $\{Sm_a; Sm_b\}$ is carried out from the set $\{Sm_i \mid i = 1, 2, ..., p\}$.

Tear index tests of the selected lubricating materials Sm_a; and Sm_b are conducted as per GOST 9490-75.

From the load series $\{P_\alpha \mid \alpha = 1, 2, ..., 23\}$ the set of adjacent loads $\{P_\beta \mid 1 \leq \beta \leq 23\} = \{P_\gamma \mid \gamma = 1, 2, ..., n\}$ is selected. The elements of this set are renumbered and located in the monotone increase or monotone decrease order. The length of the tests at fixed load from the set is $\Delta t' = (10,0 +/- 0,2)s$. The diameter of j – wear spot for lubricating material $\{Sm_i \mid i = a, b\}$ at fixed load P_γ, taking into consideration (1), is defined as follows:

$$d_j(m_i, P_\gamma) = \frac{l_j(m_i, P_\gamma) + h_j(m_i, P_\gamma)}{2}. \tag{6}$$

Mean diameter of wear spots is similarly (2):

$$d_{H\gamma}(m_i) = \frac{1}{3} \cdot \sum_{j=1}^{3} \frac{l_j(m_i, P_\gamma) + h_j(m_i, P_\gamma)}{2}. \tag{7}$$

According to GOST 9490-88 the limiting wear values series $d_{np\alpha} = d_{r\alpha} + 0,15$ mm is put as one-to-one depentanizer to the load series 1. Thereby, for the set:

$$d_{np\gamma} = d_{r\gamma} + 0,15mm, \tag{8}$$

where $d_{r\gamma}$ – diameter of the balls' elastic range of stress according to Herz (mm), at load P_γ, $H(kgf)$.

Conditional load, corresponding to axial load P_γ, at lubricating material $\{Sm_i \mid i = a, b\}$ tests can be found from the following relation:

$$Q_\gamma(m_i) = P_\gamma \cdot \frac{d_{r\gamma}}{d_{H\gamma}(m_i)}. \tag{9}$$

Tear index is calculated by the following formula:

$$И_3(m_i) = \frac{\sum_{\gamma=1}^{n} Q_\gamma(m_i)}{n}. \tag{10}$$

Initial data, measurement and calculation results are presented in Table 3.

Tab. 3. The results of tear index tests ($i = a, b$; this record means that this table is used twice)

No (γ)	P_γ		$d_j(m_i, P_\gamma)$	$d_{H\gamma}(m_i)$	$d_{np\gamma}$	$P_\gamma \cdot d_{r\gamma}$	$Q_\gamma(m_i)$
	N	kgf					
1	P_1		$d_1(m_i, P_1)$ $d_2(m_i, P_1)$ $d_3(m_i, P_1)$	$d_{H1}(m_i)$	d_{np1}	$P_1 \cdot d_{r1}$	$Q_1(m_i)$
2	P_2		$d_1(m_i, P_2)$ $d_2(m_i, P_2)$ $d_3(m_i, P_2)$	$d_{H2}(m_i)$	d_{np2}	$P_2 \cdot d_{r2}$	$Q_2(m_i)$
...	...		...	...	...	...	...
n	P_n		$d_1(m_i, P_n)$ $d_2(m_i, P_n)$ $d_3(m_i, P_n)$	$d_{Hn}(m_i)$	d_{npn}	$P_n \cdot d_{rn}$	$Q_n(m_i)$
						Tear index	$И_3(m_i)$

By the difference $\Delta И_3 = И_3(m_a) - И_3(m_b)$ the best lubricant can be found.

3. PROCESSING OF RESEARCH RESULTS

For comparative researches it is expedient to use the plastic lubricants most widely presented in the market.

„Litol-24" was selected as tested lubricating material S. The grades quantity (the number of manufacturers) for the research was taqen as $p = 4$. The lubricant material grades were as follows, m_1: "OLLRIGHT", m_2: "Misma Ross", m_3: "ARGO" and m_4: "BMP auto".

After wear tests of the lubricants and calculations using equations (1) and (2) the following values of mean diameter of the wear spot were obtained:

1. $D_H(OLLRIGHT) = 0{,}50 mm$;
2. $D_H(Misma \ Ross) = 0{,}33 mm$;
3. $D_H(ARGO) = 0{,}35 mm$;
4. $D_H(BMP \ auto) = 0{,}41 mm$.

These data confirm distinctions of a chemical compound which can be caused not only character of productions, but also changes during ageing lubricants.

Influence test specifications of lubricants and render also properties of used metal samples.

For microhardness measurement the quantity of indentor dents in each of the tested surface area was taken as $q = 5$. After marqing and measurement of indentor dents and calculations applying (3), (4) and (5), the following values of microhardness in the initial surface area were obtained:

1. $HV(OLLRIGHT) = 181{,}03 kgf \setminus mm^2$;
2. $HV(Misma \ Ross) = 146{,}09 kgf \setminus mm^2$;
3. $HV(ARGO) = 138{,}88 kgf \setminus mm^2$;
4. $HV(BMP \ auto) = 188{,}05 kgf \setminus mm^2$.

The microhardness values in the abrasive wear area:

1. $HV_{a\delta}(OLLRIGHT) = 153{,}85 kgf \setminus mm^2$;
2. $HV_{a\delta}(Misma \ Ross) = 126{,}04 kgf \setminus mm^2$;
3. $HV_{a\delta}(ARGO) = 95{,}36 kgf \setminus mm^2$;
4. $HV_{a\delta}(BMP \ auto) = 151{,}21 kgf \setminus mm^2$.

The microhardness values in the adhesive wear area:

1. $HV_{a\partial z}(OLLRIGHT) = 138{,}91 kgf \setminus mm^2$;
2. $HV_{a\partial z}(Misma \ Ross) = \varnothing$; (The sign $\varnothing$ (empty set) means the absence of adhesive wear area.)
3. $HV_{a\partial z}(ARGO) = \varnothing$;
4. $HV_{a\partial z}(BMP \ auto) = 174{,}40 kgf \setminus mm^2$.

Fluctuations of microhardness are caused by anisotropy of mechanical properties of metal samples and character of adsorption of surface-active substances on a surface of friction. Influence can render and the maintenance polarly active products of oxidation of components PL.

Considering the values of wear spot mean diameter and microhardness values (the absence of adhesive wear areas) the following lubricating materials were selected for tear index tests – Sm_2: $Litol – 24(Misma Ross)$ and Sm_3: $Litol – 24(ARGO)$. From the load series 1 the set of employment $\{P_\gamma \mid \gamma = 1, 2, ..., 6\} = \{32$ kgf, 40 kgf, 50 kgf, 63 kgf, 80 kgf, 100 kgf, $\}$ was chosen. Its elements were arranged in the monotone increase order.

After tear index tests of these lubricating materials and taking into consideration the formulas (6), (7), (8), (9) and (10) the following values of tear index were received:

1. $И_3(Misma \ Ross) = 323 N$;
2. $И_3(ARGO) = 343 N$.

Material: $Litol – 24(Misma Ross)$ has less tear index than material. The difference is the following: $\Delta И_3 = И_3(m_3) – И_3(m_2) = 343$ N – 323 N = 20 N.

Thus, in case of lubricating material change from lubricant: $Litol – 24(ARGO)$ to lubricant Sm_2: $Litol – 24(Misma Ross)$ the tear index decrease, by 5 – 6%.

It is possible to assume, that in lubricant Litol - 24 (ARGO) contains more anti-adhesion polarly-active components, than in plastic lubricant Litol - 24 (Misma Ross). It can be caused both production, and process of ageing during storage of a product.

As products of ageing there can be such polarly-active components as:
1. Fat acids;
2. Spirits;
3. Complex ethers;

The given products are formed and change properties of plastic lubricants.

4. CONCLUSIONS

1. The developed generalized methods allow us to estimate the influence of any liquid or semisolid lubricating material of different grades on tribotechnical characteristics of friction pair "steel-steel" and choose the best lubricating materials.

2. The lubricating material *Sm₂: Litol* – 24 (*Misma Ross*) has the best anti-wear properties, mean diameter of wear spot – 0,33mm.
3. Anti-adhesion properties lubricant *Litol - 24 (ARGO)* has shown the best.
4. In communication with complexity of a chemical compound of the given lubricants there is a distinction anti-adhesion properties and character of influence of surface-active substances on a surface of friction of examinees of samples.
5. Differs and the bearing ability of the lubricant layer expressed in occurrence of zones of adhesive deterioration in case of use of one lubricants and absence of given zones at use of others.
6. In communication with complexity of a chemical compound of the given lubricants there is a distinction of anti-wearing properties and character of influence of surface-active substances on a surface of friction of examinees of samples.
7. Differs and the bearing ability of the lubricant layer expressed in occurrence of zones of adhesive deterioration in case of use of one lubricants and absence of given zones at use of others.
8. Following the executed analysis of microhardness measurements in the three areas it was established that:
   − initial surface has the highest microhardness;
   − microhardness of the worn area with abrasive type of wear is 15 – 20% lower than microhardness of the initial surface;
   − microhardness of the adhesive wear areas differs in extensive limits between the microhardness of the above mentioned areas.

REFERENCES

1. **Fedosov S. A., Peshek L.** (2004), *Definition of mechanical properties of materials by mikro-indentoring: Modern foreign techniques.* M., Physical faculty of the Moscow State University.
2. **Fridman I. B. (1974),** *Mechanical of property of materials.* Third edition, In two parts. A part the second. Mechanical tests. Constructional durability. M., Mechanical engineering, 1974.
3. **Glazov V. M., Vigdorovich V. N.** (1969), *Microhardness of metals and semiconductors*, Second edition, Publishing house "Metallurgiya".
4. **Qhruschov M. M, Berqovich E. S.** (1953), *Microhardness, that is defined by indentation method. M. – L.*, Publishing house of Academy of Science.
5. **Qhruschov M. M, Berqovich E. S.** (1960), *Instrument PMT-2 and PMT-3 for microhardness tests*, Machine Science Institute, Publishing house of Academy of Science.
6. **Zukovets I. I.** (1986), *Mechanical of test of metals*, M.: Highest school.
7. *Test methods, the control and research of machine-building materials (handbook, General redaction by* **A.T.Tumanov**), Vol. II. Methods of research of mechanical properties of metals. M., Mechanical engineering, 1974.

DESIGN AND EXPERIMENTAL TEST
OF A PNEUMATIC PARALLEL MANIPULATOR TRIPOD TYPE 3UPRR

Ryszard DINDORF[*], Paweł ŁASKI[**]

[*]AGH University of Science and Technology, AL. Mickiewicza 30, 31-059 Kraków
[**]Kielce University of Technology, al. Tysiaclecia Panstwa Polskiego 7, 25-314 Kielce

dindorf@agh.edu.pl, pawell@tu.kielce.pl

Abstract: The paper presents the design and experimental test of a tripod type-3UPRR pneumatic parallel manipulator. This manipulator consists of three identical kinematic chains (pneumatic axes) connecting the fixed base and the moving platform. The tool center point TCP of the moving platform is a resultant of relocation of three pneumatic rodless cylinders independently controlled by servo-valves. For simulation purposes a solid model of pneumatic tripod parallel manipulator in SolidWorks was constructed. Since the application of 3-CAD in modelling kinematics and dynamics of parallel manipulators is restricted further simulation was carried out by means of SimMechanics library and Matlab-Simulink package. The experimental research focused on determining the precision of positioning of manipulator's end-effector point of the moving platform during point-to-point control.

1. INTRODUCTION

The development of automation and robotics has increased interest in multi-axis pneumatic systems which are highly dynamic and reliable. However, due to unsatisfactory positioning accuracy of pneumatic servo-cylinder, their application in multi-axis manipulators is restricted. Pneumatic servo-cylinders used in multi-axis electro-pneumatic systems and referred to as pneumatic axes perform operations and function as supporting structure. Cartesian manipulators with pneumatic axes connected in series are classified as open-loop chain kinematic mechanisms. In serial kinematic chain elastic strains accumulate on particular pneumatic axes, which lowers the positioning accuracy of pneumatic manipulators. Parallel mechanism is a closed-loop mechanism in which the moving platform is connected to the fixed base by independent kinematic chains. Kinematic structure in the form of a closed-loop chain finds application in parallel kinematic robot (PKR) and parallel kinematic machine (PKM) (Hebsacker, 2000). Manipulators based on parallel kinematics structure can achieve better accuracy of repeatability and they can apply larger forces than conventional serial manipulators because of the higher stiffness of their mechanical structure. By using parallel kinematics in machine tools, high stiffness and high machine dynamics is achieved. With Stewart-Gough Platform as a base, numerous kinematic structures of parallel manipulators (Nonapod, Hexapod, Tripod) and hybrid manipulators (Tricept, Dyna-M, LinaPod) were formed. The names of kinematic structures of parallel manipulators are related to the kind of kinematic joint and the number of degrees of freedom (DoF). Six basic kinematic joints used in parallel manipulators were presented by Merlet (Merlet, 2000). In order to calculate degrees of freedom of parallel manipulators the formula proposed by Tsai is used (Tsai, 1999). The family of parallel manipulators includes translational parallel manipulators (TPM) based on three degrees

of freedom (3-DoF) and containing at least one prismatic joint. In the group of 3-DoF TPM manipulators the most common are – spatial parallel mechanism of the structure: 3-PUU, 3-UPU, 3-UPS, 3-CPU, 3-PUS, 3-PCRR and planar parallel mechanism of the structure: 3-RPR, 3-PRR, 3-PPR, 3-RRR (Company, 2000).

2. PROTOTYPE PNEUMATIC PARALLEL MANIPULATOR
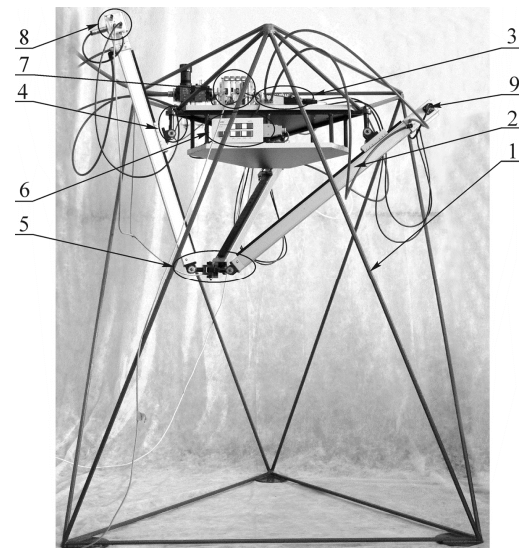
Fig. 1. Prototype of 3-UPRR pneumatic parallel manipulator:
1 – supporting structure, 2 – rodless pneumatic cylinder,
3 – proportional directional control valve, 4 – universal Cardan joint, 5 – moving platform, 6 – control panel,
7 – positioning axis controller, 8 – axis interface, 9 – axis connector

A prototype of pneumatic translational parallel manipulator (PTPM) of tripod kinematic structure was constructed in the Division of Mechatronics (Kielce University

of Technology, Poland) (Dindorf and Łaski, 2005). The prototype of tripod parallel manipulator with Festo servo-pneumatic precision positioning systems is presented in Fig. 1. The manipulator possesses a supporting structure, fixed base, moving platform and three pneumatic linear motions (servopneumatic axis). Each servo-pneumatic axis consists of: rodless pneumatic cylinder type DGPIL-25-600 with integral feedback transducer (built-in Temposonic encoders for continual positioning feedback to the master control unit), 5/3 servopneumatic valve (directional proportional control valve) type MPYE-5-1/8-HF-010B, axis interface type SPC-AIF, positioning axis sub-controller type SPC-200 (the use of a sub-controller card permits control of up to four axes) and Ethernet/Can Bus interface. Kinematic structure and structure control of the prototype of 3-DoF pneumatic translational parallel manipulators is shown in Fig. 2 and Fig. 3.
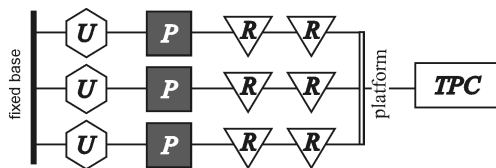

Fig. 2. Kinematic structure of 3-UPRR pneumatic parallel manipulator
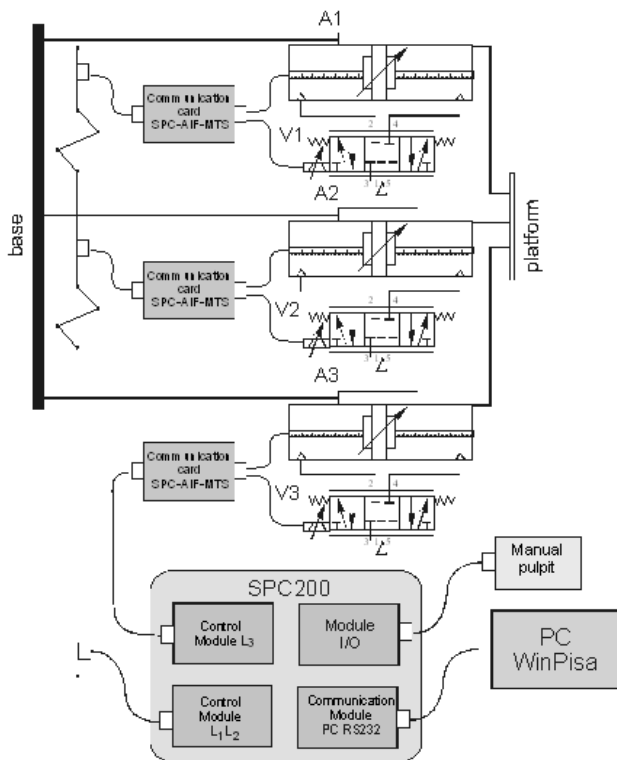

Fig. 3. Structure control of 3-UPRR pneumatic parallel manipulator

Each of the three identical closed-loop chains of the manipulator consists of serial kinematic chains: universal cardan joint (U), prismatic joint (P), formed by a rodless pneumatic cylinder and two revolute joints (2R) formed after universal cardan had been parted. The slide of rodless cylinder was connected with fixed base by means of articulated joints of U cardan and the end cap of cylinder were

connected by revolute joint R to the moving platform. The second revolute joint R was placed in tool center point (TCP) of the moving platform. The presented construction of the parallel manipulator ensures parallel position of the moving platform to the fixed base for optional position of pneumatic cylinder. The kinematic structure of a new prototype of 3-UPRR pneumatic parallel manipulator is an interesting solution expanding the architecture of parallel manipulators, type 3-DoF TPM.

3. MODEL RESEARCH ON PNEUMATIC PARALLEL MANIPULATOR

Software – CAD (*SolidWorks, Mechanical Desktop, Solid Edge*) commonly used by constructors enables designing solid models of complex mechanisms of parallel kinematics. A solid model of 3-UPRR pneumatic parallel manipulator obtained by *SolidWorks* is presented in Fig. 4.
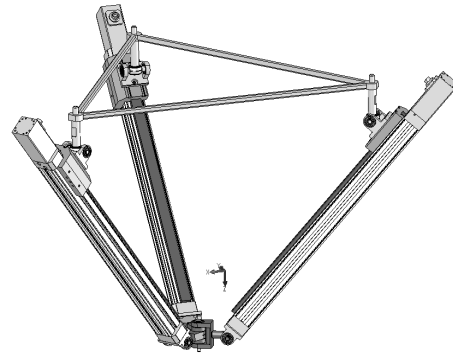
Fig. 4. Solid model of 3-UPRR pneumatic parallel manipulator

A revolute joint R is connecting the end cap of pneumatic cylinders with moving platform in point TCP and a U joint is connecting the slide pneumatic cylinder with a fixed base. In order to record geometric and kinematic relations holding for pneumatic parallel manipulator of 3-UPRR kinematics, its kinematic model presented in Fig. 5 was used (Dindorf et al., 2006). By means of *Dynamic Designer Motion*, which possesses graphic interface *SolidWorks* the simulation of pneumatic parallel manipulator's motion was conducted. In order to simulate the manipulator's motion it was necessary to define the basic parameters, kinematic joints and motion restrictions. For solid model a few composite relations were defined which enabled assigning them kinematic joints. In some cases it was necessary to introduce joints describing the construction's stiffness. Relying upon material properties and the shape of particular solids, the mass of the solid model was calculated. The simulation of manipulator's parallel mechanism motion was saved in avi format. The simulations conducted on a solid model aimed at position analysis of TCP point of the moving platform. The position of TCP point results from linear motion of pneumatic rodless cylinder, independently controlled by servo-valves.
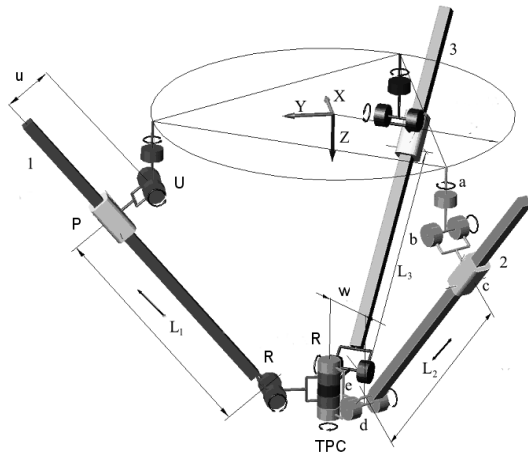
Fig. 5. Kinematic model of 3-UPRR pneumatic parallel manipulator
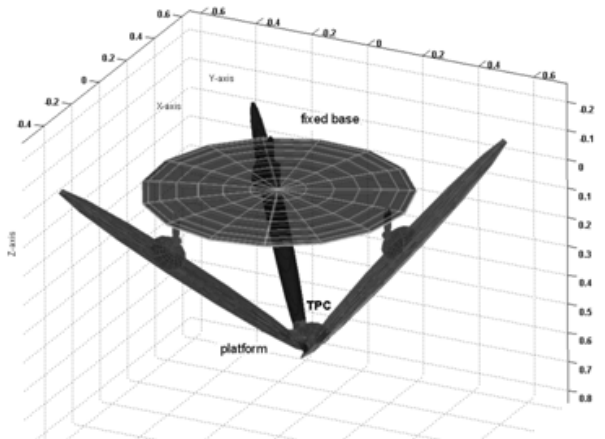
Fig. 6. Equivalent model of 3-UPRR pneumatic parallel manipulator
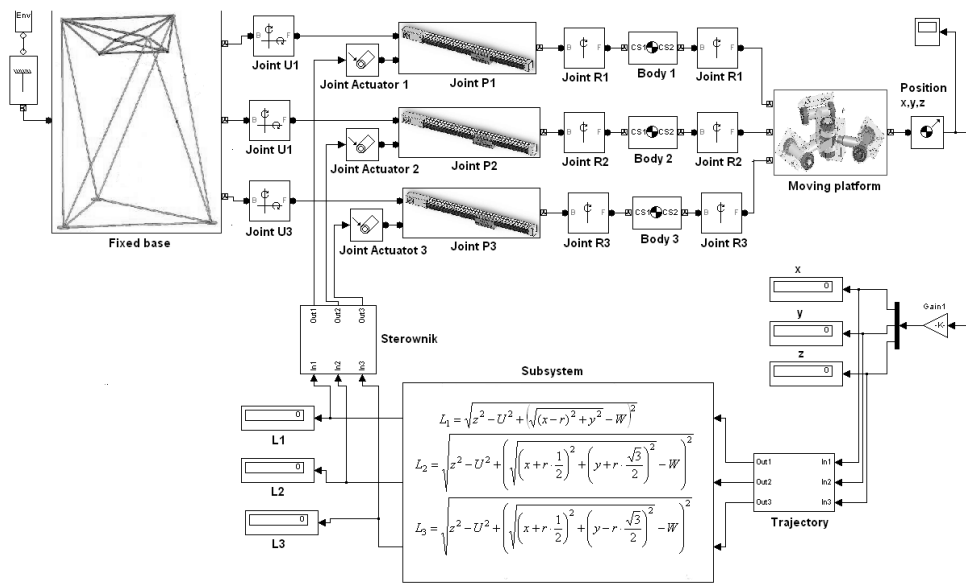
Fig. 7. Block-diagram of kinematic model of 3-UPRR pneumatic parallel manipulator

The solution of manipulator's kinematic reverse problem used in the design of control algorithm enabled to determine lengths of the movable links $L_1, L_2. L_3$ (displacement of linear pneumatic actuators) in relation to the coordinates of end-effector point $P(x,y,z)$ of tripod parallel manipulator:

$$L_1 = \sqrt{z^2 - U^2 + \left(\sqrt{(x-r)^2 + y^2} - W\right)^2} \qquad (1)$$

$$L_2 = \sqrt{z^2 - U^2 + \left(\sqrt{\left(x + r \cdot \frac{1}{2}\right)^2 + \left(y + r \cdot \frac{\sqrt{3}}{2}\right)^2} - W\right)^2} \qquad (2)$$

$$L_3 = \sqrt{z^2 - U^2 + \left(\sqrt{\left(x + r \cdot \frac{1}{2}\right)^2 + \left(y - r \cdot \frac{\sqrt{3}}{2}\right)^2} - W\right)^2} \qquad (3)$$

where: x, y, z – coordinates of end-effector point; P, r – ray of the circle circumscribing the equilateral triangle at the point where pneumatic servo-motors are fixed; z, U, W – geometric dimensions of the manipulator for the initial position of P point for the pneumatic actuators at their maximum stroke; $L_1, L_2. L_3$ - lengths of the movable links.

Since the application of *SolidWorks* in modeling kinematics and dynamics of parallel manipulators is restricted, further simulation was carried out by means of *SimMechanics* library of *Matlab-Simulink* package. The library enables the construction of complex mechanisms of parallel manipulators excluding mathematical descriptions of their kinematics and dynamics. In simulations based upon *SimMechanics* library an equivalent model of pneumatic tripod manipulator with its spatial orientation indicated was constructed. In *SimMechanics* library all the solid elements of the manipulator were described by substitute geometry by means of ellipsoids and assigned both masses and inertial tensors. In *Matlab-Simulink* environment tripod-based parallel kinematic manipulator was connected with its control system. On the basis of this scheme, the equivalent model of 3-UPRR pneumatic parallel manipulator was worked out (Fig. 6). The equivalent model retains kinematic joints and spatial orientation defined in solid model in *SolidWorks*. In order to create the

11

equivalent model, it was necessary to define the gravity centre of solids in central and local coordinates.
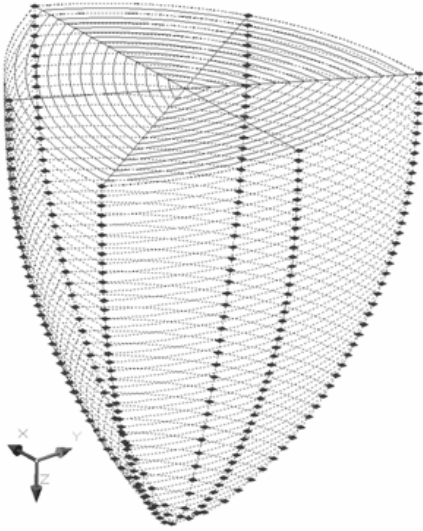

Fig. 8. Workspace of 3-UPRR pneumatic parallel manipulator

The kinematic model of 3-UPRR manipulator obtained by means of *SimMechanics* library is presented as simulation block in Fig.7. The kinematic model was used to analyse TCP trajectory of pneumatic parallel manipulator. The workspace of 3-UPRR pneumatic parallel manipulator in Cartesian coordinates is shown in Fig. 8.

4. EXPERIMENTAL RESULTS

The experimental research focused on determining the precision of positioning of manipulator's end-effector point of the moving platform during point-to-point control (Laski and Dindorf, 2007). The position and orientation of manipulator's end-effector point is dependent upon control of three pneumatic linear actuators (rodless cylinders). The maximum velocity of pneumatic actuators was $v_{max}=1,5$m/s, but their acceleration did not exceed $a_{max}=10$m/s^2. The exemplary trajectory of end-effector from P_1 point of coordinates [0,25; 0,44; 639,36] mm to P_2 point of coordinates [-91,46; 0,61; 408,22] mm, for the mass load $m = 0,2$ kg, is shown in Fig. 9.
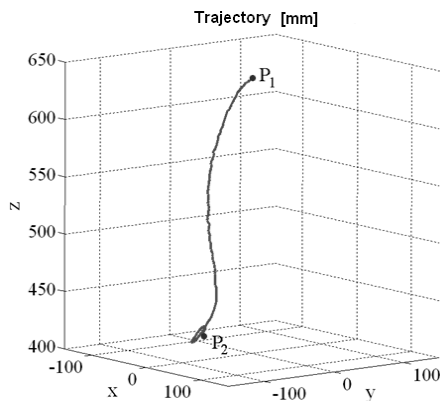
Fig. 9. Trajectory of the end-effector from point P_1 to point P_2

Fig. 10a and 10b presents the velocity and acceleration trajectories of the analyzed end-effector point in Cartesian space. The solution of manipulator's kinematic reverse problem was conducted by means of Matlab/Simulink package and toolbox SimMechanics. To control end effector from P_1 point to P_2 point in the Cartesian space XYZ it was necessary to control pneumatic linear actuators in order to change their positions according to the trajectory presented In Fig. 11a and the velocity corresponding to the trajectory given in Fig.11b.
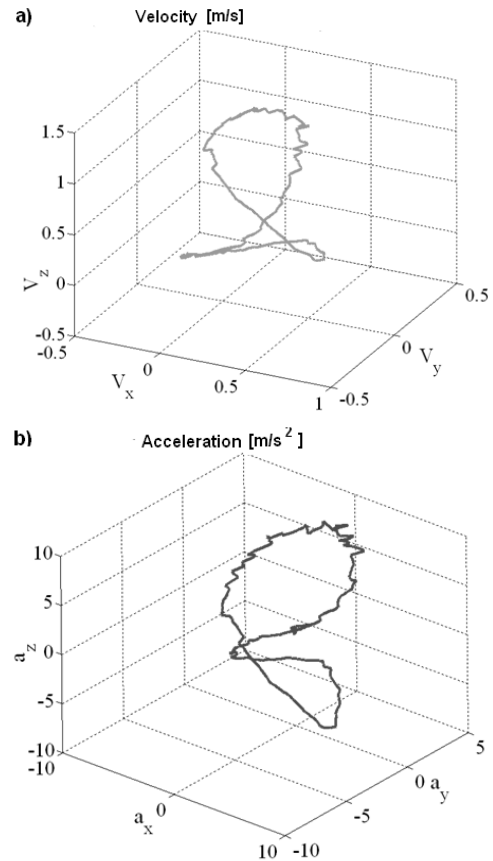
Fig. 10. Trajectories of velocity (a) and acceleration
(b) of the end effector point of a moving platform

The positioning accuracy of 3-UPRR manipulator's end-effector point from the position selected plane to the position measurement plane for different control velocity of linear pneumatic actuators was analyzed. For the purpose of the analysis 5 measurement series of manipulator's positioning accuracy were conducted. They comprised 30 measurement points fixed on measurement plane of the dimensions of 12x10 mm with a mapped grid of 2mm. The analysis was based upon the European Standard EN 29283: 1992 (Industrial Robots - Performance Criteria and Related Test Methods), which is the equivalent of ISO 9283: 1998. Fig. 12 presents the distribution of P points on measurement plane situated at the distance $z=490$mm from the manipulator's fixed base. The points were determined at the velocity of linear pneumatic actuators $v_{15}=0,15v_{max}$. On the basis of computations it may be concluded the positioning accuracy of the analyzed prototype of 3-UPRR manipulator is $\Delta xy =2,095\pm1.32$mm.
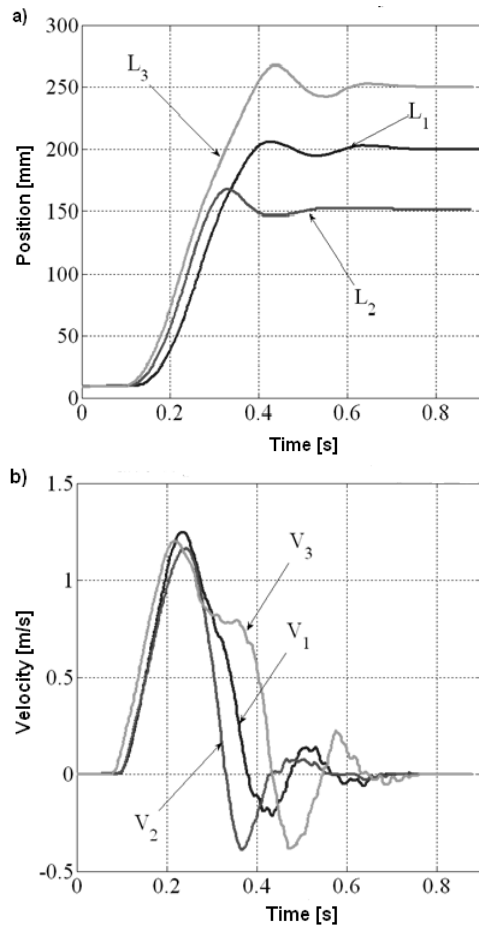
Fig. 11. Trajectories of position (a) and velocity
(b) of pneumatic linear actuators
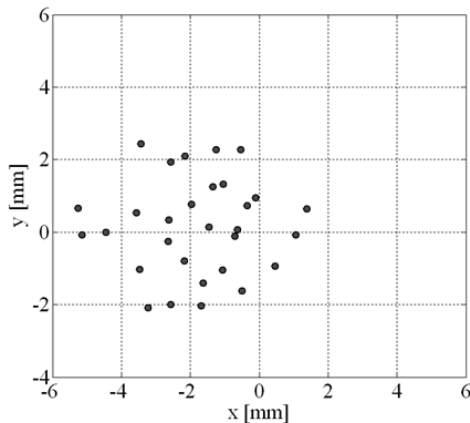
Fig. 12. Distribution of points on measurement plane
at the distance $z = 490$mm from the fixed base

The results of positioning accuracy obtained for different trajectories of end-effector point for the control of linear pneumatic actuators with v_{15} velocity were very similar. The differences in positioning accuracy result from different velocities of linear pneumatic actuators, for example for the velocity v_{10} the positioning accuracy is $\Delta xy = 1.397\pm0.893$ mm, while for the velocity of v_{30} the positioning accuracy reaches $\Delta xy = 3.616\pm2.025$ mm.

5. CONCLUSIONS

The paper presents the prototype of tripod pneumatic parallel manipulator of 3-UPRR kinematic structure. The tripod pneumatic manipulator consists of a supporting structure, fixed base, moving platform, prismatic joints (P-joints) – three servo-pneumatic axes, Cardan joints (U-joints) and rotary joints (R-joints). The single servo-pneumatic axis of the manipulator is composed of rodless pneumatic cylinder integrated with magnetostrictive measurement of position, proportional directional control valve, axis interface and axis connector, positioning axis controller. The aim of the project was to carry out model tests and simulations on a virtual model of tripod manipulator as well as conduct experimental research on a prototype of pneumatic parallel manipulator of 3-UPRR kinematics. Both the model tests and the experimental results show that the pneumatic parallel manipulator of 3-UPRR type fulfils the constructional assumptions and has satisfactory kinematic and dynamic properties. Further research will be directed towards improving the control accuracy of end-effector's trajectory by means of fuzzy logic control system (FLC) with real time interpolator and dSPACE software. The research conducted on the prototype of the pneumatic parallel manipulator of tripod kinematic structure is an original contribution towards development of parallel kinematic structures of pneumatic manipulators. The presented prototype of pneumatic parallel manipulator will find its application in both manufacturing and rehabilitation manipulators.

REFERENCES

1. **Company O**. (2000), *Machines-outils rapides à structure parallèle, Méthodologie de conception, applications et nouveaux concepts*, Universite Montpellier II, Sciences et Techniques du Languedoc, Montpellier.
2. **Dindorf R. P. Laski, Takosoglu J.** (2006), *Model research of pneumatic parallel manipulator, Virtual Design and Automation, New Trends in Collaborative Product Design*, Edited by Zenobia Weiss, Publishing House of Poznan University of Technology. Poznan.
3. **Dindorf R., Laski P.** (2005), Model research of pneumatic parallel manipulator prototype, *Mechanik*, 50, 8-9, 664-671,.
4. **Dindorf R., Laski P.** (2005), Model research of pneumatic parallel manipulator, *Pomiary Automatyka Kontrola*, 50, 6, 14-16.
5. **Hebsacker M.** (2000), *Entwurf und Bewertung Paralleler Werkzeugmaschinen - das Hexagliede*, ETH, Zürich.
6. **Laski P, Dindorf R.** (2007): Prototype of pneumatic parallel manipulator, *Hydraulika a Pneumatika* (Slovak Republic), 23, 1, 22-24.
7. **Łaski P., Dindorf R.** (2007), Prototyping of tripod-type pneumatic parallel manipulator, 11th International Scientific *Seminar on Developments in Machinery Design and Control*, Červený Kláštor (Slovak Republic), September 11-14.
8. **Merlet J. P.** (2000), *Parallel robot*, Springer Verlag, New York, London.
9. **Tsai L-W.** (1999*), Robot Analysis: The Mechanics of Serial and Parallel Manipulators*, John Wiley & Sons, New York.

COMPARISON OF GRAPH-BASED METHODS
OF KINEMATICAL ANALYSIS OF PLANETARY GEARS

Józef DREWNIAK[*], **Stanisław ZAWIŚLAK**[*]

[*]Faculty of Mechanical Engineering and Computer Science, University of Bielsko-Biała,
2 Willowa Street, 43-309 Bielsko-Biała, Poland

jdrewniak@ath.bielsko.pl, szawislak@ath.bielsko.pl

Abstract: In the paper three graph-based methods of planetary gear modeling are discussed. The following methods have been considered: Hsu's graph, contour graph and bond graphs-based methods. The theoretical ideas of the mentioned approaches were shortly revised and compared. Two of them were applied for analysis of an exemplary planetary gear. The consistency with traditional Willis method was checked. Advantages of the proposed approaches are highlighted.

1. INTRODUCTION

Design of gears especially planetary gears is a challenging engineering task. The computer or Artificial Intelligence (AI) aided approaches to design are more and more needed nowadays. In case of gears, graph-based methods for modeling of planetary gears seem to deliver a very efficient aid. The main advantages of graph-based models of planetary gears are as follows: the methods are algorithmic, they allow for comparison of results within a conceptual stage of design e.g. for kinematical analysis. They deliver algebraic structures to encode a planetary gear what allows in turn for evolutionary (Rao, 2000) or neuronal networks approaches to design (Zhang et al., 2010). They allow for creation of complete atlases of design solutions (functional schemes of planetary gears) which can not be done by means of any other tool (Tsai, 2001). The aim of the present paper is to present a rough comparison of three chosen graph based methods used for modeling of planetary gears and additionally an application of two of them for an analysis of an exemplary planetary gear. The practical engineering task e.g. kinematical analysis shows some details of modeling. Moreover, it allows for proving of usability of the proposed approach.

2. GRAPH-BASED MODELS OF PLANETARY GEARS

In the present paper, the graph-based methods of modeling of planetary gears were utilized for their kinematical analysis. The obtained results were compared with the traditional Willis method and the method of geometrical scheme of velocities. Three considered graph-based methods are as follows:
- Hsu graph-based (Drewniak and Zawiślak, 2009a, 2009b, 2010a; Zawiślak, 2008) which can be also called linear graph-based method; the original method were tailored by the authors to the analysis of some special types of planetary gears;
- contour graph-based (Marghitu, 2005; Drewniak and Zawiślak, 2010b; Zawiślak, 2010);
- bondgraph-based method (Cervantes et al., 2009, Wojnarowski et al., 2006).

Moreover, other tasks of planetary gear analysis (e.g. analysis of dynamics) can be performed by means of other graph-based approaches:
- vector network method (especially forces and moments of forces) (Lang 2005, Prahasto 1992);
- flow-graphs method (Nagaraj and Hariharan, 1973; Wojnarowski and Lidwin, 1975).

The ideas of three first mentioned methods are roughly compared in Tab. 1. The detailed description of the theoretical background for these methods can be found in cited references (Marghitu 2005, Tsai 2001) as well as in other works of the authors of the present paper. The application of these methods for an analysis of the exemplary planetary gear (Fig.1) is presented underneath.

3. EXEMPLARY PLANETARY GEAR

The exemplary planetary gear is presented in Fig.1 and Fig. 2. It has the following elements: main axis *I* with gear wheel *1*, planet carrier (arm) *h*, special rotating elements carried by the planet carrier (suns) i.e. on levels *b* and *d*. These elements have two toothings mounted on common axes i.e.: *2* and *3* as well as *4* and *5*, respectively - corresponding to axes *b* and *d*. Wheel *6* has an internal toothing.
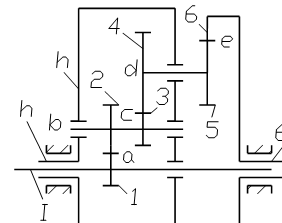
Fig. 1. Exemplary planetary gear; general layout

Other aspects of the gear are not taken into account in the considerations. Several modes of operation of the planetary gear are usually possible. If we brake a particular element (link) then the obtained ratio changes. In our case we consider the mode when link *6* is braked, e.g.: element *I* is considered as an input. An output is the arm *h* which external surface can be consider as a drum for a rope. Planet carrier *h* creates a housing form for majority of the gear

elements. The numbers of teeth for the considered planetary gear are as follows: $z_1=18$; $z_2=36$; $z_3=24$; $z_4=36$; $z_5=18$; $z_6=90$ or -90 – in case of Willis-method notation. We assume that modules are: $m_1=1$; $m_2=1.5$ and $m_3=2mm$, respectively.

   Additionally we consider two modes of working (operating) conditions:

(mode 1) - inputs: links I and h; output element 6;

       W – mobility (DOF – degree of freedom);

       $W = 3n – 2p_5 – p_4 = 3·5 – 2·5 – 3 = 2$;

(mode 2) - input: link I, output: link h and element 6

       is braked (is fixed);

       $W = 3n – 2p_5 – p_4 = 3·4 – 2·4 – 3 = 1$;

where: n – number of movable links, p_5, p_4 : numbers of full and half joints.

Fig. 2. Exemplary planetary gear; second operational mode

Tab. 1. Comparison of ideas of three graph based models of planetary gears

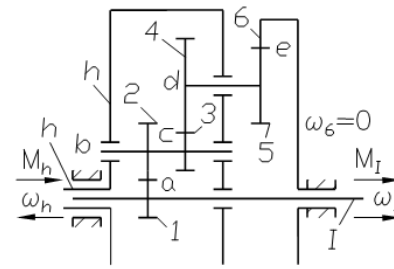| Task	General Comments	Graph-based methods		
		Hsu's graph	Contour graph	Bond graph
1	2	3	4	5
Abstracting Discretization Modeling	Rules of assignment	Relation between planetary gear elements, consideration of kinematical pairs: - meshing pair (gear pair), - rotating around common axis and - 'arm-planetary wheel' pair	Closed sequence of pairs of planetary gear elements e.g. starting and ending in fixed elements (e.g. bearings), relative rotational speeds of theses elements (links)are taken into account	General rules of assignment of bondgraphs to technical systems; in our case to mechanical system.
Generation of special graph structures: e.g: f-cycles, contours, … and cuts, paths etc.	Subgraphs used in modeling routines	f-cycles (Tsai, 2001) so called fundamental cycles in the meaning of their usage for representing some important features of mechanical system which is modeled via a graph with f-cycles	contours - (Marghitu, 2005) they can be recognized also as cycles but due to several books of Marghitu, the original notion is used	Assignment of physical properties and parameters to the set of nodes (bondgraph elements). Bonds (corresponding to the edges of common graph). Analysis of power flow paths.
	Method of making a representative set	Every meshing pair is taken into account plus additionally traditional meshing pairs (what is just considered)	All independent contours are taken into account. Every contour generates several equations e.g. sum of relative rotational velocities, sum of vector products: arm multiplied by an adequate rotational velocity	Bond-graph rules for creation of equations for particular types of nodes
Generation of codes Transfer of knowledge	Numerical/symbolical codes	Code of f-cycle: (a,b)c where: (a,b) meshing pair; a,b – geared wheels or a pinion or a ring with internal tooth, c – arm (planet carrier)	$0 \rightarrow 1 \rightarrow 2 \rightarrow … \rightarrow 0$; string of descriptions of consecutive gear elements; where: every of them passes rotary movement and power alongside a gear	Constitutional equations of bondgraph elements
Solution of the considered problem	Generation of Equations	E.g.: $\omega_a – \omega_c = \pm N_{ba}(\omega_b – \omega_c)$ where: + for internal and – for external meshing.	E.g.: $\Sigma \, \omega_{ij} = 0$ where: ω_{ij} - relative velocities	Generalized Kirchhoff laws
	Solution	Solution of system of algebraic equations	Turning of vector equations into scalar ones, e.g. due to the fact that all vectors act along the same direction. Solving the system of algebraic equations	Solution of DAE (differential and algebraic equations) system
Further possibilities	Different tasks: e.g.: synthesis, enumeration; which are possible especially due to graph-based methods	Enumeration according to functions, atlases of solutions, evolutionary design, neuronal network based analysis (graphs deliver a code of mechanical object)	Analysis of forces and moments; e.g. via contour method	Analysis of forces and moments, analysis of vibrations
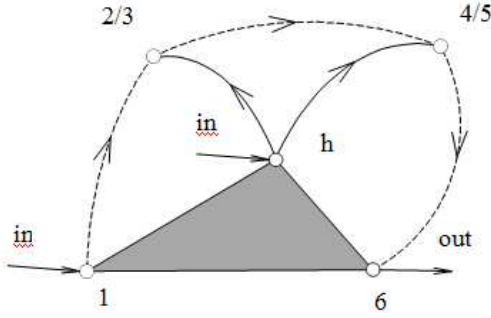
Fig. 3. Linear graph assigned to the exemplary gear
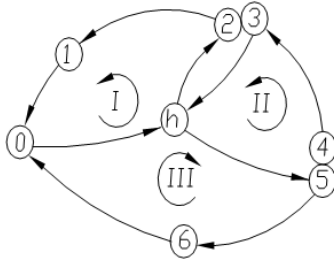
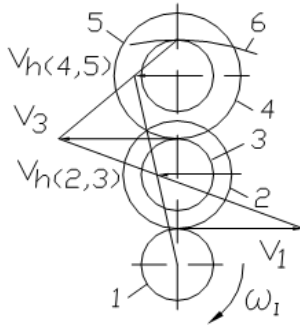**Fig. 4.** Contour graph assigned to the exemplary gear

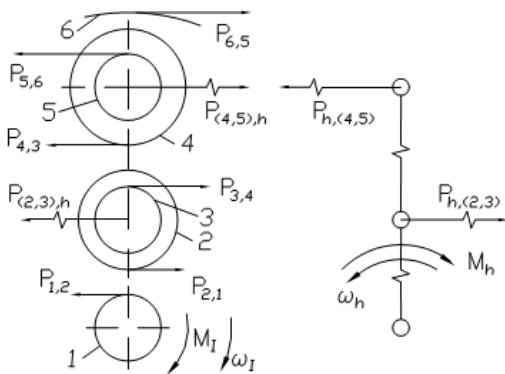**Fig. 5.** Scheme of linear and rotational velocities

Fig. 6. Scheme of forces and moments

3.1. Linear-graph-based model of planetary gear

The linear graph assigned to the planetary gear is presented in Fig. 3. This type of graph was introduced by Hsu (enclosing a polygon instead of a clique) but the method was slightly updated (Zawiślak, 2008). The polygon represents the links rotating around the main axis of the

planetary gear. Stripped line-edges represent pairs of links which are in mesh. Continuous line-edges represent pairs: planet wheel and planet carrier (arm). The notions 'in' and 'out' in Fig. 3 represent inputs and outputs, respectively. The paths from inputs to the output were introduced what was not considered by Hsu.

The graph based-method is performed in the following steps (Tab. 1): (a) abstraction i.e. process of generalization by reducing the information content – taking into consideration only gear kinematics and consideration of the moving chosen gear links; (b) discretization performed simultaneously with the step "a"; addionally – labeling the links; (c) distinguishing of relations among the elements (gear links); (d) assignment of a linear graph to a planetary gear – represented via its functional scheme; (e) transfer of knowledge from mechanics to graph theory; (f) generation of needed graph structures e.g. distinguishing of f-cycles; (g) generation of their codes; (h) generation of equations; (e) solving of equation system receiving – in the considered case – ratio or the output rotational velocity of the modeled planetary gear.

The structures related to a graph of the planetary gear are: so called f-cycles: *(1,2)h* and *(5,6)h*. Moreover we consider a pair *(3,4)* which represents two mating elements i.e. toothings *3* (on the link *2/3*) and toothings *4* (on the link *4/5*). For the last considered pair, the wheels have axes mounted on the arm which are not moved in mutual relation to themseves (axes fixed in relation to the arm *h*). However, they move always simultaneously with the arm. We consider the case when the gear works in the mode 1. Therefore, for the first mode of operation, the obtained system of equation is as follows: two equationns for two f-cycles plus one equation for traditional meshing of two geared wheels:

$$\begin{cases} \omega_1 - \omega_h = -N_{21}(\omega_2 - \omega_h) \\ \omega_5 - \omega_h = +N_{65}(\omega_6 - \omega_h) \\ \omega_5 = -N_{34}\omega_2 \end{cases} \quad (1)$$

where: ω_i ($i = 1,2, ..., 6$) and ω_h rotational velocities of the links; $N_{ij} = z_i/z_j$ local ratios; sign $\pm$ depends on external (-) or internal (+) meshing of a geared pair.

Taking into account ω_2 calculated from the first and ω_5 calculated from the second equation we have:

$$\omega_2 = \frac{\omega_h(N_{21}+1) - \omega_1}{N_{21}} \quad (2)$$

$$\omega_2(-N_{34}) = \omega_5 = +N_{65}\omega_6 + \omega_h(1-N_{65}) \quad (3)$$

Taking into account the equations (2),(3) and after some transformations we can calcutate the wanted ω_6:

$$\omega_6 = \frac{\omega_1 - \omega_h\left[\left(1 + \dfrac{z_2}{z_1}\right) + \dfrac{z_4}{z_3}\dfrac{z_2}{z_1}\left(1 - \dfrac{z_6}{z_5}\right)\right]}{\dfrac{z_2}{z_1}\dfrac{z_4}{z_3}\dfrac{z_6}{z_5}} \quad (4)$$

The same formula was obtained by means of the Willis method.

3.2. Contour-graph-based model of planetary gear

Contour graph method consists in the following steps: (a) distinguishing of independent contours; (independence is considered here in the light of graph theory); (b) listing the codes of the contours and sets of indexes; (c) generation of system of equations; (d) solution of this system of equations. The similarities and differences between linear-graph and contour-graph based methods are listed in Tab. 1. The main advantage is: that they are algorithmic some procedures can be turned into computer programs. The contours for the planetary gear presented in Fig. 2 can be written upon the contour graph assigned to the considered planetary gear (Fig. 4). These contours are as follows:

(I): $0 \rightarrow h \rightarrow 2/3 \rightarrow 1 \rightarrow 0$
(II): $h \rightarrow 2/3 \rightarrow 4/5 \rightarrow h$ (5)
(III): $0 \rightarrow h \rightarrow 4/5 \rightarrow 6 \rightarrow 0$

Every contour generates a system of equations concerning velocities, forces and moments (Marghitu, 2005). Here, we analyze kinematics, only, therefore we assign two equations to every contour. We consider the second mode of operation. The code of a contour generates a list of indexes – e.g. (I): *(h,0)*; *(2,h)*; *(1,2)*; *(0,1)*. Therefore the system of equations for the contour graph based method is as follows:

$$\begin{cases} \omega_h + \omega_{2h} + \omega_{12} - \omega_1 = 0 \\ \omega_{5h} + \omega_{34} + \omega_{h3} = 0 \\ \omega_{06} + \omega_h + \omega_{5h} + \omega_{65} = 0 \\ \omega_{2h}(r_1 + r_2) + \omega_{12} \cdot r_1 = 0 \\ \omega_{5h}(r_1 + \ldots + r_4) + \omega_{34}(r_1 + r_2 + r_3) + \omega_{h3}(r_1 + r_2) = 0 \\ \omega_{5h}(r_1 + \ldots + r_4) + \omega_{65}(r_1 + \ldots + r_5) = 0 \end{cases} \quad (6)$$

where the following formulas – coming off the method – are necessary to solve the system:

$$\omega_{h3} = \omega_{h2} \qquad \omega_{i0} = \omega_i$$
$$\omega_6 = 0 \qquad \omega_{ij} = -\omega_{ji} \qquad (7)$$
$$r_6 = r_1 + \ldots + r_5 \qquad r_i = \frac{m_i z_i}{2}$$

where: ω_{ij} – is a relative rotational velocity of the link *i* in relation to the link *j*.

Let's take into account ω_{i0} - so we consider a relative velocity in relation to the support (*0*) then we can omit this *0* and consider a general rotational velocity. The adequate notions were placed in the respective equations e.g.: the first in the system (6).

The last equation of the set (7) means that we consider the cylindrical geared wheels and we do not assume any corrections – therefore the distance between axes is equal to the sum of respective radiuses (pitch radiuses).

Originally, the equations of the system (6) enclose the vector quantities. However, cross products can be turned into scalar ones due to the physical and geometrical properties of planetary gear: rotational velocities as vectors act along the same axis and angles between radiuses and rotational velocities are equal to 90°. So, the transformed system is discussed for simplicity reasons. Solving the system (6) we eliminate all relative velocities which are not important for us, leaving only the general rotational velocities.

The solution of the system is as follows:

$$\frac{\omega_1}{\omega_h} = 1 - \frac{r_6 \cdot r_4 \cdot r_2}{r_5 \cdot r_3 \cdot r_1} = 1 - \frac{z_6 \cdot z_4 \cdot z_2}{z_5 \cdot z_3 \cdot z_1} \quad (8)$$

The equality of the expressions for radiuses and numbers of teeth holds due to the fact that there are the pairs of teeth being in mesh - in the numerator and denominator of the fraction so modules are pairwise reduced. So, it is interesting feature that the ratio does not depend on modules in consecutive geared pairs. Therefore we have finally:

$$\frac{\omega_1}{\omega_h} = 1 - \frac{90 \cdot 36 \cdot 36}{18 \cdot 24 \cdot 18} = -14 \quad (9)$$

The obtained result will be compared with the traditional methods of an analysis of planetary gears.

3.3. Willis formulas for the considered planetary gear

In case of the second mode of operation for the considered planetary gear, the Willis formulas are as follows:

$$i_{14}^h = \frac{\omega_1 - \omega_h}{\omega_4 - \omega_h} = \left(-\frac{z_2}{z_1} \right) \cdot \left(-\frac{z_4}{z_3} \right)$$
$$i_{56}^h = \frac{\omega_5 - \omega_h}{\omega_6 - \omega_h} = \left(-\frac{z_6}{z_5} \right) \quad (10)$$

Additionally, we have:

$$\omega_6 = 0 \quad \omega_5 = \omega_6 \quad (11)$$

The first condition from (11) confirms that this is the second mode of operation. The next expression means that elements *5* and *6* are stiffly mounted on the same axis. The solution is as follows:

$$\left. \frac{\omega_1}{\omega_h} \right|_{\omega_6 = 0} = 1 + \frac{z_6 \cdot z_4 \cdot z_2}{z_5 \cdot z_3 \cdot z_1} = -14 \quad (12)$$

Traditionally in the Willis method, the number of teeth for an internal toothing is consider as negative. Therefore the formulas (8) and (12) are equivalent because it was assumed that $z_6 = -90$.

In the same manner the Willis formula was generated for the first mode of operation of the considered planetary gear.

4. GRAPHICAL-PHYSICAL ANALYSIS OF THE PLANETARY GEAR

Graphical physical analysis of planetary gear can also be performed. It allows for additional confirmation of the obtained results as well as for further insight into the working conditions of a gear.

Like it was mentioned above also this phase of considerations can be done via graph based approach (Prahasto, 1992) but it is beyond the scope of the presented paper.

The scheme of linear and rotational velocities is presented in Fig. 5 and the scheme of forces and moments in Fig. 6, respectively. Based upon the Fig. 5 the following formulas can be written:

$$v_1 = \omega_1 \cdot r_1 = \frac{\pi \cdot n_1}{30} \cdot \frac{d_1}{2} \qquad (13)$$

The value of ω_I is the input velocity which is passed on the gear from the drive system (motor).

The next three relationships can be deduced upon the scheme presented in Fig. 5.

$$\frac{v_1 + v_{h,(2,3)}}{r_2} = \frac{v_3 - v_{h,(2,3)}}{r_3} \qquad (14)$$

$$\frac{v_3}{r_4 + r_5} = \frac{v_{h,(4,5)}}{r_5} \qquad (15)$$

$$\frac{v_{h,(2,3)}}{r_1 + r_2} = \frac{v_{h,(4,5)}}{r_1 + r_2 + r_3 + r_4 + r_5} \qquad (16)$$

Finally we can calculate the output rotational velocity:

$$\omega_h = -\frac{v_{h,(2,3)}}{r_1 + r_2} = \frac{v_{h,(4,5)}}{r_1 + r_2 + r_3 + r_4 + r_5} \qquad (17)$$

Solving the system of the above formulas the searched ratio of the gear can be calculated:

$$i_{1,h}^{6} = \left(\frac{\omega_1}{\omega_h} \right)_{\omega 6 = 0} = -14 \qquad (18)$$

The same result as previously was obtained.

Based upon the scheme of forces and moments further analyses of the planetary gear can be performed. Taking into account geometrical relationships as well as equilibrium conditions e.g.: $P_{1,2} = -P_{2,1}$ we can deduce that input and output rotational velocities have opposite directions and that the arm is a passive link.

5. CONCLUSIONS

Based upon the above presented considerations and references review, the following conclusions can be drawn:
1. the goals of modeling of planetary gears by means of graphs are versatile, for example:
   – derivation of calculation methods equivalent to traditional ones which however are algorithmic and allow for comparison of results;
   – performance of some tasks which could not be done in any other way e.g.: creating of complete atlases of design solutions;
   – creation of algebraic models for further theoretical analyses e.g.: isomorphism of structures representing gears (equivalence of kinematical schemes of relevant planetary gears);
2. there are many different methods of assignment 'planetary gear' ↔ 'graph';
3. some tasks can be done via several different graph-based methods, some of them are dedicated for particular purposes;
4. due to the fact that assignment of a graph generates inevitably an algebraic code of a planetary gear it – in

consequence – allows for evolutionary, neuronal network and immune analysis of gears;
5. three graph methods were theoretically compared;
6. two methods were used for kinematical analysis of an exemplary gear;
7. compatible results were obtained for them and the traditional Willis method as well as the graphical-physical analysis;
8. the graph-based methods of modeling of planetary gears are just recently after a constant development due to a possibilities of artificial intelligence consequences of this modeling – e.g. possibility of algorithmic synthesis of gears.

REFERENCES

1. **Cervantes-Sanchez J.J., Rico-Martinez J.M., Lasesma-Jaime R., Barroso-Hernandez J.L.** (2009), Simulation of planetary gear trains, modeling and numerical validation, *J. Multi-body dynamics*, Vol. 223, 53-71.
2. **Drewniak J., Zawiślak S.** (2009a), Synthesis of planetary gears by means of artificial intelligence approach especially graph-theoretical modeling, *Mechatronic Systems and Materials*, Vilnius, 126-128.
3. **Drewniak J., Zawiślak S.** (2009b), Analysis and Modification of Planetary Gears Based upon Graph-theoretical Models, *Transactions of the Universities of Košice*, No 2, 84-87.
4. **Drewniak J., Zawiślak S.** (2010a), Kinematical and dynamical analysis of closed kinematical chains using graphs and profile equations, *PAMM*, No 9, 547-548.
5. **Drewniak J., Zawiślak S.** (2010b), Linear-graph and contour-graph-based models of planetary gears, *J. of Applied and Theoretical Mechanics*, Vol. 48 No 2, 415-433.
6. **Lang S.Y.T.** (2005), Graph-theoretic modelling of epicyclic gear system, *Mech. Mach. Theory*, Vol.40, 511-529.
7. **Marghitu D.B.** (2005), *Kinematic chains and machine components design*, Elsevier, Amsterdam, San Diego; Academic Press, London.
8. **Nagaraj H.S., Hariharan R.** (1973), Flow-graph techniques for epicyclic gear train analysis, *International Journal of Control*, Vol. 17, No 2, 263-272.
9. **Prahasto T.** (1992), *Planetary gear analysis using the vector network method*, MSc-Thesis, (Supervisor: Prof. Andrews), University of Waterloo.
10. **Rao A.C.** (2000), A genetic algorithm for topological characteristics of kinematic chains, *ASME J. of Mechanical design*, Vol. 122, 228-231.
11. **Tsai L.W.** (2001), *Mechanism design. Enumeration of kinematic structures according to function*, CRC Press Boca Raton, Florida.
12. **Wojnarowski J., Kopeć J., Zawiślak S.** (2006), Gears and graphs. *J. of Applied and Theoretical Mechanics*, Vol. 44, No 1, 139-162.
13. **Wojnarowski J., Lidwin A.** (1975), The application of signal flow graphs - the kinematic analysis of planetary gear trains, *Mechanism and Machine Theory*, Vol. 10 (1-B), 17-31.
14. **Zawiślak S.** (2008), *Graph theoretic based models of planetary gears*, Teoria Maszyn i Mechanizmów, Editors.: J. Wojnarowski, I. Adamiec-Wójcik, Wyd. ATH, 67-74.
15. **Zawiślak S.** (2010), *Graph-base methodology as an artificial intelligence aid for mechanical engineering design*, Bielsko-Biała.
16. **Zhang M., Liao N., Zhou C.** (2010), A modified Hopfield neuronal networks model for graphs-based kinematic structure design, *Engineering with Computers*, Vol. 26, 75-80.

SEARCHING FOR THE VALUES OF DAMPING ELEMENTS
WITH REQUIRED FREQUENCY SPECTRUM

Andrzej DYMAREK[*], **Tomasz DZITKOWSKI**[*]

[*]Institute of Engineering Processes Automation and Integrated Manufacturing Systems,
Silesian University of Technology, Konarskiego 18A, 44-100 Gliwice, Poland

andrzej.dymarek@polsl.pl, tomasz.dzitkowski@polsl.pl

Abstract: This paper concerns formulating and solving the problem of synthesis of vibrating discrete mechanical systems with two – terminal damper. In this paper a method of synthesis to determination of structure and inertial, elastical, damping parameters has been presented. Such task may be classified as a reverse problem dynamics of vibration subsystems.

1. INTRODUCTION

Vibration damping occupies a significant place among the extensive issues of machinery and apparatus dynamics. It is one of the factors of mechanical energy dissipation, inseparably connected with mechanical systems movement.
A proper selection of frequency and operation outside the resonance range solve the problem of vibration avoidance. Leaving the resonance zone is the basic condition of apparatus functioning, however, it does not eliminate the problem completely. In many machines a lot of free vibration frequencies appear. In these cases damping is of crucial importance, because it lowers vibration amplitude significantly.

Equally important phenomenon, in which damping plays a major role, is the phenomenon of transition through the resonance zone (Buchacz, 1995, 2004, 2006; Buchacz et al., 2005). A number of components are adapted to operate in supercritical zone i.e. at frequencies higher than resonance frequency. In such a case transition through the resonance zone occurs during machine movement. Then poorly damped components are becoming temporarily subjected to strong vibrations. When damping phenomenon limits vibration amplitude insufficiently, additional damping is introduced (Buchacz, 2004, 2006; Buchacz et al., 2005; Dymarek and Dzitkowski, 2005; Dzitkowski, 2004; Dzitkowski and i Dymarek, 2005). The problem of searching damping component values, existing in mechanical systems, is a typical task of parametric synthesis due to required dynamical properties (Bellert and Woźniacki, 1968; Berge, 1973; Buchacz, 1991, 1997, 1995; Dymarek, 2000, 2004; Dymarek and Dzitkowski, 2005; Dzitkowski, 2001, 2004; Dzitkowski and Dymarek, 2005).

In the study the methods for synthesis of discrete vibration systems (Bellert and Woźniacki, 1968; Berge, 1973; Buchacz, 1991, 1997, 1995; Dymarek, 2000, 2004; Dymarek and Dzitkowski, 2005; Dzitkowski, 2001, 2004; Dzitkowski and Dymarek, 2005) with damping was presented.

The synthesis was done, using well-known methods of discrete vibration systems synthesis and by introduction of an assumption concerning damping type element, existing in the sought after system, and taking rheological Voigt's-Kelvin's model and Rayleigh's damping assumption as a mass damping model (Dymarek, 2000; Dymarek i Dzitkowski, 2005).

2. THE SYNTHESIS OF MECHANICAL SYSTEM WITH DAMPING

In this section the algorithm for actions taken during discrete damping systems synthesis will be presented.

In order to start the synthesis of damping systems (Dymarek, 2000; Dymarek i Dzitkowski, 2005; Dzitkowski and Dymarek, 2005) we should specify the properties of the sought-after system and the damping model, in accordance with the presented course of action:
1. Specify the values of resonance and anti-resonance frequencies in case of free vibration, i.e.:

$$\begin{cases} \omega_{b1}, \omega_{b2}, ..., \omega_{bn}, \\ \omega_{z1}, \omega_{z2}, ..., \omega_{zn}. \end{cases} \tag{1}$$

2. Determine the value of dimensional vibration factor λ, in case of V-K model:

$$b_{ci} = \lambda\, c_i \ , \tag{2}$$

$$0 < \lambda < \frac{2}{\omega_n}, \tag{3}$$

where: b_{ci} – damping, c_i – stiffness resulting from the synthesis carried out, λ=idem – dimensional vibration factor
3. Determine the parameter corresponding to damping in the system h_n in case of V-K model:

$$h_n = \frac{\lambda\, \omega_{bn}^2}{2} \ , \tag{4}$$

or by providing damping decrement for the individual resonance frequencies and anti-resonance frequencies:

$$\delta_n \approx \frac{2\pi h_n}{\omega_n}. \tag{5}$$

4. Determine the value of dimensional vibration factor h in case of mass model of damping:

$$b_{mi} = 2h \cdot m_i \ , \tag{6}$$

where: b_{mi} – damping, h – parameter corresponding to damping in the system, having frequency dimension, m_i – the value of inertia element determined as a result of synthesis.

The h parameter in the discussed case is constant, i.e.:

$$h = \text{idem} , \tag{7}$$

and its value should be chosen from the following bracket

$$0 < h < |\omega_{min}| , \tag{8}$$

where: $|\omega_{min}| \neq 0$ – the smallest value of resonance frequency, when the system restrained is synthesized or the smallest value which is equal to anti-resonance frequency when the half-defined system is synthesized.

5. Determine the value of dimensional vibration factor h in case of Rayleigh model of damping:

$$h_{Rn} = h_n + h \tag{9}$$

The examined characteristics are immobility $U(s)$ and mobility $V(s)$ built on the basis of assumed dynamic properties as described in 1-5.

The immobility function $U(s)$

$$U(s) = H \frac{d_l s^l + d_{l-1} s^{l-1} + \ldots + d_0}{c_k s^k + c_{k-1} s^{k-1} + \ldots + c_1 s} \tag{10}$$

and the mobility function $V(s)$

$$V(s) = H \frac{c_k s^k + c_{k-1} s^{k-1} + \ldots + c_1 s}{d_l s^l + d_{l-1} s^{l-1} + \ldots + d_0}, \tag{11}$$

where: l-odd or even numerator order with $l-k=1$, k- denominator order, H- any real positive number.

In order to determine elastic and inertial values, characteristic functions describing free vibrations in the form of immobility $U'(s)$ (12) and mobility $V'(s)$ (13) should be subject to the synthesis.

The immobility function $U'(s)$

$$U'(s) = H \frac{d_l s^l + d_{l-2} s^{l-2} + \ldots + d_0}{c_k s^k + c_{k-2} s^{k-2} + \ldots + c_1 s} , \tag{12}$$

The mobility function $V'(s)$

$$V'(s) = H \frac{c_k s^k + c_{k-2} s^{k-2} + \ldots + c_1 s}{d_l s^l + d_{l-2} s^{l-2} + \ldots + d_0}. \tag{13}$$

Then, the values of two-terminal damping type are to be determined on the basis of the relationship between (2) and (6), using inertial and elastic elements obtained in the first step of the synthesis

3. EXAMPLE

The assumed requirements of the desired system structure are:

$$\begin{cases} \omega_1 = 10\,\tfrac{\text{rad}}{\text{s}}, \omega_3 = 20\,\tfrac{\text{rad}}{\text{s}}, \omega_5 = 30\,\tfrac{\text{rad}}{\text{s}} - \text{resonance frequencies}, \\[2mm] \omega_0 = 0\,\tfrac{\text{rad}}{\text{s}}, \omega_2 = 15\,\tfrac{\text{rad}}{\text{s}}, \omega_4 = 25\,\tfrac{\text{rad}}{\text{s}} - \text{anti-resonance frequencies}. \end{cases}$$

In order to determine the analytical form of dynamical characteristics, the following assumptions should be taken.
Assumption 1
The characteristic sought after function is slowness $U(s)$.
Assumption 2
The requirements concerning damping for the two cases are assumed:
The mass model of damping:

$$b_{mi} = 2hm_i\,\frac{\text{Ns}}{\text{m}},$$
$$h = 0.8\,\frac{1}{\text{s}}. \tag{14}$$

The V-K model of damping:

$$b_{ci} = \lambda c_i\,\frac{\text{Ns}}{\text{m}}, \quad h_n = \frac{\lambda \omega_n^2}{2}\,\frac{1}{\text{s}},$$
$$\lambda = 0.01\,\text{s}. \tag{15}$$

The Rayleigh model of damping:

$$b_{ci}\,\frac{\text{Ns}}{\text{m}},\, b_{mi}\,\frac{\text{Ns}}{\text{m}},\, h_{Rn} = h_n + h\,\frac{1}{\text{s}} \tag{16}$$

The dynamical characteristics takes the form as follows:
- when the assumption of (14) is met:

$$U(s) = H \frac{\left(s^2 + 2hs + \omega_1^2\right)\left(s^2 + 2hs + \omega_3^2\right)\left(s^2 + 2hs + \omega_5^2\right)}{s\left(s^2 + 2hs + \omega_2^2\right)\left(s^2 + 2hs + \omega_4^2\right)}, \tag{17}$$

- when the assumption of (15) is met:

$$U(s) = H \frac{\left(s^2 + 2h_1 s + \omega_1^2\right)\left(s^2 + 2h_3 s + \omega_3^2\right)\left(s^2 + 2h_5 s + \omega_5^2\right)}{s\left(s^2 + 2h_2 s + \omega_2^2\right)\left(s^2 + 2h_4 s + \omega_4^2\right)}, \tag{18}$$

- when the assumption of (16) is met:

$$U(s) = H \frac{\left(s^2 + 2h_{R1} s + \omega_1^2\right)\left(s^2 + 2h_{R3} s + \omega_3^2\right)\left(s^2 + 2h_{R5} s + \omega_5^2\right)}{s\left(s^2 + 2h_{R2} s + \omega_2^2\right)\left(s^2 + 2h_{R4} s + \omega_4^2\right)}. \tag{19}$$

What should be submitted when carrying out the synthesis of characteristics (17), (18) and (19) is immobility, which describes free vibration in the form of:

$$U'(s) = H \frac{\left(s^2 + \omega_1^2\right)\left(s^2 + \omega_3^2\right)\left(s^2 + \omega_5^2\right)}{s\left(s^2 + \omega_2^2\right)\left(s^2 + \omega_4^2\right)}, \tag{20}$$

$$U'(s) = \frac{s^6 + 1400s^4 + 490000s^2 + 36000000}{s^5 + 850s^3 + 140625s}, \tag{21}$$

then, assumptions concerning damping (13), (14) and (15) should be taken into account.

As a result of synthesis carried out with the use of the method of characteristics function (21) distribution on continued fraction the values of inertial and elastic elements are obtained:
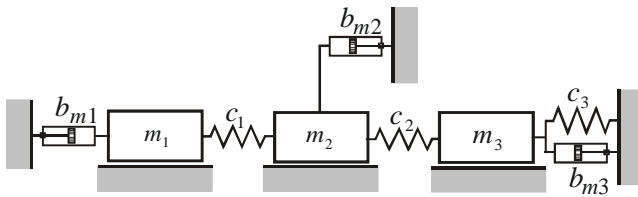
$$m_1 = 1.000\text{kg}, \, m_2 = 2.561\text{kg}, \, m_3 = 6.061\text{kg},$$
$$c_1 = 550.000\tfrac{\text{N}}{\text{m}}, \, c_2 = 730.424\tfrac{\text{N}}{\text{m}}, \, c_3 = 1390.822\tfrac{\text{N}}{\text{m}}. \tag{22}$$

Assuming that damping should be proportional to two-terminal inertial type:

$$\begin{cases} h = 0.8\dfrac{1}{\text{s}}, \\ b_{mi} = 2hm_i\,\dfrac{\text{Ns}}{\text{m}}, \end{cases} \tag{23}$$

the values elements of the system obtained (Fig. 1.) are as follows:

$$m_1 = 1.000\text{kg}, \, m_2 = 2.561\text{kg}, \, m_3 = 6.061\text{kg},$$
$$c_1 = 550.000\tfrac{\text{N}}{\text{m}}, \, c_2 = 730.424\tfrac{\text{N}}{\text{m}}, \, c_3 = 1390.822\tfrac{\text{N}}{\text{m}}, \tag{24}$$
$$b_{m1} = 1.600\tfrac{\text{Ns}}{\text{m}}, \, b_{m2} = 4.097\tfrac{\text{Ns}}{\text{m}}, \, b_{m3} = 9.697\tfrac{\text{Ns}}{\text{m}}.$$

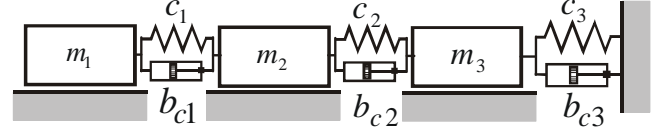**Fig. 1.** Synthesised mechanical system with the mass model of damping

Assuming the V-K model of damping:

$$\begin{cases} h_n = \dfrac{\lambda\omega_n^2}{2}\,\dfrac{1}{\text{s}}, \\ b_{ci} = \lambda c_i\,\dfrac{\text{Ns}}{\text{m}}, \\ \lambda = 0.01\,\text{s}, \end{cases} \tag{25}$$

the values of damping elements are in the form of:

$$b_{c1} = 5.500\,\tfrac{\text{Ns}}{\text{m}},$$
$$b_{c2} = 7.304\,\tfrac{\text{Ns}}{\text{m}}, \tag{26}$$
$$b_{c3} = 13.908\,\tfrac{\text{Ns}}{\text{m}}.$$

The structures of mechanicals systems with damping were created and its parameters are presented in Figs. 2, 3.

Fig. 2. Synthesised mechanical system with the K-V model of damping
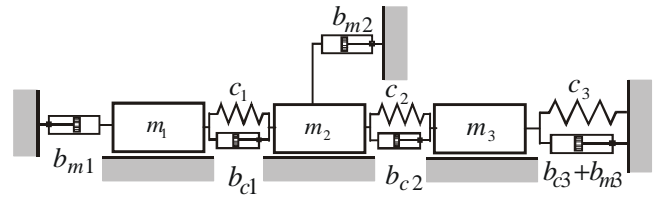
Fig. 3. Synthesised mechanical system with the Rayleigh's model of damping

where:

$$m_1 = 1.000\text{kg}, \, m_2 = 2.561\text{kg}, \, m_3 = 6.061\text{kg},$$
$$c_1 = 550.000\tfrac{\text{N}}{\text{m}}, \, c_2 = 730.424\tfrac{\text{N}}{\text{m}}, \, c_3 = 1390.822\tfrac{\text{N}}{\text{m}},$$
$$b_{m1} = 1.600\tfrac{\text{Ns}}{\text{m}}, \, b_{m2} = 4.097\tfrac{\text{Ns}}{\text{m}}, \, b_{m3} = 9.697\tfrac{\text{Ns}}{\text{m}}, \tag{27}$$
$$b_{c1} = 5.500\tfrac{\text{Ns}}{\text{m}}, \, b_{c2} = 7.304\tfrac{\text{Ns}}{\text{m}}, \, b_{c3} = 13.908\tfrac{\text{Ns}}{\text{m}}.$$

4. CONCLUSION

As a result of damped systems synthesis, when damping is proportional to stiffness and to values of mass, in case of synthesis of immobility, systems with cascade and branched structure are received. Received as a result of the synthesis inertial, elastic and damped parameters of the model are not the only ones which meet the assumed requirements referring to resonant frequencies – polars and zeros (Dymarek, 2000, 2004). Development of synthesis methods gives the possibilities of designing more and more complex mechanical systems with regard to requested dynamic features.

REFERENCES

1. **Bellert S., Woźniacki H.** (1968), *Analysis and synthesis of electrical systems by means of the method of structural numbers*, PWN, Warszawa (in Polish).

2. **Berge C.** (1973), *Graphs and hypergraphs*, Amsterdam-London: North Holland Publishing Co, American Elsevier Publishing Co, Inc., New York.

3. **Buchacz A.** (1991), The synthesis of vibrating bar systems represented by graphs and structural numbers, Scientific Letters of Silesian University of Technology, *Mechanics*, z.104, Gliwice (in Polish).

4. **Buchacz A.** (1995), Modelling, synthesis and analysis of bar systems characterized by a cascade structure represented by graphs, *Mech. Mach. Theory*, Vol. 30, No 7, 969-986.

5. **Buchacz A.** (2004), Modifications of cascade structure in computer aided design of mechanical continuous vibration bar systems represented by polar graph and structural numbers, *Journal of Materials Processing Technology*, Vol. 157-158, 45-54.

6. **Buchacz A.** (2006), Sensitivity of mechatronical systems represented by polar graphs and structural numbers as models of discrete systems, *Journal of Materials Processing Technology*, Vol. 175, 55-62.

7. **Buchacz A.** (Ed.) (1997), Computer aided synthesis and analysis of mechanical subsystems modelled with graphs and structural numbers. Letters of Silesian University of Technology, *Mechanics*, z.127, Gliwice (in Polish).

8. **Buchacz A., Dymarek A., Dzitkowski T.** (2005), *Design and examining of sensitivity of continuous and discrete- continuous mechanical systems with required frequency spectrum represented by graphs and structural numbers*, Monograph No. 88, Silesian University of Technology Press, Gliwice (in Polish).

9. **Dymarek A.** (2000), *The reverse task of vibrating mechanical systems with damping represented graphs and structural numbers*, PhD dissertation, Gliwice (in Polish).

10. **Dymarek A.** (2004), The Sensitivity as a Criterion of Synthesis of Discrete Vibrating Fixed Mechanical System, *Journal of Materials Processing Technology*, Vol. 157-158, 138-143.

11. **Dymarek A., Dzitkowski T.** (2005), Modelling and synthesis of discrete – continuous subsystems of machines with damping, *Journal of Materials Processing Technology*, Vol. 164-165, 1317-1326.

12. **Dzitkowski T.** (2001), *The reverse task of dynamics discrete-continuous mechanical systems represented graphs and structural numbers*, PhD dissertation, Gliwice 2001 (in Polish).

13. **Dzitkowski T.** (2004), Computer aided synthesis of discrete – continuous subsystems of machines with the assumed frequency spectrum represented by graphs, *Journal of Materials Processing Technology*, Vol. 157-158, 144-149.

14. **Dzitkowski T., Dymarek A**. (2005), The synthesis of machine driving systems, *Twelfth International Scientific and Engineering Conference - Machine-Building and Technosphere on the Border of the XXI Century*, Donetsk – Sevastopol 2005, Vol. 5, 66-70.

FINITE ELEMENT ANALYSIS OF TEMPERATURE DISTRIBUTION IN AXISYMMETRIC MODEL OF DISC BRAKE

Piotr GRZEŚ[*]

[*]Faculty of Mechanical Engineering, Białystok Technical University, ul. Wiejska 45 C, 15-351 Białystok

p.grzes@doktoranci.pb.edu.pl

Abstract: A transient thermal analysis is developed to examine temperature expansion in the disc and pad volume under simulated operation conditions of single braking process. This complex problem of frictional heating has been studied using finite element method (FEM). The Galerkin algorithm was used to discretize the parabolic heat transfer equation for the disc and pad. FE model of disc/pad system heating with respect to constant thermo-physical properties of materials and coefficient of friction was performed. The frictional heating phenomena with special reference to contact conditions was investigated. An axisymmetric model was used due to the proportional relation between the intensity of heat flux perpendicular to the contact surfaces and the rate of heat transfer. The time related temperature distributions in axial and radial directions are presented. Evolution of the angular velocity and the contact pressure during braking was assumed to be nonlinear. Presented transient finite element analysis facilitates to determine temperature expansion in special conditions of thermal contact in axisymmetric model.

1. INTRODUCTION

The automotive application of the disc brakes is susceptible to relatively high and stability of the friction coefficient. However its value affects the temperature rise, which is firmly intensive during repetitive braking process or emergency, high-speed stops. It is essential to predict the impact of the real geometrical set of the disc brake system to facilitate evaluation of the heat expansion with special operation conditions. High temperature exceeding permitted values may cause premature wear, brake fade, thermal judder or thermal cracks in the rotor material.

The calculation of the heat generated between two bodies in sliding contact such as disc brake systems necessitates appropriate model including contact conditions to obtain reliable outcomes. Various techniques have been employed for the computation of sliding surface temperatures. Analytical methods of heat conduction problem are limited of the half-space or the half-plane. More accurate for finite object, transform technique have been used, but numerous mathematical difficulties implies simplifications in geometry. The finite element method among numerical techniques is held as the most suitable for thermal problem investigation recently.

Talati and Jalalifar (2008, 2009) proposed two models of frictional heating in automotive disc brake system: namely macroscopic and microscopic model. In the macroscopic model the first law of thermodynamics has been taken into account and for microscopic model various characteristics such as duration of braking, material properties, dimensions and geometry of the brake system have been studied. Both disc and pad volume have been investigated to evaluate temperature distributions. The conduction heat transfer was investigated using finite element method (Talati and Jalalifar, 2008). The same authors solved heat conduction problem analytically using Green's function approach (2009).

For simulation cause of the experimental results, the finite element method is proposed as a relevant numerical simulation of disc/pad interface temperature estimation by Qi and Day (2007). Special effort is employed in the real and apparent area of contact between two sliding bodies due to topography of the friction surface. Authors attempt to determine range of the affection on its performance including temperature growth and wear presence.

Choi and Lee (2004) deal with the thermoelastic behaviour of disc brakes. Contact problems in disc/pad interface including heat transfer and elastic problem have been studied. In addition, the influence of the material properties were analysed. Based on numerical results, the carbon-carbon materials with expected excellent characteristics were compared.

Heat transfer problem in the mine winder disc brake using FE modelling technique has been developed by Ścieszka and Żolnierz (2007). Temperature distributions including thermoelastic instability phenomena were analysed. Wide variety of the parameters used in the computations were adopted from examinations comprising infrared mapping. The numerical simulation was confirmed in the experimental investigations.

In this paper the finite element method for temperature assessment due to frictional heating in an axisymmetric arrangement of the disc brake model is developed. Irresistible advantages of this numerical technique are reported by Grześ (2009). Perfect contact conditions of thermal behavior of disc/pad zone have been established.

2. STATEMENT OF THE PROBLEM

Considering physical substance of the friction systems, the energy conversion should be noticeable as a dominant. The large amount of the thermal energy are transferred into kinetic energy to decelerate vehicle being in motion. In the disc brake systems two major parts may be distinguished: rotating axisymmetric disc and immovable non-axisymmetric pad (Fig. 1). While braking process occurs total heat is dissipated by conduction from disc/pad interface to adjacent components of brake assembly and hub and by convection to atmosphere in accordance to Newton's law. In common the radiation is neglected due to relatively low temperature and short time of the braking process.
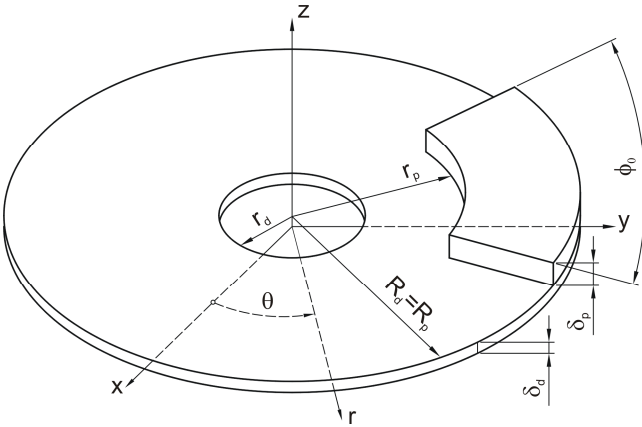

Fig. 1. The schematic assignment of disc brake system

The procedure of the temperature distribution assessment utilizing finite element method, adapted in an axisymmetric model is an efficient method which has already been reported in the area of frictional heating problem (Choi and Lee, 2004; Grześ, 2009; Ramachandra Rao et al., 1989). Grześ (2009) analyzed two types of the disc brake assembly related to different boundary conditions including evolution of contact pressure and velocity of the vehicle for validation purposes of the developed numerical technique.

In this paper temperature distributions in the disc and the pad volume have been studied. Material properties are assumed to be isotropic and independent of the temperature. The real surface of contact between a brake disc and pad in operation is equal to the apparent surface in the sliding contact. Perfect contact conditions for simplification purposes were assumed.

Single disc with pad presence has been analyzed with its simplification to symmetrical problem. Hence one side of the disc has been insulated in the FE model. Furthermore adiabatic boundary conditions are prescribed on the boundary of the inner radii of the disc and on the piston side of the pad.

Excluding both thermally insulated boundaries and the area of sliding contact where the intensity of heat flux has been established, on all remaining surfaces to consider realistic heat conditions, the exchange of thermal energy by convection to atmosphere has been implied.

It is assumed that the pressure varies with time (Chichinadze et al., 1979)

$$p(t) = p_0\left(1 - e^{-\frac{t}{t_m}}\right), \ 0 \le t \le t_s, \tag{1}$$

where: p_0 is the nominal pressure, t_m is the growing time, t_s is the braking time.

The angular velocity corresponding to pressure (1) equals (Yevtushenko et al., 1999)

$$\omega(t) = \omega_0\left[1 - \frac{t}{t_s^0} + \frac{t_m}{t_s^0}\left(1 - e^{-\frac{t}{t_m}}\right)\right], \ 0 \le t \le t_s, \tag{2}$$

where: ω_0 is the initial angular velocity, t_s^0 is the time of braking with constant deceleration.

3. MATHEMATICAL MODEL

To evaluate the contact temperature conditions, both analytical and numerical techniques have been developed. The starting point for the analysis of the temperature field in the disc and pad volume is the parabolic heat conduction equation given in the cylindrical coordinate system which is centered in the axis of disc and z points to its thickness (Nowacki, 1962)

$$\frac{\partial^2 T}{\partial r^2} + \frac{1}{r}\frac{\partial T}{\partial r} + \frac{\partial^2 T}{\partial z^2} = \frac{1}{k_d}\frac{\partial T}{\partial t}, r_d \le r \le R_d, 0 < z < \delta_d, t > 0,$$

$$\frac{\partial^2 T}{\partial r^2} + \frac{1}{r}\frac{\partial T}{\partial r} + \frac{\partial^2 T}{\partial z^2} = \frac{1}{k_p}\frac{\partial T}{\partial t}, r_p \le r \le R_p, \delta_d < z < \delta, t > 0 \tag{3}$$

where $k_{d,p}$ is the thermal diffusivity, $\delta_{d,p}$ is the thickness, $r_{d,p}$ and $R_{d,p}$ are the internal and external radius of the disc and pad respectively, $\delta = \delta_d + \delta_p$. The subscripts p and d imply the pad and the disc respectively. The substantiation of the axisymmetric arrangement of the problem has already been reported as a relevant foundation (Grześ, 2009).

Two-dimensional model of disc brake is presented in Fig. 3. The boundary and initial conditions for the disc and pad are given as follows:

$$K_d\frac{\partial T}{\partial z}\bigg|_{z=\delta_d} = \begin{cases} h[T_a - T(r,\delta_d,t)], r_d \le r \le r_p, \ t \ge 0, \\ q_d(r,\delta_d,t), \ r_p \le r \le R_d, 0 \le t \le t_s, \end{cases} \tag{4}$$

$$K_p\frac{\partial T}{\partial z}\bigg|_{z=\delta_d} = -q_p(r,\delta_d,t), \ r_p \le r \le R_p, 0 \le t \le t_s, \tag{5}$$

$$K_d\frac{\partial T}{\partial r}\bigg|_{r=R_d} = h[T_a - T(R_d,z,t)], \ 0 \le z \le \delta_d, \ t \ge 0, \tag{6}$$

$$K_p\frac{\partial T}{\partial r}\bigg|_{r=r_p} = -h[T_a - T(r_p,z,t)], \ \delta_d \le z \le \delta, \ t \ge 0, \tag{7}$$

$$K_p\frac{\partial T}{\partial r}\bigg|_{r=R_p} = h[T_a - T(R_p,z,t)], \delta_d \le z \le \delta, t \ge 0, \tag{8}$$

$$\left.\frac{\partial T}{\partial r}\right|_{r=r_d} = 0, \; 0 \le z \le \delta_d, \; t \ge 0, \tag{9}$$

$$\left.\frac{\partial T}{\partial z}\right|_{z=0} = 0, \; r_d \le r \le R_d, \; t \ge 0, \tag{10}$$

$$\left.\frac{\partial T}{\partial z}\right|_{z=\delta} = 0, \; r_p \le r \le R_p, \; t \ge 0, \tag{11}$$

$$T(r,z,0) = T_0, \; r_d \le r \le R_d, \; 0 \le z \le \delta_d, \tag{12}$$

$$T(r,z,0) = T_0, \; r_p \le r \le R_p, \; \delta_d \le z \le \delta, \tag{13}$$

where (Ling F. F., 1973)

$$q_d(r,z,t)\big|_{z=\delta_d} = \frac{\phi_0}{2\pi} \gamma f p(t) r \omega(t), \; r_p \le r \le R_p, 0 \le t \le t_s, \tag{14}$$

$$q_p(r,z,t)\big|_{z=\delta_d} = (1-\gamma) f p(t) r \omega(t), \; r_p \le r \le R_p, 0 \le t \le t_s, \tag{15}$$

f is the friction coefficient, p is the contact pressure, ω is the angular velocity, t is the time, r is the radial coordinate, z is the axial coordinate.

The above cases are two-dimensional problem for transient analysis. The boundary and initial conditions are specified for disc and pad volume respectively.

4. FE FORMULATION

Understanding of overall formulation is crucial for the solution of the considering thermal problem. In Fig. 2 the interface conditions of contact model are shown. In order to simulate perfect contact during braking process, two terms at the subsequent pair of nodes on the contact surfaces have been imposed
1) the equality of the temperature at any instant of time

$$T_{pi}(0+,t) = T_{dj}(0-,t) \tag{16}$$

2) and the following heat balance condition at each of the contact surfaces given by

$$q_{pi}(0+,t) + q_{dj}(0-,t) = q(t) \tag{17}$$

The object of this section is to develop approximate time-stepping procedures for axisymmetric transient governing equations. The detailed description of the two-dimensional discretization was presented by Grześ (2009).

Using Galerkin's approach the following matrix form of the Eq. (3) is formulated (Lewis et al., 2004)

$$[\mathbf{C}]\left\{\frac{d\mathbf{T}}{dt}\right\} + [\mathbf{K}][\mathbf{T}] = \{\mathbf{R}\} \tag{18}$$

where $[\mathbf{C}]$ is the heat capacity matrix, $[\mathbf{K}]$ is the heat conductivity matrix, and $\{\mathbf{R}\}$ is the thermal force matrix.
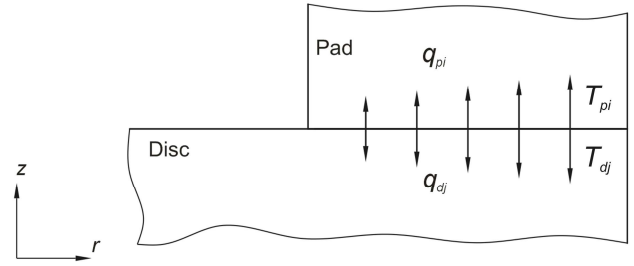

Fig. 2. Contact model for the thermal problem

In order to solve the ordinary differential equation (18) the direct integration method was used. Based on the assumption that temperature $\{T\}_t$ and $\{T\}_{t+\Delta t}$ at time t and $t+\Delta t$ respectively, the following relation is specified

$$\{\mathbf{T}\}_{t+\Delta t} = \{\mathbf{T}\}_t + \left[(1-\beta)\left\{\frac{d\mathbf{T}}{dt}\right\}_t + \beta\left\{\frac{d\mathbf{T}}{dt}\right\}_{t+\Delta t}\right]\Delta t \tag{19}$$

Substituting Eq. (19) to Eq. (18) we obtain the following implicit algebraic equation

$$([\mathbf{C}] + \beta\Delta t[\mathbf{K}])\{\mathbf{T}\}_{t+\Delta t} = ([\mathbf{C}] - (1-\beta)[\mathbf{K}]\Delta t)\{\mathbf{T}\}_t + (1-\beta)\Delta t\{\mathbf{R}\}_t + \beta\Delta t\{\mathbf{R}\}_{t+\Delta t} \tag{20}$$

where β is the factor which ranges from 0.5 to 1 and is given to determine an integration accuracy and stable scheme.
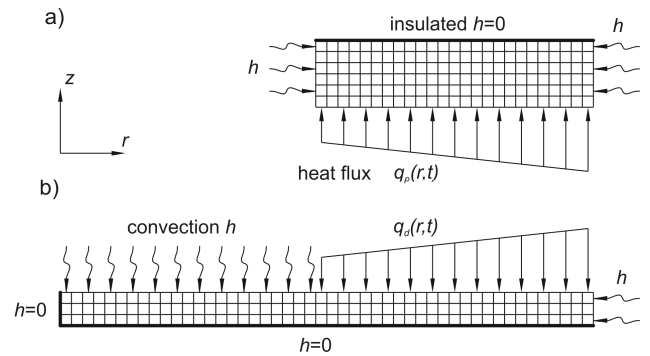
Fig. 3. FE model with boundary conditions
for the transient analysis: a) pad, b) disc

The finite element formulation of the disc brake with boundary conditions is shown in Fig. 3. Disc and pad components described below were analyzed using the MD Patran/MD Nastran software package (Reference Manual MD Nastran, 2008; Reference Manual MD Patran, 2008). In the thermal analysis of disc brake an appropriate finite element division is indispensable. In this study eight-node quadratic elements were used for the finite element analysis. The disc brake FE model consists of 576 elements and 1933 nodes of disc and 663 elements and 2118 nodes of pad. High order of elements ensure appropriate numerical accuracy. For the purpose of providing perfect contact conditions between each pair of nodes in the disc/pad interface, 103 Multipoint Constraints (MPC) were used.

To avoid inaccurate or unstable results, a proper initial time step associated with spatial mesh size is essential (Reference Manual MD Nastran, 2008).

$$\Delta t = \Delta x^2 \frac{\rho_d c_d}{10 K_d} \qquad (21)$$

where ρ is the density, c is the specific heat and K is the thermal conductivity, Δt is the time step, Δx is the mesh size (smallest element dimension). In this paper fixed $\Delta t = 0.005$s time step was used.

5. RESULTS AND DISCUSSION

In this paper thermal FE models of the disc brake with pad presence have been investigated. Proposed FE modeling technique (Grześ, 2009) was confronted with the analytical solution (Talati and Jalalifar, 2009) and FEA (Gao and Lin, 2002). The simulation includes conductive and convective terms of the real brake exert. Temperature distributions were predicted for the operation conditions given in Tab. 2. Material properties adopted in the analysis for FE model are specified in Tab. 1. The transient solution was performed for the pressure p and angular velocity of the disc ω evolution shown in Fig. 4.
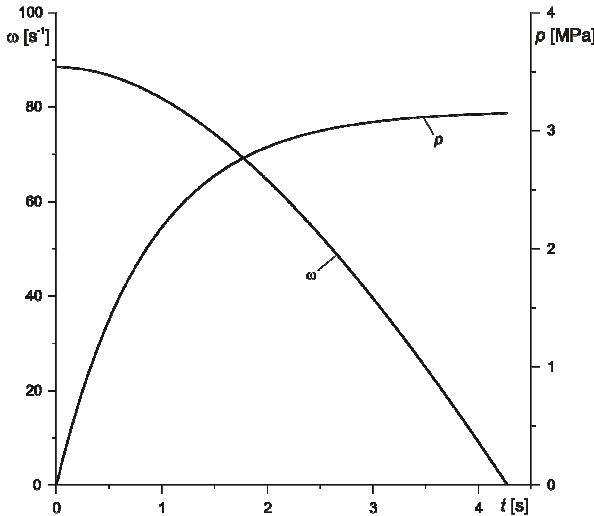

Fig. 4. Evolution of the pressure p and angular velocity ω during braking

The temperature distributions in arbitrarily specified instants of braking time are presented in Fig. 5. The equilibrium of the temperatures on contact surfaces at the z position of 0.006mm is noticeable in the solution. The intensity of heat flux entering into the disc and pad respectively excites growth of the temperature from the contact zone, which in subsequent measures extends particularly into the disc volume. Temperature variations through braking duration in z coordinate are relatively smooth in the disc area and rapid in the pad zone. The dissimilarity of heat dissipation between disc and pad volume in axial coordinate at the each step of the analysis are fundamentally dictated by the properties of materials adopted in this study. At the

time of t=4s temperature distribution of the disc is approximately equal at any position in radial direction. Temperature field of the pad is constant upwards of r=0.010m at any moment of presented results. The highest value of the temperature obtained in the analysis occurred at radius of r=0.127m at the contact surface. The results are believed to be physically justifiable values.
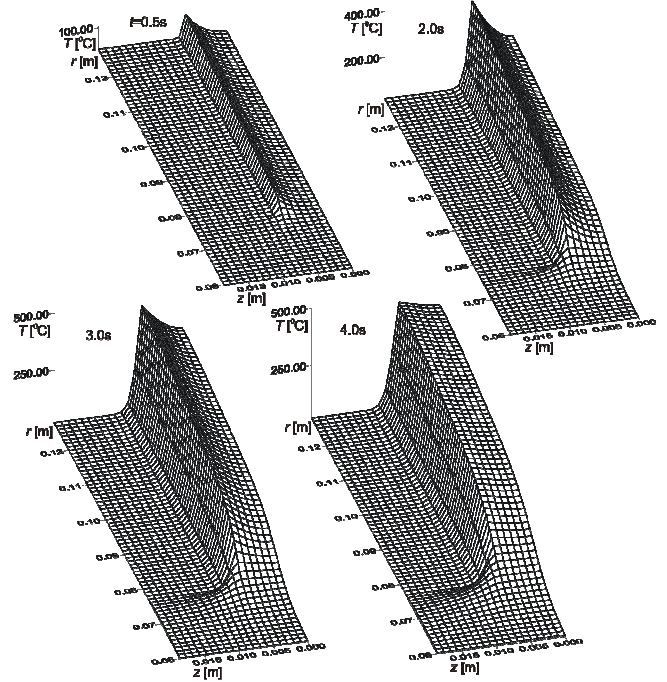
Fig. 5. The temperature distribution in the disc and pad volume at specified instants of braking time

Axial temperature distributions at the radius of 0.127m of disc brake are presented in Fig. 6. Within the analysis time of t_s=4.274s heat was generated due to friction behavior at the disc/pad interface. Therefore temperature increase is noticeable. Over the final time step of braking (t=3.5-4.274s) the interface temperatures can be seen to decrease slightly. This effect corresponds intermediately to the intensity of heat flux, which rises with time until the value of velocity and pressure product attains highest, critical value at the particular, radial position. The temperature expansion is significantly affected by the thermo-physical properties of materials submitted to the thermal load. As it can be seen the differences in axial directions are sufficiently high, particularly in pad zone. The gradient of temperatures in subsequent periods of time during single braking action is an issue of transformation of large amounts of the kinetic energy into heat energy in relatively short time. In addition, temperature of the disc and pad are affected by external convective conditions and decreases due to Newton's law of cooling. This phenomenon may be intensified when the vehicle is still moving and cooling is forced by the air flow.

Comparison of the radial temperature values at the contact surfaces including free surface of the disc during braking process is illustrated in Fig. 7. Maximum temperature rise up to 496.6°C at 0.127m of radial position and 3.375s

of time However, it can be seen that at the external location of the radius in the range of 0.001m, the temperature varies slightly. The impact of the intensity of heat flux entering the disc and pad respectively is noticeable above the radial location of 0.077m. Presented isotherms validate the adiabatic boundary condition at the inner radius of the disc where the temperature value is constant during braking process.
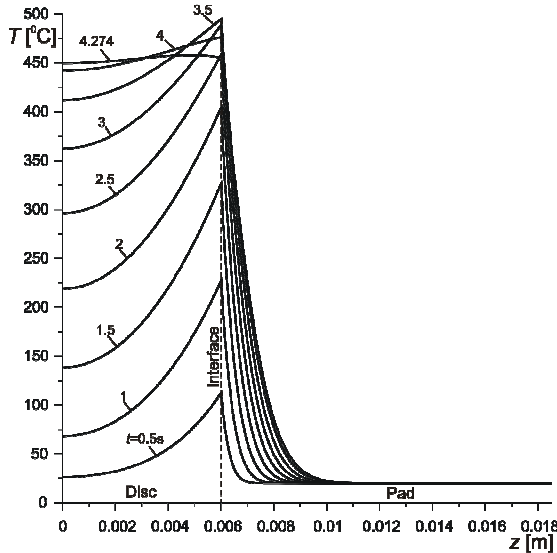

Fig. 6. Axial temperatures profiles at radius of 0.127m
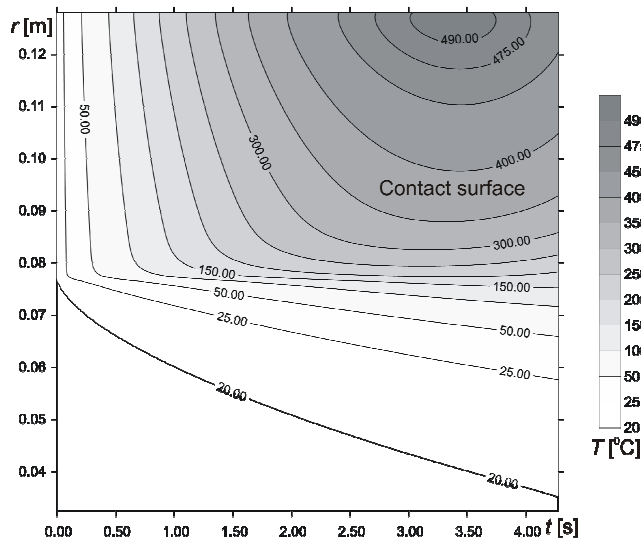
Fig. 7. Radial isotherms at the disc/pad interface

In Fig. 8 axial temperature evolution in the period of single braking process is shown. Fundamental differences of the temperature expansion between two considered zones of the disc and pad are noticeable. Temperature of the disc in axial coordinate rises relatively rapidly in the entire thickness at considered radius of 0.127m, while majority of pad area remains unheated. The isotherm of the highest value of temperature of 490°C obtained in the analysis outlines slight area near to the contact position of z direction.

In Fig. 9 disc temperature at r=0.127m and at different

axial positions are presented. The symmetry in axial coordinate z has been assumed. Profiles from z=0m which indicates central location of the real disc to its maximum thickness of z=0.006m are evaluated. At the initial period of braking process maximum temperature appears at the disc/pad interface (z=0.006m). Tendency to convergence of temperature at different axial positions at the end of braking process is noticeable. It is connected with alignment of temperatures in disc area in subsequent stage of the process when the intensity of heat flux descents.
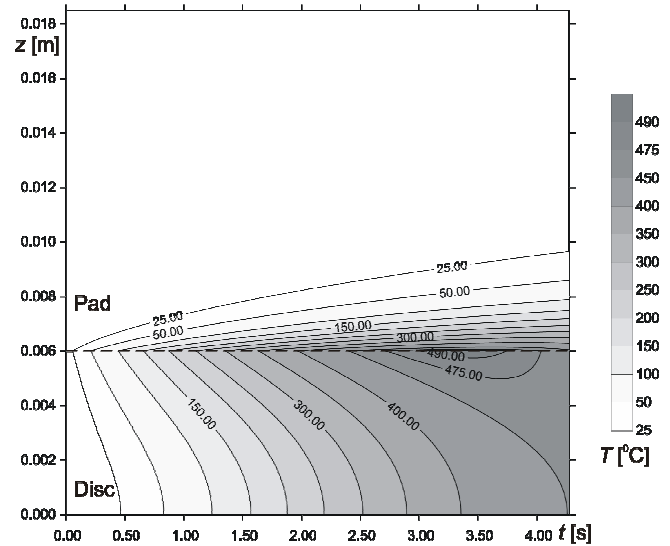
Fig. 8. Axial isotherms at radius of 0.127m
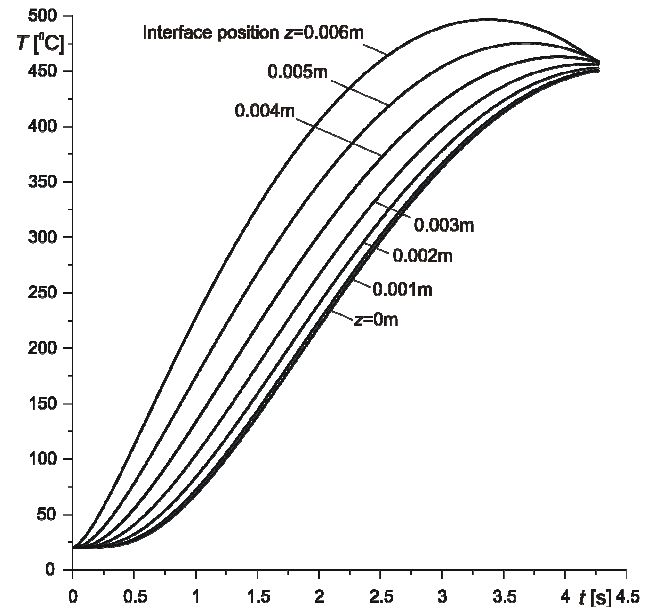
Fig. 9. Evolution of the disc temperature
at different axial distances and at radial position of 0.127m

In Fig. 10 the pad temperature distributions at r=0.127m in different axial positions are shown. As it can be seen the pad temperature at the contact surface (z=0.006m) has the highest value obtained during simulation process and gradual decay of the temperature should be noticed at different axial positions up to z=0.010m (0.004m of pad

thickness), where temperature remains approximately constant.
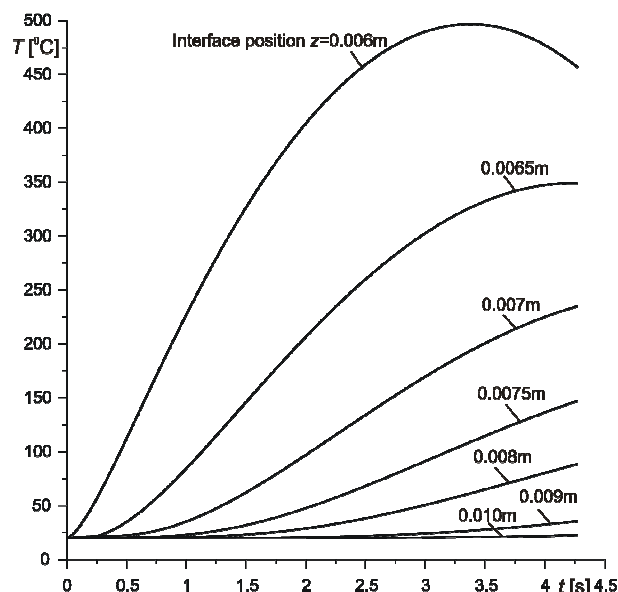
Fig. 10. Evolution of the pad temperature at different axial distances and at radial position of 0.127m

Tab. 1. Material properties [2]

Thermo-physical properties	Disc	Pad
Thermal conductivity, $K_{d,p}$ [W/mK]	48.46	1.212
Specific heat, $c_{d,p}$ [J/kgK]	419	1465
Density, $\rho_{d,p}$ [kg/m³]	7228	2595

Tab. 2. Operation conditions [2]

Operation conditions	Disc	Pad
Inner radius, $r_{d,p}$[mm]	32.5	77
Outer radius, $R_{d,p}$ [mm]	128	
Cover angle of pad, ϕ_0		64.5
Thickness $\delta_{d,p}$ [mm]	6	12.5
Initial velocity ω_0 [s⁻¹]	88.46	
Time of braking, t_s [s]	4.274	
Pressure p_0 [MPa]	3.17	
Coefficient of friction f	0.5	
Heat transfer coefficient h[W/m²K]	100	
Initial temperature T_0 [⁰C]	20	
Ambient temperature T_a [⁰C]	20	
Time step Δt [s]	0.005	

6. CONCLUSION

In this paper transient thermal analysis of disc brake in the single brake application was developed. The frictional heating phenomena using the finite element method of the thermal contact problem was performed. This study provides an evaluation of temperature distribution during braking action including both the disc and pad presence in an axisymmetric arrangement.

The outcomes obtained in the analysis show inequality in the temperature distribution of axial positions at the subsequent values of radial locations considering the disc and pad areas due to the different thermal properties of materials.

The influence of the convective heat transfer terms has been found relatively insignificant in the temperature distributions of considering behavior of single, emergency braking.

In view of the disc geometry aspect the results shows negligibly low temperature variations in the area of the disc beneath internal radius of the pad.

However imposed terms of perfect contact of disc/pad interface specify special, idealized conditions neglecting wear and debris (third body), the behavior of considering phenomena characterizes nature of the heat expansion and facilitates predicting the magnitude of the temperature rise during braking process.

REFERENCES

1. **Chichinadze A. V., Braun E. D., Ginsburg A. G. et al.** (1979), *Calculation, test and selection of frictional couples*, Science, Moscow *(in Russian)*.
2. **Gao C. H., Lin X. Z.** (2002), Transient temperature field analysis of a brake in a non-axisymmetric three-dimensional model, *J. Mater. Proc. Technol.*, Vol. 129, No. 1, 513–517.
3. **Grześ P.** (2009), Finite element analysis of disc temperature during braking process, *Acta mechanica et automatica*, Vol. 3, No. 4, 36-42.
4. **Lewis R. W., Nithiarasu P., Seetharamu K. N.** (2004), *Fundamentals of the finite element method for Heat and Fluid Flow*, John Wiley & Sons.
5. **Ling F. F.** (1973), *Surface mechanics*, John Wiley & Sons, New York.
6. **Nowacki W.** (1962), *Thermoelasticity*, Pergamon Press, Oxford.
7. **Qi H.S., Day A.J.** (2007), Investigation of disc/pad interface temperatures in friction braking, *Wear*, Vol. 262, No. 5-6, 505–513.
8. **Ramachandra Rao V. T. V. S., Ramasubramanian H. and Seetharamu K. N.** (1989), Analysis of temperature field in brake disc for fade assessment, *Wärme- und Stoffübertragung*, Vol. 24, No. 1, 9-17.
9. **Ścieszka S., Żołnierz M.** (2007), Wpływ cech konstrukcyjnych hamulca tarczowego maszyny wyciągowej na jego niestabilność termosprężystą. Część I. Budowa modelu MES i jego weryfikacja, *Zagadnienia Eksploatacji Maszyn*, Vol. 42, No. 3, 111-124.
10. **Ścieszka S., Żołnierz M.** (2007), Wpływ cech konstrukcyjnych hamulca tarczowego maszyny wyciągowej na jego niestabilność termosprężystą. Część II. Badania symulacyjne, *Zagadnienia Eksploatacji Maszyn*, Vol. 42, No 4, 183-193.
11. **Taguchi G.** (1993), *Taguchi on Robust Technology Development*, ASME Press, New York.
12. **Talati F., Jalalifar S.** (2008), Investigation of heat transfer phenomena in a ventilated disk brake rotor with straight radial rounded vanes, *Journal of Applied Sciences*, Vol. 8, No. 20, 3583-3592.
13. **Talati F., Jalalifar S.** (2009), Analysis of heat conduction in a disk brake system, *Heat Mass Transfer*, Vol. 45, No. 8, 1047-1059.
14. **Yevtushenko A. A., Ivanyk E. G., Yevtushenko O. O.** (1999), Exact formulae for determination of the mean temperature and wear during braking. *Heat and Mass Transfer*, Vol. 35, No. 2, 163–169.
15. **MSC.Software** (2008), *Reference Manual MD Nastran, Version r2.1*.
16. **MSC.Software** (2008), *Reference Manual MD Patran, Version r2.1*.

OVERLAY DENTURES – CONSTRUCTIONAL AND RESEARCH ASPECTS

Marek JAŁBRZYKOWSKI[*], **Joanna MYSTKOWSKA**[*]

[*]Faculty of Mechanical Engineering, Bialystok University of Technology, Wiejska 45 C, 15-351 Białystok

m.jalbrzykowski@pb.edu.pl, j.mystkowska@pb.edu.pl

Abstract: The paper presents selected issues relating to movable dentures with their general characteristics of fixings. Reference was made to the most important material-constructional aspects and the problems that arise with this type of solutions. In the work the method of durability and reliability evaluation and selection of materials for the kinematics connections of this type of structure was proposed.

1. INTRODUCTION

Modern dental prosthetics is a very vast area of science that makes it possible to reconstruct the shortcomings of teeth in the form of fixed or movable additions. The group of prosthetic permanent additions includes: crowns, bridges, inlays. In the group of movable dentures are: partial, complete and skeletal. As regards of design, the construction of each of these elements can be distinguished on: skeleton, prosthetic superstructure and fixing elements (Ciaputa, 2009). Fig. 1 shows the modules of the traditional components of a prosthetic bridge. In sense of the operational life and reliability, the key technological process elements include: material, design and technology implementation. The process of securing dentures in the oral cavity and clinical aspects are also important, but these problems are not the subject of work.

Crowns and bridges are permanently embedded, without need to remove it from the mouth. They do not perform well, when the shortcomings are more extensive, covering several cavities. In case of several teeth lost, the denture making is considered. At present, the most popular are acrylic prosthesis in which the artificial teeth are mounted in acrylic plate lying on the palate and gums (Ciaputa, 2009; Hupfauf, 1997). Such a structure is a burden on the bone and soft tissues and does not provide a stable support in the mouth. Much better results provide skeleton denture application. Metal, individually matched frame by braces and prosthetic thorns tightly embeds the patient's own teeth. Such a solution minimizes the chewing forces, transferred to the soft tissues and bone. In order to strengthen the location of the prosthesis in the mouth, a number of precise fixing elements such as latches, slides, telescopes and magnetic fastening is applying. These details allow easy removing off the prosthesis, ensure its stable maintenance and fully comfortable use.

Constantly evolving dental technique makes it impossible to present in this work all types of kinematic connections currently used in the overlay dentures. Thus, only selected types of precise elements are presented, with objective of assessment of their possible approximations immutability and operational reliability. In this context, the author's method of assessment their durability is proposed.
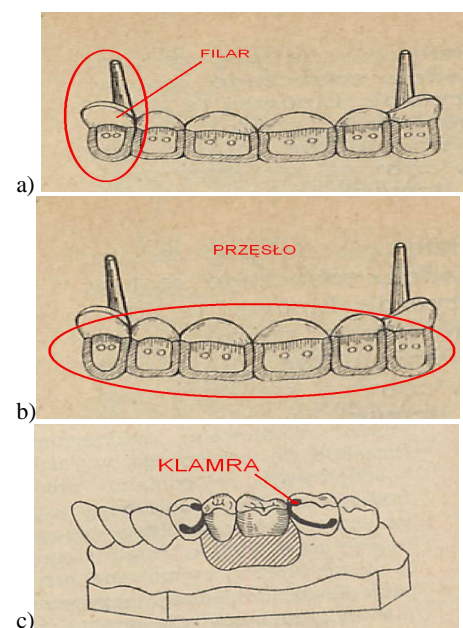
Fig. 1. The construction of prosthetic bridge: a) the pillar of a bridge, b) bridge span, c) buckle (fixing elements)

2. OVERLAY DENTURES JOINTS

It is well known that the precise fastenings are applying to stable or movable prostheses. There are fixed on the prosthetic pillars (natural teeth or implants). They are constructed with two main elements forming the mechanical connection between them. One part is the matrix – seated on the tooth or several teeth, the root of the tooth or at implant, and the second part – quite often is fixed in the mobile denture. In comparison to clasps, precise fasteners have many advantages, for example (Ciaputa, 2009; Hupfauf, 1997; Raszewski, 2009; Sajewicz, 2008):

– they allow to get a good aesthetic effect (avoid metal on the vestibular surface of tooth),
– during the dynamic phase of mastication, precise components ensure impact of only vertical forces on the pillar teeth and preferred stimulation of the toothless segments of prosthetic foundation in a static phase, causing that the prosthesis rely only on the mucous membrane,

− the denture track introduce is always a parallel trajectory to the long axis of resistance tooth,
− in case of the deterioration of prosthesis maintenance, the individual connectors elements can be activated or replaced.
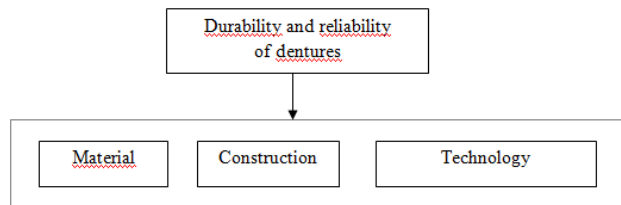
Fig. 2. The denture operational durability using engineering conditions
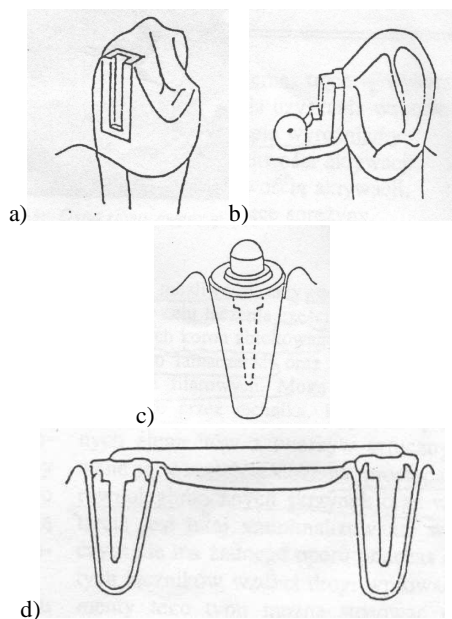
Fig. 3. The examples of precisely constructional joints:
a) inside the tooth, b) outside the crown, c) root clasps, d) crosspieces
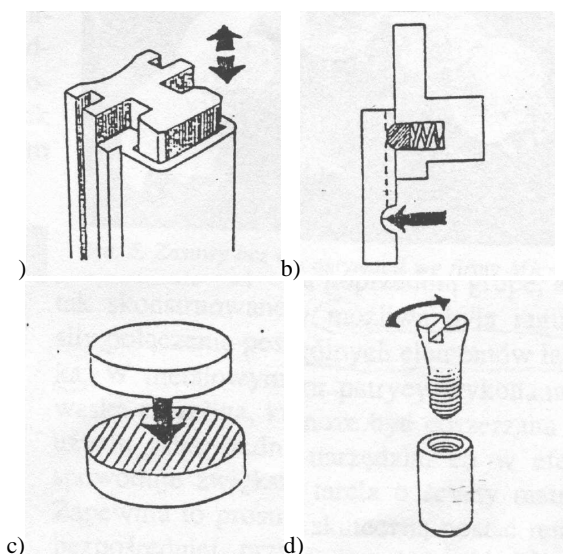
Fig. 4. The overlay dentures fixing methods: a) friction forces, b) mechanical, c) magnetical, d) using screw

In addition, they can be used in many constructions, such as (Ciaputa, 2009; Hupfauf, 1997; Raszewski, 2009):
− skeletal prostheses,
− overdentures,
− partial settling denture,
− stable fastenings.

As mentioned earlier, durability and reliability of teeth prostheses in engineering terms depend primarily on three aspects: construction, material and technology. It is illustrated by the pattern set in Fig. 2.

For the manufacturing process of dentures, noble metals (platinum gold, platinum-iridium gold) and chrome-nickel steels are used. In recent years plastic materials (such as teflon, nylon, silicone) are utilized.
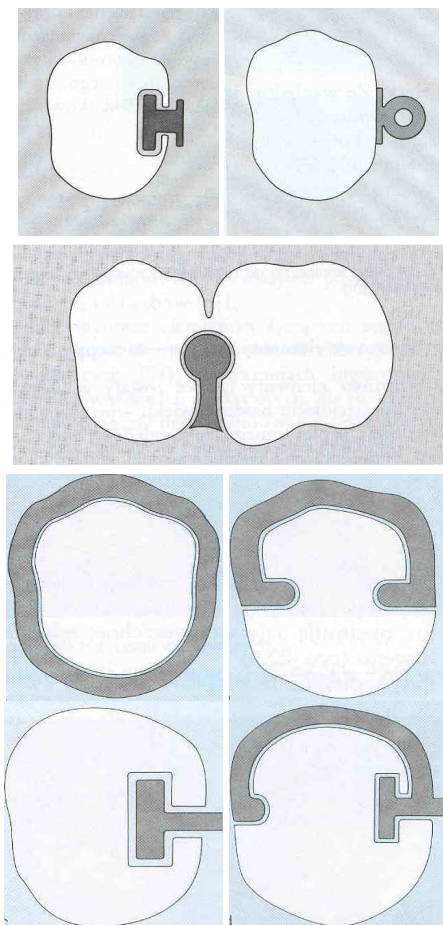
Fig. 5. The examples of the overlay dentures fastening

In case of construction process, the applied connectors are divided into few groups taking into account their physicochemical action (Hupfauf, 1997; Raszewski, 2009; Ciaputa, 2009):
− inside the tooth – stiff joints, screwing, fastening (Fig. 3a),
− outside the crown – screwing joints, hinge and screwing – rotating (Fig. 3b) connectors,
− root clasps – rigid screwing and screwing – rotating (Fig. 3c),
− crosspieces – rigid and resilient (Fig. 3d).

For durability and operational reliability, the fixing type of moving parts of overlay dentures is of high importance.

Those fixing (connections) are obtained by using (Ciaputa, 2009; Hupfauf, 1997; Raszewski, 2009):
- friction forces (Fig. 4a),
- mechanical retention (Fig. 4b),
- the use of magnetic forces (Fig. 4c),
- the use of forces from the screwing (Fig. 4d).

Above (Fig. 5) some fastening construction solutions of overlay dentures are presented. Having in mind research targeted for the purpose of this study these are mainly fixations which use a friction forces. It should be noted that studies of this type of fixations for dentures are now one of the main areas of research of the Department of Materials and Biomedical Engineering at Bialystok Technical University.

3. RESEARCH CAPABILITIES OF ELEMENTS OF DENTURES

For the purpose of assessing the performance of materials for dentures in engineering term, various tribological testers are applied. It should be noted that variations in the use of materials, the scope of external conditions during their real work, or a specific of micro-and macro environment leads to the fact that the overwhelming number of testers are the testers that combine the multiplicity of factors. Often these are testers, in which the construction of a working node is based on the already known schematic friction nodes, such as: pin / disc, ball / disc, pad / roller, roller / disc, etc. As a result, a newer modifications of already known friction testers are constructed, the use of which is addressed primarily to assess the performance of friction elements, not the team of elements, as dental prosthesis. As an example of such a tester is UMT-2 tester presented in Fig. 6 (CETR Tribometers).

Fig. 6. Micro-tribometer model UMT-2 (CETR Tribometers)

Presented in Fig. 6 tribometer is the universal device for evaluation of tribological characteristics and selected mechanical properties of biomaterials, including dentures materials, tools and medical instruments. However, in spite of its versatility and wide range of research opportunities, this device works in the couple of pin/disc or ball/disc. Moreover, studies involving this tester are limited to the evaluation of two co-partners.
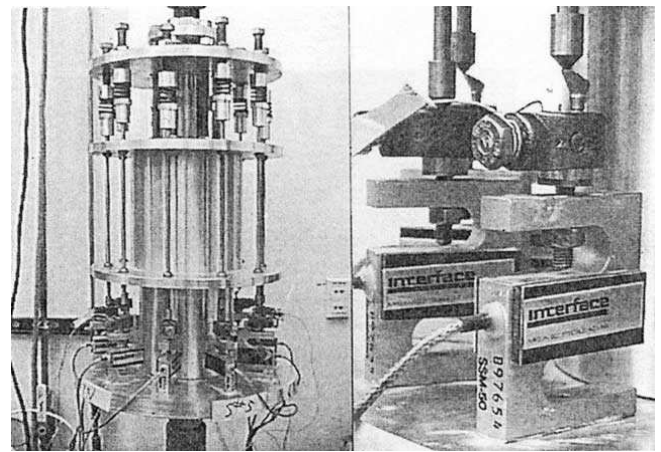

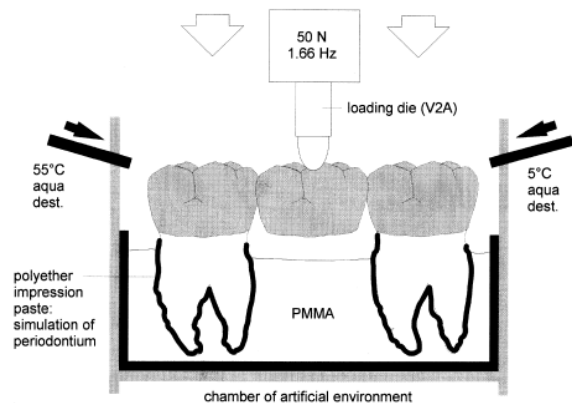**Fig. 7.** Cibirka's carousel device (Cibirka, 2001)

Fig. 8. The example of machine for denture's operational reliability test (Behr, 1999)
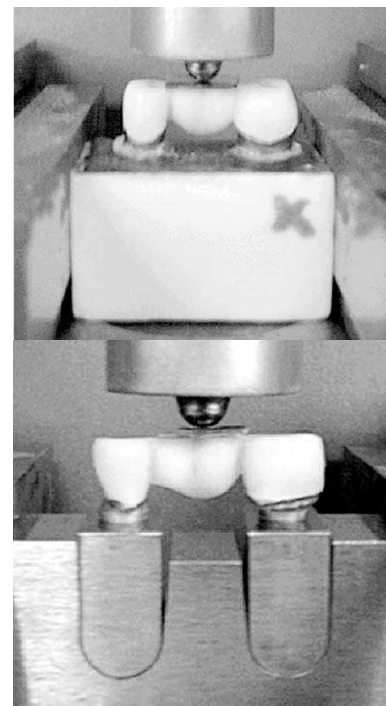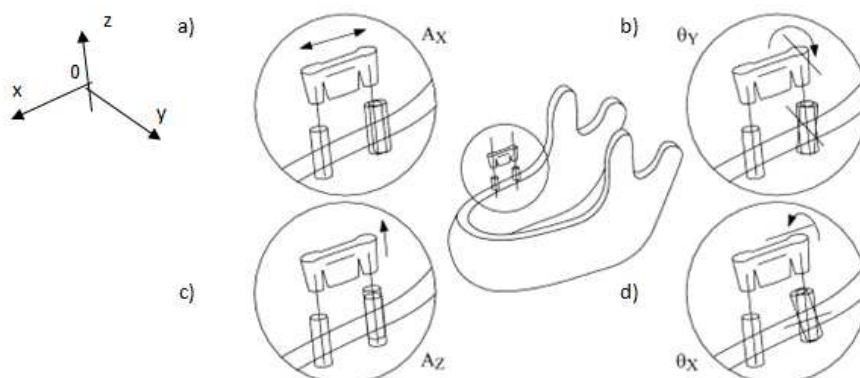

Fig. 9. An example of model for prosthetic bridges tests (Fischer, 2004): a) stable part of bone, b) movable part of bone

In view of the fact that the dental prosthesis is a team of various interconnected components, there is a need to

study under the same conditions the external extortions and kinematics of the load of team elements simultaneously. In Fig. 7 the tester used by the Cibirka (Cibirka, 2001) in which 10 elements were analyzed simultaneously (dental implants) is shown. The studies were conducted in a fatigue cycle to determine the operational durability of the analyzed elements. However, this research was orientated only for a rapid review of implant materials, thus in effect only the implant was tested. Aspects of more elaborate construction dentures were omitted.

Further research focused on the operational reliability of dentures resulted in the appearance of works, which used a simple linear bridge restorations.

An example of a more advanced device is shown in Fig. 8. This machine reflects in a greater degree the working conditions of dentures in the mouth. However, the modeled load takes into account only the movement in the vertical plane, which greatly simplifies the real conditions of the prosthesis work.

Some modification of the device shown in Fig. 8 is an apparatus model whose view is given in Fig. 9 (Fischer, 2004). The advantage of this solution is the ability of a deviation from the equilibrium position (vertical) of the bearing screws mounted in tooth socket.

Fig. 10. The examples of errors resulting from load-bearing pillars in teeth sockets (Pietrabissa, 2000): a) an error of the implant's fastening distance, b) bend to OY axis, c) an error of implant fastening depth, d) screwing to OX axis
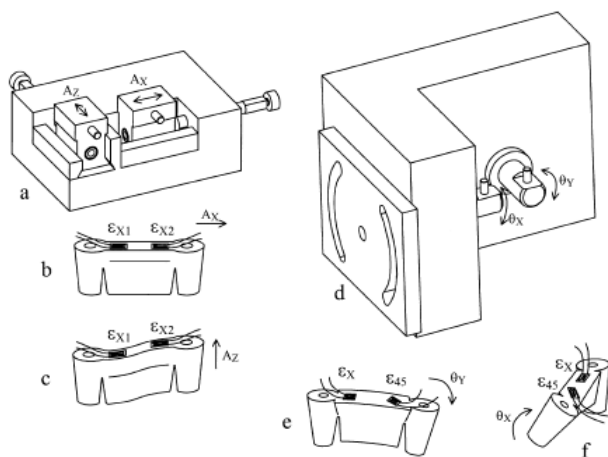
Fig. 11. The example of test machines and types of modeled external extortions (Pietrabissa, 2000): a) the simulation of error of the implant's fastening distance, b) straighting the implants, c) bending, d) screwing, e) the element to incorrect modeling of implants in X and Y axis determine, f) an element for double-axis screwing

Other interesting proposal was submitted by the authors of work (Pietrabissa, 2000). They established that the most common form of errors in the functioning of prosthetic bridges are errors resulting from different axis fixation of load-bearing pillars in relation to the geometry of the prosthetic bridge. Fig. 10 shows the analyzed errors.

The analysis of cases presented in Fig. 10, allowed authors of work (Pietrabissa, 2000) to build a model test

which integral part is shown in Fig. 11 (11e and 11f). This figure illustrates the diagrams of machines enable to get analyzed earlier states of deformations. The test stand prepared in this way provides much more research combinations and gives better opportunities to assess the real state of a prosthesis, taking into account the possible, future implantologist's errors. However, it lacks a constant reference to the quality of service of the dental prosthesis.

Another example of the dentures diagnostic test stand is an instrument shown in Fig. 12 (Kuchta, 2006). The advantage of this instrument is that it allows richer kinematics of the motion and putted loads, but the simulation of the conditions of micro-and macrosurroundings corresponding to the mouth environment is missing. It is mostly long-term effects of various types of liquids and gases, such as saliva, alcohol, juice, coffee, tobacco smoke, etc. In this solution there is also no reference to co-partner, which is the opposite jaw. However it is worth to remember that the instrument is intended to prosthetics diagnosis and not to assess their operational strength.

On the above examples of different instruments for the dentures evaluation, the best seems to be a device presented in Fig. 13 (Studium Famulaturen&Auslandsaufenthalte). The main advantage of this model is the using in its construction the classical testing machine. There is no need to build a separate, specialized facilities and it provides an easy way to rebuild the test stand for other kind of tests. In addition, it is possible to assess both the whole – complete dentures, as well as smaller sets, which in a sense indicates the test stand universality.

a)

b)

1- tested denture,
2- table,
3- pressure pin,
4- nut,
5- loads axis,
6- loads,
7- distance plate,
8- transfer process,
9- measure ending,
10- adjustable disk,
10a- apparatus stand,
11- column,
12- movable clamping ring,
13- nut,
14- clamp screw,
15- motor,
16- ball bearing,
17- secure screws,
18- pressure screws,
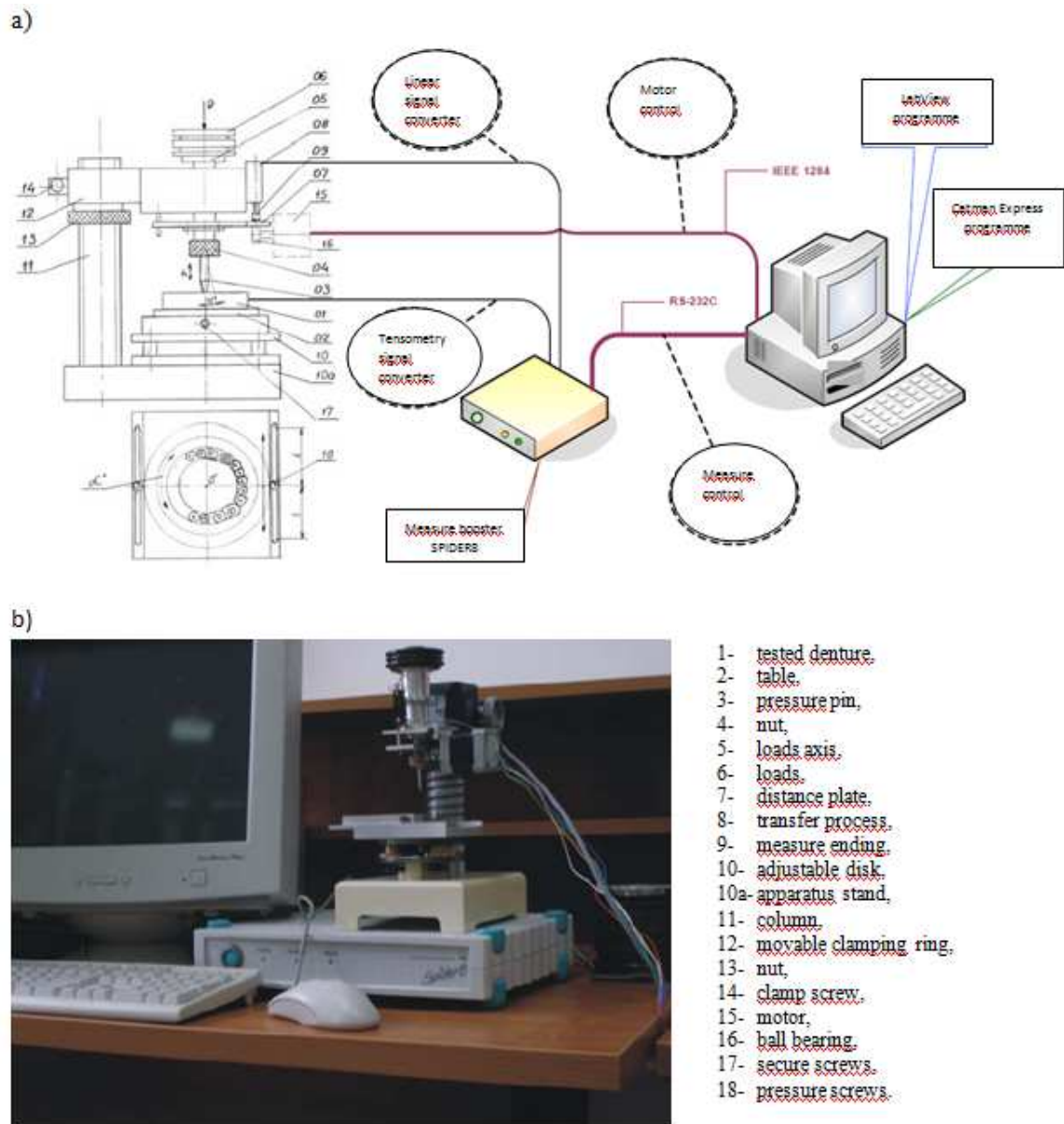
Fig. 12. The laboratory stand for dentures diagnostic (Kuchta, 2006): a) the stand's diagram, b) view of apparatus and system register

Fig.13. The stand for denture tests – artificial mouth
(Studium Famulaturen&Auslandsaufenthalte)

It is also worth mentioning that the operating system is locked in a casing, which also makes it possible to use liquid and gaseous media. As a drawback of this test stand (shown in Fig. 8) can be considered very small movement kinematics of the analyzed elements. Indeed, it is confined to put loads in the vertical plane and turnover in the axis of the prosthesis.

Given by the examples presented above and the literature analysis of utilized methods and apparatus for testing dentures a device of own design was proposed.

4. THE PROPOSITION OF OWN DEVICE FOR ASSESSMENT THE OPERATIONAL RELIABILITY OF THE DENTAL PROSTHETICS ELEMENTS

Due to the patent process started, this paper shows only a simplified working area of the device with the possibilities of movement and load (Fig. 14). Designed device

is intended to serve both the individual components like crown or permanent fillings, through simple and diagonal bridges to full dentures. Fig. 14a illustrates view of the working node of the device in lateral position. This projection shows the load pins movement (up-down) in the vertical plane. Because of the possibility of three or more (optional) pins, Fig. 14b and 14c presented the placement and the full range of designed moving elements. Working pins are driven by a special mechanism, which makes their movement is shifted in phase. This gives the so-called 'wave' effect. Thus, in Fig. 14b is indicated the swinging movement of the lower table in relation to horizontal surface. At the same time the lower table has the ability to perform lateral movement (right-left) and rising and sinking to the bottom (Fig. 14c shows the example of fitting the prosthesis to match its location on one of the tables). Normal operation of the device intersects with each other all these movements, thereby making the complex movements of the test pieces - both sinusoidal in longitudinal and transverse table axis.

Optionally, the removal of the lower table is expected in case of evaluating of the individual components like crown or materials on permanent dental fillings. In such cases, the test sample is fixed onto the table top in front of the loading pin.

Another important element of the designed tester is the possibility to choose the number of pins. Minimally it may be one, with maximum of 5 pins, as illustrated in Fig. 14c. Starting situation involves the use of three pins, but there is the possibility to use also five pins. There is also an option of changing the position of pins, depending on the size of the prosthesis.

With respect to the external forcing parameters it should be mentioned that the load on test samples will be regulated by appropriate setting of the upper table, the number of working pins cycles, electric motor's speed, therefore time of device work may be set in any way.
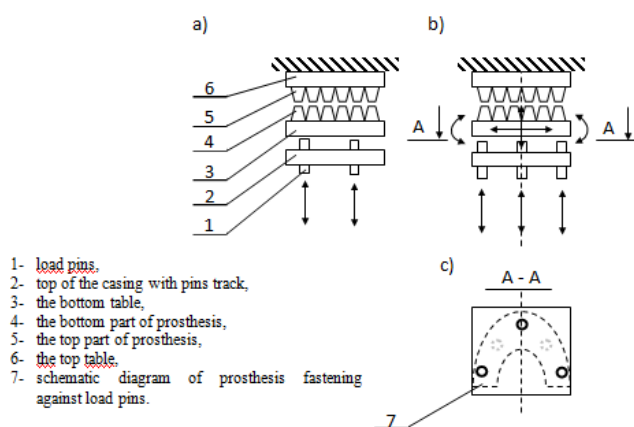
Fig. 14. The working couple of the device for exploitation stability assessment of the dentures elements: a) view of the side, b) view of the back, c) section A-A

It is assumed that the tester's work will enable the measurement of maximum force. In addition to the loading force measurement the possibility of the measurement of friction force between the cooperating elements is anticipated. During analysis the generalized friction force will be taken under account - as the resultant of the all partial fric-

tion forces. Tests can be conducted either within a specified time or until the first of any damages of assessed elements. It is envisaged that the quality of prostheses will be decided by reliability coefficients or tribological factors. It should be noted that the entire work space will be closed in a transparent chamber with the corresponding connecting pieces, which can be pressed distorting medium, such as: tobacco smoke. By the droplet method or aerosol will be added liquids such as alcohol, tea, coffee, artificial saliva, etc. In addition there is the possibility of heating the system to the temperature of 37 ° C.

The designing tester in such a way gives a good approximation (with respect to the kinematics of motion of working elements and micro- and macrosurroundings) of dental prosthetics elements work in the real conditions of mastication in mouth. At the same time the usage of various media will enable to assess their impact on the reliability of tested items, but above all it is necessary to model a real "microclimate" of the mouth.

5. SUMMARY AND CONCLUSIONS

In the work the closer construction problems of overlay dentures fixings was elaborated. The sustainability and reliability of this type of construction in terms of research opportunities was discussed. A few types of testers for assessing the performance of biomaterials used in dentistry and the durability and reliability of prosthetic dentistry elements was presented. The existence of numerous test stands, which kinematics of motion is based on the well-known for a long time tribological testers, such as: stem / disc, ball / disc, etc was indicated. The presented test equipments are helpful in evaluating of the materials and components of dental prosthetics, but in their construction it is not possible to simulate the complex movements of the stomatognathic system, or simulate the microclimate of the mouth.

According to above testers analysis, the own construction solution of tester which asses the reliability of dental prosthetics elements was proposed. Due to the patent procedure taken, this paper presents only the simulated conditions of external forcing in the form of a simplified kinematic scheme. It should be noted that the tester is designed to allow simulation of complex movements of the tested components, and additionally it is envisioned to maintain artificial -model climate corresponding to the microenvironment of the mouth.

REFERENCES

1. **Behr M., Rosentritt M., Leibrock A., Schneider-Feyrer S., Handel G.** (1999), In-vitro study of fracture strength and marginal adaption of fibre-reinforced adhesive fixed partial inlay dentures, *Journal of Dentistry*, 27 (2), 163–168.
2. **Ciaputa T., Ciaputa A.** (2009), *Podstawy wykonawstwa prac protetycznych*, Wydawnictwo ELAMED, Katowice 2009.
3. **Cibirka R. M.** (2001), Examination of the implant–abutment interface after fatigue testing, *Journal of Prosthetic Dentistry*, 85 (3), 268-275.

4. **Fischer H., Weber M., Eck M., Erdrich A., Marx R.** (2004), Finite element and experimental analyses of polymer-based dental bridges reinforced by ceramic bars, *Journal of Biomechanics*, 37 (3), 289–294.

5. **Hupfauf L.** (red.) (1997), *Protetyka stomatologiczna* – praca zbiorowa, Wydawnictwo Urban&Partner, Wrocław.

6. **Kuchta M., Kwiatos K., Fokow K.** (2006), Measuring system for diagnostics of dental prostheses, *Diagnostyka*, 3 (39), 187-192.

7. **Pietrabissa R., Contro R., Quaglini V., Soncini M., Gionso L., Simion M.** (2000), Experimental and computational approach for the evaluation of the biomechanical efects of dental bridge misfit, *Journal of Biomechanics*, 33 (11), 1489-1495.

8. **Raszewski Z.** (2009), *Nowe spojrzenie na tworzywa akrylowe*, Wydawnictwo ELAMED, Katowice..

9. **Sajewicz E.** (2008), *Tribologiczne aspekty funkcjonowania narządu zębowego człowieka*, Rozprawa habilitacyjna.

10. CETR TRIBOMETERS, Nano- and Micro- Tribometer UMT-2- http://www.cetr.com/brochures/tester_bio-medical_materials.html

11. Studium Famulaturen & Auslandsaufenthalte, Auslandssemester in Minneapolis Auslandssemester von September bis Dezember 2005 – http://www.dental.uni-greifswald.de/ausland /2005/ usa/usa-seiten/bild4.html

POSITIVE SWITCH 2D LINEAR SYSTEMS DESCRIBED BY THE GENERAL MODELS

Tadeusz KACZOREK[*]

[*]Bialystok University of Technology, Faculty of Electrical Engineering, Wiejska 45D, 15-351 Bialystok

kaczorek@isep.pw.edu.pl

Abstract: The positive switched 2D linear systems described by the general models are addressed. Necessary and sufficient conditions for the asymptotic stability of the positive switched system are established for any switching. The considerations are illustrated by numerical examples.

1. INTRODUCTION

In positive systems inputs, state variables and outputs take only non-negative values. Examples of positive systems are industrial processes involving chemical reactors, heat exchangers and distillation columns, storage systems, compartmental systems, water and atmospheric pollution models. A variety of models having positive linear behavior can be found in engineering, management science, economics, social sciences, biology and medicine, etc.

Positive linear systems are defined on cones and not on linear spaces. Therefore, the theory of positive systems is more complicated and less advanced. An overview of state of the art in positive systems theory is given in the monographs Farina and Rinaldi (2000) and Kaczorek (2009).

The most popular models of two-dimensional (2D) linear systems are the discrete models introduced by Roesser (1975), Fornasini and Marchesini (1976, 1978) and Kurek (1985). These models have been extended for positive systems in Kaczorek (1996; 2005) and Valcher (1997). An overview of standard and positive 2D systems theory is given in Bose (1985), Gałkowski (2001) and Kaczorek (1985) and some recent results in positive systems have been given in Kaczorek (1996, 2001, 2002, 2005, 2007a, b, 2009). The stability of switched linear systems has been investigated in many papers and books (Colaneri, 2009; Liberzon, 2003, 2009; Sun and Ge, 2004). The disturbance decoupling problem for switched linear continuous-time systems by state-feedback has been considered in Otsuka (2010) and the stabilizer design of planar switched linear systems in Hu and Cheng (2008).

In this paper the positive switched 2D linear system described by the general models will be considered. We shall analyze the following question: When is a positive switched 2D linear system defined by linear general models and a rule describing the switching between them asymptotically stable. It is well known (Liberzon, 2003, 2009) that a necessary and sufficient conditions for stability under arbitrary switching is the existence of a common Lyapunov function for the family of subsystems. This result will be extended for positive switched 2D linear systems described by the general models.

The paper is organized as follows. Preliminaries and the problem formulation are given in section 2. The main results of the paper are presented in section 3, where necessary and sufficient conditions are established for the asymptotic stability of the positive switched 2D linear systems described by the general model for any switching. Illustrating examples are presented in section 4. Concluding remarks are given in section 5. In Appendix the definition of equilibrium point is given and the formula determining the point is derived.

To the best of the author's knowledge the positive switched 2D linear systems have not been considered yet.

2. PRELIMINARIES AND THE PROBLEM FORMULATION

Let $\Re^{n \times m}$ be the set of $n \times m$ real matrices. The set $n \times m$ matrices with nonnegative entries will be denoted by $\Re_+^{n \times m}$ and $\Re_+^n = \Re_+^{n \times 1}$. A matrix $A = [a_{ij}] \in \Re^{n \times m}$ (vector x) is called strictly positive and denoted by $A > 0$ ($x > 0$) if $a_{ij} > 0$ for $i = 1,\dots,n; j = 1,\dots,m$. The et of nonnegative integers will be denoted by Z_+ and the $n \times n$ identity matrix will be denoted by I_n.

The general model of 2D linear system has the form (Kurek, 1985):

$$x_{i+1, j+1} = \overline{A}_0 x_{i, j} + \overline{A}_1 x_{i+1, j} + \overline{A}_2 x_{i, j+1}$$
$$+ \overline{B}_0 u_{i, j} + \overline{B}_1 u_{i+1, j} + \overline{B}_2 u_{i, j+1} \quad (2.1a)$$

$$y_{i, j} = \overline{C} x_{i, j} + \overline{D} u_{i, j}, \ i, j \in Z_+. \quad (2.1b)$$

where $x_{i, j} \in \Re^n$, $u_{i, j} \in \Re^m$ and $y_{i, j} \in \Re^p$ are the state, input and output vectors and

$\overline{A}_k \in \Re^{n \times n}$, $\overline{B}_k \in \Re^{n \times m}$, $k = 0,1,2$; $\overline{C} \in \Re^{p \times n}$,

$\overline{D} \in \Re^{p \times m}$.

Boundary conditions for (2.1a) have the form

$$x_{i0} \in \Re^n, i \in Z_+ \text{ and } x_{0j} \in \Re^n, j \in Z_+ \qquad (2.2)$$

The model (2.1) is called (internally) positive general model if $x_{i,j} \in \Re_+^n$, and $y_{i,j} \in \Re_+^p, i, j \in Z_+$ for any non-negative boundary conditions

$$x_{i0} \in \Re_+^n, i \in Z_+, \ x_{0j} \in \Re_+^n, j \in Z_+ \qquad (2.3)$$

and all input sequences $u_{i,j} \in \Re_+^m, i, j \in Z_+$.

Theorem 2.1. [13] The general model is positive if and only if

$$\overline{A}_k \in \Re_+^{n \times n}, \ \overline{B}_k \in \Re_+^{n \times m}, \ k = 0,1,2,$$
$$\overline{C} \in \Re_+^{p \times n}, \ \overline{D} \in \Re_+^{p \times m} \qquad (2.4)$$

The positive general model (2.1) is called asymptotically stable if for any boundary conditions (2.3) and zero inputs $u_{i,j} = 0, \ i, j \in Z_+$

$$\lim_{i,j \to \infty} x_{i,j} = 0 \qquad (2.5)$$

Theorem 2.2. (Kaczorek, 2009) The positive general model (2.1) is asymptotically stable if and only if there exists a strictly positive vector $\lambda \in \Re_+^n$ such that

$$[\overline{A} - I_n]\lambda < 0 \text{, and } \overline{A} = A_0 + A_1 + A_2 \qquad (2.6)$$

Theorem 2.3. (Kaczorek, 2009a, b) The positive general model (2.1) is asymptotically stable if and only if the positive 1D linear system

$$x_{i+1} = \overline{A}x_i \qquad (2.7)$$

is asymptotically stable, where matrix $\overline{A}$ is given by (2.6).

Theorem 2.4. (Kaczorek, 2009) The positive general model is asymptotically stable if and only if one of the following equivalent conditions is met:

– Eigenvalues $z_1, ..., z_n$ of the matrix $\overline{A}$ have modules less than 1, i.e.

$$|z_k| < 1 \text{ for } k = 1, ..., n \qquad (2.8a)$$

– All coefficients $a_i, i = 0,1, ..., n-1$ of the characteristic polynomial

$$p(z) = \det[I_n(z+1) - \overline{A}] = z^n + a_{n-1}z^{n-1} + ... + a_1 z + a_0 \quad (2.8b)$$

are positive, i.e. $a_i > 0, i = 0,1, ..., n-1$.

– All principal minors of the matrix

$$\hat{A} = I_n - \overline{A} = \begin{bmatrix} \hat{a}_{11} & \hat{a}_{12} & ... & \hat{a}_{1n} \\ \hat{a}_{21} & \hat{a}_{22} & ... & \hat{a}_{2n} \\ \vdots & \vdots & \vdots & \vdots \\ \hat{a}_{n1} & \hat{a}_{n2} & ... & \hat{a}_{nn} \end{bmatrix} \qquad (2.8c)$$

are positive, i.e.

$$\hat{a}_{11} > 0, \ \begin{vmatrix} \hat{a}_{11} & \hat{a}_{12} \\ \hat{a}_{21} & \hat{a}_{22} \end{vmatrix} > 0, ..., \det \hat{A} > 0 \qquad (2.8d)$$

Consider the switched positive system consisting of q autonomous positive general models of the form

$$x_{i+1,j+1} = A_{l0}x_{i,j} + A_{l1}x_{i+1,j} + A_{l2}x_{i,j+1}, \ l = 1, ..., q \quad (2.9)$$

It is assumed that in the point $(p_i, t_i), \ p_i, t_i \in Z_+, i = 1, ..., q$ the matrices of the general model jump instantaneously from A_{ik} to A_{jk} for some $i \neq j, \ i, j = 1, ..., q; \ k = 0,1,2$.

The following question arises: when the switched positive general model (2.9) is asymptotically stable for every switching if every positive general model of the set is asymptotically stable.

3. PROBLEM FORMULATION

To simplify the notation it is assumed $q = 2$. In this case the switched positive system consists of two positive general models

$$x_{i+1,j+1} = A_{10}x_{i,j} + A_{11}x_{i+1,j} + A_{12}x_{i,j+1} \qquad (3.1a)$$

$$x_{i+1,j+1} = A_{20}x_{i,j} + A_{21}x_{i+1,j} + A_{22}x_{i,j+1} \qquad (3.1b)$$

where $A_{lk} \in \Re_+^{n \times n}, \ l = 1,2; \ k = 0,1,2$ and the switching between them occur in the points

$$(p_1, t_1), ..., (p_k, t_k), (p_{k+1}, t_{k+1}), ... \qquad (3.2)$$

satisfying the condition

$$p_{k+1} \geq p_k, \ t_{k+1} \geq t_k \text{ and } p_{k+1} + t_{k+1} > p_k + t_k, \qquad (3.3)$$
$$k = 1,2,...$$

Theorem 3.1. (Kaczorek, 2001) The solution of the autonomous ($u_{i,j} = 0, \ i, j \in Z_+$) positive general model (3.1a) with boundary conditions (2.3) is given by

$$x_{i,j} = T_{i-1,j-1}A_0 x_{00} + \sum_{t=1}^{i-1} T_{i-t-1,j-1}A_0 x_{t0}$$
$$+ \sum_{v=1}^{j-1} T_{i-1,j-v-1}A_0 x_{0v} + \sum_{t=1}^{i} T_{i-t,j-1}A_1 x_{t0} \qquad (3.4)$$
$$+ \sum_{v=1}^{j} T_{i-1,j-v}A_2 x_{0v}$$

where the transition matrix T_{ij} is defined by

$$T_{ij} = \begin{cases} I_n & \text{for} \quad i = j = 0 \\ A_0 T_{i-1,j-1} + A_2 T_{i-1,j} + A_1 T_{i,j-1} & \text{for } i, j \geq 0 \ (i+j > 0) \\ 0 & \text{for} \quad i < 0 \text{ or } j < 0 \end{cases} \qquad (3.5)$$

Using (3.4), (3.5) and the boundary conditions (2.3) we can compute the state vector x_{ij} for $i, j \in Z_+$.

Theorem 3.2. The switched positive system (3.1) is asymptotically stable for any switching (3.2) satisfying (3.3) only if both positive models (3.1) are asymptotically stable.

Proof. Without loss of generality we may assume that the first model (3.1a) is asymptotically stable and the second (3.1b) is unstable. For any bounded boundary conditions (2.3) using (3.4), (3.5) and the first model we may compute boundary conditions for the second model which will be bounded since the first model is asymptotically stable. In the similar way we may compute the boundary conditions for the first model but those boundary conditions will be greater than those for the second model since it is unstable. Therefore, the switched positive general model will be unstable.

In (Kaczorek, 2007) it was shown that for positive model (2.1a) as a Lyapunov function a linear form $V(x_{ij}) = \lambda^T x_{ij}$ can be chosen, where $\lambda \in \Re_+^n$ is strictly positive.

For the switched positive system consisting of positive models (3.1) we choose Lyapunov functions in the form

$$V_1(x_{ij}) = \lambda_1^T x_{ij} \text{ and } V_2(x_{ij}) = \lambda_2^T x_{ij} \qquad (3.6)$$

where the strictly positive vectors λ_1 and λ_2 satisfy the equations

$$\lambda_1 = A_1 \lambda_1 + 1_n, \ \lambda_2 = A_2 \lambda_2 + \lambda_1, \ 1_n = [1 \ 1 \ ... \ 1]^T \in \Re_+^n \quad (3.7)$$

and $A_k = A_{k0} + A_{k1} + A_{k2}$, $k = 1,2$.

If A_1 and A_2 are Schur matrices then from (3.7) we have

$$\lambda_1 = [I_n - A_1]^{-1} 1_n \text{ and } \lambda_2 = [I_n - A_2]^{-1} \lambda_1 \qquad (3.8)$$

Remark 3.1. From the comparison of (3.3) and (A.2), (A.3) it follows that as λ_1 we can choose equilibrium point x_e for $Bu = 1_n$ and as λ_2 the vector x_e for $Bu = \lambda_1$.

Lemma 3.1. The function

$$V_2(x_{ij}) = \lambda_2^T x_{ij} \qquad (3.9)$$

is a common Lyapunov function for the both positive general models (3.1) if

$$A_1 A_2 = A_2 A_1 \qquad (3.10)$$

Proof. The function (3.9) for both positive Roesser models (3.1) for strictly positive $\lambda_2 \in \Re_+^n$ is positive if and only if $x_{ij} \neq 0$. Note that the dual general models

$$x_{i+1,j+1} = A_{10}^T x_{i,j} + A_{11}^T x_{i+1,j} + A_{12}^T x_{i,j+1} \qquad (3.11a)$$

$$x_{i+1,j+1} = A_{20}^T x_{i,j} + A_{21}^T x_{i+1,j} + A_{22}^T x_{i,j+1} \qquad (3.11b)$$

are positive and asymptotically stable if and only if the corresponding general models (3.1) are positive and asymptotically stable (Kaczorek, 2007). Taking into account Theorem 2.3 and using (3.9) for the positive general model (3.1a) we obtain

$$\Delta V_2(x_{ij}) = \lambda_2^T [A_1 - I_n] x_{ij} \qquad (3.12)$$

and

$$\lambda_2^T = \lambda_1^T [I_n - A_2]^{-1} \qquad (3.13)$$

since $\lambda_2 = A_2^T \lambda_2 + \lambda_1$.

Substitution of (3.13) into (3.12) yields

$$\Delta V_2(x_{ij}) = \lambda_1^T [I_n - A_2]^{-1} [A_1 - I_n] x_{ij}$$
$$= \lambda_1^T [A_1 - I_n][I_n - A_2]^{-1} x_{ij} \qquad (3.14)$$
$$= -1_n^T [I_n - A_2]^{-1} x_{ij} < 0$$

for every $x_{ij} \in \Re_+^n$, $x_{ij} \neq 0$, since (3.10) implies $[A_1 - I_n][I_n - A_2]^{-1} = [I_n - A_2]^{-1}[A_1 - I_n]$ and the sum of entries of each column of the matrix $1_n^T [I_n - A_2]^{-1}$ is positive for the positive asymptotically stable general model (3.1b).

Similarly, using (3.9) for positive general model (3.11b) we obtain

$$\Delta V_2(x_{ij}) = \lambda_2^T [A_2^T - I_n] x_{ij} < 0 \qquad (3.15)$$

for every $x_{ij} \in \Re_+^n$, $x_{ij} \neq 0$, since $\lambda_2^T [A_2^T - I_n] < [0 \ ... \ 0]$.

Theorem 3.3. Let the matrices A_1 and A_2 of (3.1) satisfy the conditions (3.10). The positive switched system (3.1) is asymptotically stable for any switching (3.2) satisfying (3.3) if and only if the positive models (3.1) are asymptotically stable.

Proof. Necessity follows immediately from Theorem 3.2. If the condition (3.10) is met and the models (3.1) are asymptotically stable then by Lemma 3.1 the function (3.9) is a common Lyapunov function for the positive models (3.1) which satisfies the conditions (3.14) and (3.15). Therefore, the positive switched system (3.1) is asymptotically stable.

Remark 3.2. It is well-known (Kaczorek, 2001) that substituting $B_1 = B_2 = 0$ into (2.1) we obtain the first Fornasini-Marchesini model and substituting $A_0 = 0$ and $B_0 = 0$ we obtain second Fornasini-Marchesini model.

Consider the positive 2D Roesser model (Kaczorek, 2001):

$$\begin{bmatrix} x_{i+1,j}^h \\ x_{i,j+1}^v \end{bmatrix} = \begin{bmatrix} A_{11} & A_{12} \\ A_{21} & A_{22} \end{bmatrix} \begin{bmatrix} x_{i,j}^h \\ x_{i,j}^v \end{bmatrix} + \begin{bmatrix} B_{11} \\ B_{22} \end{bmatrix} u_{i,j} \qquad (3.16a)$$

$$y_{i,j} = \begin{bmatrix} C_1 & C_2 \end{bmatrix} \begin{bmatrix} x_{i,j}^h \\ x_{i,j}^v \end{bmatrix} + D u_{i,j} \quad i,j \in Z_+ \qquad (3.16b)$$

where $x_{i,j}^h \in \Re_+^{n_1}$ and $x_{i,j}^v \in \Re_+^{n_2}$ are the horizontal and vertical state vectors at the point (i,j) $u_{i,j} \in \Re_+^m$ and $y_{i,j} \in \Re_+^p$ are the input and output vectors and $A_{kl} \in \Re_+^{n_k \times n_l}$, $k,l = 1,2$, $B_{11} \in \Re_+^{n_1 \times m}$, $B_{22} \in \Re_+^{n_2 \times m}$, $C_1 \in \Re_+^{p \times n_1}$, $C_2 \in \Re_+^{p \times n_2}$, $D \in \Re_+^{p \times m}$.

The positive 2D Roesser model (3.16) is a particular case of the positive second Fornasini-Marchesini model for

$$A_1 = \begin{bmatrix} 0 & 0 \\ A_{21} & A_{22} \end{bmatrix}, \quad A_2 = \begin{bmatrix} A_{11} & A_{12} \\ 0 & 0 \end{bmatrix}, \tag{3.17a}$$

$$B_1 = \begin{bmatrix} 0 \\ B_{22} \end{bmatrix}, \quad B_2 = \begin{bmatrix} B_{11} \\ 0 \end{bmatrix} \tag{3.17b}$$

Therefore, the presented results are also valid for the positive Fornasini-Marchesini models and the positive Roesser model.

4. ILLUSTRATING EXAMPLES

Example 4.1. Consider the positive switched system consisting of two general models (3.1) with the matrices

$$A_{10} = \begin{bmatrix} 0.5 & 0.3 \\ 0 & 0.1 \end{bmatrix}, \quad A_{11} = \begin{bmatrix} 1 & 0.5 \\ 0 & 0.2 \end{bmatrix}, \quad A_{12} = \begin{bmatrix} 0.5 & 0.2 \\ 0 & 0.1 \end{bmatrix},$$

$$A_{20} = \begin{bmatrix} 0.05 & 0 \\ 0.2 & 0.1 \end{bmatrix}, \quad A_{21} = \begin{bmatrix} 0 & 0 \\ 0.4 & 0.05 \end{bmatrix}, \quad A_{22} = \begin{bmatrix} 0.05 & 0 \\ 0.3 & 0.05 \end{bmatrix}$$

$$\tag{4.1}$$

and the boundary conditions

$$x_{00} = \begin{bmatrix} 1 \\ 1 \end{bmatrix}, \quad x_{i0} = x_{0j} = \begin{bmatrix} 0 \\ 0 \end{bmatrix}, \quad i, j = 1, 2, \ldots \tag{4.2}$$

The switching occurs between them in the points

$$(2,1), (3,3), (5,4), (6,6), \ldots \tag{4.3}$$

The first model is unstable since the matrix $A_1 = A_{10} + A_{11} + A_{12} = \begin{bmatrix} 2 & 1 \\ 0 & 0.4 \end{bmatrix}$ has one diagonal entry greater than 1 (Kaczorek, 2009) and the second model is asymptotically stable. By Theorem 3.2 the positive switched system is unstable since $\lim x_{i,j} = \infty$ (Fig.1).

Example 4.2. Consider the positive switched system consisting of two general models (3.1) with the matrices

$$A_{10} = \begin{bmatrix} 0.1 & 0.05 \\ 0.1 & 0 \end{bmatrix}, \quad A_{11} = \begin{bmatrix} 0.2 & 0.05 \\ 0.1 & 0.1 \end{bmatrix}, \quad A_{12} = \begin{bmatrix} 0.1 & 0 \\ 0.1 & 0.1 \end{bmatrix},$$

$$A_{20} = \begin{bmatrix} 0.3 & 0 \\ 0.2 & 0.1 \end{bmatrix}, \quad A_{21} = \begin{bmatrix} 0.1 & 0.1 \\ 0.2 & 0 \end{bmatrix}, \quad A_{22} = \begin{bmatrix} 0.2 & 0.1 \\ 0.2 & 0.1 \end{bmatrix}$$

$$\tag{4.4}$$

and the boundary conditions (4.2).

Fig. 1a. State variables of the first system with A_1
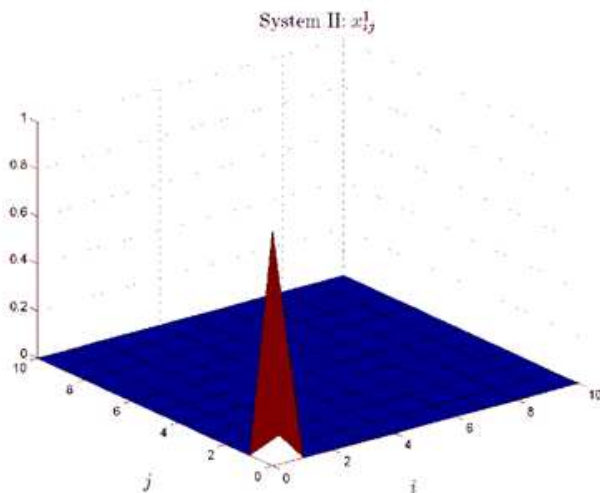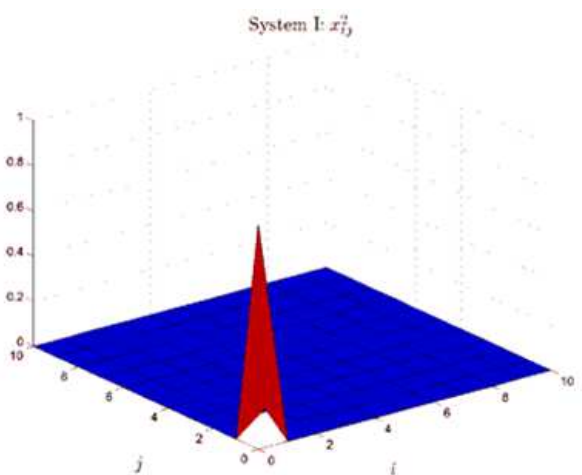
Fig. 1b. State vector for second system with A_2
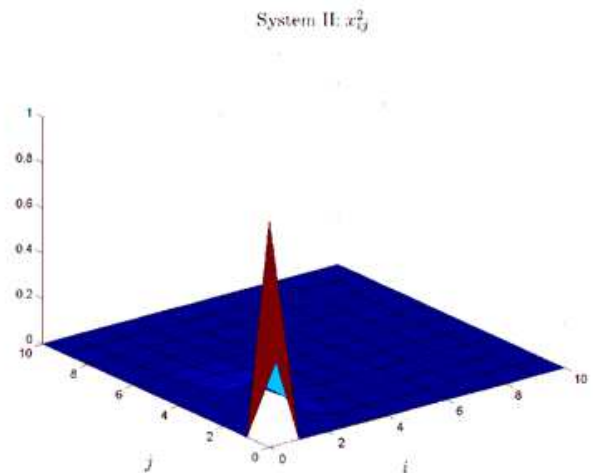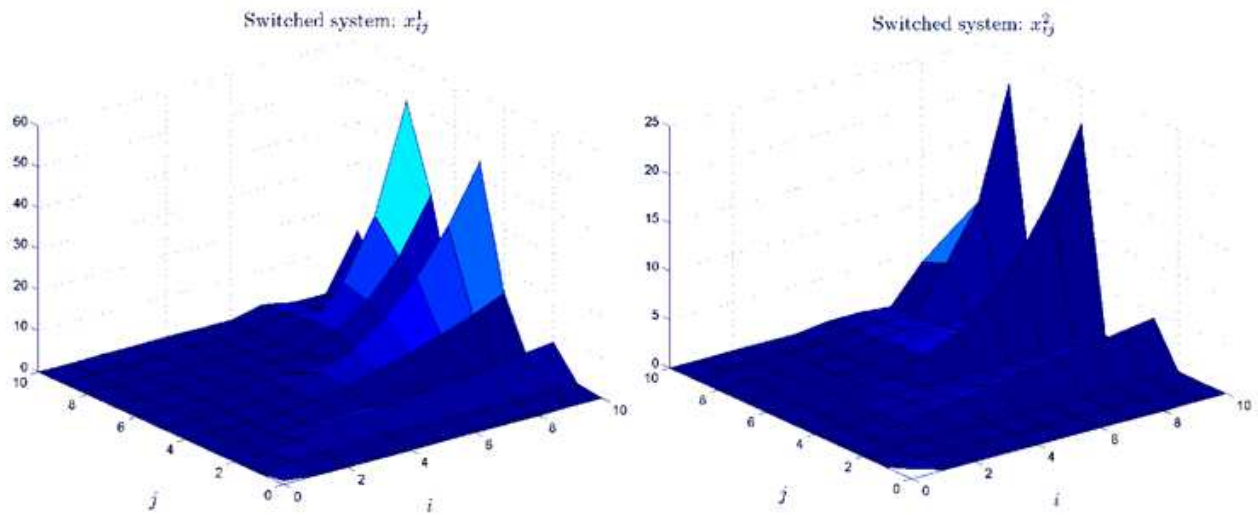
Fig. 2. State variables of the system with switches
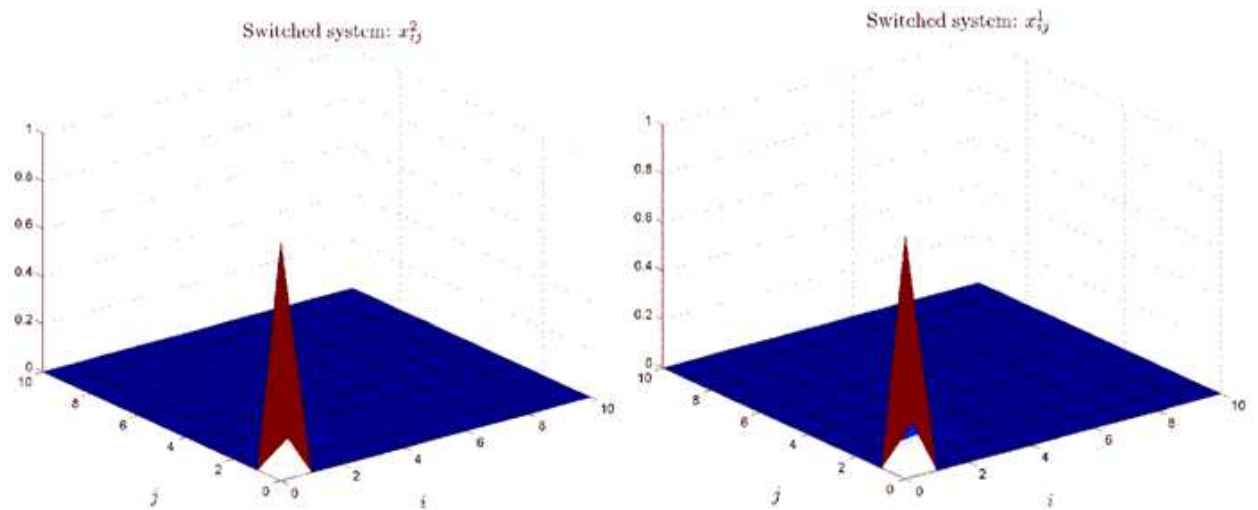
Fig. 3. State variables of the system with switches

The switching occur between them in the points (4.3).

In this case both general models are asymptotically stable and the matrices satisfy the condition (3.10). By Theorem 3.3 the positive switched system with (4.3) and (4.2) is asymptotically stable (Fig. 2).

The presented considerations can be easily extended to the positive switched linear systems consisting of q ($q > 2$) autonomous general models.

5. CONCLUDING REMARKS

The positive switched 2D linear systems described by the general models have been addressed. Necessary and sufficient conditions have been established for the asymptotic stability of the positive switched systems for any switching.

The considerations for positive switched 2D linear systems described by the Fornasini-Marchesini models and the Roesser 2D model are particular cases of the positive switch 2D linear systems described by the general model.

REFERENCES

1. **Bose N. K.** (1985), *Multidimensional Systems Theory Progress, Directions and Open Problems*, D. Reidel Publishing Co..

2. **Buslowicz M.** (2008), Simple stability conditions for linear discrete-time systems with delays, *Bull. Pol. Acad. Sci.*, Vol. 56, No. 4, 325-328.

3. **Colaneri P.** (2009), Dwell time analysis of deterministic and stochastic switched systems, *European Journal of Control*, 3-4, 228-248.

4. **Farina L., Rinaldi S.** (2000), *Positive Linear Systems; Theory and Applications*, J. Wiley, New York..

5. **Fornasini E., Marchesini G.** (1978), Double indexed dynamical systems, *Math. Sys. Theory*, 12:59-72.

6. **Fornasini E., Marchesini G.** (1976), State-space realization theory of two-dimensional filters, *IEEE Trans, Autom. Contr.*, Vol. AC-21, 481-491.

7. **Gałkowski K.** (2001), *State Space Realizations of Linear 2D Systems with Extensions to the General nD (n>2) Case*, Springer -Verlag London.

8. **Hu Q., Cheng D.** (2008), Stabilizer design of planar switched linear systems, Systems& Control Letters, vol. 57, 876-879.

9. **Kaczorek T.** (2009), Asymptotic stability of positive 2D linear systems with delays, *Bull. Pol. Acad. Sci. Techn.*, Vol. 27, No. 2, 133-138.
10. **Kaczorek T.** (2007), Choice of the forms of Lyapunov functions for positive 2D Roesser model, *Int. J. Appl. Math. Comput. Sci.*, Vol. 17, No. 4, 471-475.
11. **Kaczorek T.** (2009), Independence of the asymptotic stability of positive 2D linear systems with delays of their delays, *Int. J. Appl. Match. Comput. Sci.*, Vol. 19, No. 2, 255-261.
12. **Kaczorek T.** (2001), *Positive 1D and 2D Systems*, Springer - Verlag, London.
13. **Kaczorek T.** (1996), Reachability and controllability of non-negative 2D Roesser type models, *Bull. Acad. Pol. Sci. Techn.*, Vol. 44, No 4, 405-410.
14. **Kaczorek T.** (2005), Reachability and minimum energy control of positive 2D systems with delays, *Control and Cybernetics*, vol. 34, No 2, 411-423.
15. **Kaczorek T.** (1985), *Two-dimensional Linear Systems*, Springer Verlag, Berlin.
16. **Kaczorek T.** (2002), When do equlibria of the positive 2D Roesser model are strictly positive*, Bull. Acad. Pol. Sci. Techn.*, Vol. 50, No 1, 221-227.
17. **Kurek J.** (1985), The general state-space model for a two-dimensional linear digital systems, *IEEE Trans. Autom. Contr.* AC-30, 600-602.
18. **Liberzon D.** (2009), On new sufficient conditions for stability of switched linear systems, *Proc. European Control Conf.*, Budapest, 3257-3262.
19. **Liberzon D.** (2003), Switching in Systems and Control, Birkhoiser, Boston.
20. **Otsuka N.** (2010), Disturbance Decoupling Problems with Quadratic Stability for Switched Linear Systems via State Feedback, *proceedings of MTNS'2010*, Budapest, Hungary, 487-490.
21. **Roesser R. P.** (1975), A discrete state-space model for linear image processing, *IEEE Trans. Autom. Contr.*, AC-20, 1,1-10.
22. **Sun Z. D., Ge S. S.** (2004), *Switched Linear Systems: Control and Design*, Springer.
23. **Valcher M. E.** (1997), On the internal stability and asymptotic behavior of 2D positive systems, *IEEE Trans. On Circuits and Systems – I*, vol. 44, No 7, 602-613.

APPENDIX

Consider the positive asymptotically stable general model (2.1) for the positive constant input $u_{i,j} = u$.

Definition A.1. A state x_e satisfying the equation

$$x_e = \overline{A} x_e + \overline{B} u, \quad \overline{A} = \overline{A}_0 + \overline{A}_1 + \overline{A}_2, \quad \overline{B} = \overline{B}_0 + \overline{B}_1 + \overline{B}_2 \quad \text{(A.1)}$$

is called the equilibrium point of the positive asymptotically stable general model (2.1) for $u > 0$.

Theorem A.1. The equilibrium point of the positive general model (2.1) is given by

$$x_e = [I - \overline{A}]^{-1} \overline{B} u . \qquad \text{(A.2)}$$

Proof. If the system is asymptotically stable then the matrix $[I - \overline{A}]$ is invertible and from (A.1) we obtain (A.2).

From (A.1) it follows that for positive general model x_e is strictly positive if Bu is strictly positive vector.

In particular case from (A.2) for $\overline{B}u = 1_n$, $1_n = [1 \quad ... \quad 1]^T \in \Re_+^n$ we obtain strictly positive vector

$$x_e = [I - \overline{A}]^{-1} 1_n > 0 . \qquad \text{(A.3)}$$

ELASTOSTATIC PROBLEM FOR AN INTERFACE RIGID INCLUSION IN A PERIODIC TWO-LAYER SPACE

Andrzej KACZYŃSKI[*], Wojciech KOZŁOWSKI[*]

[*]Faculty of Mathematics and Information Science, Warsaw University of Technology, Plac Politechniki 1, 00-661 Warsaw

akacz@mini.pw.edu.pl, wojthekk@wp.pl

Abstract: The article is devoted to the elastostatic three-dimensional problem of an interface sheet-like inclusion (anticrack) embedded into a periodic two-layered unbounded composite. An approximate analysis is carried out within the framework of the homogenized model with microlocal parameters. The formulation and the method of solving the general problem for an arbitrarily shaped inclusion is presented. As an example illustrating this method, the problem for a rigid circular inclusion under perpendicular tension is solved explicitly and discussed from the point of view of failure theory.

1. INTRODUCTION

Problems dealing with stress concentrations in deformable solids containing different kinds of defects attract the attention of specialists from many areas, such as geomechanics, metallurgy, materials science. In recent decades interest in the study of interface fracture phenomena has grown considerably (see, for example, the proceedings edited by Rossmanith (1997)). Rigid inclusions (called anticracks) are the counterpart of cracks. From the standpoint of inhomogeneities in solids, these defects are the two dangerous extreme cases, namely, for a rigid inclusion $\mu \to \infty$, and for a crack $\mu \to 0$, where μ is the shear modulus of the inhomogeneity phase. Interfacial inclusions play a significant role in the failure behavior. As well known, serious stress concentrations occur near the sharp edges of the inclusions, from which cracking, debonding, damage and so on may emanate. Therefore, the studies in this area with the aim of obtaining the theoretical solutions of the problems involving rigid inclusions under different loading conditions are important for structural integrity assessments. In comparison with crack problems, the investigation of anticracks problems is rather limited, and basic research has been performed on two-dimensional problems involving rigid line inclusions in elastic homogeneous media (see the monographs by Berezhnitskii et al. (1983) and Ting (1996)). The corresponding, more practical three-dimensional problems dealing with rigid sheet-like disc inclusions seem to remain inadequately treated and have been performed to a much lesser extent. Much of the past works related in this field can be found in Kassir and Sih (1968), Selvadurai (1982), Silovanyuk (1984), Podil'chuk (1997), Rahman (1999), and in the basic monographs by Mura (1981) and Panasyuk et al. (1986). The studies of 3D problems of rigid inclusions at the interface a bimaterial have been found only in Gladwell (1999), Selvadurai (2000), Li and Fan (2001), Chaudhuri (2006). The results show that the asymptotic stress elastic fields near the rigid inclusion front exhibit the oscillatory singularity similar to that for interface cracks. This physically anomalous behaviour does not occur in numerous problems of interface cracks or anticracks in a periodically layered space (see, for example, Kaczyński and Matysiak 1997, 1999) treated within the framework of linear thermoelasticity with microlocal parameters (Woźniak, 1987; Matysiak and Woźniak, 1988).

This paper is devoted to a three-dimensional static problem of an arbitrary shaped rigid inclusion lying on one of the interfaces in a periodic two-layer laminated space subjected to some external loads. An approximate analysis is based on the concept of microlocal homogenization that leads to a replacement of the considered periodic composite by some homogenized model with microlocal parameters. In Section 2 we review governing equations and formulate the anticrack problem within this model. Section 3 presents a general method of solving the resulting boundary value problem. As an illustration, a closed-form solution is given and discussed in Section 4 for a circular rigid inclusion subjected to tension at infinity.

2. GOVERNING EQUATIONS AND FORMULATION

The composite being considered is a periodic laminated space consisting of thin repeated fundamental layers of thickness δ which is composed of two bonded homogeneous isotropic layers denoted by 1 and 2 as shown in Fig. 1. In the following, all quantities (material constants, stresses, etc.) pertinent to these sublayers will be denoted with the index l or (l) taking the values 1 and 2, respectively. Let λ_1, μ_1 be the Lamé constants, and δ_l be the thicknesses of subsequent sublayers, thus $\delta = \delta_1 + \delta_2$.

Referring to the rectangular Cartesian coordinate system $OX_1X_2X_3$ with the X_3 – axis directed normal to the layering and the X_1X_2 – plane being one of the interfaces of the materials, denote at the typical point $x = (x_1, x_2, x_3)$ the components of the displacement vector and stress tensor by w_i and σ_{ij}, $i, j \in \{1, 2, 3\}$, respectively.

Suppose that a rigid sheet-like inclusion (anticrack) serving as a mechanical defect in this periodically layered composite occupies a domain S with smooth boundary at the interface $x_3 = 0$ and is subjected to some external loads.

To analyze the elastic field disturbed by this defect, a direct analytical approach becomes intricate because of the complicated geometry and complex boundary conditions. Therefore, the special homogenization procedure called microlocal modelling will be employed in order to seek an approximate solution within the homogenized model of the considered composite. Next, we recall only some relevant results from this approach (see Matysiak and Woźniak (1988), Kaczyński (1993) for more details).
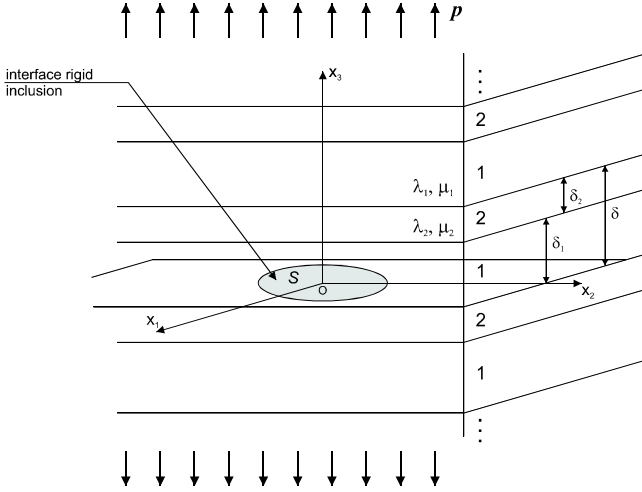

Fig. 1. Two-layer periodic space with an interface anticrack

In the subsequent considerations the following notation will be used: Latin subscripts always assume values 1, 2, 3 and the Greek ones 1,2. The Einstein summation convention holds and a comma followed by an index denotes the partial differentiation with respect to the corresponding coordinate variable.

The microlocal modelling is based on the following displacement representations:

$$w_i(\boldsymbol{x}) = u_i(\boldsymbol{x}) + \underline{s(x_3) d_i(\boldsymbol{x})}. \tag{1}$$

Here the unknown functions u_i and d_i are interpreted as macro-displacements and microlocal parameters, respectively. Moreover, the postulated *a priori* function s, called the shape function, characterises the special approximate model of the treated composite. It is chosen to be sectionally linear, δ – periodic, defined as

$$s(x_3) = \begin{cases} x_3 - 0.5\delta_1, & x_3 \in \langle 0, \delta_1 \rangle \\ (\delta_1 - \eta x_3)/(1-\eta) - 0.5\delta_1, & x_3 \in \langle \delta_1, \delta \rangle \end{cases} ; \eta = \delta_1 / \delta. \tag{2}$$

The underlined term in Eq. (1) represents the microdisplacements due to the microperiodic material structure of the composite. Note, that for thin layers (δ is small) this term may be treated as small and can be neglected, but the derivative s' is a sectionally constant function (taking the value 1 if $l = 1$ and $-\eta/(1 - \eta)$ if $l = 2$) that is not small even for small δ. Hence, the following approximations for the displacements and stresses (according to Hooke's law) hold:

$$w_i \approx u_i, \quad w_{i,\alpha} \approx u_{i,\alpha}, \quad w_{i,3} \approx u_{i,3} + s' d_i,$$

$$\sigma_{\alpha\beta} \approx \mu_l\left(u_{\alpha,\beta} + u_{\beta,\alpha}\right) + \delta_{\alpha\beta} \lambda_l\left(u_{i,i} + s' d_3\right),$$

$$\sigma_{\alpha 3} \approx \mu_l\left(u_{\alpha,3} + u_{3,\alpha} + s' d_\alpha\right), \tag{3}$$

$$\sigma_{33} \approx \left(\lambda_l + 2\mu_l\right)\left(u_{3,3} + s' d_3\right) + \lambda_l u_{\gamma,\gamma},$$

where $\delta_{\alpha\beta}$ is the Kronecker delta.

By using methods of the nonstandard analysis to the homogenization procedure, the asymptotic approach to the macro-modelling of the laminated space under study leads to the governing relations of certain macro-homogeneous medium (the homogenized model), given by means of macro-displacements (after eliminating the microlocal parameters) and taking the following form (in the absence of body forces and in the static case):

$$\begin{cases} \frac{1}{2}(c_{11} + c_{12})u_{\gamma,\gamma\alpha} + \frac{1}{2}(c_{11} - c_{12})u_{\alpha,\gamma\gamma} + \\ + c_{44} u_{\alpha,33} + (c_{13} + c_{44})u_{3,3\alpha} = 0, \\ (c_{13} + c_{44})u_{\gamma,\gamma3} + c_{44} u_{3,\gamma\gamma} + c_{33} u_{3,33} = 0 \end{cases} \tag{4}$$

$$\begin{cases} \sigma_{\alpha 3} = c_{44}\left(u_{\alpha,3} + u_{3,\alpha}\right), \\ \sigma_{33} = c_{13} u_{\gamma,\gamma} + c_{33} u_{3,3}, \\ \sigma_{12}^{(l)} = \mu_l\left(u_{1,2} + u_{2,1}\right), \\ \sigma_{11}^{(l)} = d_{11}^{(l)} u_{1,1} + d_{12}^{(l)} u_{2,2} + d_{13}^{(l)} u_{3,3}, \\ \sigma_{22}^{(l)} = d_{12}^{(l)} u_{1,1} + d_{11}^{(l)} u_{2,2} + d_{13}^{(l)} u_{3,3}. \end{cases} \tag{5}$$

Positive coefficients appearing in the above equations, describing the material and geometrical characteristics of the subsequent layers, are given in Appendix A.

The advantage of the governing equations is their relatively simple form resembling fundamental equations for a transversely isotropic body. Moreover, the condition of perfect mechanical bonding between the layers (the continuity of the stress vector at the interfaces) is satisfied, so hereafter we shall omit the index (l) in the components σ_{i3}. Note, however, that the stress components $\sigma^{(l)}_{\alpha\beta}$ are discontinuous at the interfaces. Finally, putting $\lambda_1 = \lambda_2 \equiv \lambda$, $\mu_1 = \mu_2 \equiv \mu$ entails $c_{11} = c_{33} = d^{(l)}_{11} = \lambda + 2\mu$, $c_{11} = c_{33} = d^{(l)}_{11} = d^{(l)}_{13} = \lambda$, $c_{44} = \mu$, and Eqs (4) and (5) reduce to the well-known equations of elasticity for a homogeneous isotropic body with Lamé's constants λ, μ.

Within the scope of the presented homogenized model we are concerned with the problem of a rigid inclusion occupying a region S at the interface $x_3 = 0$ and subjected to external loadings. In order to satisfy the global mechanical boundary condition ensuring that the faces of inclusion are free from displacements, superposition is applied to separate this problem into two parts: the first one (attached by 0) relating to a basic state of the homogenized space with no inclusion subjected to the given loads and the second, corrective part (with tilde) in which the displacements along S are prescribed as the negative of those generated in the first part. In addition, the displacement and rotation of the inclusion as a rigid body ought to be taken into

consideration. Thus, the complete field of the displacements u_i and stresses σ_{ij} in the composite with the inclusion can be represented in the form

$$u_i = \overset{0}{u}_i + \tilde{u}_i, \quad \sigma_{ij} = \overset{0}{\sigma}_{ij} + \tilde{\sigma}_{ij} \tag{6}$$

and in the following we assume that $\overset{0}{u}_i$ and $\overset{0}{\sigma}_{ij}$ are known from the solution to the first problem. In fact, only the values of $\overset{0}{u}_i (x_1, x_2, 0)$, $\forall (x_1, x_2) \in S$ are needed in the subsequent analysis. Next, special attention is paid to the second non-trivial perturbed problem involving the local disturbance due to the presence of the anticrack S. The mathematical formulation of this boundary value problem is as follows: find fields $\tilde{u}_i$ and $\tilde{\sigma}_{ij}$, decaying at infinity, suitable smooth on $R^3 - S$, such that Eqs (4) and (5) hold subject to the boundary conditions on S

$$\tilde{u}_1 = -\overset{0}{u}_1 + \varepsilon_1 - \omega_3 x_2,$$
$$\tilde{u}_2 = -\overset{0}{u}_2 + \varepsilon_2 + \omega_3 x_1 \tag{7}$$
$$\tilde{u}_3 = -\overset{0}{u}_3 + \varepsilon_3 - \omega_2 x_1 + \omega_1 x_2,$$

where ε_i and ω_i are the unknown components of a small displacement vector and a small angle of rotation describing a motion of the inclusion as a rigid whole under the action of external loads. These parameters will be determined later in the course of solving the problem in hand from the equilibrium conditions of the anticrack (no resultant forces and zero-moments).

To reduce the above problem to mixed boundary value problems of potential theory associated with a half-space region (say, at $x_3 \geq 0$) and further, to integral equations (Kaczyński, 1999), we invoke the relevant symmetry properties about the plane $x_3 = 0$ and can split the problem into two subproblems:

(A) – the antisymmetric problem with the mixed conditions

$$\tilde{u}_3 = -\overset{0}{u}_3 + \varepsilon_3 - \omega_2 x_1 + \omega_1 x_2, \quad \forall (x_1, x_2) \in S,$$
$$\tilde{u}_1 = \tilde{u}_2 = 0, \qquad\qquad \forall (x_1, x_2) \in R^2, \tag{8}$$
$$\tilde{\sigma}_{33} = 0, \qquad\qquad \forall (x_1, x_2) \in R^2 - S$$

and supplemented by the corresponding equilibrium conditions to determine ε_3, ω_α

$$\iint_S \left[\tilde{\sigma}_{33}\left(x_1, x_2, 0^+ \right) - \tilde{\sigma}_{33}\left(x_1, x_2, 0^- \right) \right] dx_1 dx_2 = 0,$$
$$\iint_S x_{3-\alpha} \left[\tilde{\sigma}_{33}\left(x_1, x_2, 0^+ \right) - \tilde{\sigma}_{33}\left(x_1, x_2, 0^- \right) \right] dx_1 dx_2 = 0 \tag{9}$$

(B) – the symmetric problem with the mixed conditions

$$\tilde{u}_1 = -\overset{0}{u}_1 + \varepsilon_1 - \omega_3 x_2, \quad \forall (x_1, x_2) \in S,$$
$$\tilde{u}_2 = -\overset{0}{u}_2 + \varepsilon_2 + \omega_3 x_1, \quad \forall (x_1, x_2) \in S,$$
$$\tilde{u}_3 = 0, \qquad\qquad \forall (x_1, x_2) \in R^2, \tag{10}$$
$$\tilde{\sigma}_{31} = \tilde{\sigma}_{32} = 0, \qquad\qquad \forall (x_1, x_2) \in R^2 - S$$

and additional equilibrium conditions to determine ε_α, ω_3

$$\iint_S \left[\tilde{\sigma}_{3\alpha}\left(x_1, x_2, 0^+ \right) - \tilde{\sigma}_{3\alpha}\left(x_1, x_2, 0^- \right) \right] dx_1 dx_2 = 0,$$
$$\iint_S \left\{ x_2 \left[\tilde{\sigma}_{31}\left(x_1, x_2, 0^+ \right) - \tilde{\sigma}_{31}\left(x_1, x_2, 0^- \right) \right] \right. \tag{11}$$
$$\left. - x_1 \left[\tilde{\sigma}_{32}\left(x_1, x_2, 0^+ \right) - \tilde{\sigma}_{32}\left(x_1, x_2, 0^- \right) \right] \right\} dx_1 dx_2 = 0.$$

3. SOLVING THE ANTICRACK PROBLEM

For the solution of the problems (A) and (B) we use the potential function approach based on representing the components of displacements $\tilde{u}_i$ in terms of quasi-harmonic functions that satisfy the governing equations (4) and are well suited to the mixed boundary conditions (8) an (9).

According to the results obtained by Kaczyński (1993) the potential displacement representation is dependent on the material constants of the sublayers. Hereafter, only the general case $u_1 \neq u_2$ will be considered in which the displacements and stresses are expressed in terms of three harmonic potentials $\phi_i(x_1, x_2, z_i)$, $z_i = t_i x_3$, $\forall i \in \{1, 2, 3\}$ as

$$u_1 = (\phi_1 + \phi_2)_{,1} - \phi_{3,2}, \quad u_2 = (\phi_1 + \phi_2)_{,2} + \phi_{3,1}$$

$$u_3 = \sum_{\alpha=1}^{2} m_\alpha t_\alpha \frac{\partial \phi_\alpha}{\partial z_\alpha}, \tag{12}$$

$$\frac{\sigma_{31}}{c_{44}} = \left[\sum_{\alpha=1}^{2} (1+m_\alpha) t_\alpha \frac{\partial \phi_\alpha}{\partial z_\alpha} \right]_{,1} - t_3 \frac{\partial^2 \phi_3}{\partial z_3 \partial x_2},$$

$$\frac{\sigma_{32}}{c_{44}} = \left[\sum_{\alpha=1}^{2} (1+m_\alpha) t_\alpha \frac{\partial \phi_\alpha}{\partial z_\alpha} \right]_{,2} + t_3 \frac{\partial^2 \phi_3}{\partial z_3 \partial x_1},$$

$$\frac{\sigma_{33}}{c_{44}} = \sum_{\alpha=1}^{2} (1+m_\alpha) \frac{\partial^2 \phi_\alpha}{\partial z_\alpha^2},$$

$$\sigma_{12}^{(l)} = \mu_l \left[2\left(\phi_1 + \phi_2\right)_{,12} + \phi_{3,11} - \phi_{3,22} \right],$$

$$\sigma_{11}^{(l)} = d_{11}^{(l)}\left(\phi_1 + \phi_2\right)_{,11} + d_{12}^{(l)}\left(\phi_1 + \phi_2\right)_{,22}$$
$$+ d_{13}^{(l)} \sum_{\alpha=1}^{2} m_\alpha t_\alpha^2 \frac{\partial^2 \phi_\alpha}{\partial z_\alpha^2} - 2\mu_l \phi_{3,12}, \tag{13}$$

$$\sigma_{22}^{(l)} = d_{12}^{(l)}\left(\phi_1 + \phi_2\right)_{,11} + d_{11}^{(l)}\left(\phi_1 + \phi_2\right)_{,22}$$
$$+ d_{13}^{(l)} \sum_{\alpha=1}^{2} m_\alpha t_\alpha^2 \frac{\partial^2 \phi_\alpha}{\partial z_\alpha^2} + 2\mu_l \phi_{3,12},$$

where the constants t_i, m_α are defined in Appendix B.

We now proceed to construct the potentials separately in subproblems (A) and (B) with the aim of their reducing to some mixed problems of potential theory.

Subproblem (A)

An appropriate displacement representation in terms of a single harmonic function $f(x_1, x_2, x_3)$ that frees the plane

$x_3 = 0$ of the displacement $\tilde{u}_\alpha$ is obtained by taking in the general solution (12)

$$\phi_\alpha\left(x_1, x_2, z_\alpha\right) = (-1)^\alpha f\left(x_1, x_2, z_\alpha\right), \quad \phi_3 \equiv 0. \tag{14}$$

Then the displacement and stress components are

$$\tilde{u}_\alpha = \sum_{\beta=1}^{2} (-1)^\beta \frac{\partial f\left(x_1, x_2, z_\beta\right)}{\partial x_\beta},$$

$$\tilde{u}_3 = \sum_{\beta=1}^{2} (-1)^\beta m_\beta t_\beta \frac{\partial f\left(x_1, x_2, z_\beta\right)}{\partial z_\beta},$$

$$\tilde{\sigma}_{3\alpha} = c_{44}\left[\sum_{\beta=1}^{2} (-1)^\beta \left(1 + m_\beta\right) t_\beta \frac{\partial^2 f\left(x_1, x_2, z_\beta\right)}{\partial z_\beta \partial x_\alpha}\right],$$

$$\tilde{\sigma}_{33} = c_{44}\left[\sum_{\beta=1}^{2} (-1)^\beta \left(1 + m_\beta\right) \frac{\partial^2 f\left(x_1, x_2, z_\beta\right)}{\partial z_\beta^2}\right],$$

$$\tilde{\sigma}_{12}^{(l)} = 2\mu_l \sum_{\beta=1}^{2} (-1)^\beta \frac{\partial f\left(x_1, x_2, z_\beta\right)}{\partial x_1 \partial x_2},$$

$$\tilde{\sigma}_{11}^{(l)} = \sum_{\beta=1}^{2} (-1)^\beta \left[d_{11}^{(l)} \frac{\partial^2 f\left(x_1, x_2, z_\beta\right)}{\partial x_1^2} + d_{12}^{(l)} \frac{\partial^2 f\left(x_1, x_2, z_\beta\right)}{\partial x_2^2}\right]$$
$$+ d_{13}^{(l)} \sum_{\beta=1}^{2} (-1)^\beta m_\beta t_\beta^2 \frac{\partial^2 f\left(x_1, x_2, z_\beta\right)}{\partial z_\beta^2},$$

$$\tilde{\sigma}_{22}^{(l)} = \sum_{\beta=1}^{2} (-1)^\beta \left[d_{12}^{(l)} \frac{\partial^2 f\left(x_1, x_2, z_\beta\right)}{\partial x_1^2} + d_{11}^{(l)} \frac{\partial^2 f\left(x_1, x_2, z_\beta\right)}{\partial x_2^2}\right]$$
$$+ d_{13}^{(l)} \sum_{\beta=1}^{2} (-1)^\beta m_\beta t_\beta^2 \frac{\partial^2 f\left(x_1, x_2, z_\beta\right)}{\partial z_\beta^2}. \tag{15}$$

Across the interface $x_3 = 0^\pm$ equations (15) become

$$\tilde{u}_1 = \tilde{u}_2 = 0,$$

$$\tilde{u}_3^\pm = \left(m_2 t_2 - m_1 t_1\right)\left[f_{,3}\left(x_1, x_2, x_3\right)\right]_{x_3 = 0^\pm},$$

$$\tilde{\sigma}_{3\alpha}^\pm = c_{44}\left(t_- + m_2 t_2 - m_1 t_1\right)\left[f_{,3\alpha}\left(x_1, x_2, x_3\right)\right]_{x_3 = 0^\pm},$$

$$\tilde{\sigma}_{33}^\pm = c_{44}\left(m_2 - m_1\right)\left[f_{,33}\left(x_1, x_2, x_3\right)\right]_{x_3 = 0^\pm}, \tag{16}$$

$$\tilde{\sigma}_{12} = 0,$$

$$\tilde{\sigma}_{11}^\pm = \tilde{\sigma}_{22}^\pm = d_{13}^{(l)}\left(m_2 t_2^2 - m_1 t_1^2\right)\left[f_{,33}\left(x_1, x_2, x_3\right)\right]_{x_3 = 0^\pm}$$

$$\left(\text{substitute } d_{13}^{(1)} \text{ for } x_3 = 0^+, \ d_{13}^{(2)} \text{ for } x_3 = 0^-\right).$$

The application of conditions (8) leads to the boundary conditions

– for $\left(x_1, x_2\right) \in S$

$$\left[f_{,3}\left(x_1, x_2, x_3\right)\right]_{x_3 = 0^+} = \frac{-\overset{0}{u}_3\left(x_1, x_2, 0^+\right) + \varepsilon_3 - \omega_2 x_1 + \omega_1 x_2}{m_2 t_2 - m_1 t_1},$$

– for $\left(x_1, x_2\right) \in R^2 - S$

$$\left[f_{,33}\left(x_1, x_2, x_3\right)\right]_{x_3 = 0^+} = 0. \tag{17}$$

The mixed boundary value problem posed by the above equations is regarded as the classical one appearing in typical electrostatic and punch problems (Sneddon, 1966). It is reduced to an integral equation by assuming the following representation for the unknown potential f and its derivative $f_{,3}$:

$$f\left(\boldsymbol{x}\right) = -\frac{1}{2\pi c_{44}\left(m_2 - m_1\right)} \iint_S q(\boldsymbol{\xi}) \ln\left(\left|\boldsymbol{x} - \boldsymbol{\xi}\right| + x_3\right) dS_{\boldsymbol{\xi}},$$

$$f_{,3}\left(\boldsymbol{x}\right) = -\frac{1}{2\pi c_{44}\left(m_2 - m_1\right)} \iint_S \frac{q(\boldsymbol{\xi}) dS_{\boldsymbol{\xi}}}{\left|\boldsymbol{x} - \boldsymbol{\xi}\right|}. \tag{18}$$

Here, the unknown layer density $q(\xi_1, \xi_2)$ can be identified as the stress $\tilde{\sigma}_{33}\left(\xi_1, \xi_2, 0^+\right)$, $\forall \left(\xi_1, \xi_2\right) \in S$ and $\left|\boldsymbol{x} - \boldsymbol{\xi}\right|$ is a distance between the field point $\boldsymbol{x} = (x_1, x_2, x_3)$ and the integration point $\boldsymbol{\xi} = (\xi_1, \xi_2, 0)$. Due to the well-known properties of the potential of a simple layer (given by (18)$_2$), the last condition in (17) is satisfied, and the first one leads to the following integral equation for the stress $q \equiv \tilde{\sigma}_{33}\big|_{S^+}$:

$$H \iint_S \frac{\tilde{\sigma}_{33}\left(\xi_1, \xi_2\right) d\xi_1 d\xi_2}{\sqrt{\left(x_1 - \xi_1\right)^2 + \left(x_2 - \xi_2\right)^2}} = -\hat{u}_3\left(x_1, x_2\right), \tag{19}$$

where the following notations are used:

$$H = \frac{m_2 t_2 - m_1 t_1}{2\pi c_{44}\left(m_2 - m_1\right)},$$

$$\hat{u}_3\left(x_1, x_2\right) = -\overset{0}{u}_3\left(x_1, x_2, 0^+\right) + \varepsilon_3 - \omega_2 x_1 + \omega_1 x_2. \tag{20}$$

It is noteworthy that this governing equation has a similar form as that arising in the classical contact problem (Fabrikant, 1989). Generally, it can be solved by numerical methods. However, in the case where S is an ellipse and $\hat{u}_3$ is an arbitrary polynomial, a closed-form exact solution can be obtained (Rahman, 2002).

Subproblem (B)

The mathematical formulation satisfying the conditions (10) is more complex that than used in subproblem (A) and requires the introduction of two harmonic functions $G(x_1, x_2, x_3)$, $H(x_1, x_2, x_3)$ such that their relationships to ϕ_i in Eqs. (12) are

$$\phi_1(x_1, x_2, z_1) = -\frac{m_2 t_2}{m_2 t_2 - m_1 t_1} F_1(x_1, x_2, z_1),$$

$$\phi_2(x_1, x_2, z_2) = \frac{m_1 t_1}{m_2 t_2 - m_1 t_1} F_2(x_1, x_2, z_2), \qquad (21)$$

$$\phi_3(x_1, x_2, z_3) = F_3(x_1, x_2, z_3),$$

where

$$F_1(x_1, x_2, z_1) = \frac{\partial G(x_1, x_2, z_1)}{\partial x_1} + \frac{\partial H(x_1, x_2, z_1)}{\partial x_2},$$

$$F_2(x_1, x_2, z_2) = \frac{\partial G(x_1, x_2, z_2)}{\partial x_1} + \frac{\partial H(x_1, x_2, z_2)}{\partial x_2}, \qquad (22)$$

$$F_3(x_1, x_2, z_3) = \frac{\partial G(x_1, x_2, z_3)}{\partial x_2} - \frac{\partial H(x_1, x_2, z_3)}{\partial x_1}.$$

Inserting Eqs (21) into (12) yields the displacements

$$\tilde{u}_1 = \frac{[m_1 t_1 F_2 - m_2 t_2 F_1]_{,1}}{m_2 t_2 - m_1 t_1} - \frac{\partial F_3}{\partial x_2},$$

$$\tilde{u}_2 = \frac{[m_1 t_1 F_2 - m_2 t_2 F_1]_{,2}}{m_2 t_2 - m_1 t_1} + \frac{\partial F_3}{\partial x_1}, \qquad (23)$$

$$\tilde{u}_3 = \frac{t_1 t_2}{m_2 t_2 - m_1 t_1}\left(\frac{\partial F_2}{\partial z_2} - \frac{\partial F_1}{\partial z_1}\right).$$

By the same procedures, the corresponding stress components are found from Eqs (13) as

$$\frac{\tilde{\sigma}_{31}}{c_{44}} = \frac{t_1 t_2}{m_2 t_2 - m_1 t_1}\left[(1+m_1)\frac{\partial^2 F_2}{\partial x_1 \partial z_2} - (1+m_2)\frac{\partial^2 F_1}{\partial x_1 \partial z_1}\right] \qquad (24)$$
$$- t_3 \frac{\partial^2 F_3}{\partial x_2 \partial z_3},$$

$$\frac{\tilde{\sigma}_{32}}{c_{44}} = \frac{t_1 t_2}{m_2 t_2 - m_1 t_1}\left[(1+m_1)\frac{\partial^2 F_2}{\partial x_2 \partial z_2} - (1+m_2)\frac{\partial^2 F_1}{\partial x_2 \partial z_1}\right]$$
$$+ t_3 \frac{\partial^2 F_3}{\partial x_1 \partial z_3},$$

$$\frac{\tilde{\sigma}_{33}}{c_{44}} = \frac{1}{m_2 t_2 - m_1 t_1}\left[t_1(1+m_1)\frac{\partial^2 F_2}{\partial z_2^2} - t_2(1+m_2)\frac{\partial^2 F_1}{\partial z_1^2}\right],$$

$$\frac{\tilde{\sigma}_{12}^{(l)}}{\mu_l} = \frac{2[m_1 t_1 F_2 - m_2 t_2 F_1]_{,12}}{m_2 t_2 - m_1 t_1} + F_{3,11} - F_{3,22},$$

$$\tilde{\sigma}_{11}^{(l)} = \frac{d_{11}^{(l)}[m_1 t_1 F_2 - m_2 t_2 F_1]_{,11} + d_{12}^{(l)}[m_1 t_1 F_2 - m_2 t_2 F_1]_{,22}}{m_2 t_2 - m_1 t_1}$$
$$+ \frac{d_{13}^{(l)} t_1 t_2}{m_2 t_2 - m_1 t_1}\left[t_2 \frac{\partial^2 F_2}{\partial z_2^2} - t_1 \frac{\partial^2 F_1}{\partial z_1^2}\right] - 2\mu_l F_{3,12},$$

$$\tilde{\sigma}_{22}^{(l)} = \frac{d_{12}^{(l)}[m_1 t_1 F_2 - m_2 t_2 F_1]_{,11} + d_{11}^{(l)}[m_1 t_1 F_2 - m_2 t_2 F_1]_{,22}}{m_2 t_2 - m_1 t_1}$$
$$+ \frac{d_{13}^{(l)} t_1 t_2}{m_2 t_2 - m_1 t_1}\left[t_2 \frac{\partial^2 F_2}{\partial z_2^2} - t_1 \frac{\partial^2 F_1}{\partial z_1^2}\right] + 2\mu_l F_{3,12}.$$

The above expressions simplify considerable on the plane $x_3 = 0$ (then $\forall i$, $z_i = 0$, $F_i(x_1, x_2, z_i) = F_i(x_1, x_2, x_3)$

$$\frac{\partial F_i(x_1, x_2, z_i)}{\partial z_i} = \frac{\partial F_i(x_1, x_2, x_3)}{\partial x_3}, \text{ and } F_1 = F_2 = G_{,1} + H_{,2},$$

$F_3 = G_{,2} - H_{,1}$). Moreover, by letting

$$g(x_1, x_2, x_3) = \frac{\partial G(x_1, x_2, x_3)}{\partial x_3},$$
$$\qquad (25)$$
$$h(x_1, x_2, x_3) = \frac{\partial H(x_1, x_2, x_3)}{\partial x_3},$$

Eqs (23) and (24) yield the displacement and stress components across the plane of symmetry $x_3 = 0$

$$\tilde{u}_1 = \left[g_{,3}\right]_{x_3=0},$$

$$\tilde{u}_2 = \left[h_{,3}\right]_{x_3=0},$$

$$\tilde{u}_3 = 0,$$

$$\frac{\tilde{\sigma}_{31}^{\pm}}{C^*} = \left[g_{,33} + \kappa g_{,22} - \kappa h_{,12}\right]_{x_3=0^{\pm}},$$
$$\qquad (26)$$

$$\frac{\tilde{\sigma}_{32}^{\pm}}{C^*} = \left[h_{,33} + \kappa h_{,11} - \kappa g_{,12}\right]_{x_3=0^{\pm}},$$

$$\tilde{\sigma}_{33} = -c_{44}\left(1 + \frac{t_-}{m_2 t_2 - m_1 t_2}\right)\left[g_{,31} + h_{,32}\right]_{x_3=0},$$

$$\tilde{\sigma}_{12}^{(l)} = \mu_l\left[g_{,32} + h_{,31}\right]_{x_3=0}.$$

Expressions for $\tilde{\sigma}_{11}^{(l)}$ and $\tilde{\sigma}_{22}^{(l)}$ have been omitted because of their complexity. The constants C^* and κ stand for

$$C^* = c_{44}\frac{t_1 t_2(m_2 - m_1)}{m_2 t_2 - m_1 t_1}, \qquad \kappa = 1 - \frac{t_3}{C^*}. \qquad (27)$$

We see that the boundary value problem posed by Eqs (10) is equivalent to that of finding two harmonic functions g and h in $x_3 \geq 0$ such that their partial derivatives up to the third order vanish at infinity and satisfies the following mixed conditions on $x_3 = 0$:

– for $(x_1, x_2) \in S$

$$\left[g_{,3}(x_1, x_2, x_3)\right]_{x_3=0^+} = -\tilde{u}_1^0 + \varepsilon_1 - \omega_3 x_2, \quad \forall(x_1, x_2) \in S,$$

$$\left[h_{,3}(x_1, x_2, x_3)\right]_{x_3=0^+} = -\tilde{u}_2^0 + \varepsilon_2 + \omega_3 x_1, \quad \forall(x_1, x_2) \in S,$$

– for $(x_1, x_2) \in R^2 - S$ $\qquad (28)$

$$\left[g_{,33} + \kappa g_{,22} - \kappa h_{,12}\right]_{x_3=0^+} = 0,$$

$$\left[h_{,33} + \kappa h_{,11} - \kappa g_{,12}\right]_{x_3=0^+} = 0.$$

It can be observed that this formulation is dual to the well-known obtained for the shear loading crack problem (see Kassir and Sih, 1975). To solve the problem, we make use of the integral method developed by Kaczyński (1999). The harmonic functions g and h are expressed as Fourier's integrals (Sneddon, 1972)

$$\begin{bmatrix} g(\boldsymbol{x}) \\ h(\boldsymbol{x}) \end{bmatrix} = \iint\limits_{R^2} \frac{\exp\left[-x_3|\boldsymbol{\xi}| + i(x_\alpha \xi_\alpha)\right]}{|\boldsymbol{\xi}|^2} \begin{bmatrix} A_g(\boldsymbol{\xi}) \\ A_h(\boldsymbol{\xi}) \end{bmatrix} dS_{\boldsymbol{\xi}}, \quad (29)$$

where $\boldsymbol{\xi} = (\xi_1, \xi_2, 0) \in S$, $|\boldsymbol{\xi}| = \sqrt{\xi_1^2 + \xi_2^2}$ and the unknown functions A_g and A_h, in view of (28), must satisfy the following system

$$\begin{bmatrix} 1 - \dfrac{\kappa \xi_2^2}{|\boldsymbol{\xi}|^2} & \dfrac{\kappa \xi_1 \xi_2}{|\boldsymbol{\xi}|^2} \\[2mm] \dfrac{\kappa \xi_1 \xi_2}{|\boldsymbol{\xi}|^2} & 1 - \dfrac{\kappa \xi_1^2}{|\boldsymbol{\xi}|^2} \end{bmatrix} \begin{bmatrix} A_g(\boldsymbol{\xi}) \\ A_h(\boldsymbol{\xi}) \end{bmatrix} = $$
$$= \frac{1}{4\pi^2 C^*} \iint\limits_S \begin{bmatrix} \sigma_{31}(\eta_1, \eta_2) \\ \sigma_{32}(\eta_1, \eta_2) \end{bmatrix} \exp\left[-i(\eta_\alpha \xi_\alpha)\right] dS_{\boldsymbol{\eta}}. \quad (30)$$

Its solution is

$$4\pi^2 C^* (1 - \kappa) \begin{bmatrix} A_g(\boldsymbol{\xi}) \\ A_h(\boldsymbol{\xi}) \end{bmatrix} = $$
$$\begin{bmatrix} 1 - \dfrac{\kappa \xi_1^2}{|\boldsymbol{\xi}|^2} & -\dfrac{\kappa \xi_1 \xi_2}{|\boldsymbol{\xi}|^2} \\[2mm] -\dfrac{\kappa \xi_1 \xi_2}{|\boldsymbol{\xi}|^2} & 1 - \dfrac{\kappa \xi_2^2}{|\boldsymbol{\xi}|^2} \end{bmatrix} \iint\limits_S \begin{bmatrix} \sigma_{31}(\boldsymbol{\eta}) \\ \sigma_{32}(\boldsymbol{\eta}) \end{bmatrix} \exp\left[-i(\eta_\alpha \xi_\alpha)\right] dS_{\boldsymbol{\eta}}. \quad (31)$$

Now, making use of these expressions it follows from Eqs (29) that (see Silovanyuk, 1984 and Kaczyński, 1999 for more details)

$$C g_{,3}(\boldsymbol{x}) = \iint\limits_S \frac{\tilde{\sigma}_{31}(\boldsymbol{\xi}) dS_{\boldsymbol{\xi}}}{|\boldsymbol{x} - \boldsymbol{\xi}|} - \kappa \iint\limits_S \frac{\tilde{\sigma}_{31}(\boldsymbol{\xi})(x_2 - \xi_2)^2 dS_{\boldsymbol{\xi}}}{|\boldsymbol{x} - \boldsymbol{\xi}|^3}$$
$$+ \kappa \iint\limits_S \frac{\tilde{\sigma}_{32}(\boldsymbol{\xi})(x_1 - \xi_1)(x_2 - \xi_2) dS_{\boldsymbol{\xi}}}{|\boldsymbol{x} - \boldsymbol{\xi}|^3},$$
$$C h_{,3}(\boldsymbol{x}) = \iint\limits_S \frac{\tilde{\sigma}_{32}(\boldsymbol{\xi}) dS_{\boldsymbol{\xi}}}{|\boldsymbol{x} - \boldsymbol{\xi}|} - \kappa \iint\limits_S \frac{\tilde{\sigma}_{32}(\boldsymbol{\xi})(x_1 - \xi_1)^2 dS_{\boldsymbol{\xi}}}{|\boldsymbol{x} - \boldsymbol{\xi}|^3}$$
$$+ \kappa \iint\limits_S \frac{\tilde{\sigma}_{31}(\boldsymbol{\xi})(x_1 - \xi_1)(x_2 - \xi_2) dS_{\boldsymbol{\xi}}}{|\boldsymbol{x} - \boldsymbol{\xi}|^3} \quad (32)$$

where

$$C = -2\pi(1 - \kappa) C^* = -2\pi t_3. \quad (33)$$

Finally, from the first conditions of (28), one obtains the following integral equations for the stresses $\tilde{\sigma}_{3\alpha}\big|_{S^+}$:

$$\iint\limits_S \frac{\tilde{\sigma}_{31}(\boldsymbol{\xi}) dS_{\boldsymbol{\xi}}}{|\boldsymbol{x^*} - \boldsymbol{\xi}|} - \kappa \iint\limits_S \frac{\tilde{\sigma}_{31}(\boldsymbol{\xi})(x_2 - \xi_2)^2 dS_{\boldsymbol{\xi}}}{|\boldsymbol{x^*} - \boldsymbol{\xi}|^3}$$
$$+ \kappa \iint\limits_S \frac{\tilde{\sigma}_{32}(\boldsymbol{\xi})(x_1 - \xi_1)(x_2 - \xi_2) dS_{\boldsymbol{\xi}}}{|\boldsymbol{x^*} - \boldsymbol{\xi}|^3} = -2\pi t_3 \,\hat{u}_1(x_1, x_2),$$
$$\iint\limits_S \frac{\tilde{\sigma}_{32}(\boldsymbol{\xi}) dS_{\boldsymbol{\xi}}}{|\boldsymbol{x^*} - \boldsymbol{\xi}|} - \kappa \iint\limits_S \frac{\tilde{\sigma}_{32}(\boldsymbol{\xi})(x_1 - \xi_1)^2 dS_{\boldsymbol{\xi}}}{|\boldsymbol{x^*} - \boldsymbol{\xi}|^3}$$
$$+ \kappa \iint\limits_S \frac{\tilde{\sigma}_{31}(\boldsymbol{\xi})(x_1 - \xi_1)(x_2 - \xi_2) dS_{\boldsymbol{\xi}}}{|\boldsymbol{x^*} - \boldsymbol{\xi}|^3} = -2\pi t_3 \,\hat{u}_2(x_1, x_2), \quad (34)$$

where the following notations were introduced:

$$\boldsymbol{x^*} = (x_1, x_2) \in S, \quad \boldsymbol{\xi} = (\xi_1, \xi_2) \in S,$$
$$\hat{u}_1(x_1, x_2) = -\overset{0}{u}_1\left(x_1, x_2, 0^+\right) + \varepsilon_1 - \omega_3 x_2,$$
$$\hat{u}_2(x_1, x_2) = -\overset{0}{u}_2\left(x_1, x_2, 0^+\right) + \varepsilon_2 + \omega_3 x_1. \quad (35)$$

Note that the form of (34) is similar to that given for the corresponding homogeneous isotropic problem. Moreover, it is verified that the derived governing integral equations are in agreement with those achieved by Silovanyuk (1984) in the homogeneous case. Knowing the stresses $\tilde{\sigma}_{3\alpha}(x_1, x_2)$ acting on the side S^+ of the rigid inclusion from the solution of Eqs (34), the stress and displacement fields can be found from the main potentials g and h, determined by means of (32).

4. EXAMPLE: ANTICRACK UNDER TENSION

For illustration, presented is a solution to the problem of a rigid circularly-shaped interface inclusion (such that $S = \left\{(x_1, x_2, 0) : r \equiv \sqrt{x_1^2 + x_2^2} \leq a\right\}$) in a periodic two-layer laminated space subjected to a constant normal stress p at infinity (see Fig. 1), i.e.

$$\sigma_{33}(\infty) = p, \quad \sigma_{31}(\infty) = \sigma_{32}(\infty) = 0. \quad (36)$$

The results for the 0-displacements of the inclusion-free problem involving the solution of the basic equations (4) and (5) with conditions (36) are readily obtained to be

$$\overset{0}{u}_1 = -A p x_1, \quad \overset{0}{u}_2 = -A p x_2,$$
$$\overset{0}{u}_3 = A_3 p x_3, \quad (37)$$

where

$$A = \frac{c_{13}}{c_{33}(c_{11}+c_{12})-2c_{13}^2} \,,$$

$$A_3 = \frac{c_{11}+c_{12}}{c_{33}(c_{11}+c_{12})-2c_{13}^2} \,. \tag{38}$$

Now invoking the displacements in Eqs (37) on the plane $x_3 = 0$, we deduce by consideration of symmetry in (8) that $\varepsilon_3 = \omega_1 = \omega_2 = 0$. Thus, we proceed to solving the sub-problem B (cf (10) and (11)) in which the appropriate conditions are

$$\tilde{u}_1(x_1,x_2,0^+) = A\,p\,x_1 + \varepsilon_1 - \omega_3 x_2, \quad \forall\,(x_1,x_2)\in S\,,$$

$$\tilde{u}_2(x_1,x_2,0^+) = A\,p\,x_2 + \varepsilon_2 + \omega_3 x_1, \quad \forall\,(x_1,x_2)\in S\,,$$

$$\tilde{u}_3(x_1,x_2,0^+) = 0, \quad \forall\,(x_1,x_2)\in R^2\,, \tag{39}$$

$$\tilde{\sigma}_{31}(x_1,x_2,0^+) = \tilde{\sigma}_{32}(x_1,x_2,0^+) = 0, \forall\,(x_1,x_2)\in R^2- S\,,$$

$$\tilde{u}_i = O\!\left(\frac{1}{|\boldsymbol{x}|}\right) \quad \text{as} \quad |\boldsymbol{x}|\to\infty\,.$$

This problem is reduced to the set of coupled two-dimensional integral equations (34) in which the right sides are determined by the following polynomials:

$$\hat{u}_1(x_1,x_2) = \varepsilon_1 + A\,p\,x_1 - \omega_3 x_2\,,$$

$$\hat{u}_2(x_1,x_2) = \varepsilon_2 + \omega_3 x_1 + A\,p\,x_2\,. \tag{40}$$

An exact solution of these integral equations, obtained by using Galin's theorem, has the form

$$\tilde{\sigma}_{3\alpha}(x_1,x_2) = \frac{b_{0\alpha}+b_{1\alpha}x_1+b_{2\alpha}x_2}{\sqrt{a^2-r^2}}\,, \ \forall\alpha\in\{1,2\}, \tag{41}$$

where $b_{i\alpha}$, $i\in\{0,1,2\}, \alpha\in\{1,2\}$ are the unknown constants to be determined. Putting (41) into (34) and calculating the resulting integrals (see Vorovich et al.,1974), we arrive at the equalities of two polynomials. Hence, a system of algebraic equations for $b_{i\alpha}$ can be obtained, and their solving yields

$$b_{0\alpha} = -\frac{4t_3}{\pi(2-k)}\,\varepsilon_\alpha\,, \ \forall\,\alpha\in\{1,2\},$$

$$b_{12} = b_{21} = \frac{4t_3}{\pi}\,\omega_3\,, \tag{42}$$

$$b_{11} = b_{22} = -\frac{4}{\pi}AC^*p\,.$$

If we now make use of the equilibrium conditions (11) on the anticrack we find (as might be expected) that

$$\varepsilon_1 = \varepsilon_2 = \omega_3 = 0 \tag{43}$$

and the solution given by (41) can be written in the simple form

$$\tilde{\sigma}_{3\alpha}(x_1,x_2) = B\,\frac{x_\alpha}{\sqrt{a^2-r^2}}\,, \ (x_1,x_2,0^+)\in S\,, \tag{44}$$

where

$$B = -\frac{4}{\pi}AC^*p\,. \tag{45}$$

Accordingly, the problem is axially symmetric and the full elastic field is determined if we find the main potentials g and h (see (21) - (25)). Substituting (44) into (32) we get

$$g_{,3} = \frac{B}{C}\left(\varphi + \kappa x_2\,\varphi_{,2} - \kappa x_1\,\psi_{,2}\right),$$

$$h_{,3} = \frac{B}{C}\left(\psi + \kappa x_1\,\psi_{,2} - \kappa x_2\,\varphi_{,1}\right). \tag{46}$$

Here φ and ψ are the potentials of simple layers defined as

$$\varphi(\boldsymbol{x}) = \iint\limits_S \frac{\xi_1\,d\xi_1\,d\xi_2}{\sqrt{(x_1-\xi_1)^2+(x_2-\xi_2)^2+x_3^2}\ \sqrt{a^2-\xi_1^2-\xi_2^2}}\,,$$

$$\psi(\boldsymbol{x}) = \iint\limits_S \frac{\xi_2\,d\xi_1\,d\xi_2}{\sqrt{(x_1-\xi_1)^2+(x_2-\xi_2)^2+x_3^2}\ \sqrt{a^2-\xi_1^2-\xi_2^2}}\,, \tag{47}$$

for which the method of Fabrikant (1989) yields the explicit results in elementary functions as follows

$$\varphi(\boldsymbol{x}) = \pi x_1\left(\arcsin\frac{a}{l_2} - \frac{a\sqrt{l_2^2-a^2}}{l_2^2}\right),$$

$$\psi(\boldsymbol{x}) = \pi x_2\left(\arcsin\frac{a}{l_2} - \frac{a\sqrt{l_2^2-a^2}}{l_2^2}\right), \tag{48}$$

where in his notation

$$l_1 \equiv l_1(a,r,x_3) = \frac{1}{2}\left[\sqrt{(r+a)^2+x_3^2} - \sqrt{(r-a)^2+x_3^2}\right],$$

$$l_2 \equiv l_2(a,r,x_3) = \frac{1}{2}\left[\sqrt{(r+a)^2+x_3^2} + \sqrt{(r-a)^2+x_3^2}\right]. \tag{49}$$

All the necessary partial derivatives or some integrals of potentials (48) can be found in Appendix 5 of the book by Fabrikant (1991), which allows us to write a complete solution to problem under study.

It is of interest to record and discuss the relevant interfacial stresses in the plane of the anticrack. They are given below:

$$\tilde{\sigma}_{3r}(r,0^\pm) = \begin{cases} \mp\dfrac{4\beta_r\,p\,r}{\pi\sqrt{a^2-r^2}}\,, & 0\le r<a, \\[3mm] 0, & r>a, \end{cases} \tag{50}$$

$$\hat{\sigma}_{33}(r,0^\pm) = \begin{cases} -\beta_3\,p\,, & 0\le r<a, \\[3mm] \dfrac{2\beta_3\,p}{\pi}\left(\dfrac{a}{\sqrt{r^2-a^2}} - \arcsin\dfrac{a}{r}\right), & r>a\,, \end{cases} \tag{51}$$

where (see Appendices)

$$\beta_r = A\,C^* = \frac{c_{11}\,c_{33}\,c_{44}\,t_+}{\left[c_{33}\left(c_{11}+c_{12}\right)-2c_{13}^2\right]\left(c_{11}+c_{44}\right)}\,, \qquad (52)$$

$$\beta_3 = \frac{2c_{13}\,c_{44}\left(\sqrt{c_{11}\,c_{33}}-c_{13}\right)}{\left(\sqrt{c_{11}\,c_{33}}+c_{44}\right)\left[c_{33}\left(c_{11}+c_{12}\right)-2c_{13}^2\right]}\,. \qquad (53)$$

Now, it is significant to observe that the singularity of the stresses close to the edge of the anticrack has the order $r^{-1/2}$, contrary to oscillatory type observed in the elastic fields relating to bimaterial interfaces. From the standpoint of classical fracture mechanics, two failure mechanisms are possible:

− separation of the material from the inclusion characterized by the stress singularity coefficients

$$S_{\mathrm{II}}^{\pm} = \lim_{r\to a^-}\sqrt{2\pi\left(a-r\right)}\,\tilde{\sigma}_{3r}\left(r,0^{\pm}\right) = \mp\frac{4\beta_r\,p\,\sqrt{a}}{\sqrt{\pi}} \qquad (54)$$

− mode I (edge-opening) deformation characterized by the stress intensity factor

$$K_{\mathrm{I}} = \lim_{r\to a^+}\sqrt{2\pi\left(r-a\right)}\,\sigma_{33}\left(r,0\right) = \frac{2\beta_3\,p\,\sqrt{a}}{\sqrt{\pi}}\,. \qquad (55)$$

These parameters may be used to the determination of the limiting equilibrium of the considered composite weakened by the anticrack (see, e.g. Rahman, 2002).

Finally, the solution to the corresponding homogeneous material problem is the special case when $\lambda_1 = \lambda_2 \equiv \lambda$, $\mu_1 = \mu_2 \equiv \mu$, and hence $c_{11} = c_{33} = \lambda + 2\mu$, $c_{12} = c_{13} = \lambda$, $c_{44} = \mu$. Then Eqs (52) and (53) become

$$\beta_r = \frac{\lambda\left(\lambda+2\mu\right)}{\left(\lambda+3\mu\right)\left(3\lambda+2\mu\right)} = \frac{2\nu\left(1-\nu\right)}{\left(1+\nu\right)\left(3-4\nu\right)}\,,$$
$$\beta_3 = \frac{2\lambda\mu}{\left(\lambda+3\mu\right)\left(3\lambda+2\mu\right)} = \frac{2\nu\left(1-2\nu\right)}{\left(1+\nu\right)\left(3-4\nu\right)} \qquad (56)$$

with $\nu = \dfrac{\lambda}{2\left(\lambda+\mu\right)}$ being Poisson's ratio, and the results are in agreement with those obtained differently by Kassir and Sih (1968).

APPENDIX A

Denoting by

$$b_l = \lambda_l + 2\mu_l \quad \left(l=1,2\right), \quad b = \left(1-\eta\right)b_1 + \eta\,b_2\,,$$

the positive coefficients in governing equations (4) and (5) are given by the following formulas:

$$c_{33} = b_1\,b_2\,/\,b\,,$$
$$c_{11} = c_{33} + \left[4\eta\left(1-\eta\right)\left(\mu_1-\mu_2\right)\left(\lambda_1-\lambda_2+\mu_1-\mu_2\right)\right]/\,b\,,$$
$$c_{13} = \left[\left(1-\eta\right)\lambda_2\,b_1 + \eta\,\lambda_1\,b_2\right]/\,b\,,$$
$$c_{12} = \left\{\lambda_1\,\lambda_2 + 2\left[\eta\,\mu_2+\left(1-\eta\right)\mu_1\right]\left[\eta\,\lambda_1+\left(1-\eta\right)\lambda_2\right]\right\}/\,b\,,$$
$$c_{44} = \mu_1\mu_2\,/\left[\left(1-\eta\right)\mu_1 + \eta\,\mu_2\right]\,,$$
$$d_{11}^{(l)} = \left[4\mu_l\left(\lambda_l+\mu_l\right)+\lambda_l\,c_{13}\right]/\,b_l\,,$$
$$d_{12}^{(l)} = \left[2\mu_l\,\lambda_l+\lambda_l\,c_{13}\right]/\,b_l\,,$$
$$d_{13}^{(l)} = \lambda_l\,c_{33}\,/\,b_l\,.$$

APPENDIX B

The constants appearing in Eqs (12) and (13) are given as follows:

$$t_1 = \tfrac{1}{2}\left(t_+-t_-\right), \qquad t_2 = \tfrac{1}{2}\left(t_++t_-\right),$$
$$t_3 = \sqrt{\left(c_{11}-c_{12}\right)/2c_{44}}\,,$$
$$m_\alpha = \frac{c_{11}\,t_\alpha^{-2}-c_{44}}{c_{13}+c_{44}}\,, \quad \forall\alpha\in\{1,2\},$$

where

$$t_\pm = \sqrt{\frac{\left(A_\pm\pm2\,c_{44}\right)A_\mp}{c_{33}\,c_{44}}}\,,$$
$$A_\pm = \sqrt{c_{11}\,c_{33}}\pm c_{13}\,.$$

Note that $t_1\,t_2 = \sqrt{c_{11}\,/\,c_{33}}$, $m_1\,m_2 = 1$.

REFERENCES

1. **Berezhnitskii L.T., Panasyuk V.V., Stashchuk N.G.** (1983), *The interaction of rigid linear inclusions and cracks in a deformable body*, (in Russian), Naukowa Dumka, Kiev.
2. **Chaudhuri R.A.** (2006), Three-dimensional asymptotic stress field in the vicinity of the circumference of a bimaterial penny-shaped interfacial discontinuity, *Int. J. Fracture*, Vol. 141, 211-225.
3. **Fabrikant V.I.** (1989), *Applications of potential theory in mechanics: a selection of new results*, Kluwer Academic Publishers, Dordrecht.
4. **Fabrikant V.I.** (1991), *Mixed boundary value problems of potential theory and their applications in* e*ngineering*, Kluwer Academic Publishers, Dordrecht.
5. **Gladwell L.B.M.** (1999), On inclusions at a bi-material elastic interface, *J. Elast.*, Vol. 54, 27-41.
6. **Kaczyński A.** (1993), On the three-dimensional interface crack problems in periodic two-layered composites, *Int. J. Fracture*, Vol. 62, 283-306.
7. **Kaczyński A.** (1999), Rigid sheet-like interface inclusion in an infinite bimaterial periodically layered composites, *J. Theor. Appl. Mech.*, Vol. 37, No 1, 81-94.
8. **Kaczyński A., Matysiak S.J.** (1997), Some 2D interface crack and rigid inclusion problems in microperiodically

layered elastic composites, *J. Theor. Appl. Mech.*, Vol. 35, No 4, 751-762.

9. **Kaczyński A., Matysiak S.J.** (1997), Three-dimensional thermoelastic problems of interface cracks and rigid inclusions in bimaterial layered composites, *Thermal Stresses '99. Third International Congress on Thermal Stresses*, Cracow University of Technology, Cracow, Poland, 287-290.

10. **Kassir M.K, Sih G.C.** (1968), Some three-dimensional inclusion problems in elasticity, *Int. J. Solids Structures*, Vol. 4, 225-241.

11. **Kassir M.K, Sih G.C.** (1975), *Three-dimensional crack problems*, Mechanics of Fracture 2, Noordhoof Int. Publ., Leyden.

12. **Li X.F., Fan T.Y.** (2001), The asymptotic stress field for a rigid circular inclusion at the interface of two bonded dissimilar elastic half-space materials, *Int. J. Solids Structures*, Vol. 38, 8019-8035.

13. **Matysiak S.J., Woźniak Cz.** (1988), On the microlocal modelling of thermoelastic periodic composites, *J. Tech. Phys.*, Vol. 29, 85-97.

14. **Mura T.** (1982), *Micromechanics of defects in solids*, Martinus Nijhoff, The Hague.

15. **Panasyuk V.V., Stadnik M.M., Silovanyuk V.P.** (1986), *Stress concentrations in three-dimensional bodies with thin inclusions*, (in Russian), Nuakova Dumka, Kiev.

16. **Podil'chuk Y.N.** (1997), Stress state of a transversely-isotropic body with elliptical inclusion, *Int. Appl. Mech.*, Vol. 33, 881-887.

17. **Rahman M.** (1999), Some problems of a rigid elliptical disc-inclusion bonded inside a transversely isotropic space, *ASME J. Appl. Mech.*, Vol. 66, 612-630.

18. **Rahman M.** (2002), A rigid elliptical disc-inclusion, in an elastic solid, subjected to polynomial normal shift, *J. Elasticity*, Vol. 66, 207-235.

19. **Rossmanith H-P. (Ed.)** (1997), *Damage and failure of interfaces*, A.A. Balkema, Rotterdam.

20. **Selvadurai A.P.S.** (1982), On the interaction between an elastically embedded rigid inhomogeneity and a laterally placed concentrated force, *ZAMP*, Vol. 33, 241-249.

21. **Selvadurai A.P.S.** (2000), An inclusion at a bi-material elastic interface, *J. Eng. Math.*, Vol. 37, 155-170.

22. **Silovanyuk V.P.** (1984), A rigid lamellate inclusion in elastic space, (in Russian), *Fiz.-Chem. Mech. Mat.*, Vol. 20, No 5, 80-84.

23. **Sneddon I. N.** (1966), *Mixed boundary value problems in potential theory*, North-Holland Publ. Comp., Amsterdam.

24. **Sneddon I. N.** (1972), *The use of integral transforms*, McGraw-Hill, New York .

25. **Ting T.C.T.** (1966), *Anisotropic elasticity: theory and applications*, Oxford University Press, New York.

26. **Vorovich I.I., Alexandrov V.V., Babeshko V.A.** (1974), *Non-classical mixed boundary problems of the theory of elasticity*, (in Russian), Nauka, Moscow.

27. **Woźniak Cz.** (1987), A nonstandard method of modelling of thermoelastic periodic composites, *Int. J. Engng. Sci.*, Vol. 25, 483-499.

A ROLE OF CYCLIC LOADING AT MODIFICATION
OF SIMPLE DEFORMATION PROCESSES OF METALLIC MATERIALS

Zbigniew L. KOWALEWSKI[*, **], **Tadeusz SZYMCZAK** [*, ***]

[*]Motor Transport Institute, ul. Jagiellońska 80, 03-301 Warszawa
[**]Institute of Fundamental Technological Research, ul. Pawińskiego 5B, 02-106 Warszawa
[***]Białystok Technical University, Faculty of Mechanical Engineering, ul. Wiejska 45 C, 15-351 Białystok

zkowalew@ippt.gov.pl, tadeusz.szymczak@its.waw.pl

Abstract: The paper presents experimental results of investigations carried out on the 2024 aluminium alloy and P91 steel under biaxial stress state. The loading programme comprised a monotonic tension assisted by torsion-reverse-torsion cycles. An influence of the cyclic loading and its delay with respect to uniaxial tension on the selected mechanical parameters taken on the basis of tensile characteristics was investigated. Additionally, a relative variation of the proportional limit and yield point due to the loading history applied was analyzed. A permanency of effects observed during combination of tension and cyclic torsion was experimentally assessed on the basis of an initial yield surface evolution.

1. INTRODUCTION

An activity of many research groups is focused on experimental evaluation of an influence of cyclic loading on material behaviour under complex stress states being combination of an axial force and twisting moment (Niewielski et. al. 2006; Xiang, 2003; Correa et. al., 2003; Gronostajski and Jaśkiewicz, 2004; Kowalewski and Szymczak, 2007, 2008, 2009). The results achieved from such investigations are important from technological point of view because they are providing a knowledge necessary for modification of some metal forming processes, such as drawing, extrusion (Kong and Hodgson, 2000) or forging (Bochniak et al. 2006).
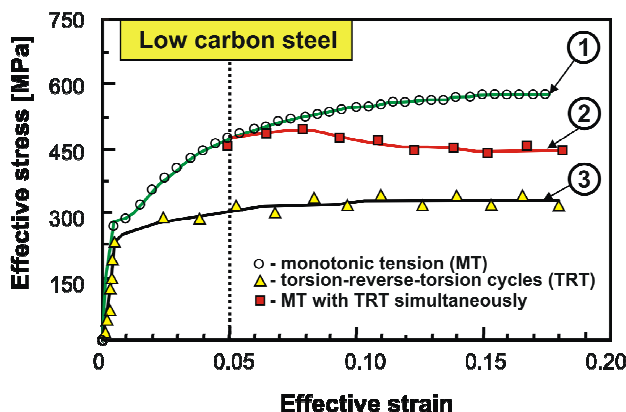
Moreover, these results are also important for developing of a new theoretical formulas and modelling of material effects observed (Kong and Hodgson, 2000).

An essential change of the stress-strain characteristic in the form of stress drop for the same magnitude of strain is the typical material effect associated with cycles acting in the perpendicular direction with respect to the monotonic loading (Correa et. al., 2003; Gronostajski and Jaśkiewicz, 2004; Kowalewski and Szymczak 2007, 2008, 2009), Fig. 1. As it is presented in Fig.1, a switching on of the cyclic loading caused 33% drop of the monotonic tension curve. However, a comparison of the stress-strain curve for the tests carried out under combination of monotonic tension and cyclic torsion against to the curve representing a cyclic torsion only, exhibits a hardening effect.
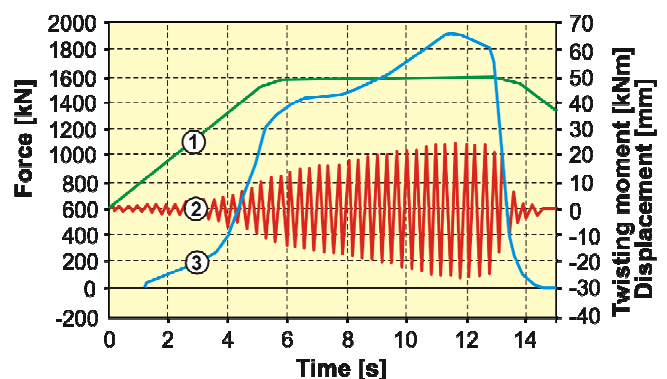

Fig. 1. Variations of the effective stress-effective strain characteristics due to different types of loading: 1 – monotonic tension, 2 – monotonic tension and torsion-reverse-torsion cycles, 3 – torsion-reverse-torsion-cycles (Correa et. al. 2003)

Fig. 2. A scheme of loading programme for optimisation of forces during the bevel gears forging at temperature equal 850°C, 1 – displacement of stamp, 2 – twisting moment, 3 – forging force (Bochniak et. al. 2006)
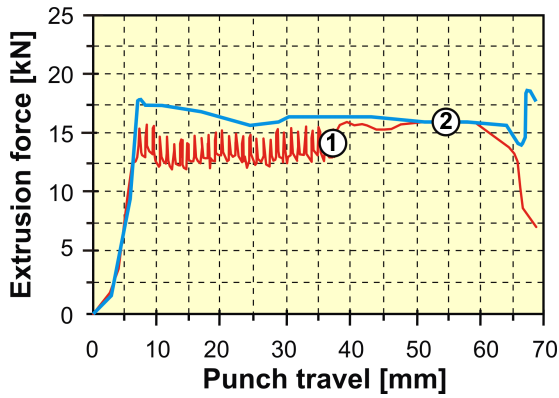
Fig. 3. Force variations during extrusion process by application
of the KOBO method, 1 – using torsional loading,
2 – without torsional loading (Kong and Hodgson, 2000)

A cyclic loading was successfully applied to improve forging processes, Fig. 2 (Bochniak et. al.). The loading was programmed in such a way, that the torsion cycles were activated during the stamp movement. A magnitude of the cyclic loading amplitude was dependent on the forging force. It gradually increased as the forging force was increased. This type of loading reduced the axial force during forging more than four times. Similar effect was achieved during extrusion, however, it was much weaker, Fig. 3. (Kong and Hodgson, 2000).

2. DETAILS OF EXPERIMENTAL PROCEDURE

The main experimental programme was carried out for a small value of the total strain, less than 1%. The main experimental objectives were focused on evaluation of:
− an influence of torsion-reverse-torsion cycles on the tensile characteristic and conventional mechanical parameters of engineering materials;
− a role of delayed torsion cycles on behaviour of materials during the monotonic tension;
− an influence of the cyclic loading frequency on the tensile characteristics.

Three materials were tested: P91 steel (commonly applied in the power industry), 2024 aluminium alloy from aircraft industry and M1E pure cooper (mainly used in the electronic industry). A control parameter in the form of the cyclic strain amplitude was designed to have a triangular shape and frequency equal to 1 Hz.

All tests were carried out at room temperature using thin-walled tubular specimens with 1.5 mm wall thickness. The biaxial stress state was obtained using various combinations of an axial force and twisting moment. All loading programmes were strain controlled. The experimental programme contained selected combinations of monotonic and cyclic loadings, i.e. the torsion-reverse-torsion cycles were superimposed on the monotonic tension.

In the last part of the experimental programme subsequent yield surfaces for a plastic offset strain equal to 10^{-5} were determined. It enabled investigation of an initial yield surface evolution due to the loading history applied.

3. THE EXPERIMENTAL RESULTS

At the beginning of the main experimental programme a material behaviour was investigated under torsion-reverse-torsion. Figure 4 presents representative variations of shear stress for two tested materials. The results for the pure copper exhibit a significant cyclic softening effect (Fig. 4a), but in the case of steel a little cyclic hardening takes place (Fig. 4b). These effects are also well visible in Fig. 5 which presents hysteresis loops evolution for both materials.
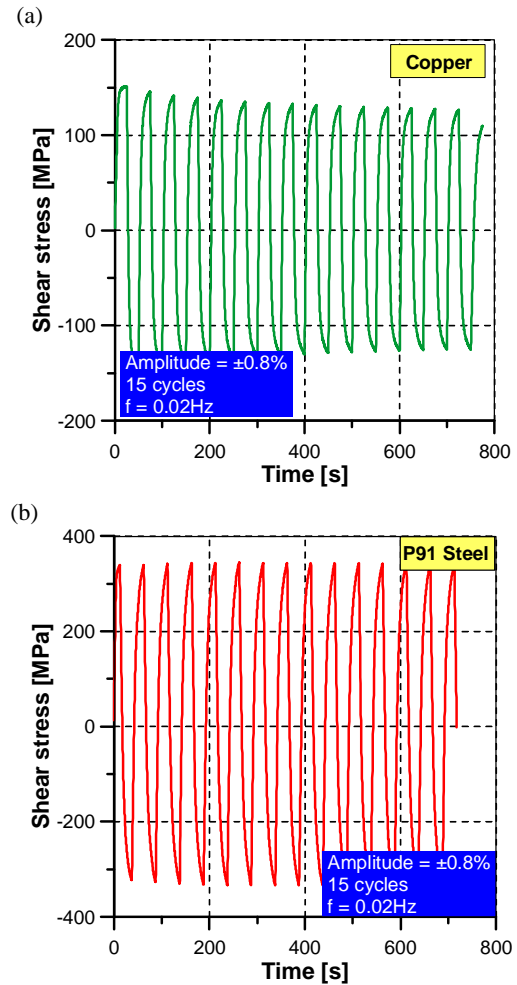

Fig. 4. Variations of a shear stress due to torsion-reverse-torsion
cycles for: (a) M1E copper; (b) P91 steel

The main representative loading programme is shown in Fig. 6a for the P91 steel. It presents some variations of the axial and shear strain components versus time. Stress responses into the programme are illustrated in Fig.6b. Variations of the axial stress express the material hardening in the tension direction, while those for the shear stress observed identify a lack of any significant effects.

In the first part of experiment an influence of the cyclic strain amplitude on the basic mechanical parameters evolution was investigated. As it is shown in Figs. 6-10, the torsion-reverse-torsion cycles associated with monotonic tension caused variations of the tensile characteristic. For both materials, a significant decrease of the axial stress can be

observed. An increase of the cyclic shear strain amplitude led to the further decrease of the stress-strain characteristic.

(a)

(b)
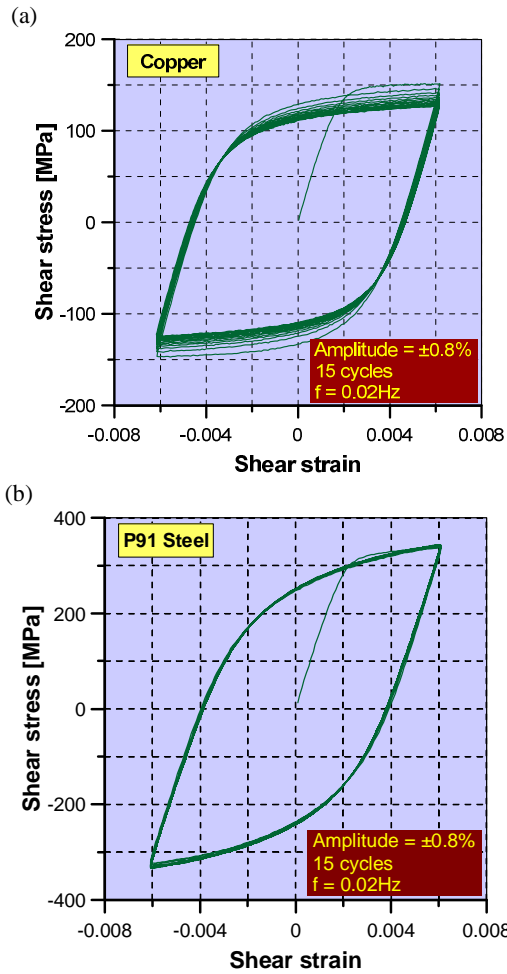
Fig. 5. Hysteresis loops evolution due to torsion-reverse-torsion cycles for: (a) M1E copper; (b) P91 steel

As a consequence, due to the cyclic loading applied the conventional mechanical parameters, such as the proportional limit and yield point, were reduced significantly. It is expressed by an essential drop of the yield point from 240 MPa to 25 MPa for the cooper (Fig. 7) and from 550 MPa to 125 MPa for the steel (Fig. 9). The effect is much stronger for the copper, since the yield point reduction (8 times) is greater than that for the steel achieved (more than 4 times).

Taking into account a percentage decrease of the proportional limit and yield point in comparison to their magnitudes determined from standard tension test it corresponds to around 90% drop of these parameters in the case of copper (Fig. 8), and around 70% for the steel, Fig.10.

The next part of the experimental programme was focused on investigations evaluating an influence of the torsion-reverse-torsion cycles delay on the tensile characteristic. The results for the P91 steel are presented in Fig. 11. It is clearly seen, that a drastic axial force drop is related to the assistance of cyclic loading. The axial force decreased rapidly (370 MPa) directly after switching on of the torsion cycles. Similar effect was earlier observed for the 2024 aluminium alloy, Fig.12 (Kowalewski and Szymczak 2007).

(a)
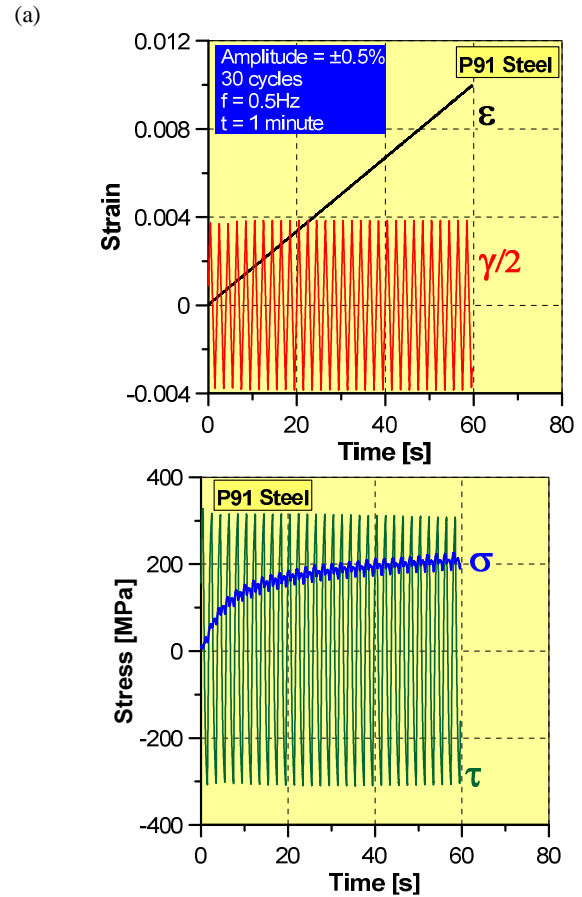
Fig. 6. Strain controlled loading paths (a), (b) – stress responses into the loading program shown in (a), ε – axial strain, γ/2 – shear strain, σ – axial stress, τ – shear stress
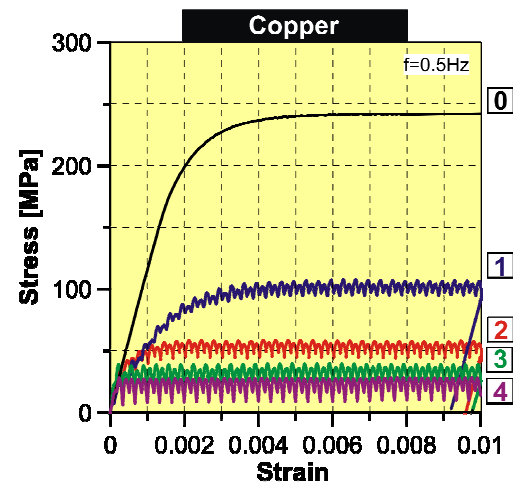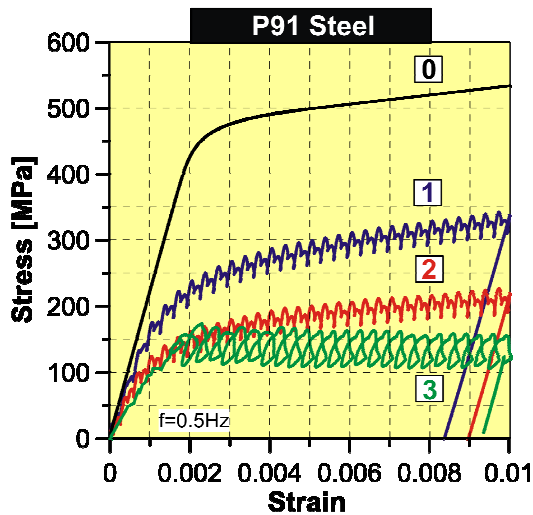

Fig. 7. A comparison of typical tensile characteristic (0) with tensile characteristics due to monotonic tension superimposed on the torsion-reverse-torsion cycles for strain amplitude equal to: ±0.3% (1), ±0.5% (2), ±0.7% (3), ±0.9% (4)

The stress – strain diagrams showing the results from tests 2024 aluminium alloy identify a transient character of the force reduction during tension associated with cyclic loading (Fig.12). This conclusion can be proved by determination of the yield surfaces for materials after standard tension tests and after tension carried out in the presence of torsion cycles.
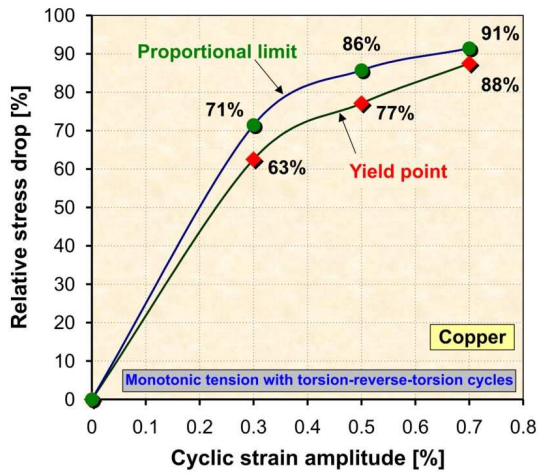
Fig. 8. Variations of the relative stress drop versus cyclic strain amplitude during monotonic tension superimposed on the torsion-reverse-torsion-cycles for strain amplitude varying from 0% to 0.7%


Fig. 9. A comparison of typical tensile characteristic (0) with tensile characteristics due to monotonic tension superimposed on the torsion-reverse-torsion cycles for strain amplitude equal to: ±0.3% (1), ±0.5% (2), ±0.7% (3)
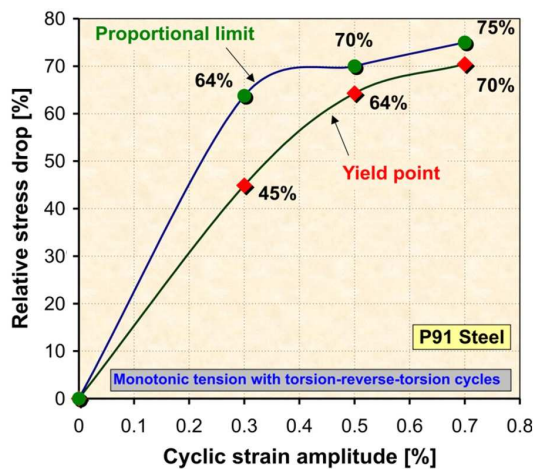
Fig. 10. Variations of the relative stress drop versus cyclic strain amplitude during monotonic tension superimposed on the torsion-reverse-torsion-cycles for strain amplitude varying from 0% to 0.7%
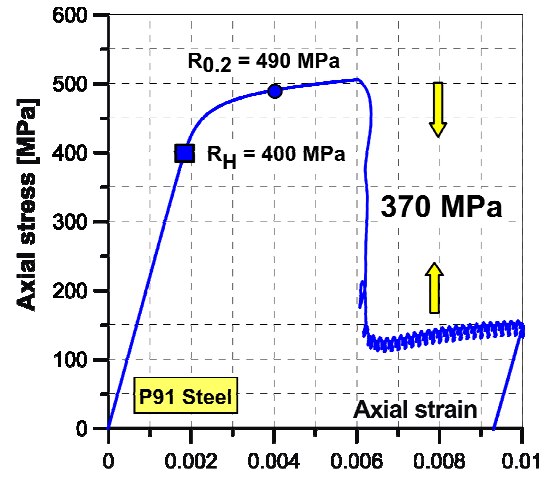
Fig. 11. Tensile characteristic of the P91 steel determined in assistance of torsion cycles delayed with respect to monotonic axial loading
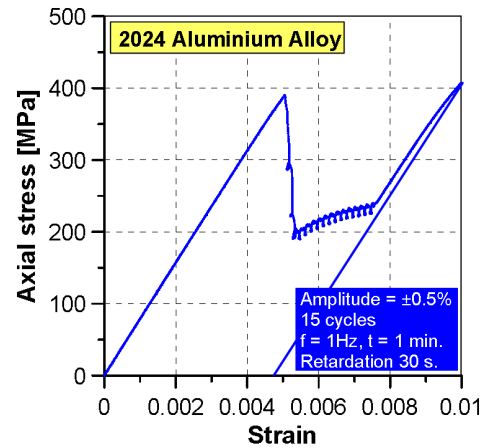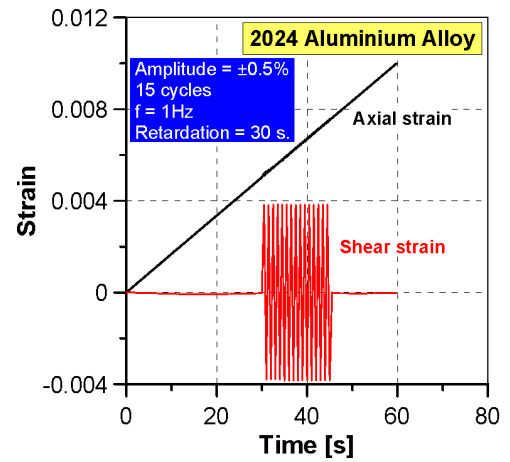

Fig. 12. Tensile characteristic of the 2024 aluminium alloy characteristic determined in assistance of torsion cycles delayed with respect to monotonic axial loading (programme of monotonic and cyclic loads is shown in the upper diagram)

Thus, the last step of the experimental programme comprised tests the main aim of which was to check whether the force reduction during tension had the permanent character. The yield surface concept was applied. For each yield surface determined it was assumed that the total strain in the axial direction must be the same.

The representative results for the copper and P91 steel are presented in Figs. 13 and 14, respectively. As it is clearly seen the subsequent yield surfaces for both materials confirm that the axial force reduction is only related to torsion cycles during monotonic tension. Looking at the magnitudes of tension stress instead of reduction an increase can be observed (little for the P91 steel, but significant for the copper). Therefore, it can be concluded that the comparison of the subsequent yield loci with the initial yield surface exhibits only an influence of the loading history applied, and moreover, proves a transient character of the axial force drop, which can be solely attributed to cycles acting in the perpendicular direction.
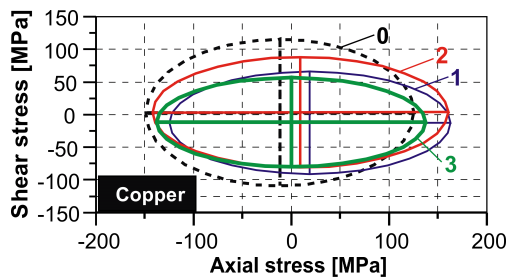
Fig. 13. An evolution of the initial yield surface (0) for the M1E copper due to torsion-reverse-torsion cycles for strain amplitude equal to: ±0.3% (1), ±0.5% (2), ±0.7% (3)
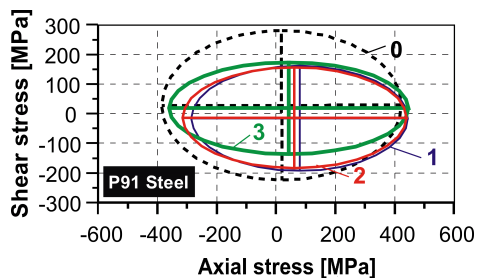
Fig. 14. An evolution of the initial yield surface (0) for the P91 steel due to torsion-reverse-torsion cycles for strain amplitude equal to: ±0.3% (1), ±0.5% (2), ±0.7% (3)

4. CONCLUSIONS

The investigations carried out on both materials allow to formulate the following conclusions and remarks:
− torsion-reverse-torsion cycles during monotonic tension cause a significant decrease of the proportional limit and yield point;
− an increase of the strain amplitude of torsion cycles improves material ductility in the tension direction;
− a reduction of the yield point and proportional limit increases with the cyclic strain amplitude increase;
− axial force reduction due to presence of the torsion cycles is not permanent, it vanishes after cyclic loading interruption;
− an initial yield surface evolution does not confirm rapid reduction of selected mechanical parameters during tension assisted by cyclic torsion, it only points out their variations due to loading history applied.

REFERENCES

1. **Bochniak W., Korbel A., Szyndler R., Hanarz R., Stalony-Dobrzański F., Błaż L., Snarski P.** (2006), New forging method of bevel gears from structural steel, *J. Mater. Proc. Tech.*, 173, 75-83.
2. **Correa E.C.S., Aguilar M.T.P., Silva E.M.P., Cetlin P.R.** (2003), The effect of sequential tensile and cyclic torsion straining on work hardening of steel and brass, *J. Mater. Proc. Tech.* 142, 282-288.
3. **Gronostajski Z., Jaśkiewicz K.** (2004), The effect of complex strain path on the properties of CuSi5 silicon bronze, *J. Mater. Proc. Tech.*, 155-156, pp. 1144-1149, 2004.
4. **Kong L. X., Hodgson P. D.** (2000), Constitutive modelling of extrusion of lead with cyclic torsion, *Mater. Sci. Eng.*, A 276, pp. 32-38.
5. **Kowalewski Z., Szymczak T.** (2007), Effect of cyclic loading due to torsion on the monotonic tension parameters of engineering materials, *13th International Symposium PLASTICITY'07*, Girwood, Alaska, June 2-6, 2007, USA, pp. 181-183, 2007.
6. **Kowalewski Z., Szymczak T.** (2008), An influence of torsional cycles on the uni-axial tension of selected materials, *XXII International Congress of Theoretical and Applied Mechanics, ICTAM 2008 Adelaide*, 24-29 August, Australia, pp. 304.
7. **Kowalewski Z. Szymczak T.** (2009), Effects observed in engineering materials subjected to monotonic and cyclic loading due to tension-torsion combinations, *15th International Symposium* PLASTICITY '09, St. Thomas, Virgin Islands, USA, Jan. 3-8 2009, pp. 196-198.
8. **Niewielski G., Kuc D., Rodak K., Grosman F., Pawlicki J.** (2006), Influence of strain on the copper structure under controlled deformation path conditions, *Journal of Achievements in Materials and Manufacturing Engineering*, 17, 1-2, 109-112.
9. **Szymczak T.** (2007), *An influence of loading history on mechanical parameters of engineering materials*, supervisor Kowalewski Z.L., Warsaw University of Technology, Faculty of Automotive and Construction Machinery Engineering, Poland, PhD Thesis.
10. **Xiang M.** (2003), *Compression and Extrusion of Metals Using Rotating Die*", Deakin University, Norwegia, PhD Thesis.

PARAMETRICAL MODELS OF WORKING ROTOR MACHINE BLADE DIAGNOSTICS WITH ITS UNMEASURABLE ENVIRONMENT ELIMINATION

Paweł LINDSTEDT[*], Rafał GRĄDZKI[*]

[*]Bialystok Technical University, Department of Mechanical Engineering, PL 15-351 Białystok, Poland

p.lindstedt@pb.edu.pl, r.gradzki@pb.edu.pl

Abstract: The paper presents the basic of the new method of rotor machine blades during their operation. The method utilizes such diagnostic models as a quotient of diagnostic signal y(t) amplification being a result of blade operation and x(t) signal of its environment as the blade tip approaches the sensor as well as amplification of these signals as the blade tip recedes from the sensor and phase shift difference of these signals as the blade tip approaches and recedes from the sensor. The adopted diagnostic models indirectly take the current blade environment x(t) into account with no necessity of measuring (Kotowski and Lindstedt, 2007; Lindstedt and Kotowski, 2004). Therefore the model is sensitive to blade technical condition changes remaining only slightly sensitive to environment changes. Suggested method may prove very important in diagnostics of rotor blades during operation of rotor machines (turbines, compressors etc.).

1. INTRODUCTION

Rotor machine is complex technical object (combined of multiple parts such as blades, bearings, shields) operating in complex environment (affected by variable stress, pressure, temperature, vibration etc.). The trouble spot of machine are, except bearings, blades. These are technically simple, however hard in matter of use and maintenance mainly due to high risk of aptitude assessment. Experience shows that fall of one blade of several dozen or hundreds almost always leads to serious breakdown of the whole (often very expensive) rotor machine (axis compressor, turbine). This causes huge interests in methods of routine diagnostics (monitoring) of blades technical condition during its operation.

Nowadays multiple methods of working rotor blades technical condition are in use. Diagnostic research in these methods are based on 'non-contact' measurement of values of tip of the blade current moves when in area below dedicated sensor. Many non-contact measuring systems have been designed and introduced. These are commonly known and used measuring system produced by: Hood, Aqilis, Pratt&Whithey (USA), Rolls Royce (UK), Turbocharges (Switzerland), MTU (Germany) as well as other Russian, Chinese and Indian manufacturers (Bovishanskii, 2000; Duan et al., 2005; Von Flotow and Mercadal, 2000; High Cycle Fatigue S & program 1997, 1998, 1999, 2000, 2001, 2002; Klein, 2004; Roberts, 2007; Zieliński and Ziller, 2005).

Polish measuring systems are also used, particularly those designed and introduced by Air Force Institute of Technology (AFIT) in Warsaw. Amongst the non-contact measurement of blade translocation systems manufactured by AFIT the following are to be mentioned (Lindstedt et al., 2009; Szczepanik and Przysowa, 2004; Szczepanik, 1999):

− blade fracture indicator: SPŁ – 29;
− blade excessive vibration indicator: SNDŁ – 2b;
− microwave sensors: MUH, PIT;

These systems are successfully implemented in specific operating technical objects (SO-3 engines).

Diagnostic inference used in hitherto methods are based on elaboration of signals obtained during diagnostic analysis coming as a result of blade activity without sufficient (according to authors) consideration being given to the signals of its variable environment.

Measurement of blade environment signals during operation of rotor machine are often hard or impossible to proceed thus are not sufficiently considered in blades diagnostics. Therefore statement can be made that hitherto methods of rotor blades technical condition in-work assessment do not realize the basic rule of technical diagnostics compelling research and analysis of object technical condition in environment (PN-90/N-04002) thus being not accurate and reliable enough.

Hence the need emerged to elaborate the new method of in-work diagnostics of blade technical condition that would take the environment into consideration and, if possible, would not require the use of unavailable or hard to measure signals. This problem is solved by blade analysis method that base on special diagnostic model allowing to eliminate its practical environment with specific methods.

2. BLADE ACTIVITY IN UNMEASURABLE ENVIRONMENT

Blade, its construction and activity while in variable environment (Lindstedt et al., 2009; Skubacziewskij, 1974) are presented in Fig. 1.

During blade operation its technical condition changes until occurrence of various damage (deformation, fractures). Causes and places of possible occurrence are shown in Fig.2 (Skubacziewskij, 1974).
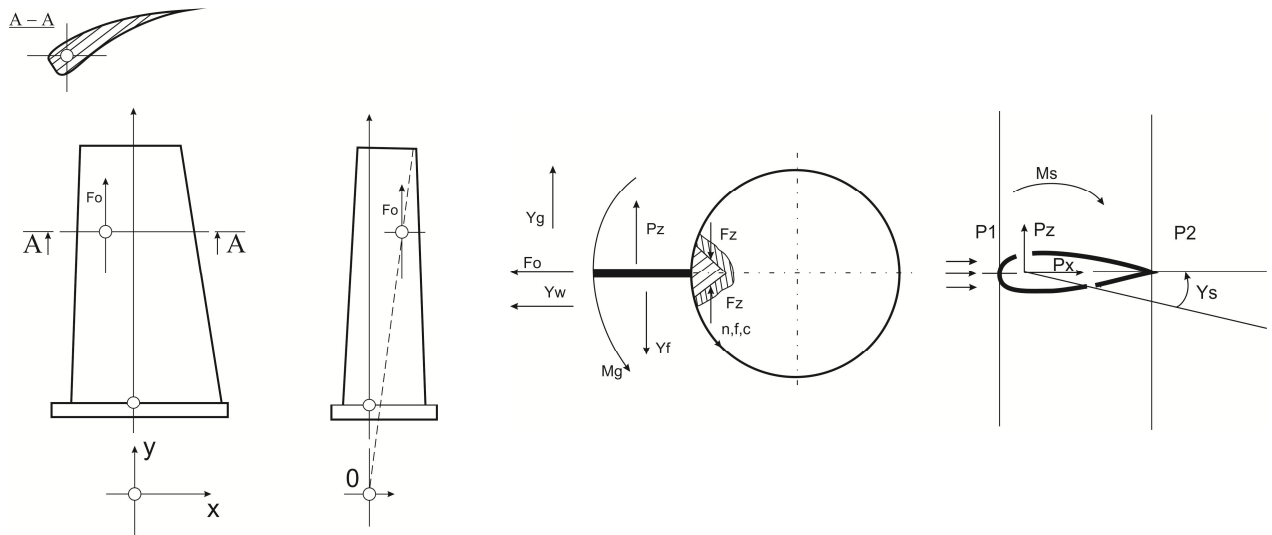
Fig. 1. Rotor machine blade in variable environment (F_0 – centrifugal force; F_z – lock grip force; n – rotational speed; P_z – blade aerodynamic lift; P_x – resisting force; M_s – torque M_g – bending moment, p_1 – gas pressure on blade rim input, p_2 – gas pressure on blade rim output; Y_g – blade deflection; Y_s – blade torsion angle; Y_w – blade lengthwise translocation; Y_f – various vibration signal (bending, lengthwise, torsional); Y_c – thermal deformation; f – vibration signal; f_{ob} – casing vibration signal; c – thermal decomposition signal)
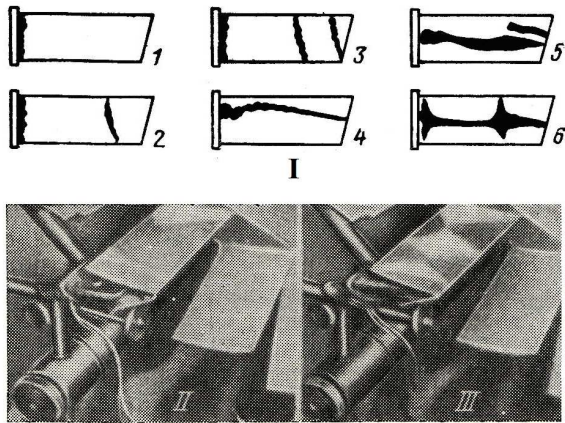
Fig. 2. Forms of vibration and lines indicating traces of vibration nodes (Chart I: 1,2,3 – first, second and third form of bending vibration; 4 – first kind torsional vibration; 5 – second kind torsional vibration; 6 – combined bending-torsional vibration. Chart II: photograph of nodes traces in second form of bending vibration. Chart III: photograph of nodes traces in third form of bending vibration)

Fig. 1. and Fig. 2. show that blade is a technical object with complex activity that need to be described with multi-dimensional blade deformation state. These deformations originate from environment and are caused by multiple reasons such as:

- centrifugal force stresses F_0 depending on rotational speed that cause lengthwise and bending deformations (Fig.1.) – Y_w, Y_g
- gas stresses P_z and P_x caused by air stream depending on speed and altitude (Fig.1.) – Y_s (in case of rotor machine being an engine turbine or compressor)
- stresses caused by curvilinear flight trajectory (Fig.1.) – Y_g, Y_s
- dynamic stresses accompanying mechanical vibration (particularly in resonant range) caused by pressure p_1, p_2 pulsation, rotation fluctuation etc. (Fig.2.) – Y_f
- blade and casing vibration f, f_{ob} (Fig.1.) and thus Y_g, Y_s

- thermal stresses c caused by uneven thermal distribution (Fig.2. - combined deformation, e.g. I-6) – Y_c.

Comprehensive, blade working status in environment may be described with a signal of tip of the blade translocation y(t) which is a resultant of Y_w, Y_g, Y_s, Y_f, Y_c, (Fig. 1. and Fig. 2.):

$$y(t) = f\left(Y_w, Y_g, Y_s, Y_f, Y_c\right) \qquad (1)$$

and signal of environment x(t) which is a resultant of: n, F_o, P_z, P_x, P_1, P_2, f, f_{ob}, c (Fig. 1. and Fig. 2.):

$$x(t) = f\left(n, F_o, P_z, P_x, P_1, P_2, f, f_{ob}, c\right) \qquad (2)$$

Technical condition of blade $S_T(\theta)$ according to diagnostic rules, results from relation between activity signal y(t) and environment signal x(t) in the current θ_1 beginning moment of diagnostics θ_0 (while θ is the time of the technical condition changes - evolution)

Therefore, the following may be noted:

$$S_T\left(\theta\right) = f(y(t)_{\theta_0}, x(t)_{\theta_0}, y(t)_{\theta_1}, x(t)_{\theta_1}, \theta, t) \qquad (3)$$

Exploitation experience proved the existence of real difficulties in measuring signals for y(t), especially x(t), thus in blade technical condition in-work assessment as well (Kotowski and Lindstedt, 2007; Lindstedt and Kotowski, 2004; Lindstedt et al., 2009).

3. THEORETICAL BASES OF BLADE DIAGNOSTICS METHOD DURING OPERATION OF ROTOR MACHINE

The matter of blade diagnostics during rotor machine operation is very complex, because only one measurable and yet interfered signal y(t) and actually immeasurable (except for n signal and without Δn) environment signal x(t) are available. Exemplary course of y(t) signal is presented in Fig.3 (Szczepanik and Przysowa, 2004; Szczepa-

nik, 1999). Course of signal x(t), being a resultant of multiple signals is shown in Fig.4. (Dołgolienko, 1984)
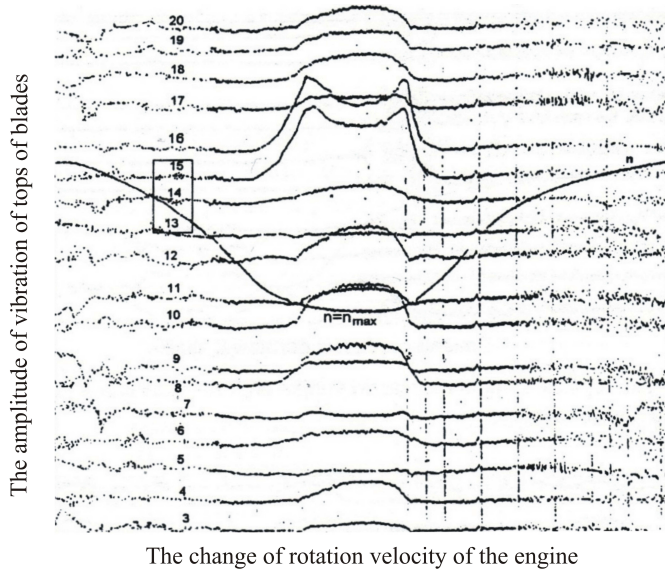
Fig. 3. Signal y(t) course for various blades depending on rotational speed
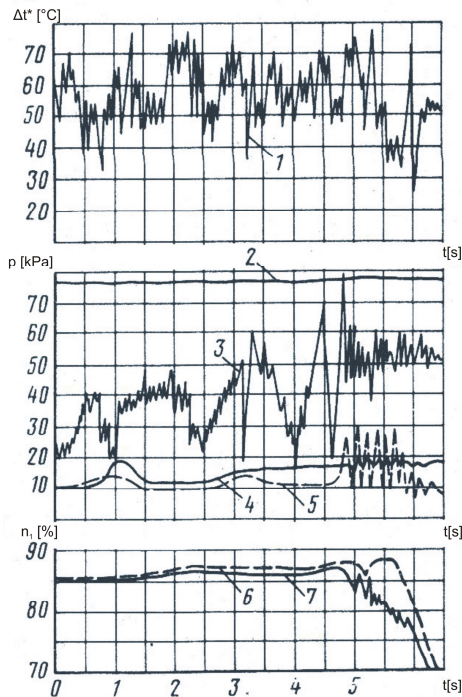
Fig. 4. Change of temperature and pressure of air stream on outlet in specific flight conditions 1 – in lower part of right engine intake, 2 – on side of right engine intake, 3 – in lower part of left engine intake, 4 – on upper part of left engine intake, 5 – on side of left engine intake, 6 – change of rotational speed of right engine rotor, 7 – change of rotational speed of left engine rotor

Tentatively signals x(t) and y(t) are assumed to be temporal, stochastic and interfered courses. In this case switching from space domain „t" of signals x(t) and y(t) to space domain „τ" of correlation function $R_{xx}(\tau), R_{yy}(\tau)$ and $R_{xy}(\tau)$

proves reasonable (Bendat and Piersol, 1976; Kotowski and Lindstedt, 2007; Lindstedt and Kotowski, 2004; Lindstedt et al., 2009; Niederliński, 1985; Szabatin, 2000).

The effects of such approach are:
− noise suppression for signals and possibility of amplifying them
− possibility of simple expressing signals $R_{xx}(\tau)$, $R_{yy}(\tau)$ and $R_{xy}(\tau)$ as analytic functions, what allows further processing to new functions of specific properties in frequency domain (ω), which are functions of density of singular power of signals $S_{xx}(\omega)$ and $S_{yy}(\omega)$ and reciprocal $S_{xy}(\omega)$.

Expressing functions x(t) and y(t) as $S_{xx}(\omega)$, $S_{yy}(\omega)$ and $S_{xy}(\omega)$ allows taking relations between diagnostic signals y(t) and environment signals x(t) into consideration very simply (Fig.3., 4.), as this may be noted:

$$A_{T01}^2 = \frac{S_{yy}^{T01}}{S_{xx}^{T01}} \qquad\qquad \varphi_{T01} = Arg\, \frac{S_{xy}^{T01}}{S_{xx}^{T01}} \qquad (4)$$

$$A_{T12}^2 = \frac{S_{yy}^{T12}}{S_{xx}^{T12}} \qquad\qquad \varphi_{T12} = Arg\, \frac{S_{xy}^{T12}}{S_{xx}^{T12}} \qquad (5)$$

where: A_{T01}^2, φ_{T01}^2 – amplification and phase shift of signals x and y while the blade approaches the sensor and A_{T12}^2, φ_{T12} – amplification and phase shift of signals x and y while the blade recedes from the sensor.

Furthermore assumption can be made that time of signal T_{12} observation comes shortly (ms) after observation of T_{01} signals.

In such case the following may by assumed:

$$S_{xx}^{T12} = S_{xx}^{T01} \qquad (6)$$

Then, on the basis on 4, 5, 6 equations new, abstract and physically interpretable quantity in form of a quotient of amplifications A_{T01}^2 and A_{T12}^2 can be achieved as well as phase shifts φ_{T01} and φ_{T12}:

$$A_{T12,T01}^2 = \frac{A_{T12}^2}{A_{T01}^2} = \frac{\dfrac{S_{yy}^{T12}}{S_{xx}^{T12}}}{\dfrac{S_{yy}^{T01}}{S_{xx}^{T01}}} \xrightarrow{S_{xx}^{T12}=S_{xx}^{T01}} \frac{S_{yy}^{T12}}{S_{yy}^{T01}} \qquad (7)$$

$$\varphi_{T12,T01} = \varphi_{T12} - \varphi_{T01} = Arg\, \frac{\dfrac{S_{xy}^{T12}}{S_{xx}^{T12}}}{\dfrac{S_{xy}^{T01}}{S_{xx}^{T01}}} = Arg\, \frac{A_{12}e^{-j\varphi_{T12}}}{A_{01}e^{-j\varphi_{T01}}} = \qquad (8)$$

$$= Arg A_{T12T01} e^{-j(\varphi_{T12}-\varphi_{T01})} \xrightarrow{S_{xx}^{T12}=S_{xx}^{T01}} Arg\, \frac{S_{xy}^{T12}}{S_{xy}^{T01}}$$

Equation $A_{T12,T01}^2$ (7) binds diagnostic signals y(t) to environment signals x(t) and so is a diagnostic model. The distinctive feature of this model is being determined only by measurable signal y(t) in closely following observation periods T_{01} and T_{12} and (what is more important), taking environment into account with no necessity to meas-

ure it as well as the noise of signal y(t) was sufficiently suppressed. (Kotowski and Lindstedt, 2007; Lindstedt and Kotowski, 2004; Lindstedt et al., 2009)

Equation $\varphi_{T12,T01}$ (8) binds diagnostic signals y(t) to environment signals x(t) as well and so it is the next diagnostic model. As in case of $A^2_{T12,T01}$ this model is also being determined without necessity of practical measurement of environment signal x(t). To determine signals S^{T12}_{xy},

S^{T01}_{xy} distribution in form of function δ (t, $\hat{t}$) is to be used. The quotient of function of signal y power density and distribution δ (t, $\hat{t}$) sufficiently representing environment signals x is assumed to eliminate real environment of model $\varphi_{T12,T01}$. (Bendat and Piersol, 1976; Lindstedt et al., 2009; Niederliński, 1985; Szabatin, 2000)
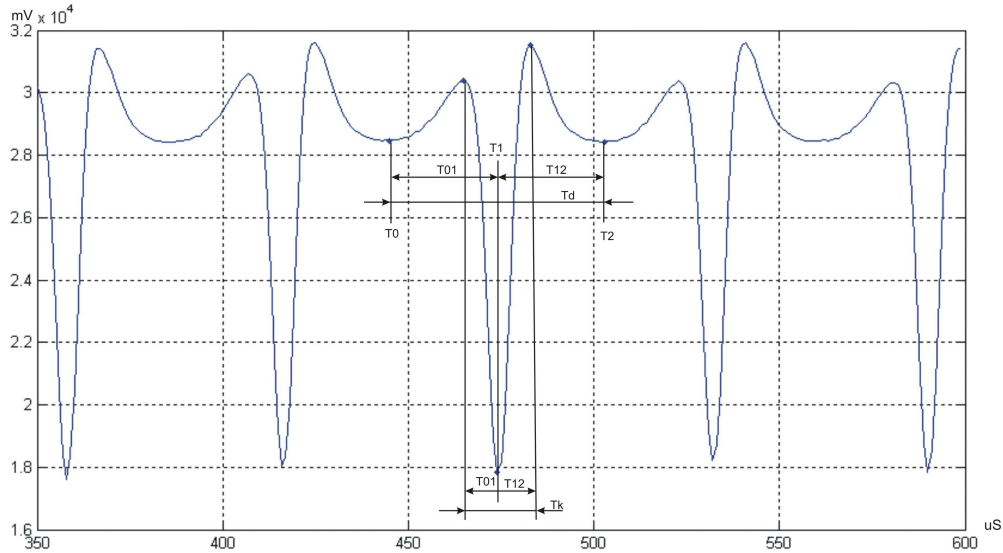
Fig. 5. Inferential sensor signals (T_d, T_k – respectively long and short observation period of tip of a blade staying in sensor area, T_0, T_1, T_2 – particular moments of observation of blade tip below the sensor, T_{01}, T_{12} – observation subperiods of blade tip for T_d and T_k respectively, mV – signal of tip of the blade translocation, uS – blade translocation time)

4. METHOD OF CURRENT ASSESSMENT OF BLADE TECHNICAL CONDITION BASING ON OBSERVATION OF PARAMETERS OF MODEL $A^2_{T12,T01}$

Method of current assessment of rotor machine blade technical condition changes basing on observation of parameters of model $A^2_{T12,T01}$ requires specific diagnostic research.

Afterwards estimates of autocorrelation function R^{*T01}_{yy} and R^{*T12}_{yy} are determined for y(t) translocation in observation periods T_{01} and T_{12} and proper analytic expressions are matched to them. (Bendat and Piersol, 1976; Kotowski and Lindstedt, 2007; Kurowski, 1994; Lindstedt and Kotowski, 2004; Lindstedt et al., 2009; Niederliński, 1985).

Registered signal courses were multiplied by Hanning window and, afterwards, its autocorrelation was calculated. The obtained autocorrelation graphs were approximated with degree 5 polynomial in form of:

$$R_{yy}(\tau) = a_1\tau^5 + a_2\tau^4 + a_3\tau^3 + a_4\tau^2 + a_5\tau + a_6 \tag{9}$$

For approximation of $R^2 > 0,997$ described by determination coefficient the following autocorrelation function forms were obtained:
– for blade no. 1.

$$R^{T01}_{yy} = 1557x^5 - 207300x^4 + 9409000x^3 -$$
$$1637 \cdot 10^5 x^2 + 4641 \cdot 10^5 x + 9485 \cdot 10^5 \tag{10}$$

$$R^{T12}_{yy} = 2345x^5 - 285600x^4 + 1182 \cdot 10^4 x^3 -$$
$$1876 \cdot 10^5 x^2 + 5033 \cdot 10^5 x + 8727 \cdot 10^6 \tag{11}$$

– for blade no. 2.

$$R^{T01}_{yy} = 1308x^5 - 182100x^4 + 8594000x^3 -$$
$$155 \cdot 10^6 x^2 + 4468 \cdot 10^5 x + 9757 \cdot 10^6 \tag{12}$$

$$R^{T12}_{yy} = 2043x^5 - 256800x^4 + 1097 \cdot 10^4 x^3 -$$
$$1798 \cdot 10^5 x^2 + 4908 \cdot 10^5 x + 9039 \cdot 10^6 \tag{13}$$

– for blade no. 3.

$$R^{T01}_{yy} = 1448x^5 - 200500x^4 + 918 \cdot 10^4 x^3 -$$
$$1607 \cdot 10^5 x^2 + 456 \cdot 10^6 s + 9428 \cdot 10^6 \tag{14}$$

$$R^{T12}_{yy} = 2548x^5 - 302300x^4 + 123 \cdot 10^5 x^3 -$$
$$1931 \cdot 10^5 x^2 + 518 \cdot 10^6 x + 8775 \cdot 10^6 \tag{15}$$

Basing on analytic forms of self correlation functions R^{T01}_{yy} and R^{T12}_{yy}, the respective power spectral density functions $S^{T01}_{yy}(\omega)$ and $S^{T12}_{yy}(\omega)$ are determined using the Fourier transformation.:

$$F\{R_{yy}\} = \int_{-\infty}^{\infty} R_{yy}(\tau)e^{-j\omega\tau}d\tau \tag{16}$$

$$S^{T01}_{yy}(\omega) = F(R^{T01}_{yy}(\tau)) \tag{17}$$

$$S_{yy}^{T12}(\omega) = F(R_{yy}^{T12}(\tau)) \tag{18}$$

The Fourier transform of polynomial (9) after moving from "jω" space to variable "s" space is as follows:

$$F\{R_{yy}\} = a_1 \frac{120}{s^6} + a_2 \frac{24}{s^5} + a_3 \frac{6}{s^4} + a_4 \frac{2}{s^3} + a_5 \frac{1}{s^2} + a_6 \frac{1}{s} \tag{19}$$

After the substitution of parameters from equations (10 – 15) to equation (19) the following is obtained:
– for blade no. 1.

$$S_{yy}^{T01}(j\omega) = (9485 \cdot 10^6 s^5 + 4641 \cdot 10^5 s^4 - 3274 \cdot 10^5 s^3 + 56454 \cdot 10^3 s^2 - 4975200s + 186840)s^{-6} \tag{20}$$

$$S_{yy}^{T12}(j\omega) = (8727 \cdot 10^6 s^5 + 5033 \cdot 10^5 s^4 - 3752 \cdot 10^5 s^3 + 7092 \cdot 10^4 s^2 - 6854400s + 281400)s^{-6} \tag{21}$$

– for blade no. 2.

$$S_{yy}^{T01}(j\omega) = (9757 \cdot 10^6 s^5 + 4468 \cdot 10^5 s^4 - 31 \cdot 10^7 s^3 + 51564 \cdot 10^3 s^2 - 4370400s + 156960)s^{-6} \tag{22}$$

$$S_{yy}^{T12}(j\omega) = (9039 \cdot 10^6 s^5 + 4908 \cdot 10^5 s^4 - 3596 \cdot 10^5 s^3 + 6582 \cdot 10^4 s^2 - 6163200s + 245160)s^{-6} \tag{23}$$

– for blade no. 3.

$$S_{yy}^{T01}(j\omega) = (9428 \cdot 10^6 s^5 + 456 \cdot 10^6 s^4 - 3214 \cdot 10^5 s^3 + 5508 \cdot 10^4 s^2 - 4812000s + 178080)s^{-6} \tag{24}$$

$$S_{yy}^{T12}(j\omega) = (8775 \cdot 10^6 s^5 + 518 \cdot 10^6 s^4 - 3862 \cdot 10^5 s^3 + 738 \cdot 10^5 s^2 - 7255200s + 305760)s^{-6} \tag{25}$$

Ultimately new abstract diagnostic model (square of module) might be determined, the parameters of which present the data on technical conditions of diagnosed blade:

$$A_{T12,T01}^2 = \frac{S_{yy}^{T12}}{S_{yy}^{T01}} = k \frac{1 + L_1 s + L_2 s^2 + \ldots}{1 + M_1 s + M_2 s^2 + \ldots} \tag{26}$$

After the substitution of parameters from equations (20 – 25) to equation (26) the following is obtained:

– for blade no. 1.

$$A_{T12,T01}^2 = 1.506 \left(\frac{31012.793 s^5 + 1788.577 s^4 - 1333.33 s^3 + 252.025 s^2 - 24.358 s + 1}{50765.361 s^5 + 2483.943 s^4 - 1752.301 s^3 + 302.151 s^2 - 26.628 s + 1} \right) \tag{27}$$

– for blade no. 2.

$$A_{T12,T01}^2 = 1.562 \left(\frac{3686.799 s^5 + 2001.958 s^4 - 1466.797 s^3 + 268.478 s^2 - 25.139 s + 1}{62162.334 s^5 + 2846.585 s^4 - 1975.025 s^3 + 328.517 s^2 - 27.844 s + 1} \right) \tag{28}$$

– for blade no. 3.

$$A_{T12,T01}^2 = 1.717 \left(\frac{28698.979 s^5 + 1694.139 s^4 - 1263.082 s^3 + 241.366 s^2 - 23.728 s + 1}{52942.498 s^5 + 2560.647 s^4 - 1804.807 s^3 + 309.299 s^2 - 27.02 s + 1} \right) \tag{29}$$

Tab. 1. The parameters of blades for the amplitude amplification

The parameters of blades for the amplitude amplification

		M_5	M_4	M_3	M_2	M_1	k
ROTOR BLADES	**S1T01**	50765.361	2483.943	-1752.301	302.151	-26.628	1.506
	S2T01	62162.334	2846.585	-1975.025	328.517	-27.844	1.562
	S3T01	52942.498	2560.647	-1804.807	309.299	-27.02	1.717
	S$_{śr}$	55290.064	2630.392	-1844.044	313.322	-27.164	1.595
		L_5	L_4	L_3	L_2	L_1	k
	S1T12	31012.793	1788.577	-1333.33	252.025	-24.358	1.506
	S2T12	36869.799	2001.958	-1466.797	268.478	-25.139	1.562
	S3T12	28698.979	1694.139	-1263.082	241.366	-23.728	1.717
	S$_{śr}$	32193.857	1828.225	-1354.403	253.956	-24.408	1.595

Process of rotor machine blade technical condition is as follows:

– in exploitation time θ_0 (monitoring beginning) function $A_{T12,T01}^2$ parameters: L_{01}, L_{02}, L_{03} ...and M_{01}, M_{02}, M_{03} ... are determined

– in exploitation time θ_1 (another blade monitoring) function $A_{T12,T01}^2$ parameters: $L_{10}, L_{11}, L_{12}, \ldots$ and M_{10}, M_{11}, M_{12} ... are determined

The technological differences between the blades bight also be determined. In such case the average values of function $A_{T12,T01}^2$: $L_{1śr}, L_{2śr}, L_{3śr}$ ...as well as $M_{1śr}, M_{2śr}, M_{3śr}$

parameters are determined and the diagnosed blades parameters are compared to them. (tab.1 and tab.2)

− the difference between technical condition of consecutive blades is determined basing on relative parameters changes:

$$\Delta \bar{L}_i = \frac{L_{i1} - L_{sr}}{L_{sr}} \quad ; i = 1,\ldots,n \tag{30}$$

$$\Delta \bar{M}_i = \frac{M_{i1} - M_{sr}}{M_{sr}} \quad ; i = 1,\ldots,m \tag{31}$$

The change of $\bar{L}_i$ and $\bar{M}_i$ parameters as well as a significant number of their configuration allows the identification of multiple various changes of the blade technical condition while the rotor machine is operating (this also applies to assessing the accuracy of performance and installation the new blades).

Tab. 2. Relative differences the parameters of blades for the amplitude amplification

		Relative differences the parameters of blades for the amplitude amplification					
ROTOR BLADES		ΔM_5	ΔM_4	ΔM_3	ΔM_2	ΔM_1	Δk
	S1T01	-0.082	-0.056	-0.050	-0.036	-0.020	-0.056
	S2T01	0.124	0.082	0.071	0.048	0.025	-0.021
	S3T01	-0.042	-0.027	-0.021	-0.013	-0.005	0.076
		ΔL_5	ΔL_4	ΔL_3	ΔL_2	ΔL_1	Δk
	S1T12	-0.037	-0.022	-0.016	-0.008	-0.002	-0.056
	S2T12	0.145	0.095	0.083	0.057	0.030	-0.021
	S3T12	-0.109	-0.073	-0.067	-0.050	-0.028	0.076

5. METHOD OF ASSESSMENT OF BLADE CURRENT TECHNICAL CONDITION BASING ON MODEL PARAMETERS OBSERVATION $\varphi_{T12,T01}$

Signal y(t) courses in observation times T_{01} and T_{02} are presented in Fig. 5. Environment is assumed to be e.g. high power noise and may be correlated with signal y(t). (Bendat and Piersol, 1976)

As an effect of mathematical operations correlation function estimators and analytic forms of correlation function were obtained:

− for blade no. 1.

$$R_{xy}^{T01} = 3196x^5 - 294900x^4 + 9775 \cdot 10^3 x^3 - $$
$$1319 \cdot 10^5 x^2 + 4442 \cdot 10^5 x + 257 \cdot 10^7 \tag{32}$$

$$R_{xy}^{T12} = 4502x^5 - 369500x^4 + 108 \cdot 10^5 x^3 - $$
$$1249 \cdot 10^5 x^2 + 2761 \cdot 10^5 x + 2767 \cdot 10^6 \tag{33}$$

− for blade no. 2.

$$R_{xy}^{T01} = 2770x^5 - 258400x^4 + 8621000x^3 - $$
$$1155 \cdot 10^5 x^2 + 3525 \cdot 10^5 x + 2649 \cdot 10^6 \tag{34}$$

$$R_{xy}^{T12} = 3578x^5 - 312500x^4 + 9769 \cdot 10^3 x^3 - $$
$$1225 \cdot 10^5 x^2 + 3334 \cdot 10^5 x + 2714 \cdot 10^6 \tag{35}$$

− for blade no. 3.

$$R_{xy}^{T01} = 3077x^5 - 285200x^4 + 95 \cdot 10^5 x^3 - $$
$$1287 \cdot 10^5 x^2 + 4335 \cdot 10^5 x + 2564 \cdot 10^6 \tag{36}$$

$$R_{xy}^{T12} = 4517x^5 - 370500x^4 + 1082 \cdot 10^4 x^3 - $$
$$1248 \cdot 10^5 x^2 + 2713 \cdot 10^5 x + 2794 \cdot 10^6 \tag{37}$$

Further, the following is determined:

− for blade no. 1.

$$S_{xy}^{T01}(j\omega) = (257 \cdot 10^7 s^5 + 4442 \cdot 10^5 s^4 - $$
$$2638 \cdot 10^5 s^3 + 5865 \cdot 10^4 s^2 - 7077600s + 383520)s^{-6} \tag{38}$$

$$S_{xy}^{T12}(j\omega) = (2767 \cdot 10^6 s^5 + 2761 \cdot 10^5 s^4 - $$
$$2498 \cdot 10^5 s^3 + 648 \cdot 10^5 s^2 - 8868 \cdot 10^3 s + 540240)s^{-6} \tag{39}$$

− for blade no. 2.

$$S_{xy}^{T01}(j\omega) = (2649 \cdot 10^6 s^5 + 3525 \cdot 10^5 s^4 - $$
$$2310 \cdot 10^5 s^3 + 51726 \cdot 10^3 s^2 - 6201600s + 332400)s^{-6} \tag{40}$$

$$S_{xy}^{T12}(j\omega) = (2714 \cdot 10^6 s^5 + 3334 \cdot 10^5 s^4 - $$
$$2450 \cdot 10^5 s^3 + 58614 \cdot 10^3 s^2 - 75 \cdot 10^5 s + 429360)s^{-6} \tag{41}$$

− for blade no. 3.

$$S_{xy}^{T01}(j\omega) = (2564 \cdot 10^6 s^5 + 4335 \cdot 10^5 s^4 - $$
$$2574 \cdot 10^5 s^3 + 57 \cdot 10^6 s^2 - 6844800s + 369240)s^{-6} \tag{42}$$

$$S_{xy}^{T12}(j\omega) = (2794 \cdot 10^6 s^5 + 2713 \cdot 10^5 s^4 - $$
$$2496 \cdot 10^5 s^3 + 6492 \cdot 10^4 s^2 - 8892000s + 542040)s^{-6} \tag{43}$$

and in the end:

$$\varphi_{T12,T01} = \frac{S_{xy}^{T12}}{S_{xy}^{T01}} = k \frac{1 + B_1 s + B_2 s^2 + ...}{1 + A_1 s + A_2 s^2 + ...} \tag{44}$$

After the substitution of parameters from equations (38 – 43) to equation (44) the following is obtained:

− for blade no. 1.

$$\varphi_{T12,T01} = Arg\,1.408(\frac{5121.798s^5 + 511.068s^4 - 462.387s^3 + 119.947s^2 - 16.415s + 1}{6701.085s^5 + 1158.219s^4 - 687.390s^3 + 152.925s^2 - 18.454s + 1}) \tag{45}$$

− for blade no. 2.

$$\varphi_{T12,T01} = Arg\,1.292(\frac{6321.036s^5 + 776.504s^4 - 570.617s^3 + 136.515s^2 - 17.468s + 1}{7969.314s^5 + 1060.469s^4 - 694.946s^3 + 155.614s^2 - 18.657s + 1}) \tag{46}$$

− for blade no. 3.

$$\varphi_{T12,T01} = Arg\,1.468(\frac{5154.601s^5 + 500.516s^4 - 460.482s^3 + 119.770s^2 - 16.405s + 1}{6943.993s^5 + 1174.033s^4 - 697.107s^3 + 154.371s^2 - 18.537s + 1}) \tag{47}$$

Blades technical condition is specified by model $\varphi_{T12,T01}$ parameters.

Rotor machine blade technical condition monitoring process is as follows:
− in exploitation time θ_0 (monitoring beginning) function $\varphi_{T12,T01}$ parameters: B_{01}, B_{02}, B_{03} ...and A_{01}, A_{02}, A_{03} ... are determined
− in exploitation time θ_1 (another blade monitoring) function $\varphi_{T12,T01}$ parameters: B_{10}, B_{11}, B_{12}, ... and A_{10}, A_{11}, A_{12} ... are determined

The technological differences between successive blades might also be determined. In such case the average values of function $\varphi_{T12,T01}$: : $A_{1śr}$, $A_{2śr}$, $A_{3śr}$ ...as well as $B_{1śr}$, $B_{2 r}$, $B_{3śr}$ parameters are determined and the diagnosed blades parameters are compared to them (tab.3 and tab.4).

− the difference between technical condition of consecutive blades is determined basing on relative parameters changes:

$$\Delta\overline{B}_i = \frac{B_{i1} - B_{sr}}{B_{sr}}\,; i = 1,\dots,n \tag{48}$$

$$\Delta\overline{A}_i = \frac{A_{i1} - A_{sr}}{A_{sr}}\,; i = 1,\dots,m \tag{49}$$

The change of $\overline{A}_i$ and $\overline{B}_i$ parameters as well as a significant number of their configuration allows the identification of multiple various changes of the blade technical condition while the rotor machine is operating (this also applies to investigate the new blades).

Tab. 3. The parameters of blades for the phase shift

		The parameters of blades for the phase shift					
		A_5	A_4	A_3	A_2	A_1	k
ROTOR BLADES	S1T01	6701.085	1158.219	-687.39	152.925	-18.454	1.408
	S2T01	7969.314	1060.469	-694.946	155.614	-18.657	1.292
	S3T01	6943.993	1174.033	-697.107	154.371	-18.537	1.468
	$S_{śr}$	7204.797	1130.907	-693.148	154.303	-18.549	1.389
		B_5	B_4	B_3	B_2	B_1	k
	S1T12	5121.798	511.068	-462.387	119.947	-16.415	1.408
	S2T12	6321.036	776.504	-570.617	136.515	-17.468	1.292
	S3T12	5154.601	500.516	-460.482	119.77	-16.405	1.468
	$S_{śr}$	5532.478	596.029	-497.829	125.411	-16.763	1.389

Tab. 4. Relative differences the parameters of blades for phase shift

		Relative differences the parameters of blades for phase shift					
		ΔA_5	ΔA_4	ΔA_3	ΔA_2	ΔA_1	Δk
ROTOR BLADES	S1T01	-0.070	0.024	-0.008	-0.009	-0.005	0.013
	S2T01	0.106	-0.062	0.003	0.008	0.006	-0.070
	S3T01	-0.036	0.038	0.006	0.000	-0.001	0.057
		ΔB_5	ΔB_4	ΔB_3	ΔB_2	ΔB_1	Δk
	S1T12	-0.074	-0.143	-0.071	-0.044	-0.021	0.013
	S2T12	0.143	0.303	0.146	0.089	0.042	-0.070
	S3T12	-0.068	-0.160	-0.075	-0.045	-0.021	0.057

6. CONCLUSIONS

Method of current assessment of blade technical condition changes basing on diagnostic models $A^2_{T12,T01}$ and $\varphi_{T12,T01}$ is innovative method of blade diagnostics without environment signal measurements.

Method of blade technical condition monitoring may be based on diagnostic model in form of quotient of output y(t) signal amplifications to environment signal x(t) for observation time T_{01} and T_{12}. This method consists in fact that time T (Fig. 5.) of blade tip movement in sensor area is divided onto two ranges: of blade tip approaching the sensor T_{01} and receding from it T_{12}.

Both observation periods T_{01} and T_{12} of y(t) are so close in time to each other that the environment for these observation periods may be considered identical $S^{T01}_{xx} = S^{T12}_{xx}$.

Method of technical condition monitoring is further distinguished by determining power spectral density S^{T01}_{yy}, S^{T12}_{yy} of signal y(t) through analytic forms of autocorrelation functions R^{T01}_{yy}, R^{T12}_{yy} and S^{T01}_{xy}, S^{T12}_{xy} through reciprocal correlation function R^{T01}_{xy}, R^{T12}_{xy} of signal y(t) and distribution function representing environment x(t). Required match (greater than 0,99) is obtained through proper choice of observation range T_d and T_k (Fig. 5.) and measurement window function: rectangular, Hamming, Hanning etc.

Another distinctive feature of models $A^2_{T12,T01}$ and $\varphi_{T12,T01}$ is no necessity of environment signals measurement although these are indirectly taken into account within special research (two observation periods, determination of diagnostic model as a quotient of models binding diagnostic and environment signals to technical condition parameters).

Method of blade technical condition monitoring may be also based on diagnostic model in form of quotient of phase shifts of output signal y(t) to environment signal x(t) for observation time T_{01} and T_{02}. Observation time T is divided onto two ranges. $\varphi_{T12,T01}$ is determined as a quotient of reciprocal power density S^{T01}_{xy} and S^{T12}_{xy} (to determine S^{T01}_{xy} and S^{T12}_{xy} noise of identical distribution of form is used $\delta(t, \hat{t})$).

REFERENCES

1. **Bendat J. S., Piersol A. G.** (1976), *Metody analizy i pomiaru sygnałów losowych*, PWN, Warszawa.
2. **Bovishanskii K. N.** (2000) A metod for continously monitoring the vibrational state of the rotating blades of turbomachines, *Thermal engineering (Teploenegetika)*, Vol 47 No 5, St. Petersburg.
3. **Dołgolienko G. P.** (1984) *Lietczyje ispytanija spienialnych ustrojstw i sistiem samolietow i wiertolietow Maszinostrożenije*, Moskwa.
4. **Duan F., Fang Z., Sun Y., Ye S.** (2005) Real-time vibration measurement technique based on tip-timing for rotating blades, *Opto-Electronic Energineering*, 30 (1) 29-31
5. **von Flotow A.**, **Mercadal H.** (2000) *Turbine rotor health management with blade-tip sensors*, From Laboratory Tool To Fielded System.
6. **High Cycle Fatigue S & program 1997** Annual Report http://stimet.dtic.mil
7. **High Cycle Fatigue S & program 1998** Annual Report http://stimet.dtic.mil
8. **High Cycle Fatigue S & program 1999** Annual Report http://stimet.dtic.mil
9. **High Cycle Fatigue S & program 2000** Annual Report http://stimet.dtic.mil
10. **High Cycle Fatigue S & program 2001** Annual Report http://stimet.dtic.mil
11. **High Cycle Fatigue S & program 2002** Annual Report http://stimet.dtic.mil
12. **Klein B.** (2004) Non-Contact Vibration measurements Turbocharges Turbine and Compressor Blades, *Proceedings of 1st EVI-GTI International Conference on Gas Turbine Instrumentation*, Barcelona.
13. **Kotowski A., Lindstedt P.** (2007) The using of signals of impulse acoustic response in test of rotor blades in stationary conditions, *The International Symposium on Stability Control of Rotating Machinery ISCORMA 4*, Calgary Alberta Canada.
14. **Kurowski W.** (1994) *Podstawy teoretyczne komputerowego miernictwa systemów mechanicznych*, Wyd. Politechniki Białostockiej, Białystok.
15. **Lindstedt P., Kotowski A.** (2004) Basic for innovations In vibroacoustic diagnostics of transport machines rotor blades, *The Archives of Transport*, Vd XVI. No 4.
16. **Lindstedt P.** (2002) *Praktyczna diagnostyka maszyn i jej teoretyczne podstaw,* Wyd. Naukowe ASKON, Warszawa.
17. **Lindstedt P., Rokicki E., Borowczyk H., Majewski P.** (2009) Application of the correlation function and Fourier transformation to evaluation of technical condition demonstrated by blade sof a rotor machine during the operation process, *Journal of KONES Powertrain and transport.* Vol 16 No 2, Warsaw.
18. **Lindstedt P., Rokicki E., Borowczyk H., Majewski P.** (2009) Rotor blades condition monitoring method based on the elimination of the environment signal, *Research Works of AFIT Issve*, 15÷24, Warsaw.
19. **Niederliński A.** (1985) *Systemy komputerowe automatyki przemysłowej T2 Zastosowania*, WNT, Warszawa.
20. **Roberts J. P.** (2007) Comparison of Tip Timing with strain Ganges for rotor blade vibration measurement, *Proceedings of lecture series on Tip Timing an Tip Clearnce Problems in Turbomachines von Belgium.*
21. **Skubaczewskij G. S.** (1974) *Awiacionnyje gazoturbinnyje dwigatieli Maszinostrojenije*, Moskwa.
22. **Szabatin J.** (2000) *Podstawy teorii sygnałów*, WKŁ Warszawa.
23. **Szczepanik R., Przysowa R.** (2004) *Wykonanie badań i pomiarów drgań łopatek metodą bezstykową w odwirowni ALSTOM Power w Elblągu*, Sprawozdanie ITWL nr 36/3/2004 Warszawa.
24. **Szczepanik R.** (1999) *Ocena propagacji pęknięć zmęczeniowych w wirujących łopatkach sprężarki turbinowego silnika lotniczego*, Książka Problemy Badań i Eksploatacji Techniki Lotniczej T4, Wyd. ITWL, Warszawa.
25. **Zieliński M., Ziller G.** (2005) Non-contact Blade Vibration Measurement system for aero engine application, *17th International Symposium on Airbreathing Engines*, Semptember 4-9 2005 Munich Germany Paper No ISABE – 2005-1220.

HUMAN CAPITAL
NATIONAL COHESION STRATEGY

EUROPEAN
SOCIAL FUND

CONTACT STRENGTH OF A SYSTEM OF TWO ELASTIC HALF SPACES WITH AN AXIALLY SYMMETRIC RECESS UNDER COMPRESSION

Bohdan MONASTYRSKYY[*], **Andrzej KACZYŃSKI**[**]

[*]Pidstryhach Institute for Applied Problems of Mechanics and Mathematics, Naukova Str. 3-b , 79053, Lviv, Ukraine
[**]Faculty of Mathematics and Information Science, Warsaw University of Technology,
Plac Politechniki 1, 00-061 Warszawa

bmonast@gmail.com, akacz@mini.pw.edu.pl

Abstract: Frictionless contact of two isotropic half spaces is considered one of which has a small smooth circular recess. A method of solving the corresponding boundary value problem of elasticity in axially symmetric case is presented via the function of gap height. The governing integral equation for this function is solved analytically by assuming a certain shape of the initial recess. On the basis of the closed-form solution obtained the strength analysis of a contact couple is performed and illustrated from the standpoint of fracture mechanics.

1. INTRODUCTION

The knowledge of the solutions (especially analytical solutions) to contact problems is a ground for the investigation of strength, durability, fatigue of contacting couples. The overwhelming majority of works devoted to strength of contacting joints utilizes the solutions to problems of penetration of rigid indenters into an elastic half-space (Hertzian contact). Extensive accounts can be found in the book by Kolesnikov and Morozov (1989). However, much research has been concerned with contact problems when conjugates solids touch at point or along the line before loading (contact with non-conformable boundaries, see a classification by Johnson, 1985). On the contrary, the contact interaction of bodies with conformable surfaces has been investigated much less. Approaches employing this kind of interaction take into account the existence of imperfections (recesses, pits, protrusions, concavities, etc.) of surfaces related to their small deviations from a flat onto local parts. Such perturbations lead to the local absence of contact, so the intercontact gaps are created.

The problem under study – compression of two semi-infinite isotropic elastic half spaces with an axially symmetric smooth recess – belongs to the class of non-classical contact problems involving contact interactions of solids with conformable boundaries. The purpose of the present work is to determine the stress distribution within the mated bodies and carry out a detailed analysis of strength of a contact couple from the point of view of fracture mechanics.

2. FORMULATION OF THE PROBLEM

Consider two isotropic elastic semi-infinite solids, being in frictionless contact due to uniform pressure p applied at infinity (see Fig. 1). The boundary of one (body 1) possesses a local deviation from the plane in the form of a small smooth circular recess with radius b. The shape of this imperfection is assumed to be axially symmetric and smooth. The boundary of the opposite body 2 is a plane.
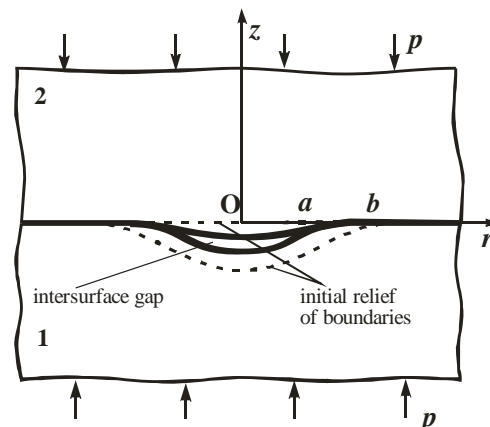
Fig. 1. Contact of two half-spaces with allowance for an intersurface gap

The problem is posed within the linear elasticity for axially symmetric case. In the cylindrical co-ordinate system the shape of the surface recess, occupying a circular region of radius b $\{(r, z = 0) : 0 \leq r \leq b\}$, is described by a function $f(r)$. This initial recess results in the formation of an intersurface gap of radius a that is unknown and depends on the pressure p (it is found in the process of solution of the problem). Thus, the nominal contact interface $z = 0$ is subdivided into two regions: the gap $\{(r, z = 0) : 0 \leq r \leq a\}$ and the region of body 1 – body 2 contact, defined by $\{(r, z = 0) : 0 \leq r \leq \infty\}$.

A method of solving the above problem is based on the

use of the principle of superposition. Knowing a trivial solution corresponding to the basic stress and strain fields formed as a result of frictionless contact of half spaces with flat surfaces, we concentrate attention on the perturbed problem associated with the excited state caused by an initial geometrically perturbed surface (recess) and the created gap between the surfaces. For this problem, we get the following boundary conditions:

at $z = \pm\infty$: $\quad \sigma_{zz}^{(i)} = 0, \quad \sigma_{zr}^{(i)} = 0,$ (1)

at $z = 0$:

$$\sigma_{rz}^{(i)} = 0, \qquad 0 < r < \infty,$$
$$\sigma_{zz}^{(1)} = \sigma_{zz}^{(2)}, \qquad 0 < r < \infty,$$
$$\sigma_{zz}^{(2)} = p, \qquad 0 < r < a,$$
$$u_z^{(1)} - u_z^{(2)} = f(r), \qquad a < r < \infty.$$
(1)

Here superscripts (*i*), *i* = 1, 2 refer the quantity to body 1 or 2, respectively.

Note, that the radius of the gap *a* is an unknown parameter. It can be found from the condition of smooth passage of gap's faces

$$h'(a) = 0,$$ (2)

where

$$h(r) = f(r) + u_z^{(2)}(r,0) - u_z^{(1)}(r,0)$$ (3)

is the height of the gap.

3. METHOD OF SOLUTION

The method of the solution to contact problems for semi-infinite solids with allowance for geometric surface disturbances has been developed in series of papers by Martynyak and co-workers (Martynyak, 1985; Shvets et al., 1996; Kit and Martynyak, 1999; Martynyak, 2000, Kit et al., 2001). Some new results dealing with the local contact absence are given in works by Kaczyński and Monastyrskyy (2002,2005), Monastyrskyy and Martynyak (2003).

The main idea of this method consists in the following: (*i*) construction of the representation of the stresses and displacements within the every of mated solids through the function of the gaps' height; (*ii*) subsequent reduction of the problem to some integral equations for this function.

3.1. Representation of stresses and displacements

Following the approach in the axially symmetric problems, developed by Monastyrskyy (2002), the appropriate representations of the displacements and stresses through the Hankel transform $H(\xi)$ of the gap's function $h(r)$ $\left(H(\xi) = \int_0^\infty \rho\, h(\rho) J_0(\xi\rho) d\rho \right)$ has been constructed. It was shown that the function $H(\xi)$ satisfies the dual integral equations

$$\int_0^\infty \xi^2 H(\xi) J_0(\xi r) d\xi = -\frac{p}{M} +$$
$$+ \int_0^\infty \xi^2 F(\xi) J_0(\xi r) d\xi, \quad 0 < r < a,$$
(4)

$$\int_0^\infty \xi H(\xi) J_0(\xi r) d\xi = 0, \qquad a < r < \infty.$$

Moreover, the expressions for components of displacement vector **u** and stress tensor **σ** through the function $H(\xi)$ are given as

$$\frac{u_r^{(i)}(r,z)\, m_i\, 2(1-\nu_i)}{M} =$$
$$= \int_0^\infty \xi(1-2\nu_i - \xi|z|)(F(\xi) - H(\xi))e^{-\xi|z|} J_1(\xi r) d\xi,$$

$$\frac{u_z^{(i)}(r,z)\, m_i\, 2(1-\nu_i)}{M} =$$
$$= (-1)^{i+1} \int_0^\infty \xi(2(1-\nu_i) + \xi|z|)(F(\xi) - H(\xi))e^{-\xi|z|} J_0(\xi r) d\xi,$$

$$\frac{\sigma_{rz}^{(i)}(r,z)}{M} = z \int_0^\infty \xi^3 (F(\xi) - H(\xi))e^{-\xi|z|} J_1(\xi r) d\xi,$$

$$\frac{\sigma_{zz}^{(i)}(r,z)}{M} = \int_0^\infty \xi^2 \left[(1+\xi|z|)(F(\xi) - H(\xi)) \right] e^{-\xi|z|} J_0(\xi r) d\xi,$$

$$\frac{\sigma_{rr}^{(i)}(r,z)}{M} = \int_0^\infty \xi^2 \left[(1-\xi|z|)(F(\xi) - H(\xi)) \right] e^{-\xi|z|} J_0(\xi r) d\xi -$$
$$- \int_0^\infty \xi \left[(1-2\nu_i - \xi|z|)(F(\xi) - H(\xi)) \right] e^{-\xi|z|} \frac{J_1(\xi r)}{r} d\xi,$$

$$\frac{\sigma_{\theta\theta}^{(i)}(r,z)}{M} = 2\nu_i \int_0^\infty \xi^2 (F(\xi) - H(\xi))e^{-\xi|z|} J_0(\xi r) d\xi +$$
$$+ \int_0^\infty \xi \left[(1-2\nu_i - \xi|z|)(F(\xi) - H(\xi)) \right] e^{-\xi|z|} \frac{J_1(\xi r)}{r} d\xi.$$
(5)

In the above, $F(\xi) = \int_0^\infty \rho\, f(\rho) J_0(\xi\rho) d\rho$ is the Hankel transform of the function of the initial recess shape $f(r)$, $m_i = \mu_i/(1 - \nu_i)$, where μ_i, ν_i stand for shear modulus and Poisson's ratio of the body denoted by $i = 1,2$ and $M = m_1 m_2/(m_1 + m_2)$. Hence the contact problem is reduced to solving the dual integral equations (5).

3.2. Integral equation and its solution

The obtained dual integral equation (5) is well studied in literature. The technique of its solution is known (Uflyand, 1977, Sneddon, 1966). Representing the sought function $H(\xi)$ as

$$H(\xi) = \xi^{-1} \int_0^a \gamma(\rho) \sin \xi\rho\, d\rho,$$ (6)

the equations (5) can be reduced to Abel's integral equation for function $\gamma(r)$

$$\frac{1}{r}\frac{\partial}{\partial r}\int_0^r \frac{\rho\,\gamma(\rho)d\rho}{\sqrt{r^2-\rho^2}}=g(r) \qquad (7)$$

with the solution (Barber, 1983)

$$\gamma(r)=\frac{2}{\pi}\int_0^r \frac{\rho\,g(\rho)d\rho}{\sqrt{r^2-\rho^2}}, \qquad (8)$$

where $g(r)$ stands for RHS of equation $(5)_1$.

To complete solving the problem in hand, it is necessary to determine the radius of the gap a. To do this, we utilize the condition (3) of smooth closure of the gap. Determining the height of the gap $h(r)$ via the function $\gamma(r)$

$$h(r)=\int_r^a \frac{\gamma(\rho)d\rho}{\sqrt{\rho^2-r^2}} \qquad (9)$$

we see that the condition (3) is equivalent to the equation

$$\gamma(a)=0. \qquad (10)$$

Once the function $\gamma(r)$ and radius of the gap a are found, the stress and displacement fields within every solid can be recovered by virtue of relations (6) with the aid of (7) and (9).

4. EXAMPLE

As an example, assume that the shape of the initial recess is given by formula

$$f(r)=h_0\left(1-r^2/b^2\right)^{3/2}. \qquad (11)$$

For this case the Hankel transform $F(\xi)$ of $f(r)$ is

$$F(\xi)=h_0 b^2 (\xi b)^{-5}\left(-3(\xi b)^2\sin(\xi b)+\right.$$
$$\left.+9\sin(\xi b)-9\xi b\cos(\xi b)\right). \qquad (12)$$

The function $\gamma(r)$, calculated from (9) is

$$\gamma(r)=-\frac{2}{\pi}\left[\frac{1}{M}p-\frac{3\pi}{4}\frac{h_0}{b}\left(1-\frac{r^2}{b^2}\right)\right]r. \qquad (13)$$

The solution of equation (11), provided the function $\gamma(r)$ is given by (14), yields the following value of the radius of the gap a:

$$a=b\sqrt{1-\frac{p}{M}\frac{3\pi}{4}\frac{h_0}{b}}. \qquad (14)$$

Now it follows that there is a certain level of external load, namely, $p=4bM/3\pi h_0$, for which the radius of the gap becomes zero. It means that for this magnitude of the pressure the gap is closed and the contact of the solids is realized through the whole contact interface $z=0$. The depen-

dence $a=a(p)$ is shown in Fig.2. The following dimensionless parameters have been introduced: $\bar{a}=a/b$, $\bar{p}=p/M$, $\bar{h}_0=h_0/b=10^{-3}$.

Whereas the function $\gamma(r)$ and the gap's radius a are known, the complete solution can be determined from relations (6) and (7). Thus, the solution to the contact problem can be rewritten through the corresponding integrals. After calculations we obtain

$$\frac{\sigma_{rz}^{(i)}(r,z)}{M}=z\frac{h_0}{b^3}\Big(-3b^2 Int_1(r,z,b)+9Int_2(r,z,b)+$$
$$+3a^2 Int_1(r,z,a)-9Int_2(r,z,a)\Big),$$

$$\frac{\sigma_{zz}^{(i)}(r,z)}{M}=-p+\frac{h_0}{b^3}\Big(-3b^2 Int_3(r,z,b)+9Int_4(r,z,b)+$$
$$+z\Big(-3b^2 Int_5(r,z,b)+9Int_6(r,z,b)\Big)+$$
$$+3a^2 Int_3(r,z,a)-9Int_4(r,z,a)+$$
$$+z\Big(3a^2 Int_5(r,z,a)-9Int_6(r,z,a)\Big)\Big),$$

$$\frac{\sigma_{rr}^{(i)}(r,z)}{M}=$$
$$-\frac{h_0}{b^3}\Big((1-2\nu_i)\Big(-3b^2 Int_7(r,z,b)+9Int_8(r,z,b)\Big)+$$
$$+z\Big(-3b^2 Int_9(r,z,b)+9Int_{10}(r,z,b)\Big)+$$
$$+(1-2\nu_i)\Big(3a^2 Int_7(r,z,a)-9Int_8(r,z,a)\Big)+$$
$$+z\Big(3a^2 Int_9(r,z,a)-9Int_{10}(r,z,a)\Big)\Big)+$$
$$+\frac{h_0}{b^3}\Big(-3b^2 Int_3(r,z,b)+9Int_4(r,z,b)+$$
$$+z\Big(-3b^2 Int_5(r,z,b)+9Int_6(r,z,b)\Big)+$$
$$+3a^2 Int_3(r,z,a)-9Int_4(r,z,a)+$$
$$+z\Big(3a^2 Int_5(r,z,a)-9Int_6(r,z,a)\Big)\Big),$$

$$\frac{\sigma_{\theta\theta}^{(i)}(r,z)}{M}=$$
$$\frac{h_0}{b^3}\Big((1-2\nu_i)\Big(-3b^2 Int_7(r,z,b)+9Int_8(r,z,b)\Big)+$$
$$+z\Big(-3b^2 Int_9(r,z,b)+9Int_{10}(r,z,b)\Big)+$$
$$+(1-2\nu_i)\Big(3a^2 Int_7(r,z,a)-9Int_8(r,z,a)\Big)+$$
$$+z\Big(3a^2 Int_9(r,z,a)-9Int_{10}(r,z,a)\Big)\Big)+$$
$$+2\nu_i\frac{h_0}{b^3}\Big(-3b^2 Int_3(r,z,b)+9Int_4(r,z,b)+$$
$$+3a^2 Int_3(r,z,a)-9Int_4(r,z,a)\Big), \qquad (15)$$

where $Int_k(r,z,b)$ $(k=\overline{1,10})$ stand for integrals given in Appendix.

The solution of the axially symmetric contact problem for semi-infinite solids with a surface recess given by formula (16) is found thus analytically.
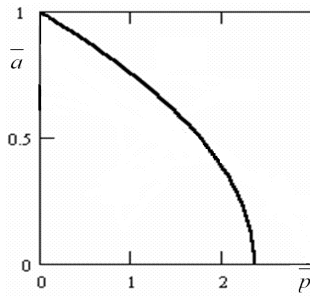

Fig. 2. Dependence of radius of the gap on the applied load

4.1. Contact strength

The obtained closed-form solution can be useful for analyzing the assessment of strength of the contacting couple. To estimate the strength of a system of two mated elastic half spaces allowing for unevenness of their boundaries, we shall use the classical criteria of fracture: the criterion of maximal principle stresses and the criterion of maximal shear stresses (Bożydarnyk and Sulym, 1999).

It's worth noting that an analysis of the stress distribution within the every solid reveals that the stresses σ_{zz}, σ_{rr}, $\sigma_{\theta\theta}$ are the principle stresses at the contact boundary ($z = 0$). Moreover, the principle stresses achieve their extreme value at $z = 0$. That's why we pay our attention to the analysis of stresses at the contact interface.

The maximum compressive stresses

Fig. 3. shows the distribution of contact normal stresses σ_{zz}, being the maximal compressive stresses. The stresses are zero within the gap region, then they increases, achieving the maximal value at $\overline{r} = 1$ which corresponds to the initial recess' tip. Then they asymptotically approach to the magnitude of external pressure p.
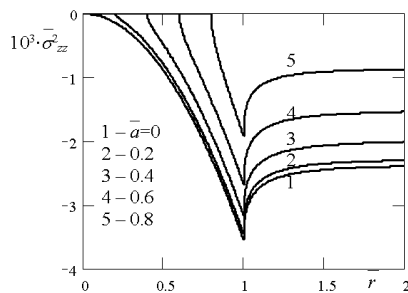

Fig. 3. The distribution of stresses σ_{zz} at the contact interface ($\overline{\sigma}_{zz} = \sigma_{zz}/M$)

According to the criteria of maximal principle stresses, from an analysis of stress distribution σ_{zz} one can conclude that the most dangerous zone is the vicinity of the recess' tip. Cracking of materials caused by the compressive stresses initiates most likely in the vicinity of the tip of the surface geometrical imperfection.

The maximum tensile stresses

Fig. 4 and 5 present the distribution of radial σ_{rr} and circular $\sigma_{\theta\theta}$ stresses at the contact interface. They reveal an interesting effect – the existence of tensile stresses at the contact interface. The stresses σ_{rr} and $\sigma_{\theta\theta}$ are: (*i*) tensile, (*ii*) constant and (*iii*) equal to each other within at the gap's faces. The magnitude of tensile stresses σ_{rr} and $\sigma_{\theta\theta}$ at the gap's faces is determined through the applied pressure and mechanical properties of the solids as

$$\sigma_{rr}^{(i)}(r,0) = \sigma_{\theta\theta}^{(i)}(r,0) = (1+2\nu_i)\,p/2, \quad 0 < r < a. \qquad (16)$$

Thus, the cracking can be initiated by tensile stresses. The most dangerous region is the gap. Moreover, the possibilities of cracks initiating along radial and circular directions are equal.
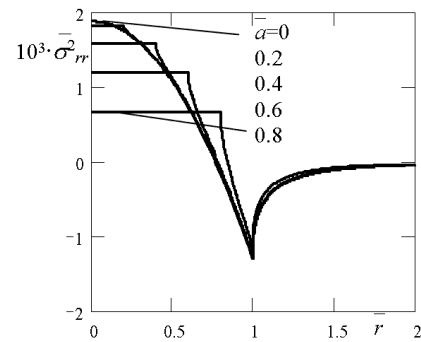

Fig. 4. The distribution of stresses σ_{rr} at the contact interface ($\overline{\sigma}_{rr} = \sigma_{rr}/M$)
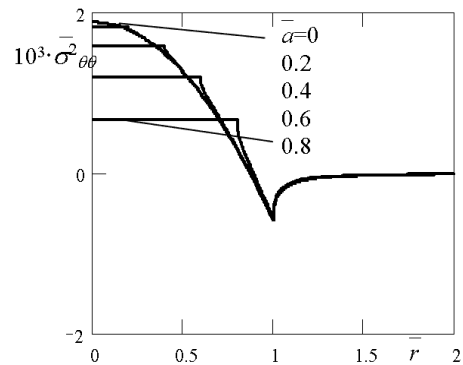

Fig. 5. The distribution of stresses $\sigma_{\theta\theta}$ at the contact interface ($\overline{\sigma}_{\theta\theta} = \sigma_{\theta\theta}/M$)

The maximum shear stresses

The analysis of maximal shear stresses at the contact interface has been carried out. Fig. 6 shows the distribution τ_{max}. Based on the criteria of maximal shear stresses, which are used for assessment of plastic zones initiated, the most dangerous zone is the vicinity of the recess' tip.
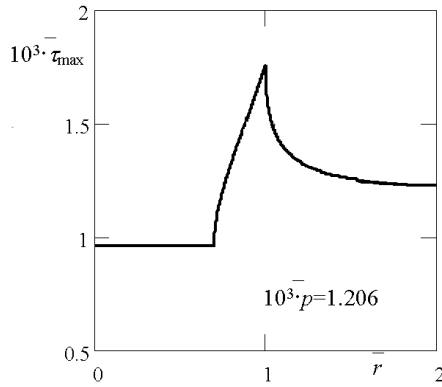
Fig. 6. The distribution of maximal shear stresses τ_{max} at the contact interface

5. CONCLUSIONS

The found closed-form solution to the contact problem has served as a theoretical basis for an analysis of strength of the contacting couple with a small surface recess. The analysis has been carried out by utilizing classical fracture criteria, namely, the criteria of maximal principle stresses and the criterion of maximal shear stresses.

The cracking of the material of the mated solids can be caused by both compressive and tensile stresses. In former case the most possible region where the cracks can be initiated is the vicinity of the recess tip. The compressive stresses achieve their maximal value at the contact interface at the tip of the recess. On other hand, the tensile stresses σ_{rr} and $\sigma_{\theta\theta}$ in the vicinity of the gap, appear at the interface. Moreover, the maximal value is achieved at the gap's faces, where σ_{rr} and $\sigma_{\theta\theta}$ are constant and equal to each other. The magnitude of the maximal tensile stress depends on Poisson's ratio of the material and lies in the range between 50% and 100% of the value of applied load at infinity. Two directions of cracking along the radial and circular co-ordinate lines are equally possible.

According to the criterion of the maximal shear stresses the most possible region where plastic zones can be initiated is the vicinity of the recess tip.

REFERENCES

1. **Barber J.R**. (1983), The solution of elasticity problems for a half-space by the method of Green and Collins, *Appl. Scientific Research,* 40, No 2, 135-157.
2. **Božydarnyk V.V., Sulym G.T.** (1999), *Elementy teorii plastyčnosti ta micnosti*, Svit, Lviv.
3. **Johnson K.L.** (1985), *Contact Mechanics*, Oxford University Press, Oxford.
4. **Kaczyński A.**, **Monastyrskyy B**. (2002), Contact problem for periodically stratified half-space and rigid foundation possessing geometrical surface defect, *J. Theor. Appl. Mech.*, 40, 985-999.
5. **Kit H.S., Martynyak R.M.** (1999), Prostorovi kontaktni zadači dlia pružnogo pivprostoru i žorstkoi osnovy z poverchnevymy vyimkamy, *Mat. Metody i Fiz.-Mech. Polia,* 42, No.3, 7-11.
6. **Kit H.S., Martynyak R.M., Monastyrskyy B. Ye**, (2001), Metod potencialiv v zadačach pro lokalnu vidsutnist kontaktu, *Visn. Dnipropetr. Univer. Ser. Mechanika*, 1, No. 4, 69-77.
7. **Kolesnikov Yu. V., Morozov E. M.** (1989), *Contact Fracture Mechanics*, Nauka, Moscow.
8. **Martynyak R.M.** (1985), Vzaimodejstvie uprugich poluploskostej pri nepolnom mechaničskom kontakte, *Mat. Metody i Fiz.-Mech. Polia*, 22, 89-92.
9. **Martynyak R.M.**, (2000), Metod funkcij mižkontaktnych zazoriv v zadačach porušennja kontaktu pružnych pivprostoriv, *Mat. Metody i Fiz.-Mech. Polia*, 43, No1., 102-108.
10. **Monastyrskyy B.** (2002), *Axially Symmetric Problems of Thermoelasticity for solids with local geometric imperfections of the boundaries*. PhD thesis, Lviv.
11. **Monastyrskyy B. , Kaczyński A**. (2005), Contact between an elastic layer and elastic semi-infinite space bounded by a plane with axially symmetric smooth dip, *Electr. J. Polish Agricultur. Univ.*, Vol. 8, No 4.
12. **Monastyrs'kyj B.E., Martynyak R.M.** (2003), Contact of two half space one of which contains a ring-shaped pit. Part 1. Singular integral equation., *Materials Science,* Vol. 39, No 2, 206-213.
13. **Sneddon I.** (1966), *Mixed Boundary Value Problems in Potential Theory*. Wiley, New York.
14. **Shvets R.M., Martynyak R.M., Kryshtafovych A.A.** (1996) Discontinuous contact of an anisotropic half-plane and a rigid base with disturbed surface, *Int. J. Engng. Sci.* 34, No 2.,183-200.
15. **Uflyand Ya. S.** (1977), *Dual Integrals Method in Mathematical Physics Problems*, Nauka, Leningrad.

APPENDIX

The values of the integrals appearing in (16) are as follows:

$$Int_1(r,z,b) = \int_0^\infty e^{-\xi z} \sin(\xi b) J_1(\xi r) d\xi = \begin{cases} \dfrac{b\cos\left(\frac{1}{2}\tan^{-1}\left(\frac{2zb}{z^2-b^2+r^2}\right)\right) - z\sin\left(\frac{1}{2}\tan^{-1}\left(\frac{2zb}{z^2-b^2+r^2}\right)\right)}{r\sqrt[4]{\left(z^2-b^2+r^2\right)^2 + (2zb)^2}}, & z \neq 0; \\[4mm] 0, & z=0, \quad r \leq b; \\[2mm] \dfrac{b}{r\sqrt{r^2-b^2}}, & z=0, \quad r > b. \end{cases}$$

$$Int_2(r,z,b) = \int_0^\infty e^{-\xi z} \frac{\sin(\xi b) - \xi b \cos(\xi b)}{\xi^2} J_1(\xi r) d\xi = \begin{cases} \int_0^b \beta Int_1(r,z,\beta)d\beta, & z \neq 0; \\[2mm] \dfrac{\pi r}{4}, & z = 0, \quad r \leq b; \\[4mm] -\dfrac{b\sqrt{r^2 - b^2}}{2r} + \dfrac{r}{2}\sin^{-1}\left(\dfrac{b}{r}\right), & z = 0, \ r > b. \end{cases}$$

$$Int_3(r,z,b) = \int_0^\infty e^{-\xi z} \frac{\sin(\xi b)}{\xi} J_0(\xi r) d\xi = \begin{cases} \sin^{-1}\left(\dfrac{2b}{\sqrt{(b+r)^2 + z^2} + \sqrt{(b-r)^2 + z^2}}\right), & z \neq 0; \\[4mm] \dfrac{\pi}{2}, & z = 0, \quad r \leq b; \\[3mm] \sin^{-1}\left(\dfrac{b}{r}\right), & z = 0, \ r > b. \end{cases}$$

$$Int_4(r,z,b) = \int_0^\infty e^{-\xi z} \frac{\sin(\xi b) - \xi b \cos(\xi b)}{\xi^3} J_0(\xi r) d\xi = \begin{cases} \int_0^b \beta Int_3(r,z,\beta)d\beta, & z \neq 0; \\[2mm] \dfrac{\pi\left(2b^2 - r^2\right)}{8}, & z = 0, \quad r \leq b; \\[3mm] \dfrac{1}{4}\left(b\sqrt{r^2 - b^2} + \left(2b^2 - r^2\right)\sin^{-1}\left(\dfrac{b}{r}\right)\right), & z = 0, \ r > b. \end{cases}$$

$$Int_5(r,z,b) = \int_0^\infty e^{-\xi z} \sin(\xi b) J_0(\xi r) d\xi = \begin{cases} \dfrac{2bz}{\sqrt{\left(\sqrt{(b+r)^2 + z^2} + \sqrt{(b-r)^2 + z^2}\right)^2 - b^2}\sqrt{(b+r)^2 + z^2}\sqrt{(b-r)^2 + z^2}}, & z \neq 0; \\[4mm] \dfrac{1}{\sqrt{b^2 - r^2}}, & z = 0, \quad r < b; \\[3mm] 0, & z = 0, \ r > b. \end{cases}$$

$$Int_6(r,z,b) = \int_0^\infty e^{-\xi z} \frac{\sin(\xi b) - \xi b \cos(\xi b)}{\xi^2} J_0(\xi r) d\xi = \begin{cases} \int_0^b \beta Int_5(r,z,\beta)d\beta, & z \neq 0; \\[3mm] \sqrt{b^2 - r^2}, & z = 0, \quad r \leq b; \\[2mm] 0, & z = 0, \ r > b. \end{cases}$$

$$Int_7(r,z,b) = \int_0^\infty e^{-\xi z} \frac{\sin(\xi b)}{\xi^2} \frac{J_1(\xi r)}{r} d\xi =$$

$$= \begin{cases} \frac{1}{r^2}\left(-zb + \frac{1}{2\sqrt{2}}\left(z\sqrt{\sqrt{\left(z^2-b^2+r^2\right)^2 + 4z^2b^2} - \left(z^2-b^2+r^2\right)} + b\sqrt{\sqrt{\left(z^2-b^2+r^2\right)^2 + 4z^2b^2} + \left(z^2-b^2+r^2\right)}\right)\right) + \\ \qquad + \frac{1}{2}\tan^{-1}\left(\frac{\sqrt{2}b + \sqrt{\sqrt{\left(z^2-b^2+r^2\right)^2 + 4z^2b^2} - \left(z^2-b^2+r^2\right)}}{\sqrt{2}z + \sqrt{\sqrt{\left(z^2-b^2+r^2\right)^2 + 4z^2b^2} + \left(z^2-b^2+r^2\right)}}\right), \quad z \neq 0; \\ \frac{\pi}{4}, \qquad z = 0, \quad r < b; \\ \frac{b}{2r^2}\sqrt{r^2-b^2} + \frac{1}{2}\tan^{-1}\left(\frac{b}{\sqrt{r^2-b^2}}\right), \qquad z = 0, \quad r > b. \end{cases}$$

$$Int_8(r,z,b) = \int_0^\infty e^{-\xi z} \frac{\sin(\xi b) - \xi b \cos(\xi b)}{\xi^4} \frac{J_1(\xi r)}{r} d\xi = \begin{cases} \int_0^b \beta Int_7(r,z,\beta)d\beta, \quad z \neq 0; \\ \frac{\pi\left(4b^2 - r^2\right)}{32}, \qquad z = 0, \quad r \leq b; \\ \frac{1}{16r^2}\left(b\left(2b^2+r^2\right)\sqrt{r^2-b^2} + \left(4b^2r^2 - r^4\right)\sin^{-1}\left(\frac{b}{r}\right)\right), \quad z = 0, \; r > b. \end{cases}$$

$$Int_9(r,z,b) = \int_0^\infty e^{-\xi z} \frac{\sin(\xi b)}{\xi} \frac{J_1(\xi r)}{r} d\xi = \begin{cases} \frac{1}{r^2}\left(b - \frac{1}{\sqrt{2}}\sqrt{\sqrt{\left(z^2-b^2+r^2\right)^2 + 4z^2b^2} - \left(z^2-b^2+r^2\right)}\right), \quad z \neq 0; \\ \frac{1}{b + \sqrt{b^2-r^2}}, \qquad z = 0, \quad r < b; \\ \frac{b}{r^2}, \qquad z = 0, \quad r > b. \end{cases}$$

$$Int_{10}(r,z,b) = \int_0^\infty e^{-\xi z} \frac{\sin(\xi b) - \xi b \cos(\xi b)}{\xi^3} \frac{J_1(\xi r)}{r} d\xi = \begin{cases} \int_0^b \beta Int_9(r,z,\beta)d\beta, \quad z \neq 0; \\ \frac{1}{3}\frac{1}{b + \sqrt{b^2-r^2}}\left(2b^2 - r^2 + b\sqrt{b^2-r^2}\right), \qquad z = 0, \quad r \leq b; \\ \frac{b^3}{3r^2}, \quad z = 0, \; r > b. \end{cases}$$

FREQUENCY AND NON-LINEAR ANALYSIS OF BUBBLE PATHS IN BUBBLE CHAIN

Romuald MOSDORF*, Tomasz WYSZKOWSKI[*]

*Bialystok Technical University, Faculty of Mechanical Engineering, ul. Wiejska 45, 15-351 Bialystok, Poland

r.mosdorf@pb.edu.pl, wyszkowski.tomasz@gmail.com

Abstract: In the paper the paths of bubbles emitted from the bras nozzle with inner diameter equal to 1.1 mm have been ana-lyzed. The mean frequency of bubble departure was in the range from 1 to 36 Hz. Bubble paths have been recorded using a high speed camera. The image analysis technique has been used to obtain the bubble paths for different mean frequencies of bubble departures. The Fourier, wavelet analysis and recurrence plots have been used to determine the strength of interac-tion between bubbles in column. It has been found that the influence of previously departing bubbles on trajectory of next bubble in the column can be significant for $f_b > 30$ Hz, in this case the bubble paths become less periodic and more instable. In this case the distance between subsequent departing bubbles (S/D) becomes close to 1. It causes that the vertical interac-tion between departing bubbles is enough strong to change the dynamical properties of bubble paths.

1. INTRODUCTION

The knowledge of bubble dynamics is of key impor-tance in physical, biological and medical processes, and particularly in industrial applications. There are numer-ous physical parameters such as: physical properties of the two phases, gas flow rate, gas pressure, height of the liquid and gravity conditions which influence on the bubbles for-mation. Hence, most of efforts have been devoted to the formation of bubbles from single nozzles or orifice plates. The study of bubble dynamics is crucial to understand bub-ble-liquid and bubble-bubble interactions. According to Luewisutthichat et al. (1997) the bubble motion and bubble shape are controlled by deterministic forces such as body force and drag force caused by the convective motion, and the complex non-linear forces generated by liquid motion around bubbles. Results of investigation show that such quantity as: bubble departure frequency (time between subsequent departing bubbles), bubble departure diameter, bubble shape and its deformation, gas pressure fluctuation in the nozzle, bubbles interaction, bubbles coalescence and bouncing, structure of liquid flow around the bubbles and bubble column change in time chaotically (Mosdorf and Shoji, 2003; Zhang and Shoji, 2003; Kikuchi et al., 1997; Femat et al., 1998; Vazquez at al., 2008).

The tubes of streamwise liquid vorticity are being left by each bubble and they are responsible for appearance of lift force acting on the bubbles (Zenit and Magnaudet, 2009). The strength of the circulation of each vortex tubes decreases with increase in the distance from the bubble. The bubbles in the bubble column create the complex struc-ture of bubble wakes. These wakes interact between each others and finally modify the bubbles trajectory. The in-crease of bubble departure frequency decreases the vertical distance between bubbles. It causes the increase of interac-tion between the bubbles and tubes of streamwise liquid vorticity generated by previously bubbles. Such interaction

changes the lift force and finally modify the oscillation bubble trajectory.

In the present paper the dynamical properties of bubble paths have been investigated to detect the strength of inte-raction between bubbles. The paths of bubbles emitted from the bras nozzle with inner diameter equal to 1.1 mm has been analyzed. The bubble departure diameter was ~4.5 mm. The laser-photodiode system has been used to measure the frequency of bubble departures. The analyzed frequen-cies ranged from 1 to 36 Hz (bubbles per second). The bubble paths have been recorded using a high speed camera. The image analysis technique enabled us to obtain the 2D bubble paths for different mean frequencies of bub-ble departures. The Fourier analysis, wavelet analysis and recurrence plots have been used to determine the strength of interaction between bubbles.

2. EXPERIMENTAL SETUP
AND BUBBLE BEHAVIOURS

The air bubble paths in bubble column in the tank (400 x 500 x 40 mm) filled with distillated water has been investigated. In the experiment bubbles were generated from the brass nozzle with inner diameter of 1.1 mm.

Because in the experiment with bubble column genera-tion both the pressure and gas mass flux fluctuated then in order to evaluate experiment conditions it was necessary to use the mean value of gas mass flux or bubble departure frequency. In the present experiment the mean bubble de-parture frequency was used as a control parameter. The frequency has been measured using simultaneously the laser - phototransistor system and gas pressure sensor. The gas pressure fluctuation has been measured using un-compensated silicon pressure sensor MPX12DP. In the laser-phototransistor system the semiconductor red laser with wave length of 650 nm, 3mW, special aperture and phototransistor BPYP22 has been used. The diameter

of laser ray was 0.2 mm. The experiment has been carried out in conditions when subsequent departing bubbles did not coalesce vertically close to the nozzle outlet. The frequency of bubble departure was in the range from 2 to 36 bubbles per second, the water temperature was 20°C.

All data was simultaneously recorded using the data acquisition system DT9800 series USB Function Modules for Data Acquisition Systems with sampling frequency of 1000 Hz. The air supply system consisted of air tank capacity of 2 dm³ and the electronically controlled air pump, where the velocity of electric engine was controlled by the chip U2008B. The scheme of experimental stand has been shown in Fig. 1.

Bubble paths have been recorded in the rectangle area of 230 x 50 mm using the high speed camera Casio EX FX1. The recorded color video (600 fps) has been divided into frames. All colored frames were converted into gray scale images. The Sobel filter based on convolution of the image with a small, integer valued filter has been used to identify the bubbles on the frames (Hedengren, 1988). Exemplary results of using the Sobel filter for bubble image are presented in Fig. 2a. Because the Sobel algorithm identifies only the edge of the bubble, therefore the additional algorithm to fill interior of the detected bubble by black pixels has been used. Finally, each bubble was visible in the frame as a set of black pixels (Fig. 2).

The path of each bubble was reconstructed by tracking the trajectory of mass center of each bubble in subsequent frames. The mass centre has been calculated according to the following formula:

$$x_c = \frac{\sum_i \sum_j k}{S} \qquad (1)$$

where $k = \begin{cases} i \; for \; black \; pixels \\ 0 \end{cases}$

$$y_c = \frac{\sum_i \sum_j k}{S} \qquad (2)$$

where $k = \begin{cases} j \; for \; black \; pixels \\ 0 \end{cases}$

where S – the area of the bubble picture.

In the paper the paths of bubbles which do not coalesce with another bubbles have been analyzed.

In Fig. 3 it has been shown the data recorded from the phototransistor and pressure sensor for different mean frequencies of bubble departures. The laser ray passed 3 mm above the nozzle outlet. When the bubble was passing through the laser ray the phototransistor sensor generated the signal of the low voltage level. The time between bubbles is visible in Fig. 3 as a signal of the high voltage level. Obtained results show that for all frequencies of bubble departures the time periods in which the bubbles pass through the laser ray are approximately the same and are equal to 0.018 ±0.002 [s], but mean time periods between subsequent departing bubbles decrease together with increase of bubble departure frequencies as it has been shown in Fig. 4.

When bubbles depart, the air pressure rapidly decreases as it has been shown in Fig. 3. The number of minimums of pressure signal and number of periods with low voltage level signal coming from phototransistor sensor have been used to determine bubble departure frequencies.
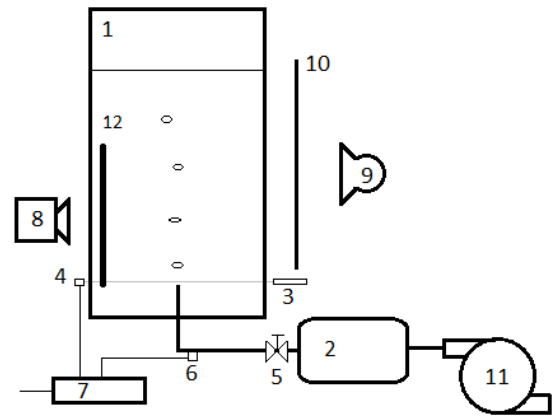
Fig. 1. Experimental setup. 1 – glass tank, 2 – air tank, 3 – laser, 4 – phototransistor, 5 – air valve, 6 – pressure sensor, 7 – computer acquisition system (DT9800 series USB Function Modules for Data Acquisition Systems), 8 – Casio EX FX1(600 fps), 9 – light source, 10 – screen, 11 – air pump with electronic control, 12 – The rectangle area of 230x50 mm where the bubble paths has been recorded
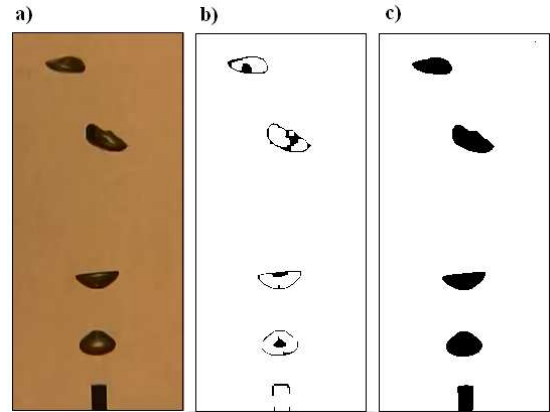
Fig. 2. The bubble identification process. a) original photo. b) results of Sobel filter, c) filling interior of the bubbles by black pixels
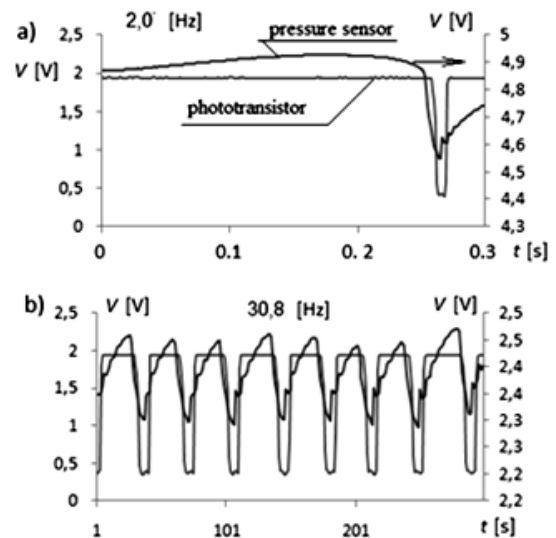
Fig. 3. Pressure and phototransistor signal recorded for different frequencies of bubble departures f_b a) $f_b = 2$ Hz, b) $f_b = 30.08$ Hz
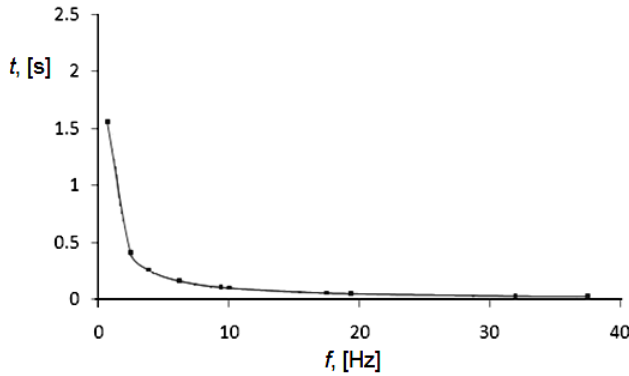
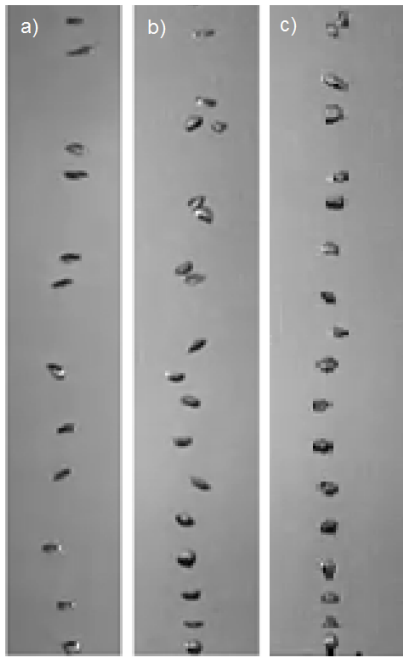**Fig. 4.** The mean time periods between subsequent departing

Fig. 5. The changes in time of the horizontal position
of the bubble and the typical behavior of bubble flow
for different mean bubble departure frequencies f_b
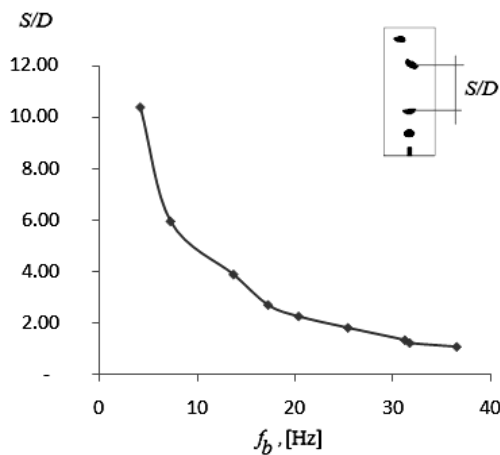a) $f_b = 14.4$ [Hz], b) $f_b = 30$ [Hz], c) $f_b = 36$ [Hz]

Fig. 6. Estimated distance between subsequent bubbles

In Fig. 5 the typical behavior of bubble flow for different mean bubble departure frequencies has been presented.

Changes of frequency of bubble departures cause the changes of average distance between bubbles in the bubble chain. The distance has been measured between two subsequent bubbles when the lower bubble was 10 mm over the nozzle outlet. In Fig. 6 it has been shown the distance between bubbles vs frequency of bubbles departure.

3. ANALYSIS OF FREQUENCY OF BUBBLE DEPARTURES

One of the main problem in investigation of bubbling flow is an analysis of frequency of bubble departure. Such frequency can be constant in time (bubbles depart periodically) or change chaotically in time (bubbles depart chaotically). The Fourier transformation allows us to represent the time-domain data in the frequency domain. The Fourier power spectrum answers the question which frequencies contain the signal power. The answer has a form of distribution of power values as a function of frequency. In the frequency domain, this is the square of Fourier transformation. For the measurement data in the form of discrete series x_n the Fourier transformation has a following form:

$$F_k = \sum_{n=0}^{N-1} x_n e^{-j\frac{2\pi}{N}kl} \qquad (3)$$

The power spectrum is defined as $P = |F_k|^2$. The examples of power spectrums of data recorded in the experiment have been shown in Fig. 7.

Obtained results for bubble paths have been compared with results of analysis prepared for the test path described by the function $x(t) = \ln(t) \cdot \sin(\omega t)$. Power spectrum of test path has been shown in Fig. 7c. In this case the dominant frequency is equal to bubble path oscillation frequency - 4.63 [Hz]. The power spectrum presented in Fig. 7c is characteristic for periodic system. Power spectrums obtained for experimental data presented in Fig. 7.a,b are characteristic for deterministic chaos system.

In case when $f_b = 0.9$ [Hz] (Fig. 7a) the bubble path oscillation frequency is a dominant frequency of power spectrum and is equal to 4.87 [Hz]. But in power spectrum we can distinguish the additional frequencies with relatively high amplitudes. These frequencies are connected with trends of bubble paths. Together with the increase of frequency of bubble departures the amplitudes of these additional frequencies (less than 5 [Hz]) increase, which is presented in Fig. 7b. It means that bubble paths become more unstable.

The Fourier power spectrum does not allow us to identify the frequency changes in time. This problem can be analyzed using the windowed Fourier transformation (Torrence and Compo, 1998, 2005), but this is an inaccurate method to localize time–frequency. The method which eliminates this inaccuracy is the wavelet analysis. It is a tool for analyzing the localized variations of power spectrum within the time series x_n, with equal time spacing δt (Torrence and Compo, 1998, 2005). The continuous wavelet transformation of a discrete sequence x_n is defined as the convolution of x_n with a scaled wavelet Ψ (Torrence and Compo, 1998, 2005):

$$W\left(t,s\right)=\sum_{t'=0}^{N-1}x_{t'}\cdot\Psi*\left[\frac{\left(t'-t\right)\delta t}{s}\right] \qquad (4)$$

where (*) indicates the complex conjugate.
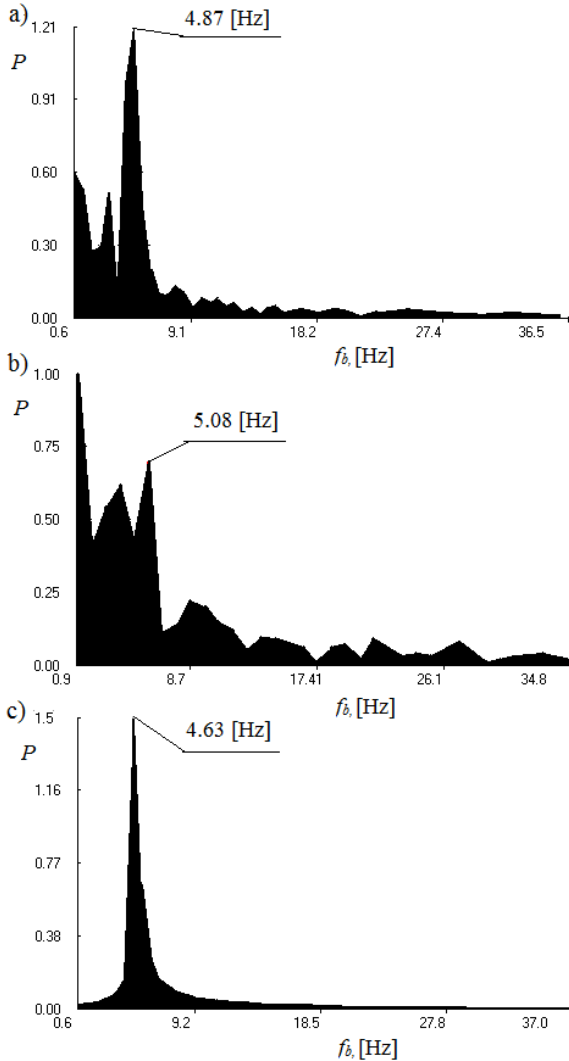
Fig. 7. Fourier power spectrums for different frequencies
of bubble departures f_b. a) f_b = 0.9 Hz, b) f_b = 36.5 Hz,
c) Test path

Because the wavelet function $\Psi_o(\eta)$ is generally complex, the wavelet transformation $W(t,s)$ is also complex. The wavelet power spectrum is defined as: $/W(t,s)/^2$ (Torrence and Compo, 1998, 2005).

In the analysis the Morlet wavelet has been used as the based wavelet and has a form (Torrence and Compo, 1998, 2005):

$$\Psi_o(\eta)=\pi^{-1/4}e^{i\omega_o\eta}e^{-\eta^2/2} \qquad (5)$$

where: ω_o – nondimensional frequency, in the paper it is equal to 6 (Torrence and Compo, 1998, 2005).

In Eq. 4 the parameter s assigns the frequency, whereas the parameter t identifies the time around which the assigned frequencies are investigated. The wavelet power spectrum is presented in the form of three dimensional map, where the horizontal axis shows the values of parameter t,

while the vertical axis shows the values of parameter s (frequencies). The values of wavelet power spectrum $/W(t,s)/^2$ are presented as an altitude. The wavelet power spectrum allows us to observe the changes of each frequency in time. In Fig.8 the contour plots of the wavelet power spectrums for selected bubble paths have been presented. The areas containing the highest value of $/W(t,s)/^2$ are filled with a grey color.

The changes of location of maximum values of $/W(t,s)/^2$ identify the changes of the dominant frequency in time. The wavelet power spectrum shows in what period of time of the pressure time series these frequencies appear.

In Fig. 8g it has been shown the wavelet power spectrum for test path. Because the value of $/W(t,s)/^2$ depends on the amplitude and frequency of data, therefore the $/W(t,s)/^2$ obtained for test path clearly identifies the oscillation frequency only when the amplitude of oscillations is enough large. It happens in certain distance from the nozzle outlet. The higher value of $/W(t,s)/^2$ have been market in Fig. 8 with grey color.

The length of the area marked with grey color is a measure of time in which the oscillatory bubble movement with frequency about 5 [Hz] is stable. The length of grey area decreases together with the increase of frequency of bubble departures.
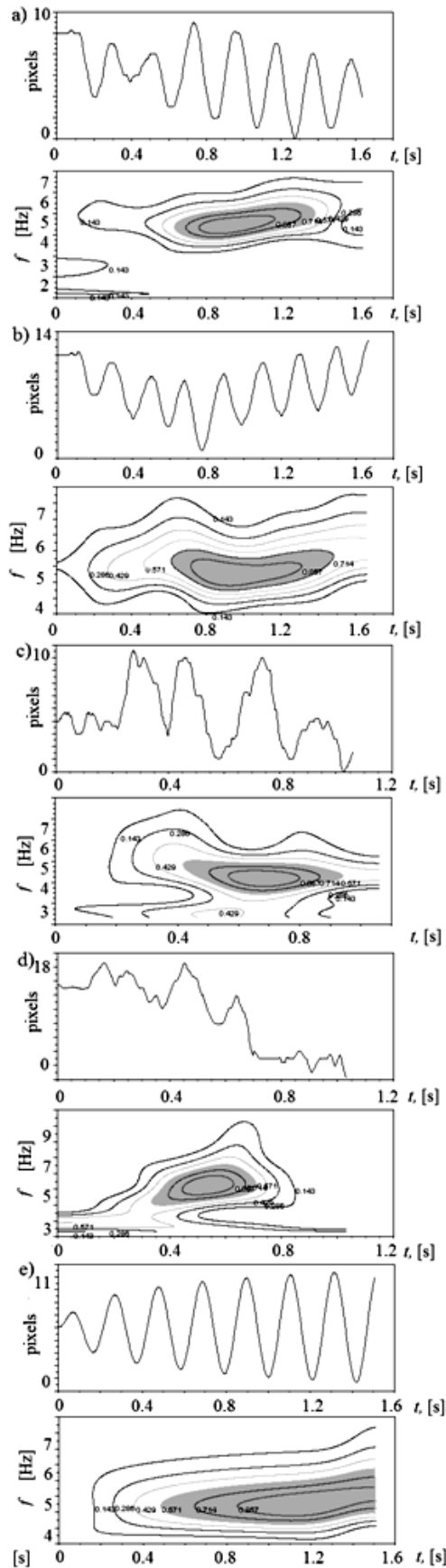
3.1. Attractor reconstruction

In order to qualitatively describe the stability of oscillatory movement of bubbles the non-linear analysis with using the recurrence plot method has been carried out.

The trajectories of the chaotic system in the phase space do not form any single geometrical object such as circle or torus, but form objects called strange attractors of the structure resembling the one of a fractal [8]. Non linear analysis starts from attractor reconstruction. Reconstruction of attractor in certain embedding dimension has been carried out using the stroboscope coordination. In this method subsequent co-ordinates of attractor points are calculated basing on the subsequent samples distant of time delay τ. The time delay is multiplication of time between the samples. The image of the attractor in n-dimensional space depends upon time-delay τ. When the time-delay is too small, the attractor gets flattened, that makes further analysis of its structure impossible. The selection of time-delay value is of great significance in the analysis of the attractor properties.

Therefore the analysis of the experimental data is initiated by determining the time-delay. For that purpose the autocorrelation function is calculated. Autocorrelation function allows identification of correlation between the subsequent samples. In case of chaotic data the value of autocorrelation function rapidly decrease when τ increase. Value of the time-delay τ is determined from the condition $C(\tau)\approx0.5*C(0)$ (Schuster, 1993).

In Fig. 9 it has been shown the 3D attractor reconstruction obtained for time delay calculated using the mutual information method. For the low frequency of bubble departure (Fig. 9a,b,c) the spiral structure of attractor is visible. For the high frequency of bubble departure (Fig. 9d) the spiral structure of attractor is invisible.
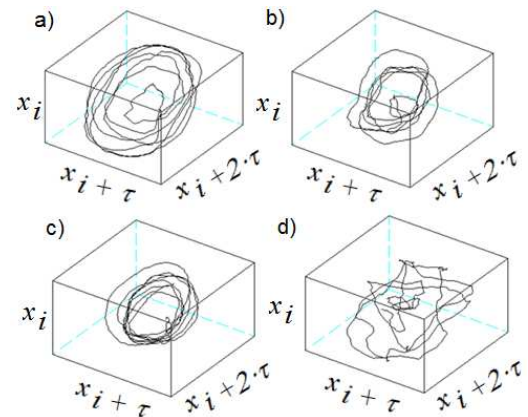
Fig. 9. 3D attractor reconstructions for different frequencies of bubble departures f_b. a) $f_b = 0.9$ [Hz], b) $f_b = 2.9$ [Hz], c) $f_b = 4.1$ [Hz], e) $f_b = 31.7$ [Hz]

3.2. Recurrence plot

Recurrence plot (RP) visualize the recurrence of states x_i in a phase space. The RP enables us to investigate the recurrence of state in m-dimensional phase. The recurrence of a state at time i at a different time j is marked within black dots in the plot, where both axes are time axes. From the formal point of view the RP can be expressed as Marwan et al. (2007):

$$R_{i,j} = \Theta\big(\varepsilon_i - \|x_i - x_j\|\big), \ x_i \in \Re^m, \ i,j - 1 \dots N \qquad (6)$$

where N is the number of considered states x_i, ε_i is a threshold distance, $\| \|$ a norm and Θ the Heaviside function.

Homogeneous RPs are typical for stationary systems in which relaxation times are short in comparison with the time of system investigation. Oscillating systems have RPs with diagonal oriented, periodic recurrent structures. For quasi-periodic systems, the distances between the diagonal lines are different. The drift is caused by systems with slowly varying parameters which cause changes of brightens of the RP's upper-left and lower-right corners. Abrupt changes in the dynamics as well as extreme events cause white areas or bands in the RP (Marwan et al., 2007).

In Fig. 10 the RPs obtained for different frequencies of bubble departure have been presented. The RP has been made for 2D attractor reconstruction and ε equal to 1% of maximal lateral bubble displacement. For each frequency of bubble departure the time series of bubble lateral displacement (upper part of figure) and RP (lower part of figure) have been shown. In Fig. 10f it has been presented the RP prepared for the test time series where $x(t) = \ln(t) \cdot \sin(\omega \cdot t)$. The distance between parallel diagonal lines identifies the time series period. The distance between parallel diagonal lines in RP (Fig. 10a,b) is a result from the period of function of bubble lateral displacement and is equal to ~80 points (about 5 [Hz]) (Marwan et al., 2007).

The recurrence rate (RR) represents the percentage of recurrence points in RP (Marwan et al., 2007). The recurrence rate corresponds to the correlation sum (Marwan et al., 2007). The number of recurrence points increases with increase of frequency of bubble departure (Mosdorf and Wyszkowski, 2010). Because all recurrence plots have been constructed basing on a single bubble trajectory, there-

Fig. 8. Bubble paths and wavelet power spectrums for different frequencies of bubble departures f_b. a) $f_b = 0.9$ Hz, b) $f_b = 4.1$ Hz, c) $f_b = 31.7$ Hz, d) $f_b = 36.5$ Hz, e) Test path

fore the increase of RR is a result of increase of complexity of attractors.
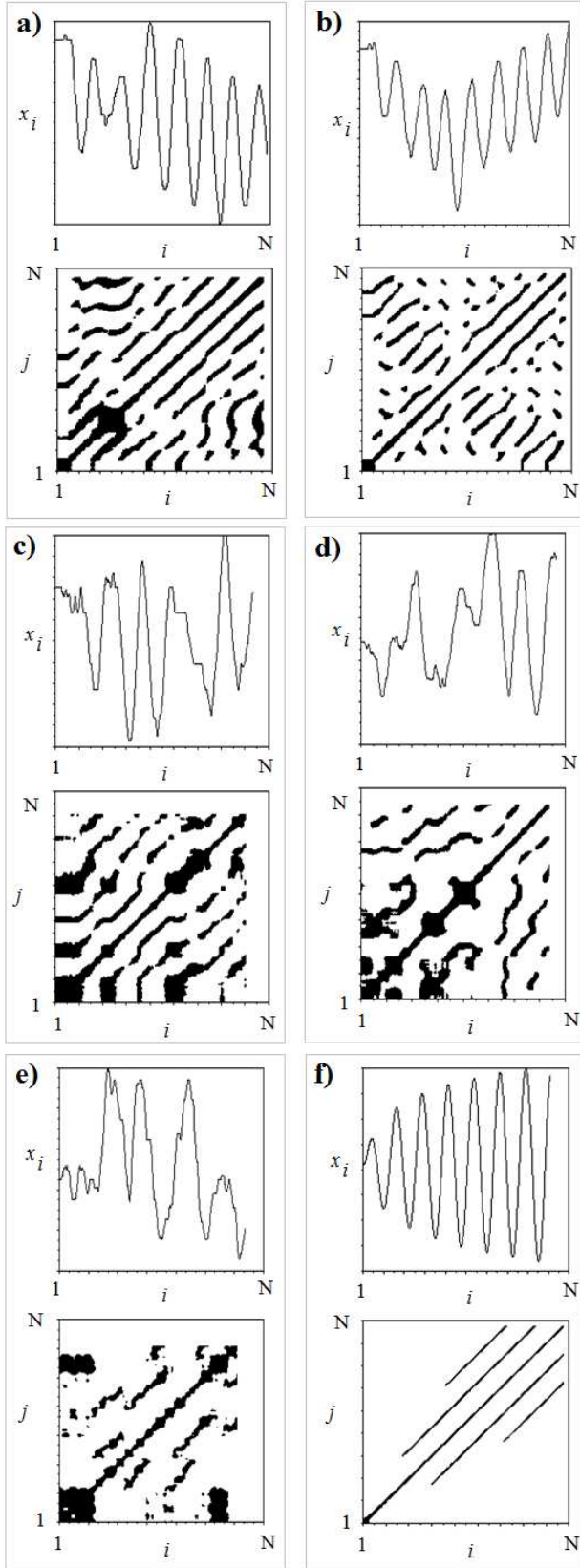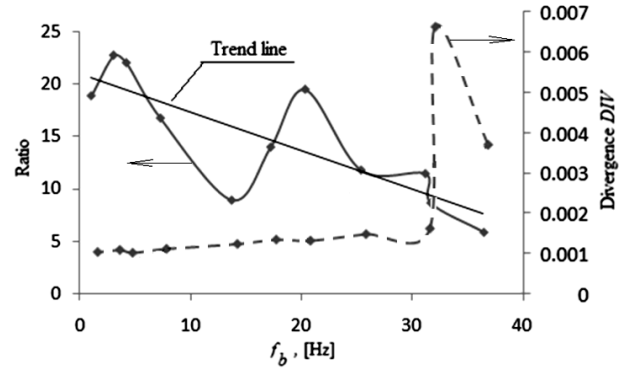
Fig. 11. The inverse of L_{max} (DIV) and the ratio between DET and RR

A diagonal line occurs in the RP when a segment of the trajectory runs parallel to another segment and the distance between trajectories is less than ε. The length of this diagonal line is determined by the duration of this phenomenon. Determinism (DET) is a percentage of recurrence points which form diagonal lines (Marwan et al., 2007). The DET can be treated as a measure of disappearance of spiral shape of the attractor.

Ratio coefficient $RATIO$ is a ratio of DET to RR defined as Marwan et al. (2007):

$$RATIO = N^2 \frac{\sum_{l=l_{min}}^{N} lP(l)}{\left(\sum_{l=1}^{N} lP(l)\right)} \qquad (7)$$

In Fig. 11 the RATIO vs frequency of bubble departure has been show. For frequency of bubble departures less than 30 [Hz] the coefficient $RATIO$ oscillates around the trend line. The oscillations become small for $f_b > 30$ [Hz]. Obtained results indicate that effect of interaction between subsequent bubbles which destroy the spiral motion of the bubble can be detected by coefficient $RATIO$ for frequencies of bubble departure greater than 30 [Hz]. Before these frequency the large fluctuation around the trend line are observed.

The longest diagonal line L_{max} determines the mean vertical length of bubble path where the phenomenon of stability loss does not cause the rapid changes in bubbles path character. The inverse of L_{max} is defined as Marwan et al. (2007):

$$DIV = \frac{1}{L_{max}} \qquad (8)$$

and it is related with the KS entropy of the system, i.e. with the sum of the positive Lyapunov exponents (Marwan et al., 2007). In Fig. 11 it has been shown the function of DIV vs frequency of bubble departure.

The positive Lyapunov exponents is a measure of instability of system trajectory. Obtained results show that bubble paths become more unstable when bubble departure frequency increases. The rapid increase of instability of bubble paths is observed for bubble departure frequency greater than 30 [Hz].

Fig. 10. Recurrence plots for different frequencies of bubble departures f_b. a) $f_b = 0.9$ [Hz], b) $f_b = 4.1$ [Hz], c) $f_b = 13.6$ [Hz], d) $f_b = 17.2$ [Hz], e) $f_b = 31.7$ [Hz], f) Test path

4. CONCLUSIONS

In the paper the paths of bubbles emitted from the nozzle with frequency of bubble departures which ranged from

1 to 36 Hz have been analyzed. The frequency analysis and recurrence plots have been used to determine the strength of interaction between bubbles in the bubble chain.

The wavelet analysis shows that the time of stable oscillatory bubble movement with oscillation frequency about 5 [Hz] decreases together with the increase of bubble departures frequency. Qualitative analysis of this phenomenon prepared with using the Recurrence Plot method has shown that the increase of frequency of bubble departure causes decrease of number of the recurrence points which form diagonal lines. This confirms that periodic character of oscillatory trajectory disappears with the increase of frequency of bubble departure. The length of the longest diagonal line can be used to estimate the stability of bubble trajectory. It has been found that the rapid increase of instability of bubble paths is observed for bubble departure frequency greater than 30 [Hz].

The average length of the vertical lines of RP indicates a time in which a bubble trajectory changes very slowly. This time is equals to ~0.05 s and corresponds to time delay obtained using the minimum mutual information method.

It has been found that the rapid increase of instability of bubble paths is observed for bubble departure frequency greater than 30 [Hz]. In this case the distance between subsequent departing bubbles (*S/D*) becomes close to 1. It causes that the vertical interaction between departing bubbles is enough strong to change the dynamical properties of bubble paths.

REFERENCES

1. **Femat R., Ramirez J. A., Soria A.** (1998), Chaotic flow structure in a vertical bubble column, *Physics Letters A*, 248, 67-79.
2. **Hedengren, K. H.** (1988), Pattern Recognition, *9th International Conference on 14-17 Nov. 1988*, vol. 2, 963 – 965.
3. **Kikuchi R. et al.** (1997), Diagnosis of chaotic dynamics of bubble motion in a bubble column, *Chemical Engng Sc.*, 52, 3741-3745.
4. **Luewisutthichat W., Tsutsumi A., Yoshida K.** (1997), Chaotic hydrodynamics of continuous single-bubble flow system, *Chemical Engng Sc.*, 52, 3685-3691.
5. **Marwan N., Romano M. C., Thiel M., Kurths J.** (2007), Recurrence Plots for the Analysis of Complex Systems, *Physics Reports*, 438 (5-6), 237-329, Recurrence Plots And Cross Recurrence Plots (www.recurrence-plot.tk).
6. **Mosdorf R., Shoji M.** (2003), Chaos in bubbling – nonlinear analysis and modelling, *Chemical Engng Sc.*, 58, 3837-3846.
7. **Mosdorf R., Wyszkowski T.** (2010), *Using the Recurrence Plot in analysis of bubble paths in a bubble column*, CHISA 2010, CD version
8. **Schuster, H. G.** (1993), *Deterministic chaos*, An introduction, PWN, Warsaw (in Polish).
9. **Torrence C., Compo G. P.** (1998), A practical guide to wavelet analysis, *Bull. Am. Meteorolog. Soc.*, 79 (1).
10. **Torrence C., Compo G. P.** (2005), *A Practical Guide to Wavelet Analysis, with Significance and Confidence Testing*, Available from: http://paos.colorado.edu/research/wavelets/.
11. **Vazquez A., Manasseh R., Sánchez R. M., Metcalfe G.** (2008), Experimental comparison between acoustic and pressure signals from a bubbling flow, *Chemical Engineering Science*, 63, 5860-5869.
12. **Zenit R., Magnaudet J.** (2009), Measurements of the streamwise vorticity in the wake of an oscillating bubble, *International Journal of Multiphase Flow*, 35, 195–203.
13. **Zhang L., Shoji M.** (2001), Aperiodic bubble formation from submerged orifice, *Chemical Engng Sc.*, 56, 5371-5381.

INVESTIGATION OF PASSIVE MAGNETIC BEARING WITH HALBACH-ARRAY

Arkadiusz MYSTKOWSKI[*], Leszek AMBROZIAK[*]

[*]Bialystok University of Technology, Faculty of Mechanical Engineering
Wiejska 45 C, 15-351 Bialystok

a.mystkowski@pb.edu.pl, leszek.ambroziak@gmail.com

Abstract: The paper has describes the complete design and investigation processes of permanent magnetic bearing. The passive magnetic bearing (PMB) rotor suspension rig employing no active control components was calculated, designed, constructed and tested. In order to increase the radial passive magnetic bearing stiffness, the Halbach-array configuration was used. The main purpose of the work was developing the nonlinear model of the PMB. Therefore, the magnetic flux circuit of the PMB was analytically calculated by using the Ohm and Kirchhoff methods. The nonlinear effects of the discrete 3D model of the PMB was analyzed using Finite Element Method (FEM). Finally, the very well matched experimental and analytical static characteristics of the passive magnetic suspension were carried out.

1. INTRODUCTION

The nowadays industrial rotor machines are more flexible and often operating with ultra-high speed. Therefore, the suspension systems must to advanced and high reliable. Another problem is connected with power consumptions, the modern suspensions should be low-power systems.

Active magnetic bearings have many disadvantages connected with complicated control hardware, such as expensive digital processors, amplifiers with limited bandwidth, sensitive sensors, and software. Thus, these systems are itself low reliable and have high energy loss index.

Passive magnetic bearings do not require control and measure hardware and advanced software, thereby they have the potential to increase system efficiency and reliability. Another advantage of PMBs is positive stiffness and self-stability. What more, they can operate with larger rotor-stator gaps since the levitation force for active magnetic bearings is inversely proportional to the square of the rotor-stator gap. The disadvantage of PMBs is lack of stiffness control due to e.g. rotor displacements and lower damping than similar size active magnetic bearings.

The beginning of the development of magnetic bearing combined with the first patent of American scientist Jesse Beams from University of Virginia during the Second World War (Beams, 1964). Passive magnetic levitation receiving one degree of freedom by using permanent magnets was achieved and described by Jansen and Di Russo (1996), Ohji et al. (1999) and Fremerey (2000). The use of superconductors in the art of passive magnetic bearings was described by Hull and Turner (2000) and Hull et al. (1994). Several papers were also published on research of the coefficients of stiffness and damping of passive magnetic bearings. Their creators are Satoh (1996), Ohji (1999) as well as previously mentioned Jansen and Di Russo (1996).

This paper concerns the design, implementation, and research studies of the PMB which consists of the permanent magnets based on the Halbach-array configuration. The main objective of this study was to design and execution of the analytical model, experimental tests and model verification of the passive magnetic bearing based on permanent magnets (Fig. 1). For this purpose the PMB test rig was designed and constructed. The experimental characteristics of the magnetic force due to radial rotor displacement were measured in the passive bearing plane and compared with the analytical one.

1.1. Halbach arrays

Using the passive magnetic bearings in certain applications, we need to take into account the occurrence of radial component in the case of axial bearings and axial component in the case of radial bearings. Journal bearings, in addition to passing load forces of the rotor, rotor weight and damping must take into account the existence and impact of this negative component forces. Therefore, in the design of passive bearings Halbach-arrays are introduced. Halbach-array is a special setup and configuration of permanent magnets, so that you can get the concentration of magnetic flux in a specific, desired items, and remove it from less important or unwanted places (Halbach, 1980).
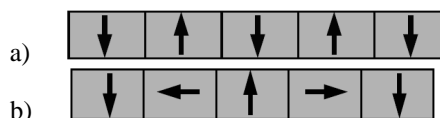

Fig. 1. Sample Halbach-array configurations, a) 180° and b) 90°
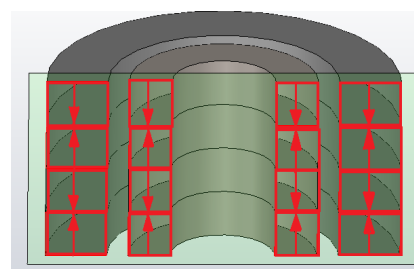

Fig. 2. Cross-section of the PMB
with Halbach-array configuration

Among the Halbach arrays, to guide the magnetic field in the desired way, we can distinguish boards between 180° and 90°. These terms relate to the relationship between the magnetization vectors.

In the construction of the passive radial magnetic bearing 180° Halbach-array was used. This kind of magnetic bearings belongs to the repulsive magnetic bearings. Full configuration of constructed Halbach-array is presented in Fig. 2.

2. DESCRIPTION OF DESIGNED RIG

The examined passive magnetic bearing is composed of four pairs of the Neodymium-iron-boron (NdFeB) magnets rings. These rings are axially magnetized, which means that magnetic poles are placed on the flat circle sides of the magnets (see Fig. 2). The dimensions of the magnets are shown in Tab. 1.

Tab. 1. Magnets dimensions

|	Material	Outer diameter\ D_Z [mm]	Inner diameter D_w [mm]	Thickness g [mm]
Outer ring	NdFeB N38	75	49	10
Inner ring	NdFeB N38	40	22	10

Magnetic parameters of the magnets are grouped in Tab. 2.

Tab. 2. Magnetic parameters of magnets

Parameter	Symbol	Unit	Value	
			MP1	MP2
Material	-	-	N38	N38
Remnant flux density	B_r	[T]	1.25	1.1
Coercivity	H_c	[kA/m]	899	854
Magnetic energy	$(BH)_{max}$	[kJ/m³]	302	243
Temp. of work	T_c	[°C]	120	180
Magnetic flux	$\phi_{e.max}$	[mWb]	4670e-3	4890e-3

The base of the magnetic bearing stator is made of a aluminum alloy PA11 and PA6, which are nonmagnetic materials. Stator consists of five parts, namely: the vertical bracket left and right (Fig. 3 {2}), middle base (Fig. 3, {3}) and the hub mounting magnets (Fig. 3, {1}). Additionally, on the stator is mounted the handle of distance sensors made of aluminum (Fig. 3, {4}).

The rotor shaft was made of constructional steel (Fig. 4, {1}) but the post of inner magnets (Fig. 4, {3}) is made of brass (Fig. 4, {4}). Distance ring (Fig. 4, {7}) are made of brass also and is mounted with a steel nut (Fig. 4, {2}). On the rotor a steel blade to implicate unbalance the rotor is placed (Fig. 4, {6}). To reduce the air gap between inner and outer magnets in magnetic bearing, the sleeve was used made of soft magnetic material (Fig. 4, {5}).
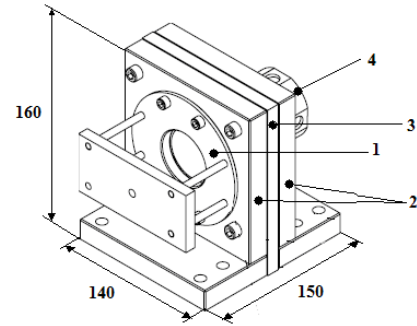
Fig. 3. Stator of the passive magnetic bearing
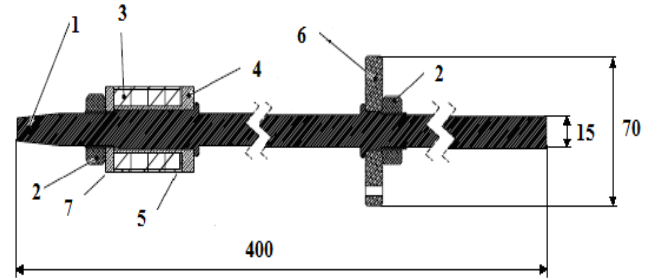
Fig. 4. Cross-section of rotor with passive magnetic bearing

3. SIMULATION RESULTS

To analyze the magnetic bearings and to estimate their radial force distribution, 3D models of the passive magnetic bearing were built. Simulation calculations were made by using the FEM via Comsol Multiphysics ver. 3.5a software. The magnetostatic module of Comsol environment was used to analyze the magnetic field distribution of the passive magnetic bearings with Halbach-array.

3.1. FEM magnets model definition

Analysis of the magnetic field of magnetic bearing is a magnetostatic problem with no current. This problem we can solve using a scalar magnetic potential. In regions with no current, where:

$$\nabla \times H = 0 \tag{1}$$

where: H – magnetic field, ∇ – nabla operator.

We can define the scalar magnetic potential V_m, from the following relation:

$$H = -\nabla V_m \tag{2}$$

It is analogous to the definition of the electric potential for static electric field.

Using the major relation between the magnetic flux density and magnetic field, which is described by:

$$B = \mu_0 (H + M) \tag{3}$$

where: B – magnetic flux density, M – magnetization vector.

Together with equation:

$$\nabla \times B = 0 \tag{4}$$

We can simply derive an equation for V_m,

$$-\nabla(\mu_0 \nabla V_m - \mu_0 M_0) = 0 \qquad (5)$$

Equation (3) supplemented by the following expressions:
− first Maxwell equation for current-less area:

$$\mu_0 rot H = 0 \qquad (6)$$

− or first Maxwell equation for conducive area:

$$rot H = J \qquad (7)$$

where: J – current density,
− magnetic field source-less condition:

$$div B = 0 \qquad (8)$$

These equations are true for stationary magnetic field of the permanent magnet in an environment of soft ferromagnetic. In order to design model of magnetic field of passive magnetic bearing, the above conditions should be applied. The analytical model of magnetic phenomena will be developed by using Comsol Multiphysics, and 3D discrete model of the PMB will be presented.

3.2. Boundary conditions

Along the boundaries far away from the two pairs of magnets (Fig. 5), the magnetic field should be tangential to the boundary as the flow lines should form closed-loops around the modeled magnets. The natural boundary condition is expressed by:

$$n(\mu_0 \nabla V_m - \mu_0 M_0) = n B = 0 \qquad (9)$$

where: n – boundary normal pointing out from the inner magnet rings.
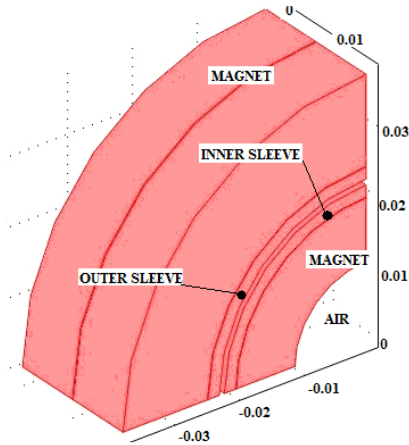
Fig. 5. Finite element model - magnets geometry

Therefore the magnetic field is made tangential to the boundary by a Von Neumann condition on the magnetic potential. Along the symmetry boundary below the magnet, the magnetic field should be tangential, and thus we can apply the same Von Neumann condition there.

Against, the magnetic field should be normal to the symmetry boundary, which is located at the front of the magnet rings cross-plane (see Fig. 5). Thus, the magnetic flow lines have formed of the closed-loops rings around the magnet.

This means that the magnetic field is symmetric with respect to the boundary. This can be achieved by setting the potential to zero along the boundary, and thus making the potential anti-symmetric with respect to the boundary.

3.3. Subdomain settings

The Fig. 5 shows all highlighted subdomains in magnetic bearing finite element model. These are: magnets of stator, magnets of rotor, outer sleeve, inner sleeve and ambient air. In order to get the detailed finite element model of the PMB, the proper parameters need to by find in the right domain of the geometric model.

Selected following settings and parameters of the highlighted domains in the magnetic bearing model are presented in Tab. 3.

Tab. 3. Subdomain settings

Settings	Subdomain 1,2	Subdomain 3	Subdomain4
Description	Rotor Magnet, Stator Magnet	Magnetically Soft Sleeve	Air
Constitutive relation	$B = \mu_0 H + \mu_0 M$	$B = \mu_0 \mu_r H$	$B = \mu_0 \mu_r H$
μ_r	-	6980	1

3.4. FEM calculations

Next, the PMB mesh model is developed. Setting the relevant parameters the mesh model is extremely important to correctly estimate all properties of the magnetic bearings and determine the maximum radial force of the bearing. Mesh was concentrated in the most important places of the magnetic bearing model, which are air gaps between pairs of stator and rotor magnets. As the most optimal mesh element tetrahedron was used. The maximum size of the mesh element was defined as 5-7% of the smallest dimension of the geometric domain. Maximum element size scaling factor was chosen as 0.5. Mesh curvature factor was set as 0.25. In the magnetic bearing air gaps, inner and outer sleeves, the gap element was used. Gap element is the special kind of mesh element. It is particularly important whenever a big impact on the field distribution have air gaps in model. Gap element reduces the growth of algebraic matrix equations in the calculations. To reduce the size of the field surrounding the magnet rings model, the infinite element was used, which improves the results of calculations by a few percent and reduced the number of elements in finite element model.

The magnetostatic solver was used to calculate the radial force and predict the distribution of magnetic field in the PMB with Halbach-array. The 3D magnetic bearing mesh model is illustrated in Fig. 6. The model have 1282681 elements. To compute magnetic forces and torques in the AC/DC Comsol Module, four methods are available. The most general method is to use the Maxwell Stress tensor described below. Force and torque calculations using Maxwell's stress tensor are available in the application modes for electrostatics, magnetostatics, and quasi-statics. In case of the magnetostatics and quasi-statics the Maxwell Stress tensor

is given by:

$$n_1 T_2 = -\frac{1}{2} n_1 (H \cdot B + n_1 \cdot H) B^T \qquad (10)$$

where: n_1 – outward normal from the object.

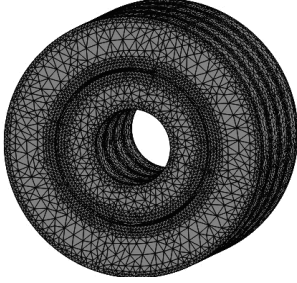The Maxwell stress tensor was integrated over the inner magnets surface.

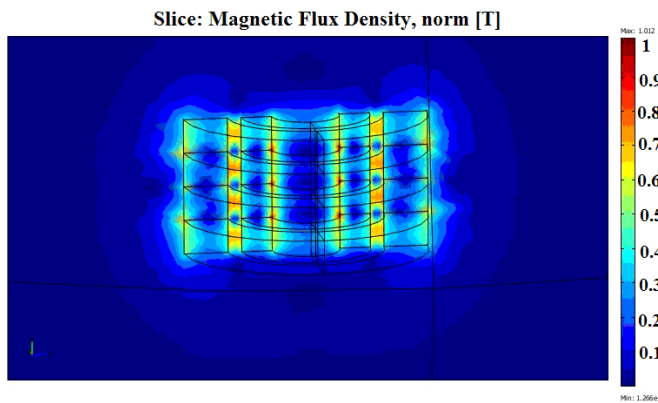**Fig. 6.** 3D mesh model of passive magnetic bearing

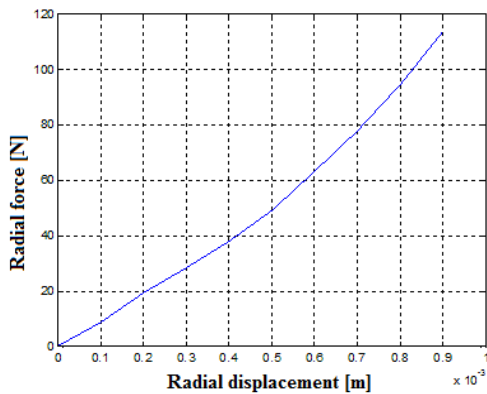**Fig. 7.** Magnetic flux density in cross section of magnetic bearing

Fig. 8. Displacement stiffness characteristic of the PMB

Three-dimensional model of magnetic bearings was used to compute the magnetic potential, magnetic flux density and magnetic energy in the air gap.

In Fig. 7 we could observed places in air gap where the field reaches the highest values and where it falls significantly. This is caused by build Halbach-array. The gaps in magnetic field observe in Fig. 7 are typical for this kind of Halbach-arrays.

Depending on the movement of the rotor in the magnetic bearing plane, the air gap is changed, and therefore the repulsive force of the magnets changed too. For the different posi-

tions of the rotor in the bearing plane, the power calculations were made based on a reduced finite element model of the PMB. The results obtained are summarized and presented in the form of static characteristics (Fig. 8).

4. EXPERIMENTAL TESTS

The experimental study have allowed to verify the finite element model of the PMB and to analyze the design and assessment of its fairness and accuracy of design assumptions bench. The lab test rig is presented in Fig. 9. The lab stand consists of rotor with electrical drive and elastic clutch, the rotor is supported by one ball bearing and passive magnetic bearing located at the end of the rotor. In order to measure the magnetic radial force, the tensometer force sensor was assembled. The radial displacement of the rotor was measured in two directions *x-y* by using inductive sensors. The total weight of the rotor is 1.07 kg, and total length of 0.4 m. The nominal radial air gap is equal to 0.001 m. The actual physical model has become a reference for early design and simulation tests.
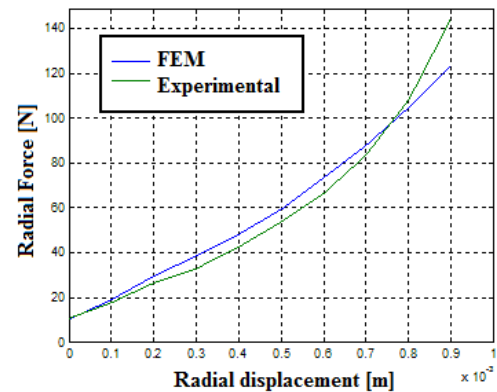

Fig. 9. Test rig

Fig. 10. Measured and calculated PMB stiffness

The first stage of the experimental tests were static stiffness measurements with no rotating rotor. As a result, the values of the magnetic repulsive forces in the radial direction due to change of the air gap were determined. Depending on the rotor load, measured by electronic scales, the value of its shipments and dial indicator has been observed using inductive sensor.

Next, the measured radial magnetic bearing force due to rotor displacements in the range of the air gap was compared with the FEM calculations (see Fig. 10).

Fig. 10 shows the rotor displacement as a function of radial load for the experimental data and finite element model. The slopes (stiffness) of these curves match quite well and equals $1.28 \cdot 10^5$ N/m. The finite element model of the PMB is sufficiently consistent with the laboratory model. Thus, the finite element method, with appropriate choice of parameters, a careful analysis and accurate modeling, may be used with quite good results in the design of passive bearings and to assess the pre-load magnetic bearing.

The axial stiffness of the passive magnetic bearing is more stronger than in radial direction and is not presented in this paper.

5. SUMMARY

A completely passive magnetic bearing rig was designed, constructed, and tested in this work. The experimental and simulation results are well matched, thus the finite element methods can be used to accurately design the size and number of the magnets for the radial support of the bearings.

The implementation of the passive magnetic bearing requires a careful analysis of the magnetic field generated by permanent magnets and assesses their material aspects. Obtained and desired distribution of magnetic field strength determines the values of the bearings, radial and axial component. The introduction of the Halbach-arrays allows the adequate orientation of the magnetic field in the placenta, and to reduce the negative impact of the active component forces. The use of Halbach-arrays and a thorough assessment and analysis of magnetic bearings, allow to develop and to implement the high performance passive magnetic bearings. Submission of the magnets in different directions of polarization is a very difficult task and unfortunately expensive too, thus always some assumption should be taken into account.

REFERENCES

1. **Asami K.. Chiba A., Rahman M. A., Hoshino T. A. H. T., Nakajima A. A. N. A**. (2005),Stiffness analysis of a magnetically suspended bearingless motor with permanent magnet passive positioning, *IEEE Transactions on Magnetics*, Vol. 41, 3820-3822.
2. **Beams J.** (1964), Magnetic Bearings, Paper 810A, *Automotive Engineering Conference*, Detroit, Michigan, USA, SAE.
3. **Bolkowski S., Stabrowski M., Skoczylas J., Sroka J., Sikora J., Wincenciak S.** (1993), *Komputerowe metody analizy pola elektromagnetycznego*, WNT, Warszawa.
4. **Burcan J.** (1996), *Łożyska wspomagane polem magnetycznym*, WNT, Warszawa.
5. **Delmare J., Rulliere E., Yonnet J. P.** (1992), Classification and Synthesis of Permanent Magnet Bearing Configurations, *IEEE Transactions on Magnetics*, Vol. 31, No. 6, 4190-4192.
6. **Earnshaw S.** (1848), On the Nature of the Molecular Forces which regulate the Constitution of the Luminiferous Ether, *Transactions of the Cambridge Philosophical Society*, Vol. VII, Part I, 97-112, London.
7. **Filatov A., Maslen E. H.** (2002), A method of non-contact suspension of rotating bodies using electromagnetic forces, *Journal of Applied Physics*, Vol. 91, No 4.
8. **Fremerey J. K.** (1999), *Magnetlager*, DE199 44 863 A1.
9. **Fremerey, J. K.** (2000), A 500-Wh Power Flywheel on Permanent Magnet Bearings, *Fifth International Symposium on Magnetic Suspension Technology*, 287–295.
10. **Geim A. K., Simon M. D., Boamfa M. I., Heflinger L. O.** (1999), Magnetic Levitation at Your Fingertips, *Nature*, Vol. 400, 232–324.
11. **Gosiewski Z., Falkowski K.** (2003), *Wielofunkcyjne łożyska magnetyczne*, Biblioteka Naukowa Instytutu Lotnictwa, Warszawa.
12. **Gosiewski Z., Osiecki W., Panasiuk M.** (2007), *Elementy mechatroniki*, Wydawnictwa WAT, Warszawa.
13. **Halbach K.** (1980), Design of permanent multipole magnets with oriented rare earth cobalt material, *Nucl. Instr. Meth.*, Vol. 169, 1-10.
14. **Hull J. R., Mulcahy T. M., Uherka K. L., Erck R. A., Abboud R. G.** (1994), Flywheel Energy Storage Using Superconducting Magnetic Bearings, *Appl. Supercond.*, Vol. 2, 449–455.
15. **Hull J. R., Turner L. R.** (2000), Magnetomechanics of Internal-Dipole, Halbach-Array Motor/Generators, *IEEE Transactions on Magnetics*, Vol. 36, No. 4, 2004–2011.
16. **Jansen R., DiRusso E.** (1996), *Passive Magnetic Bearing with Ferrofluid Stabilization*, NASA TM–107154.
17. **Ohji T., Mukhopadhyay S. C., Iwahara and Yamada S.** (1999), Permanent Magnet Bearings for Horizontal- and Vertical-Shaft Machines: A Comparative Study, *Journal of Applied Physics*, Vol. 31, 8, 4648–4650.
18. **Post R. F., Ryutov D. D.** (1997), *Ambient-Temperature Passive Magnetic Bearings: Theory and Design Equations*, LLNL Pub. #232382.
19. **Siebert M, Ebihara B., Jansen R**. (2002), *A Passive Magnetic Bearing Flywheel*, NASA/TM—2002-211159, IECEC2001 –AT–89.
20. **Yonnet J. P.** (1981), Permanent Magnet Bearings and Couplings, *IEEE Transactions on Magnetics*, Vol. Mag-17, No. 1, 1169-1173.

μ-SYNTHESIS CONTROL OF FLEXIBLE MODES OF AMB ROTOR

Arkadiusz MYSTKOWSKI[*]

[*]Bialystok University of Technology, Wiejska 45 C, 15-351 Bialystok, Poland

a.mystkowski@pb.edu.pl

Abstract: In the paper the optimal robust vibration control of flexible rotor supported by the active magnetic bearings (AMBs) is investigated. The purpose of the control system is stabilization of the high speed rotor and effective control of the rotor vibration due to noncollocation, gyroscopic effects and model uncertainties. The noncollocation effect is considered and frequency modal analysis of the noncollocated AMBs system with gyroscopic effects is presented. The μ-Synthesis control is applied to stabilize the rigid and flexible critical frequency modes of the rotor, with emphasis structural and parametric uncertainty. The input and output signals in AMBs system are limited by the weighting functions. The singular value analysis is used to obtain the robust performances of the closed-loop system. The stable operation and good stiffness of the high speed rotor supported magnetically is reached. The dynamical behaviour of the AMBs rotor is evaluated in the range up to 21 000 rpm. The experimental tests show the effectiveness of the robust control system as well as good vibrations reduction and robustness of the designed controllers.

1. INTRODUCTION

The active magnetic bearings (AMBs) are used to support a rotor without mechanical contact and to vibrations control (Schweitzer et al., 1994, 2009). The AMB uses magnetic forces to levitate the rotor between two opposing electromagnetic poles. In the AMBs systems the rotor is inherently unstable. Thus, the AMBs application must be stabilized with an active feedback control system. The rotor vibrations control and vibrations compensation is a very important problem in rotating machines operating with high rotational speeds (Stephens, 1995; Knospe, 2007; Knospe et al., 1995; Mystkowski and Gosiewski, 2008b).

The dynamics of the AMBs rotor system is influenced by external disturbances (steady sinusoidal loads), nonlinearities, uncertainties and signal limits (Mystkowski and Gosiewski, 2006, 2008a, 2009). Many active vibrations control methods are used in the rotor-bearings applications, where some can be found in papers Burrows at al. (1983, 1989) and Genta (2005). The robust optimal control methods based on the μ-Synthesis, H_∞ or H_2 algorithms are other modern/advanced solutions (Mystkowski, 2007b; Sawicki, 2008). The μ-Synthesis control permits to design the multivariable optimal robust controller for complex linear systems with any type of the uncertainties in their structure. There are many practical applications of the μ-Synthesis control in the high speed rotor AMBs systems (Knospe at al., 1997; Fittro and Knospe, 1999; Fittro et al., 2003; Sawicki and Maslen, 2006). The μ-Synthesis control methodology covers the practical issues like modelling of the uncertainties, selection of the optimal weighting functions and signal limits. The μ-controller synthesized for the augmented plant model must meet the analysis objectives presented by the maximal singular value. Furthermore, in this method the optimized performance index has a good connection with the real AMBs system. The goal of this

method is to design the stable controller which is robust to the plant dynamics variations. The μ-Synthesis control procedure is natural augmentation of the H_∞ control theory with the analysis of the structural singular value (Zhou et al., 1996). Therefore, in the case of μ-Synthesis control, the uncertainties are more simple to consider than in the H_∞ control. What more, the nonlinearities of the control plant can be also considered. Generally, in the robust control theory, if there are no limits, the greater robust control performances can be obtained by using greater control effort. However, the best control performances can be achieved with infinite controller gain.

The AMBs systems usually have noncollocated sensors and actuators. The noncollocation effect produces lack of interlacing of zeros and poles in the control plant model and causes a real stability problem (Preumont, 2002). Generally, the noncollocation is important in high speed rotor machines, where all the rigid and flexible frequency modes must be stable controlled (Spector and Flashner, 1989, 1990). Usually, the noncollocation provides limits in the rotor flexible modes control because of mode shape measurements faults. What more, the introduction of the interlacing repair controller is difficult especially in multi-input/multi-output (MIMO) rotor-bearings systems (Genta and Carabelli, 2000).

In the paper, the μ-Synthesis control method is applied to vibrations control of the high speed AMBs flexible rotor, with emphasis noncollocation, gyroscopic effects and uncertainty. The flexible rotor supported by the AMBs is analyzed using the finite element method (FEM). The mass, stiffness and damping matrices of the flexible free-free rotor are computed and analyzed using MATLAB software. The model of the AMBs system components, which includes the magnetic bearings, rotor, power amplifiers and sensors, is presented. The influence of the noncollocated sensors and actuators on the rotor dynamics stability is evaluated. The gyroscopic effects in AMBs rotor is con-

sidered and presented via Campbell diagram. The robust μ-controller is designed due to uncertainty in the AMBs rotor model. The uncertainty is considered as variability of the electromagnetic coils inductance and rotor mode shapes perturbations. The robust control performances are verified during the experimental tests. The experimental test rig with the AMBs rotor and digital power amplifiers was designed and built. The stable high speed rotor operation and good robust performances of the closed-loop control system was reached. Finally, the success of the robust control is demonstrated through results of computer simulations and experimental results.

2. MODEL OF AMB FLEXIBLE ROTOR SYSTEM

To measure the rotor displacement in two radial directions, the high precision eddy-current sensors are used. The rotor displacement sensors have a high resolution and wide bandwidth up to 10kHz, which is much over that rotor maximal angular speed. Therefore, the model of the sensors is assumed as a simple proportional gain. The rotor displacement signals are filtered by the anti-aliasing filters implemented in digital signal processor (dSpace board) in order to filter out signal components above *Nyquist* frequency of 4 kHz. The important consequence of poor anti-aliasing filtering is e.g. when the magnetic bearings react to the noise mainly in the low frequency range.

The AMBs system are operated with the current control, where at each sampling step, the digital signal processor (DSP) calculates the magnitude of the control current that

is applied to the electromagnetic coils of the AMBs. These currents are generated by the digital power amplifiers based on the pulse-width-modulation (PWM). The ten channels of digital power amplifiers are used, where each of the amplifiers has an internal current control loop with a simple proportional gain controller. Thus, the coil current is measured and subtracted from the set current, which is proportional to a voltage signal of the DSP. The demanded set current is created by means of switching among a positive or negative voltage (180 V). The switching frequency is equal to 18 kHz. Thus, the true current oscillates around the switching frequency. For a good dynamics performances of the operating AMBs the currents should be as smooth as possible. That is why, the amplifier output low-pass filters are applied. The AMBs coils are modelled as the series interconnection of a copper resistance R and an inductance L. The rate of the current change should be fast enough to follow the current command. However, the amplitude and frequency ranges are limited by the R–L curve of the power amplifier. The model of the electromagnetic coil includes first order low-pass filter with cut-off frequency $\omega_c=R/L$ (700 Hz) and gain of 1 A/V. The maximal value of the output current i_{max} is limited to 10 A. In the low frequency range up to the crossover frequency ω_k, the output current is limited by the i_{max}. Beyond the frequency ω_k, the output current is limited by the coil's low-pass characteristic denoted by the R-L curve. To simplify the AMBs open-loop model the dynamics of the DSP was neglected and only the gains of A/C and D/C converters are considered.
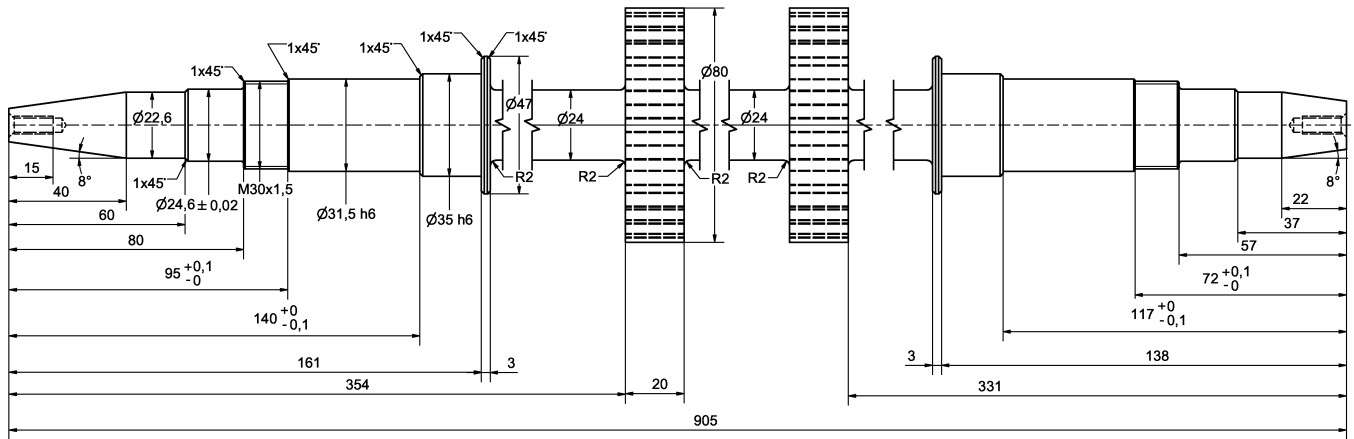

Fig. 1. Flexible rotor

The complex flexible rotor is modelled using the finite element method. Thus, the rotor was partitioned into 26 discrete elements of the simple geometry based on the Timoshenko model (Nelson, 1980). Between neighbouring elements the connecting nodes are introduced. Each of the rotor nodes has 5 degrees of freedom (DoF) and the rotor has 112 DoF. The motion equation of the free-free rotor (without external forces) is given by:

$$M\ddot{q}+(D+\Omega G)\dot{q}+Kq=0 \qquad (1)$$

where: M – symmetrical, positive definite mass matrix, D – symmetrical damping matrix, G – skew-symmetric gyroscopic matrix, K – symmetrical, positive semi-definite stiffness matrix, Ω – rotational speed, q – displacement vector.

The model of the free-free rotor is transformed to the state-space representation:

$$\dot{x}=Ax+Bu$$
$$y=Cx+Du \qquad (2)$$

where:

$$A = \begin{bmatrix} 0^{q\times q} & I^{q\times q} \\ -M^{-1}K & -M^{-1}(D+\Omega G) \end{bmatrix}, B = \begin{bmatrix} 0^{q\times 2n} \\ M^{-1}F \end{bmatrix}, \quad .$$

$$C = \begin{bmatrix} S & 0^{2l\times q} \end{bmatrix}, D = \begin{bmatrix} 0^{2l\times 2n} \end{bmatrix}.$$

The model of the external forces F acting on the rotor and model of displacement sensors S are given by matrices:

$$F = \begin{bmatrix} F_x & 0 \\ 0 & F_y \end{bmatrix}, S = \begin{bmatrix} S_x & 0 \\ 0 & S_y \end{bmatrix}. \tag{3}$$

The flexible rotor supported in the AMBs is modelled by combining the model of the flexible rotor with the model of the AMBs (Losch, 2002). Thus, the model of the flexible rotor in AMBs can by described as follows:

$$M\ddot{q} + (D+\Omega G)\dot{q} + Kq = K_s q + K_i i \tag{4}$$

where: K_s, K_i – matrices of the AMBs displacement and current stiffness coefficients.

After transformed to modal coordinates that yields:

$$M_r\ddot{q}_r + (D_r + \Omega G_r)\dot{q} + (K_r - K_{sr})q = K_{ir}i \tag{5}$$

The obtained stiffness matrix $K_r–K_{sr}$ is not exactly diagonal, but the diagonal elements are significantly larger than others elements. The total rotor mass is 6 kg and total length is 0.905 m. The rotor dimensions are presented in Fig. 1.
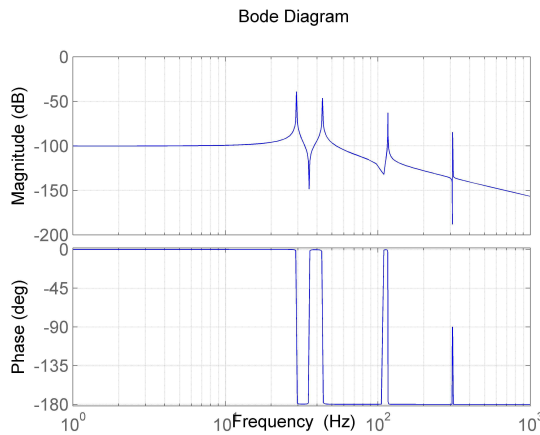
3. MODAL ANALYSIS OF AMBs GYROSCOPIC FLEXIBLE ROTOR

Fig. 2. Flexible rotor with AMBs, for Ω=0 rpm

The flexible rotor supported by the AMBs is analyzed using FEM such that rigid and flexible modes are analyzed. For the simulations and modal investigations the following magnetic bearings nominal parameters are considered: bias current i_0=2 A, nominal air gap x_0=0.0004 m, current stiffness k_i=25 A/m and displacement stiffness k_s= 97801 N/m. The modal rotor damping is chosen at 0.5% for all flexible modes. The flexible rotor model is modally reduced by using Balanced Modal Truncation Method, and only first 4 rotor modes are considered (The MathWorks, 2004).

The 5th mode is out of operating range and has no influence. The Bode plot of the modally reduced AMBs flexible rotor is presented in Fig. 2. The two rigid modes are located at 30Hz and 43Hz, the first flexible mode is placed at 116Hz.

In case of a rotating rotor (when, Ω>0), the motion in the two planes are coupled by the gyroscopic term ΩG. Thus, the gyroscopic effect causes the flexible rotor poles to move with increasing rotational frequency. The Bode plot of the AMBs flexible rotor for rotational speed Ω=300 Hz is presented in Fig. 3. The gyroscopic effect is clearly appeared in Fig. 3 and it did not appear in Fig. 2.
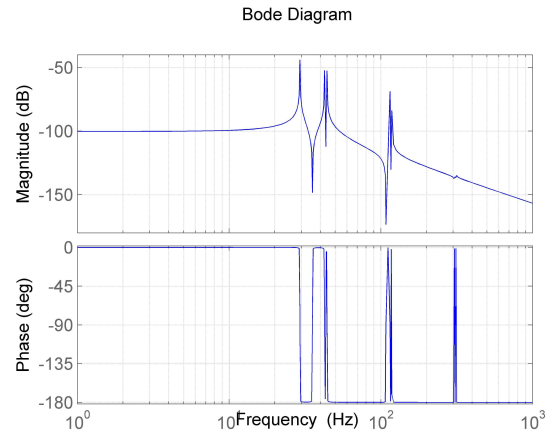

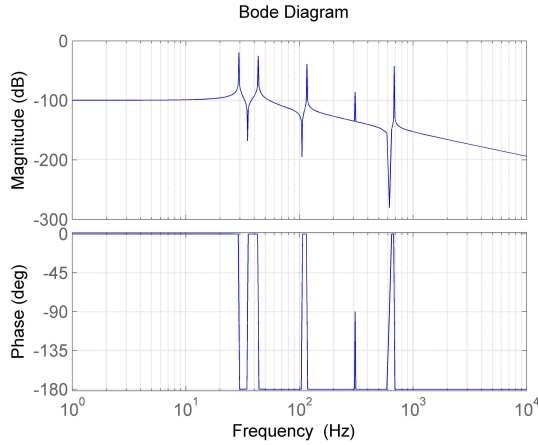**Fig. 3.** Flexible rotor with AMBs, for Ω=18 000 rpm

4. NONCOLLOCATINON ANALYSIS OF AMBs

The noncollocation of eddy-current displacement sensors and magnetic actuators of the AMBs system is considered. The noncollocation effect which produces no interlaced zeros and poles of the AMBs system is a real stability problem. When a system is collocated (sensors and actuators act at the same points along the shaft), the poles and zeros are interlaced and phase is between 0 and -180° (Fig. 4). For current example, the distance between sensors and magnetic actuators is equal to 0.035 m. Thus, AMBs system is noncollocated (Fig. 5). Here, we can notice that the poles of the AMBs model are independent of the sensor locations while the zeros are strongly sensitive to sensor locations. The poles and zeros are no longer interlaced in noncollocated case.

There is a lack of interlacing of the 5th flexible mode (Fig. 5). They can be explained that poles no stay in the left half plane with frequency (root locus analysis) but must travel into right half plane. The noncollocated system is unstable, if the rotor mode shape node leads between sensor and actuator points, and the system is nonminimum phase. In presented example, for small no collocation, which appears above high frequency, the system is still stable in considered AMBs rotor frequency operation (phase is between 0 and –180°, Fig. 5).

The interlacing repair in single-input/single-output (SISO) systems can be simply improved by adding an extra complex pair of zeros. In case of AMBs rotor system, the model is always MIMO with cross couplings between control axes. Therefore, the interlacing repair is more compli-

cated in MIMO systems. In the paper the noncollocation effect appears at high frequency and is considered as the uncertainty model of the rotor mode shapes perturbations in the μ-Synthesis control design.
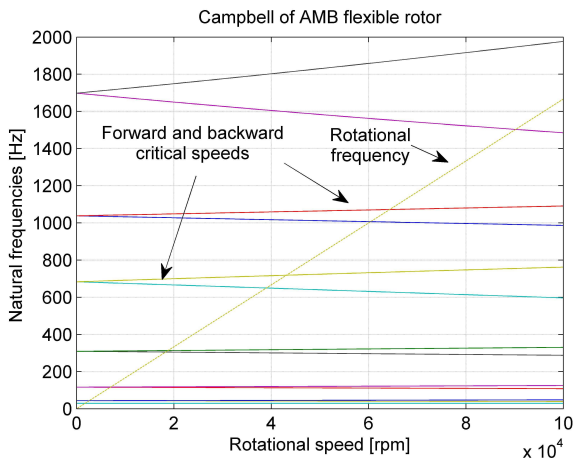

Fig. 4. Flexible rotor with AMBs for collocated sensors and actuators
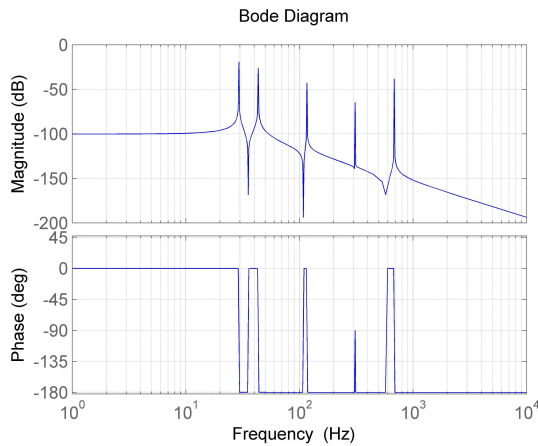
Fig. 5. Flexible rotor with AMBs for sensor located 0.035m from the magnetic actuator

5. CRITICAL SPEED ANALYSIS

Fig. 6. Campbell diagram of the flexible rotor with AMBs for Ω from 0 to 100 000 rpm

The rotor modes with increasing frequencies expose a rotation in the same direction as the rotor are called forward modes (*nutations*). The modes with decreasing frequencies rotate in the opposite direction are called backward modes (*precessions*). Fig. 6 shows the splitting of the flexible eigenfrequencies with the rotational speed from 0 to 100 000 rpm. The dashed line in Fig. 6 corresponds to rotational frequency, while the solid lines correspond to backward and forward flexible mode frequencies. The crossing of flexible modes and rotational frequency called critical speeds are sensitive points of AMBs rotor application. The critical speeds have to be stable controlled during any change of the rotor speed.

6. THE μ-CONTROLLER DESIGN

Based on the equation (5) the pole-zero distribution of the AMBs rotor open-loop model is shown in Fig. 7. Due to symmetry of the system, each pole occurs twice, once for each plane. The flexible poles are very weakly damped (damping about 0.5%). The design process of stabilizing controllers which brings all poles to the left half plane is quite difficult. With increasing the controller gain, the poles first move to the left plane, but if the gain is further increased, they split and follow the positive and negative imaginary axis. Thus, the controller with added damping should be applied. In fact, finding process of the controller that stabilizes the all rigid modes of the flexible rotor without destabilizing the weakly damped flexible modes is difficult and complicated task.
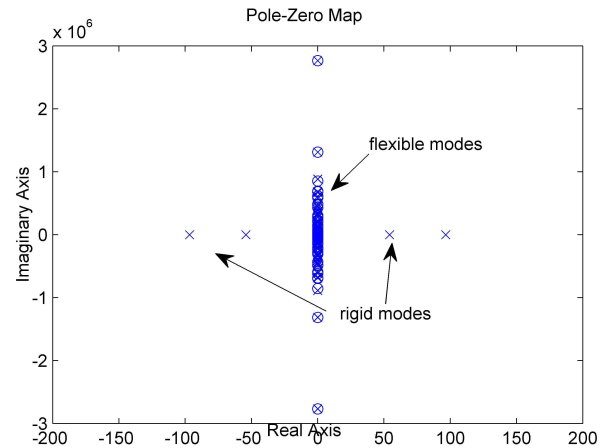

Fig. 7. Flexible rotor with AMBs (open-loop model)

In the μ-Synthesis control, the cost factor is a minimal value of the norm $\|T\|_\infty$, where T is a closed-loop transfer function. The μ-Synthesis algorithm bases on the D-K iteration procedure is natural augmentation of the H_∞ control (Zhou et al., 1996). After performed the singular value analysis, the μ-controller should satisfied the following condition in frequency domain (Zhou et al., 1996):

$$\sup_{\omega \in \mathbb{R}} \overline{\sigma}\left(T(j\omega)\right) \leq 1 \qquad (6)$$

where: $\overline{\sigma}$ - maximal singular value.

Fig. 8 shows structure of μ-Synthesis closed-loop system.
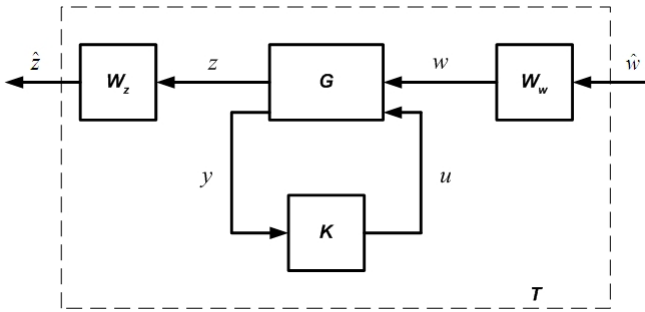
Fig. 8. μ-Synthesis system, where: G – augmented model of the plant, K – robust controller, W_w – weight of input signals, W_z – weight of output signals, z – any measured signals, w – any disturbances (loads), y – output signal, u – control signal, index {^} means weighted signal

The robust controller is designed for augmented control plant. In this case, the augmented plant includes nominal models of: rotor, magnetic bearings, power amplifiers, sensors, DSP and also models of uncertainties and weighting functions.

The weighting functions are putted on the input and output signals like error signal, control signal and rotor displacement signal (see Fig. 9). Thus, the signals of the AMBs rotor system are scaled and the performances of the real control loop are shaped by the weighting functions (Mystkowski, 2007a). The weighting functions enable us to consider signal limits, unbalance forces and external disturbances. These functions strongly influence on the performances and robustness of the system. In robust control theory, proper chosen weighting functions must pass the following conditions (Zhou et al., 1996):

$$\begin{Vmatrix} W_1(s)S(s) \\ W_2(s)R(s) \\ W_3(s)T(s) \end{Vmatrix}_{\infty} \leq 1 \qquad (7)$$

where: S, R, T are sensitivity, control and complementary sensitivity functions.

In current example, amplitude of the weighting function W_3 putted on output signal (rotor displacements) was chosen 0.1, because the rotor displacements should not exceed 10% of the nominal air gap (according to the vibration level at normal exploatation defined by ISO 14839-2 norm). The amplitude and bandwidth of the weighting function W_2 putted on the control signal should correspond to maximal current of the power amplifier (10 A) and maximal bandwidth (700 Hz). The weighting function W_2 is designed based on the R_0 control function. The proper design of the weighting function W_1 is the most important because of clear-out of steady state error, overshoot and settling time, which strongly influence on the dynamic of the AMBs closed-loop system. The W_1 weighting function are designed based on the S_0 sensitivity function. Final configu-

ration of the AMBs system with weighting functions is presented in Fig. 9.
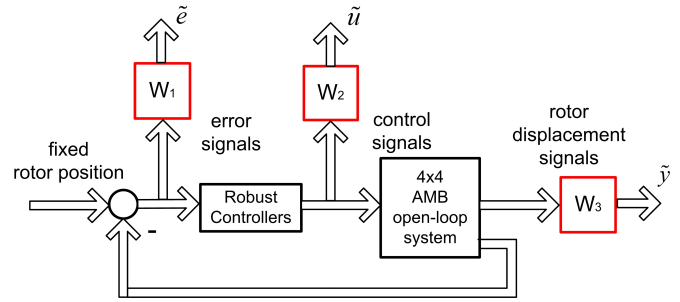
Fig. 9. AMBs weighted model

The magnetic bearing model is itself uncertain (Mystkowski and Gosiewski, 2009). The main sources of the uncertainty and nonlinearity are electromagnetic coils. The uncertainty of the AMBs system is modelled as structural uncertainty and parametric uncertainty (Knospe et al., 1996). The structural uncertainty is described by unknown norm-bounded perturbations, denoted here by Δ. This perturbation acts on the nominal model G_N via linear fractional transformation (LFT) and is represented as feedback gains connected to the control plant anywhere inside. In the rotor model, the uncertainty is connected mainly with FE nodes and can be considered as in hierarchical systems (Miatliuk et al., 2009). In this case the uncertainty was modelled as multiplicative and uncertain augmented model is given by:

$$G_R = G_N \left(1 + W_m \Delta_m\right) \qquad (8)$$

where: G_N – is a nominal model, Δ_m – perturbation satisfying $\|\Delta\|_\infty < 1$, W_m – is a stable weighting function putted on the multiplicative uncertainty.

The weighting function W_m is given by:

$$W_m(s) = 0.1 \frac{1/270s + 1}{1/728s + 1} \qquad (9)$$

At low frequency, below 270 rad/s, AMBs rotor model variation can vary up to 10% from its nominal value. After 270 rad/s the uncertainty (percentage variation) starts to increase and reaches 140% at about 728 rad/s. The frequencies 270 rad/s and 728 rad/s are the values of 2nd rigid and 1st flexible modes of the AMBs system. Also some parameters of the AMBs system can vary from nominal values during operation. The uncertain parameters are current stiffness k_i and displacement stiffness k_s, were the uncertainty is presented as perturbations of $\pm 5\%$. Also, the actuator gain uncertainty is modelled as perturbations of $\pm 1\%$. If robust controller is designed for rotational speed equal zero, there are no guarantee that the system will be stable for other values of rotational speed. The nominal value of the rotational speed Ω is equal to 10 000 rpm, with uncertainty of $\pm 100\%$. The uncertain model of the AMBs system with external signals is presented in Fig. 10.

The μ-controller was computed using function provided by the Robust Control Toolbox of MATLAB called *dksyn* (The MathWorks, 2004). Fig. 11 shows the Bode plot of designed μ-controllers computed for the AMBs system with uncertainties and weighting functions, one of them is optimized for the AMBs rotor vibrations compensation.

The optimized μ-controller was computed for the proper selected weighting functions. The magnitude of the optimized μ-controller is minimalized due to maximal value of the power amplifier current. Thus, the real controller output is not saturated and good control performances are achived.
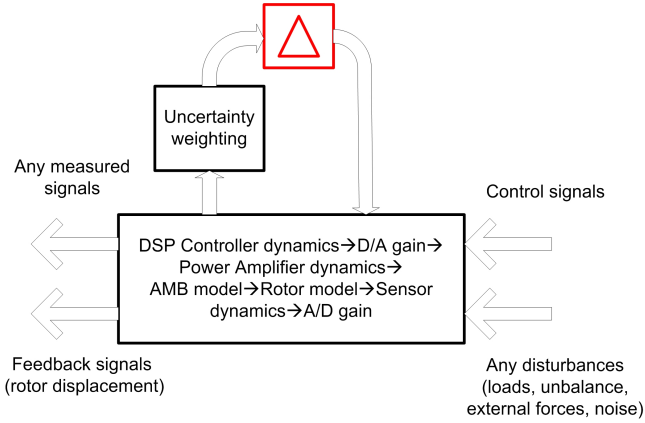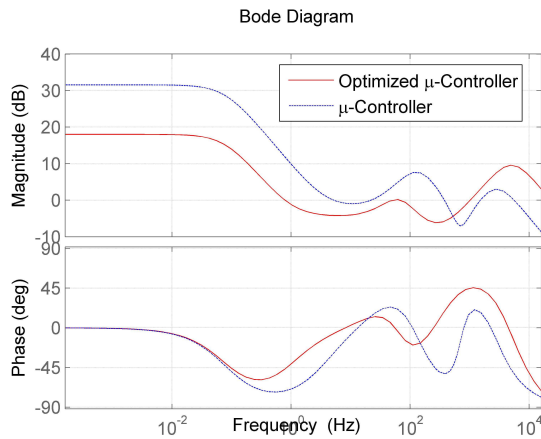

Fig. 10. Complex AMBs system

Fig. 11. Dynamics of μ-controllers

7. EXPERIMENTAL RESULTS

The laboratory stand with the high speed AMBs rotor and digital power amplifiers was designed and built during realization of the ordered research project No PBZ-KBN-109/T-10/2004 financed by the Polish Ministry of Science and Higher Education. The rotor is supported by two radial active heteropolar magnetic bearings. Each of the magnetic bearings has 8 electromagnets connected in 4 pairs in series configuration. Thus, each of the magnetic bearings demands two channels of power amplifiers. The four feedback loops are used to control the radial rotor displacements in the air gap of the radial magnetic bearings. The rotor is driven by electric motor by flexible coupling, and axial vibrations are no controlled.

The four μ-controllers are used to control the rotor motion in two radial directions for two magnetic bearing planes. Thus, the four independent feedback loops with μ-controllers are applied and experimentally verified. Each of the real feedback loops in the AMBs rotor application

includes: rotor, heteropolar magnetic bearings, digital power amplifiers (PWM), sensors and DSP with A/C and D/C converters. The control algorithm is implemented as a discrete time state-space model to the DSP by using real-time interface (RTI) and real-time workshop (RTW) provided by the MATLAB. Since the μ-controller cannot levitate the rotor alone, the program first brings the rotor into support under a low performance PID control algorithm. After that, the program switches to μ-Synthesis control algorithm. Both, the μ-Synthesis and PID control algorithms are implemented in DSP with the sampling rate of 10 kHz. The sampling rate is as high as the discrete-time controllers obtained by a bilinear approximation method good correspond to the continuous-time original system. In experimental tests the disturbances as mass unbalance, gravity loads and sensor noise are considered. The aerodynamic loads and the nonlinear phenomena like eddy-currents loses, hysteresis are neglected. Tests are performed for the rotor angular speed from 0 to 21 000 rpm. The experimental set-up is presented in Fig. 12. The orbit plot of the rotor operation at 21 000 rpm is presented in Fig. 13, where because of the following rotor modes the trajectory of the geometrical centre of rotor has elliptic shape. The controlled vibrations level for the same bearings is presented in Fig. 14.
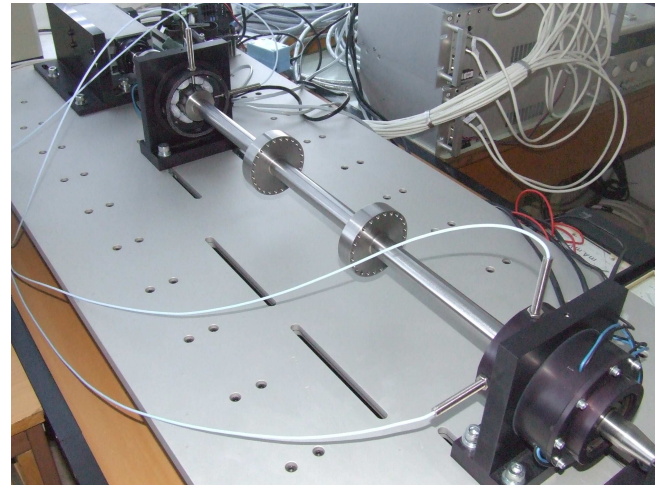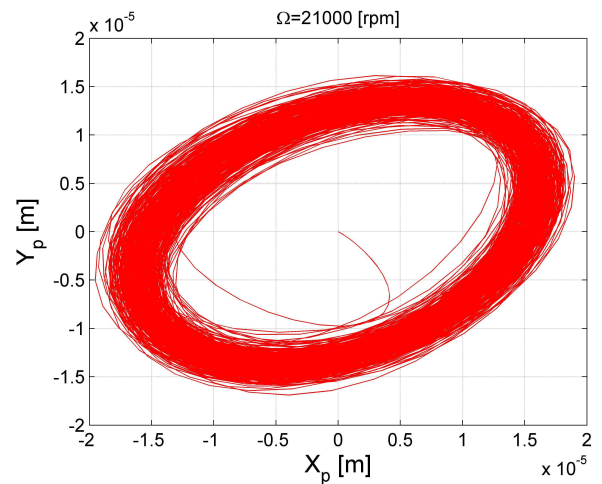

Fig. 12. Test rig

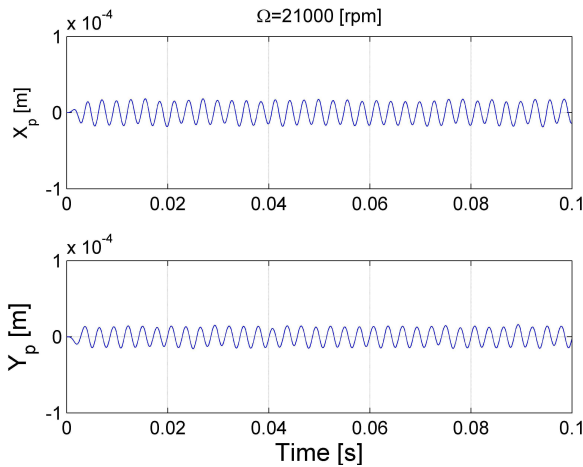**Fig. 13.** Orbit plot for rotational speed at 21000 rpm

Fig. 14. Vibrations level in two radial direction
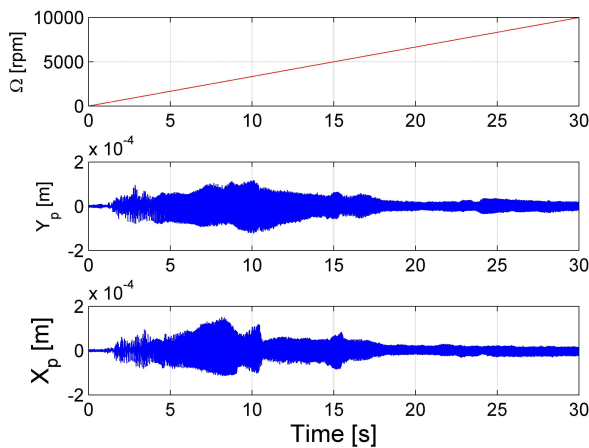for rotational speed at 21 000 rpm

Fig. 15. Rotor acceleration test from 0 to 10 000 rpm

The transient resonances (first two resonances) are shown in Fig. 15 during rotor acceleration test from 0 to 10 000 rpm, where all rotor rezonanses are sucesfully controlled. The rotor speed of 21 000 rpm was not maximal of the AMBs rotor system but of the electrical drive.

8. SUMMARY

The paper deals with optimal robust vibrations control in wide range of the AMBs rotor speed. The presented simulations and experimental results show the potential of the μ-Synthesis control applied in the AMBs rotor system. The vibrations compensation in wide range of rotation speed changes was performed successfully during experimental tests. The μ-controllers have a good vibrations damping and robustness to a plant structural uncertainty. The general disadvantage of the μ-Synthesis control is demanding a detailed model of the control plant. The maximal sampling frequency of the real digital processor is limited. Therefore, the order of μ-controller is high and must be reduced before implementation in the real-time digital processor.

REFERENCES

1. **Burrows C. R., Sahinkaya M. N, Clements S**. (1989), Active Vibration Control of Flexible Rotors: an Experimental and Theoretical Study, *Proceedings of the Royal Society of London*, Vol. 422, 123-146.
2. **Burrows C. R., Sahinkaya M. N., Clements S.** (1983), Vibration Control of Multi-mode Rotor-bearing Systems, *Proceedings of the Royal Society of London*, Vol. 386, 77-94.
3. **Fittro, R. L., Knospe, C. R.** (1999), μ Control of a High-speed Spindle Thrust Magnetic Bearing, *Proceedings of the 1999 IEEE international conference on control applications*, 570-575.
4. **Fittro, R. L., Knospe, C. R., Stephens, L. S.** (2003), μ-Synthesis Applied to the Compliance Minimization of an Active Magnetic Bearing HSM Spindle's Thrust Axis, *Machining Science and Tech.*, Vol. 7, 19-51.
5. **Genta G.** (2005), *Dynamics of Rotating Systems*, Spr.
6. **Genta G., Carabelli S.** (2000), Noncollocation effects on the Rigid Body Rotordynamics of Rotors on Active Magnetic Bearings, *7th Int. Symp. on Mag. B.*, Zurich.
7. **Knospe C. R.** (2007), Active Magnetic Bearings for Machining Applications, *Control Engineering Practice*, Vol. 15, 307-313.
8. **Knospe C. R., Hope R., Fedigan S., Williams R.** (1995), Experiments in the Control of Unbalance Response Using Magnetic Bearings, *Mechatronics*, Vol. 5, 385-400.
9. **Knospe C. R., Tamer S., Fedigan S.** (1996), Robustness of Adaptive Rotor Vibration Control to Structured Uncertainty, *Journal of Vibration and Control*, Vol. 2, 33-52.
10. **Knospe, C. R., Fittro, R. L., Stephens, L. S.** (1997), Control of a High Speed Machining Spindle via μ-Synthesis, *Proc. of 1997 IEEE international conference on control applications*, 912–917.
11. **Losch F.** (2002), *Identification and Automated Controller Design for Active Magnetic Bearing Systems*, Ph.D. Dissertation, Zurich.
12. **Miatliuk K, Kim Y. H., Kim K.** (2009), Motion control based on the coordination method of hierarchical systems, *J. of Vibroengineering*, V. 11, 523-529.
13. **Mystkowski A. Gosiewski Z.** (2009), The Robust Control of Magnetic Suspension with Rapidly Changing of Rotor Speed, *Solid State Phenomena*, Vols. 147-149, 302-306.
14. **Mystkowski A.** (2007a), *Robust Vibration Control of Rotor Supported Magnetically*, Ph.D. dissertation, AGH University of Science and Technology, Cracow.
15. **Mystkowski A.** (2007b), Comparison of H∞ and H2 Optimal Controllers for Active Magnetic Suspension, *Developments in Machinery Design and Control*, Vol. 6, 37-42.
16. **Mystkowski A., Gosiewski Z.** (2006), The Robust Control of Magnetic Bearings for Rotating Machinery, *Solid State Phenomena*, Vol. 113, 125-130.
17. **Mystkowski A., Gosiewski Z.** (2008a), Robust Control of Active Magnetic Suspension: Analytical and Experimental Results, *Mechanical Systems & Signal Processing*, Vol. 22, No. 6, 1297-1303.
18. **Mystkowski A., Gosiewski Z.** (2008b), Robust Control of High Speed Rotor Supported Magnetically, *9th International Conference on Motion and Vibration Control*, Munich, Germany.
19. **Mystkowski A., Gosiewski Z.** (2009), Uncertainty Modelling in Robust Control of Active Magnetic Suspension, *Solid State Phenomena*, 144, 22-26.
20. **Nelson H. D.** (1980), A Finite Rotating Element Using Timoshenko Beam Theory, *ASME Journal of Mechanical Design*, Vol. 102, 797-803.

21. **Preumont A.** (2002), *Vibration Control of Active Structures An Introduction 2nd Edition*, Kluwer Academic Publisher, Springer.
22. **Sawicki J. T.** (2008), Rationale for Mu-synthesis Control of Flexible Rotor-Magnetic Bearings System, *Acta Mechanica et Automatica*, Vol. 2, No. 2, 67-74.
23. **Sawicki J. T., Maslen E. H.** (2006), AMB Controller Design for a Machining Spindle using μ-Synthesis, *The 10th International Symposium on Magnetic Bearings (ISMB-10)*, Martigny, Switzerland.
24. **Schweitzer G., Bleuler H., Traxler A.** (1994), Active Magnetic Bearings, *Hoch. AG an der ETH*, Zurich.
25. **Schweitzer G., Maslen E. H, et al.** (2009), *Magnetic Bearings: Theory, Design and Application to Rotating Machinery*, Springer.
26. **Spector V. A., Flashner H.** (1989), Sensitivity of Structural Models for Noncollocated Control Systems, *ASME Journal of Dynamic Systems, Measurement and Control*, Vol. 111, 646-655.
27. **Spector V. A., Flashner H.** (1990), Modelling and Design Implications of Noncollocated Control in Flexible Systems, *ASME Journal of Dynamic Systems, Measurement and Control*, Vol. 112, 186-193.
28. **Stephens, L. S.** (1995), *Design and Control of Active Magnetic Bearings for a High Speed Spindle*, Ph.D. dissertation, University of Virginia.
29. **The MathWorks 2004**, Robust Control Toolbox User's Manual, 3rd ed.
30. **Zhou K., Doyle J. C., Glover K.** (1996), *Robust and Optimal Control*, Prentice-Hall, Inc.

INFLUENCE OF COORDINATE MEASUREMENT PARAMETERS ON A FREE-FORM SURFACE INSPECTION RESULTS

Malgorzata PONIATOWSKA[*]

* Faculty of Mechanical Engineering, Bialystok University of Technology,
ul. Wiejska 45 C, 15-351 Bialystok

mponiat@pb.edu.pl

Abstract: Coordinate measurements are the source of digital data in the form of coordinates of the measurement points of a discrete distribution on the measured surface. The local geometric deviations of free-form surfaces are determined (at each point) as normal deviations of these points from the nominal surface (the CAD model). Obtaining discrete data is inseparably connected with losing information on the surface properties. In contact measurements, the ball tip functions as a mechanical-geometric filter. The results of coordinate measurements of geometric deviations depend not only on the grid size but also on the ball tip diameter. This article presents foundations of the influence of the ball tip diameter and the grid size on coordinate measurement results along with the experimental results of measurement of a free-form milled surface in order to determine its local geometric deviations.

1. INTRODUCTION

The issue whether a product meets the appropriate construction requirements is of fundamental importance in producing machine parts. For inspecting the accuracy of parts which consist of geometric shapes such as planes, circles, or cylinders, widely known measurement techniques are used in industry. The accuracy inspection of parts containing free surfaces requires the coordinate measurement method to be applied.

The coordinate measurement technique consists in determining the coordinate values of measurement points located on the surface of an object. As a result of the measurement, a set of discrete data is obtained in the form of the coordinates of the measurement points. The dimensional/form accuracy inspection of free-form surfaces consists in digitalizing the workpiece under research (coordinate measurement with the scanning method), followed by comparing the obtained coordinates of the measurement points with the CAD design (model). The values of local geometric deviations of the free-form surface, or normal deviations of measurement points from the nominal surface, may be calculated by previously determining the deviation components in the *X*, *Y*, *Z* directions (Werner and Poniatowska, 2006; Cho and Seo, 2002). Software of coordinate measurement machines (CMMs) automatically performs such calculation for each measurement point in the *UV* scanning option designed for scanning on the basis of the CAD model (*UV* – directions of the B-spline surface parameterization).

Measurements of real surfaces produce only their approximate views. The approximation degree depends on the accuracy of the applied measuring method. Among numerous factors which have influence on the accuracy, connected with the tool instrument and the measurement environment, there are factors which can be rationally adjusted – such measurement parameters as the sampling (discretization) interval and the diameter of the measuring tip. Both these factors have a strictly specific impact on the measurement results (Adamczak, 2008).

Different sampling strategies (number and location of measurement points) provide different measurement results for the same surface. This is connected to the fact that measuring a finite number of discrete points on the measured surface is actually described by an infinite number of points. Since geometric deviations are different at each point, measurement results depend on the number and location of these points (Badar et al., 2008; Ainsworth et al., 2000). Elkott et al. (2002) proposed to sample points from free-form surfaces based on the surface NURBS features. However, in the majority of cases, measurements are carried out along a regular *u* x *v* grid with the use of *UV* scanning options, which are inbuilt in CMM software. Information on the surface is provided by data of a discrete character. Obtaining such data is inseparably connected with losing information on the surface properties. Planning an effective sampling scheme requires decisions on determining the range of active area and the size of the measurement points grid. The active research, area as well as the grid size determine the measurement results. Geometric deviations of a surface may be decomposed into three components: form deviations, waviness, and roughness. The components differ in respect of lengths of their elementary irregularities (waves). In contact measurements, the ball tip functions as a mechanical-geometric filter (Adamczak, 2008; Dong et al., 1996). The scope of information included in measurement data depends on the ball tip diameter. Therefore, results of coordinate measurements of geometric deviations of free-form surfaces depend not only on the active area and the grid size but also on the diameter of the ball tip end.

In measuring geometric surface textures (form deviations, waviness and roughness) of regular shapes, specialized stylus measurement instruments are used – profilers, roundness measuring machines, form recording instruments, etc. For the particular types of deviations, guidelines for selecting measurement parameters including the tip

radius, sampling lengths and assessment lengths, the sampling interval (the number of measurement points), as well as rules of digital roughness filtration have been developed and incorporated in standards. In standards pertaining to measuring straightness and roundness, the recommended maximum tip radii were worked out according to the principle stating that the tip radius is comparable to the boundary wavelength (the filter passing limit), while the distance between measurement points was established according to the principle holding that the number of measurement points in a segment whose length is equal to that of the boundary wavelength, amounts to 7 (Adamczak, 2008). However, there are no strict standards which would unambiguously determine what boundary length of the elementary (harmonic) wave should be adopted for waviness/form deviations, what the sampling interval should amount to, or which tip radius should be used in a specific measurement. No unambiguous criteria exist as to categorizing deviations as waviness or form deviations. Numerous literature sources relating to measuring surface roughness include analyses of the influence of tip geometry and radii on measurement results. In Poon and Bhushan (1995) showed that increasing the tip size leads to the profile deformation, and in effect to decreasing values of the height parameters. Many problems are also connected with selecting the sampling interval. If it is too small, excess data are available, data are strongly correlated, and the surface is represented by a vast number of measurement points. If, on the other hand, the sampling interval is too big, information on the surface properties is lost (the phenomenon of aliasing occurs). It is suggested that selecting the sampling interval should be made according to the tip radius size (Pawlus, 2004, 2007). The boundary length of the measured roughness depends on which parameter, the tip size or the sampling interval, is bigger (Dong et al., 1996; Szabatin, 2003). In measuring form deviations, measurement parameters are not as significant as in measuring surface roughness, although their influence on the measurement results cannot be neglected.

This article presents foundations of the influence of the ball tip diameter and the grid size on measurement results along with the experimental results of measurement of a free-form milled surface in order to determine its local geometric deviations.

2. APPROPRIATE SAMPLING PARAMETERS

The surface image obtained as a result of contact measurements depends to a great extent on the shape and size of the stylus tip, as well as on the number of measurement points (the sampling interval and strategy). Ball-tip ends are mainly recommended. The sampling parameters listed above determine the least boundary length of elementary irregularities represented in measurement data. The parameter which has a decisive influence is the one which causes a longer wave to be passed. Literature sources suggest different principles of selecting the appropriate tip radius in relation to the sampling interval, most often in the ratios

of ½ :1, 1:1 and 2:1 (Adamczak, 2008; Dong et al., 1996; Pawlus, 2007).

Contact measurements take into consideration deviations of specific wavelengths which have not been filtered by the ball tip because the ball tip functions as a mechanical-geometric low-pass filter. Thus, the scope of information included in measurement data depends on the ball tip diameter. In coordinate measurements, ball-tip styluses are used, and styluses with ball tips of $d = 1, 1.5, 2, 3$, and 4 mm in diameter are produced. The nature of a ball tip functioning in the character of a mechanical-geometric filter is illustrated in Fig. 1.
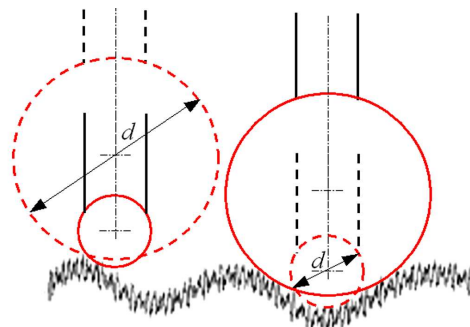
Fig. 1. The nature of a ball tip functioning in the character of a mechanical-geometric filter

In measurement planning, the choice of the d diameter of the ball tip should be made first, according to the measurement purpose and the range of information required on the characteristics of the measured surface. Defining the influence of the ball tip diameter/radius as a mechanical filter, i.e. unambiguously determining the filtration boundary, is difficult, especially in the case of changing-curvature surfaces. Adopting to measurement the principle suggested in the literature sources pertaining to measuring roundness deviations [4], which states that the boundary wave length is comparable to the tip radius value, means that in the case of using a stylus tip of $d = 1$ mm in diameter, irregularities of the length values greater than 0.5 mm is passed; in the case of the stylus tip of $d = 2$ mm in diameter, irregularities of the length values greater than 1 mm is passed, etc.

The second important factor which influences measurement results is the sampling interval, in the case of scanning a free-form surface with a CMM along a regular u x v grid, which is directly connected to the number of measurement points. For measurements with the use of machines with contact probes, the number of points is a serious limitation. In choosing the sampling interval T, the principle used in tests on measurement signals, derived from the Nyquist theory, states that a continuous signal may be reconstructed from a discrete one if the former was sampled with a frequency at least twice as big as the spectrum limit frequency should be taken into account (Szabatin, 2003)).

The knowledge of the principle mentioned above makes it easier to make decisions on the length of the sampling interval while planning coordinate measurement strategies. This particular measurement parameter also results in a mechanical-geometric filtration. According to the theorem quoted above, adopting the interval value of 1 mm

means that the obtained measurement data contain information of elementary surface irregularities of more than 2 mm in length.

Adopting the cited in literature (Pawlus, 2007) principles to selecting parameters of contact measurement at the same time, *d:T* equal to 2:1, choosing a ball of e.g. 2 mm in diameter, and the 1 mm sampling interval, the boundary length of elementary irregularities represented in measurement data amounts to 2 mm. Since there is not any unambiguous criterion for categorizing unevenness as waviness or form deviations, while presenting measurement results, it is difficult to specify what these results represent. In deciding on the ball tip diameter and the size of the measurement grid, it is advisable to focus on the purpose of measurement and to include detailed information concerning the measurement parameters in measurement reports.

3. EXPERIMENTAL INVESTIGATIONS

The experiments were performed on a free-form surface of a workpiece made of aluminium alloy with the base measuring 100 x 100 mm (Fig. 2), obtained in a three-stage milling process using in the last stage a ball-end mill of 6 mm in diameter, rotational speed equal to 7500 rev/min, working feed 300 mm/min and zig-zag cutting path in the *XY* plane. The measurements were carried out on a Global Performance Brown&Sharpe CMM (PC-DMIS software, $MPE_E = 1.5+L/333$ µm), equipped with a Renishaw SM25 scanning probe, a 20 mm stylus with a ball tips of 2 and 4 mm in diameter. Scanning of the whole surface was performed for two different combinations of the measurement parameters, the tip end diameter, and the sampling interval (the number of measurement points), observing the rule of selecting *d:T* equal to 2:1. All the measurements were repeated three times; the tables and plots present mean values of the obtained results.
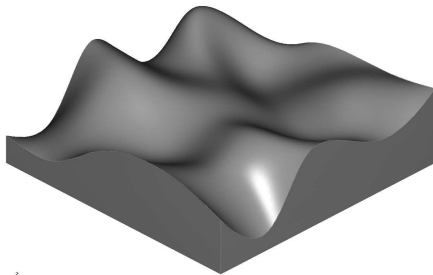

Fig. 2. The CAD model of the surface

In the first stage, the surface was scanned (without applying probe radius compensation), with the use of a ball end tip of 2 mm in diameter with the *UV* scanning option (the option built in PC-DMIS software), 10 000 uniformly distributed measurement points were scanned from the surface (100 rows and 100 columns, sampling grid 0.01*u* x 0.01*v*), and the process of fitting the data to the nominal surface was then carried out in which the least square method was applied and all the measurement points were used. The location deviation was minimized in this way. The measurement process was subsequently repeated, and ε local geometric deviations were computed. The obtained

measurement data are presented in a graphical form. Figure 6 shows a spatial plot of the ε local deviations with reference to the *x* and *y* nominal coordinates.
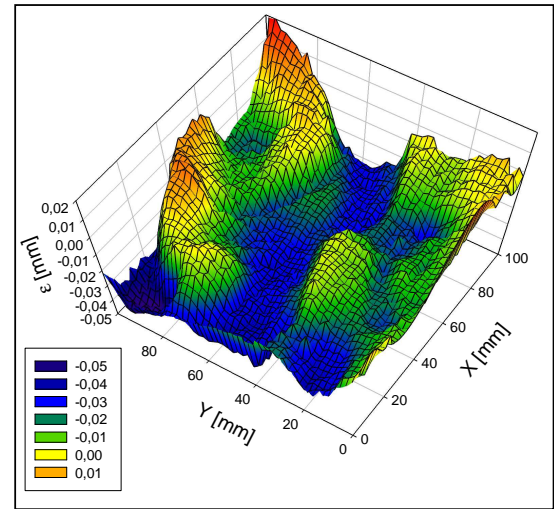

Fig. 3. Spatial plot of geometric deviations versus *XY* plane

In the subsequent stage, the measurements were carried out with the use of a ball end tip of *d* = 4 mm in diameter, and 2500 uniformly distributed measurement points (50 rows and 50 columns, sampling grid 0.02*u* x 0.02*v*) were scanned. The experiment results are compiled in Fig. 4 as well as in Tab. 1.

Tab. 1. Statistical parameters of ε local geometric deviation sets, with the whole surface scanned

Number of meas. pts.	10000	2500
Sampling grid	0.01*u*x0.01*v*	0.02*u*x0.02*v*
Sampling interval *T* [mm]	~ 1 mm	~ 2 mm
Tip diameter *d* [mm]	2	4
Std. deviation [mm]	0.011	0.009
Mean [mm]	-0.017	-0.015
Minimum ε [mm]	-0.049	-0.036
Maximum ε [mm]	+0.019	+0.013
Form/waviness dev. [mm]	0. 068	0.049

In both the cases, the principle of selecting *d:T* – 2:1 was applied. According to the principles described in Section 2, measurement data obtained in measurements performed with the tip end of *d* = 2 mm in diameter and the sampling interval of *T* = ~ 1 mm, include information on surface irregularities whose lengths exceed 2 mm. In the second case, for the tip end of *d* = 4 mm in diameter and the sampling interval *T* = ~ 2 mm, data include information on cases of wavelength longer than 4 mm.

As it had been expected, the form deviation value for the tip end of *d* = 4 mm and *T* = ~ 2 mm was smaller than that for *d* = 2 mm and *T* = ~ 1 mm (Tab. 1). The tip end of the bigger diameter did not reach points located in the irregularities indentations less than 4 mm length; additionally, some cases of irregularities on prominences were omitted because of a bigger sampling interval. Consequently, the mean plane is located higher, and the minimum value is bigger than in the case of a smaller diameter and a smaller

sampling interval (Fig. 4, Tab. 1). In order to facilitate comparison of the deviation maps, the plots in Fig. 4 were made using the same scale for the ε deviations axis. Comparing the maps, a bigger area of negative deviations can be observed in the case of measurements with the tip end of d

= 2 mm (Fig. 4a). As a result of applying different measurement strategies, significantly different results were obtained. The observed surface form/waviness deviations differed by approx. 0.02 mm, which constitutes approx. 1/3 of their values.
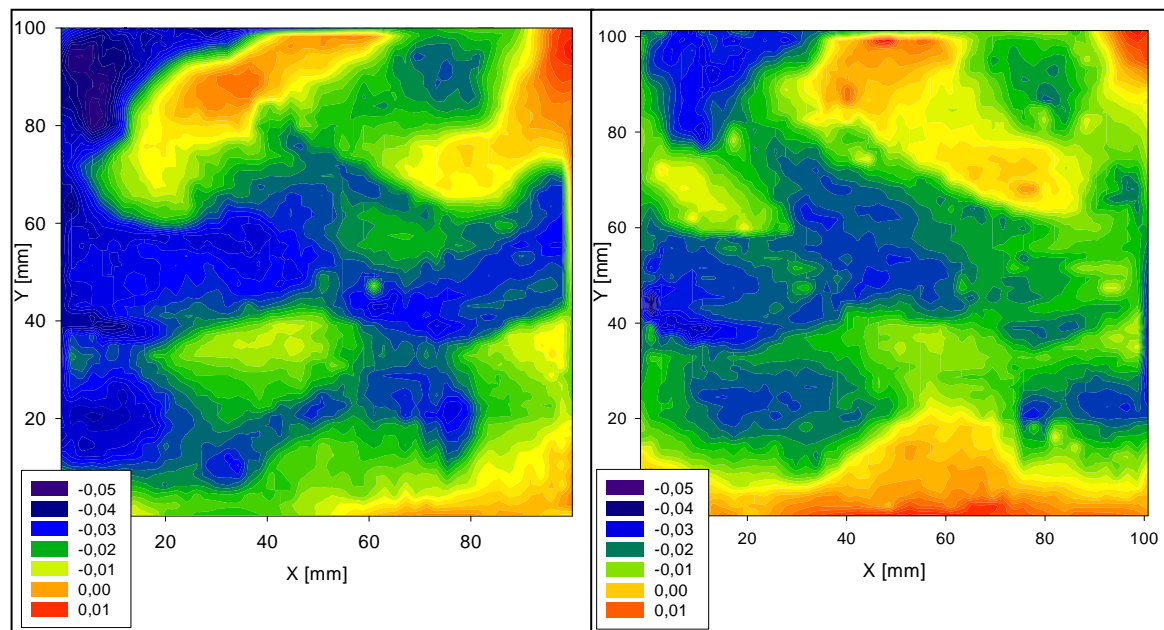

Fig. 4. Maps of geometric deviations versus *XY* plane, *a)* d = 2 mm and 10000 points, *b)* d = 4 mm and 2500 points

4. CONCLUSIONS

The article brings up the problem of selecting parameters in measuring geometric deviations of free-form surfaces, performed with the use of CMMs with contact probes. Such parameters as the tip end diameter and sampling interval determine contact measurement results because the parameters cause geometric-mechanical filtration. The parameter which determines passing longer waves exerts a decisive influence. The principles of selecting parameters, suggested in literature sources, were summed up. Two different parameter combinations were applied, observing the rule of the ratio of the ball end diameter to the sampling interval equal to 2:1. In the first measurement, the tip end amounted to d = 2 mm, and the sampling interval to $T = \sim 1$ mm; in the second one, the values were 4 mm and 2 mm respectively. The obtained measurement results differed to a great extent. In the case of the bigger diameter and the bigger sampling interval, cases of elementary irregularities of the lengths less than 4 mm were filtered mechanically, and the observed form/waviness deviation was smaller by 1/3 than when the parameters had smaller values.

REFERENCES

1. **Werner A, Poniatowska M.** (2006), Determining errors in complex surfaces machining with the use of CNC machine tools, *Arch. Mech. Technol. Automat.*, Vol. 26, No.2, 211-217.

2. **Cho M.W., Seo T.L.** (2002), Inspection Planning Strategy for the On-Machine Measurement Process Based on CAD/CAM/CAI Integration, *Int. J. Adv. Manuf. Technol.*, Vol. 19, 607-617.

3. **Adamczak S.** (2008), *Surface geometric measurements*, WNT, Warsaw.

4. **Badar M.A., Raman S., Pulat P.S.** (2008), Experimental verification of manufacturing error pattern and its utilization in form tolerance sampling, *Int. J. Mach. Tools Manuf.*, Vol. 43, 63-73.

5. **Ainsworth I., Ristic M., Brujic D.** (2000), CAD-based Measurement Path Planning for Free-Form Shapes Using Contact Probes, *Int. J. Adv. Manuf. Technol.,* Vol. 1, 23-31.

6. **Elkott D.F., Elmaraghy H.A., Elmaraghy W.H.** (2002), Automatic sampling for CMM inspection planning of free-form surfaces, *Int. J. Res.*, Vol. 40, 2653-2676.

7. **Dong W.P., Mainsah E., Stout K.I. (1996),** Determination of appropriate sampling conditions for three-dimensional micro-topography measurement, *Int. J. Mach. Tools Manuf.,* Vol. 36, 1347-1362.

8. **Poon C.Y., Bhushan B.** (1995), Comparison of surface measurement by AFM and non-contact optical profiler, *Wear*, Vol. 190, 76-88.

9. **Pawlus P.** (2007), Digitization of surface topography measurement results, *Measurement*, Vol. 40, 672-686.

10. **Pawlus P.** (2004), Mechanical filtration of surface profiles, *Measurement*, Vol. 35, 325-341.

11. **Szabatin J.** (2003), *Signal theory fundamentals*, WKŁ, Warsaw.

APPLICATION OF ACOUSTIC EMISSION IN FATIGUE FRACTURE DIAGNOSTICS

Valentyn SKALSKY[*], Pavlo HALAN[*]

[*]Karpenko Physico-Mechanical Institute of the National Academy of sciences of Ukraine,
Naukova str., 5, Lviv, Ukraine, 79060.

skal@ipm.lviv.ua, galanpol@ukr.net

Abstract: The most important peculiarities of the acoustic emission under fatigue loading are reviewed. Dependences of the AE signals and parameters of the growing fatigue crack on the basis of an existing literature source review are established. An essential role of the correlation for determining the crack growth rate in the relation between the AE parameters and crack parameters are shown. An energy approach for determination of cycle quantities till the initiation of a crack is proposed.

1. SOURCES OF AE UNDER FATIGUE FRACTURE

In the presence of a fatigue crack during one loading cycle there is a possibility of appearance of a complex aggregate of the AE signals. To describe the particularity of appearance of one or another signal component, it is necessary to consider more in detail the processes, which lead to the AE signals in the presence of a fatigue crack in a solid. To those processes one may referred: creation and growth of a plastic deformation area at the tip of a crack; an increase in the crack length (square); the crack closure (Drobot and Lazarev, 1987; Penkin and Terentev, 2006).

It is well known that a crack growth in constructive metal materials is accompanied by local plastic deformation. Its main components - sliding and twinning – generate the AE waves. Usually, the principal contribution to the emission of elastic waves is made by that part of the material, which within a certain range of relative deformation, transfers to the plastic condition. An unloading and reloading of this volume to the preceding maximum loading level in consequence of Kaiser Effect (Drobot and Lazarev, 1987; Tensi, 2004) result in – a sharp decrease in wave emission. However, under the cyclic loading, even when the maximum cycle loading level is permanent, there is a factor, which contributes to an increase in AE – that is the involving into the present deformation's interval of a new volume of the material, previously deformed outside the given interval. This is achieved, when two conditions are satisfied. The first one is accumulation of the plastic deformation under constant crack length as a result of an unclosed hysteresis loop during the elastic-plastic deformation. The second one is the crack development, i.e. the crack length (square) increase.

The first condition is typical of cyclical off-strengthened materials under the soft loading working condition. Such materials during asymmetric cycles have accumulation of the plastic deformation from a cycle to cycle. Under those circumstances there is a development of a "neck" in the specimen and fracture is of the same character as under the static tension. This effect is absent in cyclical strengthened materials. During the development of a crack a new volume of the material is involved into the plastic deformation. Since an increase in the crack square is located at the maximum of the cycle loading, the progress and growth of the plastic deformation's region and correspondingly the appearance of the AE signals from plastic deformation will be located at those maximums. An increase in the crack length also causes AE signals, which are located at the same places of cycle loading.

According to the research works (Mitchell and Egle, 1977; Mitchell at al., 1972) there was found out one more peculiarity of the AE signals. The two types of AE were established: the first one appears at the points of maximum rate in the cycle, and the second – burst emission, which appears at the point of curvature's maximum and minimum. The first type is connected with crack initiation, and the second one – with crack growth. In works (Shyrjajev and Kamyshov, 2002; Pavelko and Ozolinsh, 2002) the AE signals were divided into discrete high-range and continuous low-range components. The latter was caused by plastic yielding, and the discrete AE - by the growth of the existing crack.

A lot of experimental investigations (Drobot and Lazarev, 1987; Penkin and Terentev, 2006; Pollock, 1989) are devoted to the contact crack closure phenomenon. For a normal tear it starts when a loading falls down to zero and evolves under compression. It is well known, that a crack closure begins earlier – during a decrease in the cyclical loading. Emission waves under these circumstances are caused by the two processes – dynamic blows and mutual friction of the crack banks. If one supposes, that blowing and friction are just elastic processes, then signals generated by them can not be referred to the AE containing information on fracture, since there are not any reconstructions of the material structure in the contact area. However, a typical kind of fatigue break testifies to the presence of the local plastic friction deformation there. Thus, an aggregate acoustic signal of the crack closure phenomenon is a mixture of the useful AE signals and acoustic noises resulting from the dynamic elastic crack banks blowing. Frequency's spectrum of these noises is limited and does not reach to the working frequency's band, which is used while measuring AE. In this connection a number of the AE signals can be referred to informative signals, and it is possible to define them as AE from crack friction.

In works (Harris, 2007; Harris and Dunegan, 1974) AE from a crack closure was interpreted as a criterion of the presence of a crack growth during the cyclic loading.

In the given work we will focus on the generation of the AE waves resulting from the processes of plastic yielding and crack growth. Considering this we should keep in mind the fact that AE signals from the crack closure phenomenon can be easily separated from other AE signals with the help of time and frequency selection (Drobot and Lazarev, 1987; Penkin and Terentev, 2006).

If one registers the components of plastic deformation and crack growth only, then it is possible to mention their two typical properties. First of all: the signals are absent in certain cycles (under the given apparatus sensitivity). Thus, all the loading cycles can be divided into active (with the AE signals) and passive (without them). Secondly, in the active cycle both the single impulses and groups of impulses may arise. These particularities represent a disproportional development of the fatigue crack and possibilities of its several jumps in one cycle in the region of the maximum loading.

2. DEPENDENCE BETWEEN PARAMETERS OF THE AE AND CRACK PARAMETERS

The AE usage opportunities for the discovery and evaluation of crack parameters are fined by the presence of relations between the crack parameters and the emitted waves. The first of such relations are obtained in Morton et al. (1974). Investigating the aluminium alloy 2024 the authors obtained a good dependence between the total quantity of the AE signals and the rate of the crack growth, as well as the stress intensity factor K (k-factor). Using Paris equation for determining rate of the crack growth l' as follows:

$$l' = C\Delta K^q, \tag{1}$$

where ΔK – a changing interval of k-factor; C, q – material parameters.

To obtain a better data correlation during experiments with different values of cycle asymmetry $R = K_{min}/K_{max}$ and for maximum k-factors K_{max}, which approached the critical value K_c, the empirical Forman equation for a crack growth rate was used

$$l' = \frac{C_1\Delta K^p}{(1-R)(K_c - K_{max})}, \tag{2}$$

where C_1, p – material parameters.

Haris and Dunegan (1974), investigating the growth of a fatigue crack in the aluminium alloy 7075-T6 and in steel, considered that $\dot{N}$ is directly proportional to the energy releasing during the crack growth ($J' = B/E(\Delta K/(1-R))^2 l'$). Here J' – energy; B – specimen thickness; E – Young's modulus. To evaluate the velocity of AE the formula $\dot{N} = CJ'$ was used, where $\dot{N}$ – velocity of AE counting; C – material constant.

In work (Lindley et al., 1978) it is assumed that AE depends on the two components: the above described energy, realising during the crack growth, and also on the processes of plastic deformation and fracture in the plastic region.

Therefore, the velocity of the total measurement of the AE was given in the form of $N'_{Total} = N'_1 + N'_2 = (C_1 + C_2) \cdot J'N'_{Total}$, where N'_1 – velocity of AE counting under crack extension; N'_2 – velocity of AE counting under the processes of plastic deformation; C_1 – direct contribution of crack extension; C_2 – contribution of plastic deformation activity. To describe the crack growth rate a well known equation (Lindley et al., 1978) was applied:

$$l' = C_r \left(\frac{\Delta K^4}{\sigma_1^2 \left(K_c^2 - K_{max}^2 \right)} \right)^r, \tag{3}$$

Here σ_1 – strength limit; $r = 0{,}75$ for steels. In the work an essential difference between the total AE counting velocities for different steels and alloys is also pointed out, this difference equals to almost 4 orders of magnitude. Besides, there was an investigation of the cycle asymmetry effect on the AE velocity. It was established that the AE velocity increases with the increase of R. Also there was shown a decrease in crack growth rate near the maximum loading when an overloading took place. In the given work and also in Hreshnikov and Drobot (1976) it was established, that magnitude of the total AE counting N is proportional to the plastic region volume. The authors of the work Nagornyh and Sarafanov (1990), regarding the total AE counting as that being proportional to the plastic region and haven taken an increment of the crack as the magnitude of Irvin's correction $r = K_I^2/2\pi\sigma_T^2$, obtained the relation between the AE counting velocity and crack growth rate:

$$\dot{N} = BK_I^2 \frac{dl}{dt}. \tag{4}$$

In works (Gerberich and Hartbower, 1966, 1966) is shown, that there is a possibility of quantitative relation between the AE amplitude and the crack size increase. In work (Drobot and Lazarev, 1987) it is considered, that amplitudes of the dynamic displacements A_{ijn}, caused by an increase in the crack length (square), do not essentially exceed the corresponding increments of the static displacements Δu_{ijn} at the tip of the crack. In the mathematical form it can be given as:

$$A_{ijn} \approx \Delta u_{ijn} \tag{5}$$

An elementary act of the crack's growing-up consists in the increase in its length by a small magnitude Δl. At a sufficiently high rate of the process (while jumping) the AE impulse is generated. It is also considered, that under fatigue loading an increment of the crack Δl locates near the maximum loading. Then Δl takes sense of the crack length increment per cycle, i.e. crack growth rate $l' = dl/dn$, where n – the number of loading cycles. Taking this into account, the dependence (5) can be written as:

$$A_{ijn} = M_{ijn}(\lambda) \frac{p_{j\,max}^2}{J\sigma_p} l', \tag{6}$$

Here $M_{ijn}(\lambda)$ – a certain function, which form depends on the type and configuration of the crack, its orientation relatively to coordinates axes, geometrical parameters

of the object, and peculiarity of the applied loading [6]; λ – crack length, relative to the width of flat specimens; p_{jmax} – component of the outside specific maximum loading corresponding to the crack's type; J – shear modulus; σ_p – limit of proportionality.

During the appearance in the cycle of several subsequent crack jumps the dependence (6) remains, if l' implies the total length of these jumps, and A_{ijn} stands for equivalent amplitude a_{ijn}.

Thus, under other equal conditions the amplitude of the AE signal is proportional to the crack length. It can be also represented by the parameter λ.

If a law of the development of the fatigue crack is known, then the right side of (6) can be given the form of that having the only parameter – the crack length. To do so one should put into the equation (6) one of the equations (1), (2) or (3). In that way we will obtain a correlation between the amplitude and the crack growth.

Generalizing relations between the AE parameters and the crack parameters and resulting from the physical nature of the phenomenon and a general scheme of the measurement of the AE parameters, in work (Drobot and Lazarev, 1987) there was built a diagnostic model with the help of the operator equation:

$$E = P_E \left\{ P_A \left[P_B (T) \right] + Ш_A \right\} + Ш_E \qquad (7)$$

Here T – vector of the crack state, E – AE signal vector; P_E, P_A, P_B – operators of the electrical, acoustic and entrance conversion correspondently; $Ш_A$, $Ш_E$ – vectors of the acoustic noise in the control object and noise of the electronic equipment. As a result of the absence of the general solution to the problem of the dynamic elastic-plastic deformation theory, solid acoustics, mechanical-electrical conversion of the vibration, etc, it is not possible to define strictly operators in equation (7). So, a number of hypotheses are assumed, simplifying mutual dependencies between the properties of the object, the AE sources and its signals. Among them there are a simplification of the geometrical characteristics of the crack, the absence of noises – an ability to cut noises and select the useful AE signals with the help of active methods or equipment means (Bezimjany and Halenko, 2007; Drobot and Lazarev, 1987; Penkin and Terentev, 2006; Pollock, 1989; Skalsky and Koval, 2005). The form of operators in formula (7) also essentially depends on the choice of state parameters and informative parameters of AE. The simplification can be obtained, if one uses parameters not connected (or slightly connected) to the form of the acoustic signals.

3. DETERMINATION OF CYCLE QUANTITIES TILL THE INITIATION OF A CRACK BY THE ENERGY APPROACH

Following the previously discussed peculiarity of the relation between the AE parameters and crack parameters, it should be pointed out that the essential role of correspondence between these parameters is played by the correlation for determining the crack growth rate. It is well known that one of the widespread approaches to the research of the fatigue macro-cracks is the strength criterion. In the strength criterion the crack growth velocity is described by the function of k-factors (K_I, K_{II}, K_{III}). Besides the strength approach, the deformation approaches also applied, which is based on δ_c – model. The deformation criterion is used, when the plastic region at the crack edge is of size as the solid and the defect.

The described criteria are sufficiently effective when the loading cycle is stable (an overloading and a frequency change are absent). As well as the history of the material deformation and crack extension are not taken onto account. Then k-factors or magnitudes of the crack disclosure are fatigue fracture invariants.

For a detailed description of the pre-critical fatigue crack growth, when a change of the cycle loading and its amplitudes possible, the history of deformation, crack extension and the effect of the aggressive environment are taken into account. For this purpose energy approaches are to be used.

For the first time such an approach was offered by Cherepanov. In its basis there is a hypothesis of constancy of the dissipative energy during the creation of a unit of the fatigue fracture surface and the first thermodynamics law of energy balance. Finally Cherepanov approach also can be transformed to the representation of the crack growth rate as a function of K_I, but in a more detailed form. A more perfect approach is given in work (Shata and Terlecka, 1999). Here as the basis the first thermodynamics law is taken, according to which after N loading cycles the following energy balance condition is fulfilled:

$$A + Q = W + K_e + \Gamma \qquad (8)$$

where A – work of inner power P per N cycles; Q – heat magnitude, brought to the solid per N loading cycles; K_e – kinetic energy of the solid; W – deformation energy after N loading cycles; Γ – fracture energy of the solid with a change of its square by magnitude S.

Through the differentiation of the (8) by the cycle quantity N, was pass to velocities, and introducing a number of simplification, we obtain the equation for crack square growth velocity

$$\frac{\partial S}{\partial N} = \frac{\partial W_C}{\partial N} \bigg/ \frac{\partial (\Gamma - W_s - W_r)}{\partial S}, \qquad (9)$$

where W_c – energy of a cyclic change of deformation; W_s – static component of the energy, which changed during crack growth; W_r – energy of plastic deformation of the material before the beginning of the cyclic loading. Having determined in the relation (9) energy magnitudes according to the results of work (Shata and Terlecka, 1999), we come to the equation for definition of the crack growth rates, in the right side of which only material constants and k-factors will be present.

An investigation of the energy approach and its application to the various problems of determining a fatigue crack growth rate are carried out in works (Andrejkiv and Lischyncka, 1999, 2000; Andrejkiv and Rudavsky, 2004; Andrejkiv and Kit, 2006; Terlecka and Kit, 2004). Among the principal results there the following:

– Description of the fatigue crack growth equation in the non-homogeneous plates (Andrejkiv and Lischyncka, 1999) (the kinetic crack growth equations in

plates which are non-homogeneous in relation to the resistance to fracture were formulated; taking into consideration the preceding plastic deformation).

– Calculation model of the initiation of the fatigue crack near the notch filled with hydrogen (Andrejkiv and Rudavsky, 2004) (a calculation model of the fatigue crack initiation using the energy approach was built. The influence of hydrogen was modeled by decreasing critical deformation according to the linear law).

– Energy approach to determination of the pre-critical growth of the fatigue crack under loading with two frequencies (Andrejkiv and Kit, 2006) (loading with two frequencies: one with high amplitude and low frequency was taken into account, another with low amplitude and high frequency).

– Application of the energy approach to evaluation of the residual durability of thin-walled elements with surface cracks (Terlecka and Kit, 2004) (a formula for calculation of the number of cycles to through-extension of the crack in a thin plate was obtained).

– Residual durability of elements, which are non-homogeneous by the mechanical characteristics (Andrejkiv and Lischyncka, 2000).

4. CONLUSIONS

Under a fatigue loading the AE is characterized by a number of properties an investigation of which can provide a clue to solution of different essential problems of fracture mechanics.

Following to the reviewed literature sources, parameters of the AE particularly correlate with rate of the fatigue crack growth. Among different theoretical criteria of the crack growth rate determination, energy criterion is the most complete. It includes all factors that exist under fatigue fracture. Thus, there is a great interest in further theoretical-experimental investigations of the AE signals application for interpretation of fatigue fracture mechanisms and their combination with energy approach relations obtained in works (Andrejkiv and Lischyncka, 1999, 2000; Andrejkiv and Rudavsky, 2004; Andrejkiv and Kit, 2006; Terlecka and Kit, 2004).

REFERENCE

1. **Andrejkiv O.E., Lischyncka M.V** (2000), Zalyshkova dovgovihnist elementiv, neodnoridnyh za mehanichnymy harakterystykamy, *Fiz.-him. mehanika mater*, No. 6, 39 – 44.
2. **Andrejkiv O.E., Lischyncka M.V.** (1999), Rivnjanja rostu vtomnyh trishynh u neodnoridnyh plastynah, *Fiz.-him. mehanika mate*, No. 3, 53 – 58.
3. **Andrejkiv O.E., Rudavsky D.V.** (2004), Rozrahunkova model zarodzhenja vtomnyh trishchyn bilja navodnenogo vyrizu, *Fiz.-him. mehanika mater*, No. 5, 63 – 65.
4. **Andrejkiv O.E., Kit M. B.** (2006), Vyznachenia periodu rostu trishchyny pry ih dvochastotnomu navantazheni, *Mashynoznavstvo*, No. 2, 3 – 7.
5. **Bezimjany U. H., Halanenko D. V.** (2007), *Akusto-emisionny control v procese bysokochastotnyh ispytanij*, Konsonans, Kiev, http://www.hydromech.kiev.ua/rus/WWW-CONS/cons2007r.html
6. **Drobot U.B., Lazarev A.M.** (1987), *Nerazrushajushiy kontrol ustalostnyh treshin akustiko-emisionnym metodom*, Izd-vo standartov, 128.
7. **Gerberich W. W., Hartbower C**. (1965), *Characterization of Fatigue-Crack Growth by Stress-Wave Emission*, Aerojet-General Corporation, Sacramento, California.
8. **Gerberich W. W., Hartbower C. E.** (1966), *Feasibility Study for Measuring Fatigue-Crack Growth Rate in Welded HY-80 Steel Using Stress-Wave Emission*, Final Report of Contact N600 (167) – Sacramento, California.
9. **Harris D. O.** (1972), *Detection of Fatigue Crack Growth in a Sling Assembly by Use of Acoustic Emission Monitoring of a Periodic Proof Test*, Technical Report DC-72-3 (addition 2), Dunegan Corporation, Livermore, California.
10. **Harris D. O., Dunegan H.L.** (1974), Continuous Monitoring of Fatigue Crack Growth by Acoustic Emission Techniques, *Exper. Mech*. 17, 71–81.
11. **Hreshnikov V.A., Drobot U.B.** (1976), Akusticheskaja emisia, *Izd-vo standartov*, 272.
12. **Lindley T.C., Palmer J.C., Richards C.E**. (1978), Acoustic emission monitoring of fatigue crack growth, *Mater. Sci. Eng*., 32, No. 1, 1–15.
13. **Mitchell J.R., Egle D. M.** (1977), Acoustic emission monitoring of Fatigue Crack Propagation, Summary of paper: *ASNT Spring Conference*, Phoenix, Arizona.
14. **Mitchell J.R., Egle D. M., Appl F. J.** (1972), *Detecting Fatigue Cracks with Acoustic Emission, University of Oklahoma, school of Aerospace*, Mechanical and Nuclear Engineering, Norman, Oklahoma.
15. **Morton T.M., Smith S., Harrington R.M.** (1974), Effect of loading variables on the acoustic emission of Fatigue-Crack growth, *Exper. Stress Analysis*, 31, No. 1, 208–213.
16. **Nagornyh S.N., Sarafanov H. F.** (1990), Izluchenie AE rasprostranjajushejsa treshinoj pri ustalosti, *Nauchano-tehnicheskaja konferencia "Nerazrushajushije metody i svoistva kontrolja"*, Sverdlovsk, No. 1, 161 –162.
17. **Pavelko V., Ozolinsh E.** (2002), *Detection of Fatigue Crack by method of an Acoustic Emission*, Riga, http://www.tsi.lv/
18. **Penkin A.H., Terentev V.F.** (2006), *Akustiko-emisionyy metod kontrolja procesov plasticheskoj deformacii i razrushenia metalicheskih materialov*, ZAO SDS, Moskva, http://www.sds.ru/method.html
19. **Pollock A.A. (1989)** *Metals handbook, – ASM International*, 17, 278–294.
20. **Shata M., Terlecka Z.O.** (1999), Energetychny pidhid u mehanici vtomnogo poshyrenia mikrotrishyny, *Mehanika ruinuvania I micnist konstrukci*, T 2, Lviv: Kamenjar. 141 – 148.
21. **Skalsky V.R., Koval P.M**. (2005*), Akustychna emisia pid chas rujnuvannja matarialiv, vyrobiv i konstrukcij, Metodolohichni aspekty vidboru ta obrobky informacii*, Lviv: Spolom, – 396.
22. **Shyrjajev A.M., KamyshovA.A.** (2002), *Akusticheskaja emissia pri roste treshchin v staliah, Shestaja nauchnaja konferencia po radiofizike, Nizhnij Novgorod*, http://www.rf.unn.ru/rus/sci/books/acoust02/index.html
23. **Tensi H.M.** (2004), The Kaiser effect and its Scientific Background, *26th European Conference on Acoustic Emission Testing, Berlin*, http://www.ndt.net/article/ewgae2004 /html/htmltxt/l00tensi.htm
24. **Terlecka Z.O., Kit M. B.** (2004), Zastosuvania energetychnogo pidhodu do ocinky zalyshkovoi dovgovichnosti tonkostinnyh elementiv z poverhnevymy trishchynamy, *Mashynoznavstvo*, No. 1, 17 – 19.

MEASURING THE ACCURACY OF PRODUCING FREE-FORM SURFACES
WITH THE USE OF THE COORDINATE MEASURING METHOD

Andrzej WERNER[*]

[*]Division of Production Engineering, Faculty of Mechanical Engineering, Bialystok University of Technology,
Wiejska 45 C, 15-351 Białystok

anwer@pb.edu.pl

Abstract: The present paper presents a method of determining errors in processing complex-shape surfaces produced with the use of a CNC machine tool. In order to achieve this, the whole process of making a three-dimensional object was performed, from creating a CAD model to generating a processing programme for a CNC machine tool and producing the actual object. The obtained surface was measured with a Brown & Sharpe Mistral coordinate measuring machine with the use of a Renishaw TP200 measuring probe.

1. INTRODUCTION

Nowadays, expectations concerning the quality and accuracy of producing goods are higher and higher, which makes different companies invest in research aiming at increasing these aspects of a production process more and more often. Additionally, because of a rapid growth in computer science, the possibilities of generating and actually producing complex geometry surfaces have increased substantially (Choi at al., 2007; Surazhsky et al., 2001). Some three-dimensional objects are of such complex shapes that measuring them with the use of conventional measuring methods is inefficient or even impossible, and that is why more advanced measuring methods need to be applied in accuracy inspection (Ainsworth et al., 2000). One of these methods is undoubtedly the coordinate measuring method which is especially widely used in the automotive, aircraft, or shipbuilding industries, e.g. in producing injection moulds (Weckenmann et al., 2001).

Due to the fact that coordinate measuring machines are more and more popular, it is necessary to develop the right methods of accuracy inspection of produced objects, especially in the case of objects described with complex-shape surfaces (Cheung et al., 2007; Li et al., 2004). Such measurements may be performed with the use of the surface scanning method on the basis of an already existing CAD model.

2. DESCRIPTION OF THE TEST STAND
AND PREPARATIONS FOR MEASURING

The test stand (Fig. 1), in which the process of determining the errors in processing the shape object was performed, consists of the following elements:
- a Hartford OMNIS1020 milling centre, in which the object under research was produced;
- a DEA (Brown & Sharpe) MISTRAL coordinate measuring machine – used for measuring the accuracy of the obtained surface;
- a PC class computer integrated with a machine tool and a coordinate measuring machine;
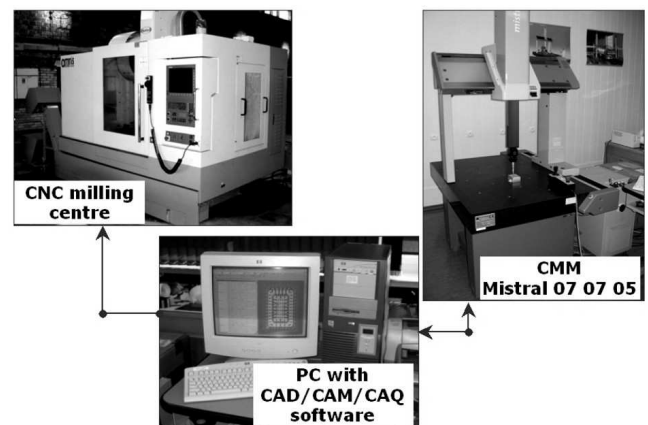- SolidWorks, MasterCAM, PC DMIS CAD++ software.

Fig. 1. The test stand

The list below is the order of preparations for measuring:
- creating a geometric model of a complex-shape object in a CAD system (Fig. 2a);
- generating a processing programme for a CNC machine tool – the obtained surface patch was saved in the IGES (*.igs) format and then imported to the MasterCAM system. Using this software, the surfaces to be processed were indicated, and the parameters necessary for carrying out the production process were defined. The final stage of the experiment performed in this system was generating by the postprocessor a processing programme 'understandable' to the control system of the given machine tool (the iTNC 530 Heidenhain control system in this case);
- producing the object with a CNC machine tool – the machining was performed with the OMNIS 1020 milling centre with the use of a ball nose end mill of 12 mm in diameter (Fig. 2b).
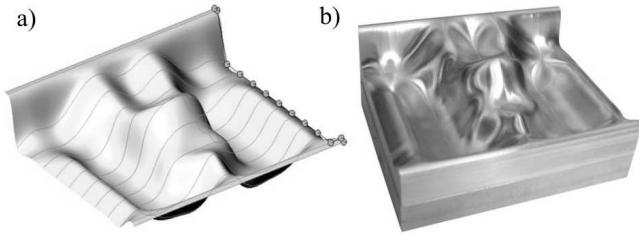
Fig. 2. Free surface: a) surface model, b) actual object

After that, the produced object underwent control measuring with a Mistral 07 07 05 coordinate measuring machine.

3. MEASURING THE ACCURACY OF FREE SURFACE PRODUCTION

The measuring was performed with a Brown & Sharpe MISTRAL coordinate measuring machine with the use of the PC DMIS CAD++3.6 software into which the model in the form of an IGES file had been imported from the MasterCAM system. A TP200 Renishaw measuring probe equipped with a measuring ball tip with an end of 2 mm in diameter was applied in the process of measuring.
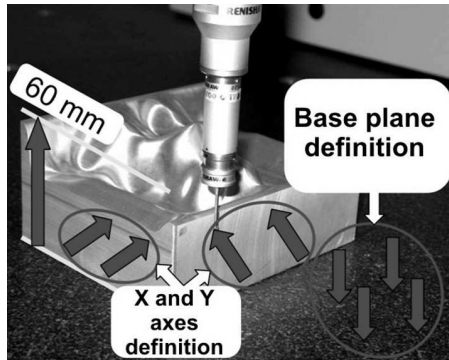

Fig. 3. Defining the measured object location in the machine measuring space

In order to perform the experiment, the measuring head had to be defined and calibrated with the use of a calibration ball. After the calibration was finished, the location of the element in the measuring space of the machine was defined (Fig. 3). The characteristic points of the object were selected in the manual control mode. This was the basis on which the coordinate system of the measured object was defined.

Additional attention shall be paid to the fact that the imported CAD model has its own coordinate system and for this reason it was necessary to transfer it to the coordinate system of the measured object, defined in the measuring space.

At the next stage of the experiment, in order to determine the accuracy of producing the shape surface of the processed object, the scanning (patch) method in the so-called UV Scan (offered by PC-DMIS software) mode was applied. This mode includes scanning a surface patch,

which results in obtaining the contact points of the measuring ball tip end and the measured object. The U and V symbols indicate the surface patch parameterisation directions (Piegl et al., 1997). Thus, in selecting the surface, the number of measurement points in the U and V directions has to be defined (in this case U=40, V=35, so measuring at 1400 points was performed accordingly) (Fig. 4).
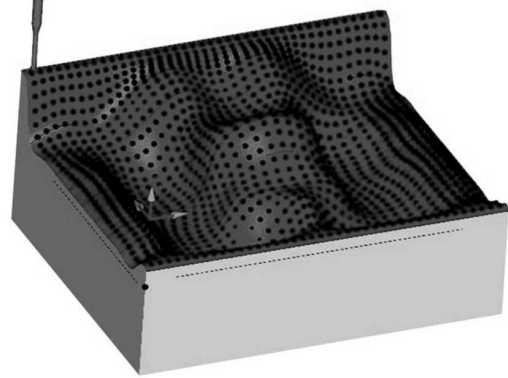
Fig. 4. Location of measurement points on the shape surface

4. PROCESSING THE OBTAINED MEASUREMENT RESULTS

In order for the accuracy of producing a free surface of the researched object to be established, the distances between the points located on the surface of the CAD model and the corresponding points obtained in the result of measuring with a coordinate machine have to be determined. The input data for determining processing errors comprises the measurement points coordinates and their corresponding nominal points (from the CAD model). This data might be obtained in two ways:

− through selecting the coordinates from the report generated in the form of a text file by the control software steering the coordinate measuring machine; or

− through generating text files with ready-to-use coordinates of the measurement and nominal points. In this case, the data in the form of an IGES file shall be imported to the do MasterCAM software (into which the modelled surface had previously been input) and these points shall subsequently be projected in the direction normal to the surface (Fig. 5). In this way, the coordinates of the nominal points are obtained.

Obtaining the data makes it possible to calculate the distances between the measurement and the expected (nominal) points. To that end, the error components in each of the three X, Y and Z axes respectively shall first be determined on the basis of the formulae below (Ainsworth et al., 2000):

$$\delta_{xi} = X_{Ri} - X_{Ni} \qquad (1)$$

$$\delta_{yi} = Y_{Ri} - Y_{Ni} \qquad (2)$$

$$\delta_{zi} = Z_{Ri} - Z_{Ni} \qquad (3)$$

where: δ_{xi}, δ_{yi}, δ_{zi} − error components in the respective axes; X_{Ri}, Y_{Ri}, Z_{Ri} − coordinates of actual points obtained during measuring; X_{Ni}, Y_{Ni}, Z_{Ni} − coordinates of nominal points

located on the geometric model surface, corresponding to the measurement points.
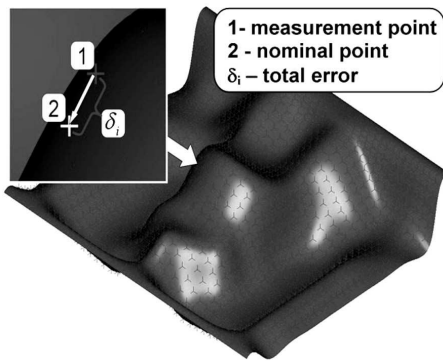

Fig. 5. Projecting the measurement points
in the direction normal to the surface

Applying the above components lets us determine the δ_i accumulated errors in producing a free surface at the respective measurement points:

$$\delta_i = \sqrt{\delta_{xi}^2 + \delta_{yi}^2 + \delta_{zi}^2} \qquad (4)$$

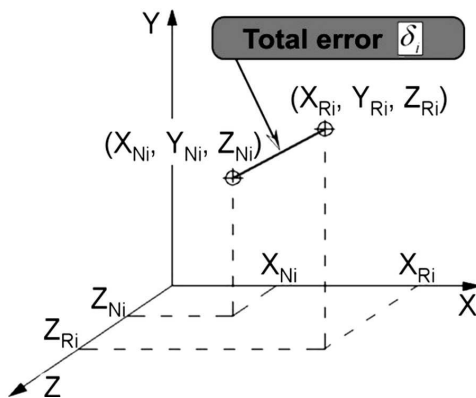where: δ_i – processing accumulated error at a point (Fig. 6)

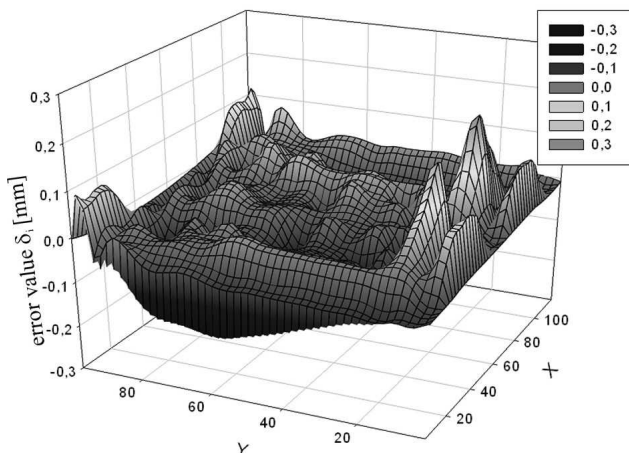**Fig. 6.** Graphical interpretation of a δ_i processing
accumulated error

Fig. 7. Error values plot for producing a free surface

On the basis of these errors, a plot presenting the error values at the respective points may be created (Fig. 7).

The plot illustrates errors at 1400 measured points. It can be seen that the inaccuracy of surface producing is significant (max. $\delta_i = 0{,}207$ mm). After an initial analysis it is possible to quickly locate the point where the errors occur. The reasons for the errors might have been, among others, shape errors of the machining tool. The obtained processing errors plot may be used in reshaping the geometric model of the object. Such reshaping serves to correct the occurring production errors as well as to generate the corrected processing programme for a numerically controlled milling machine.

5. SUMMARY

The present paper describes a method of inspecting the accuracy of producing a complex-shape surface made with the use of a numerically controlled machine tool. The presented method, owing to applying a modern coordinate technique, makes it possible to quickly inspect the accuracy in the process of object producing. On the basis of the measurement results, the values of errors and their locations may be determined. Such information enables us to take some action in order to minimise the occurring inaccuracy. This aim may be achieved for example through reshaping the geometric model of the object and re-generating the CNC machine tool control programme.

REFERENCES

1. **Choi Young-Keun, Banerjee A.** (2007), Tool path generation and tolerance analysis for free-form surfaces, *International Journal of Machine Tools and Manufacture,* Volume: 47, Issue: 3-4, 689-696.
2. **Surazhsky T., Elber G.** (2001), Matching free-form surfaces, *Computers and Graphics,* Volume: 25, Issue: 1, February, 2001, 3-12.
3. **Ainsworth I., Ristic M., Brujic, D.** (2000), CAD-Based Measurement Path Planning for Free-Form Shapes Using Contact Probes, *International Journal of Advanced Manufacturing Technology* Volume: 16, Issue: 1, 23-31.
4. **Weckenmann, A., Knauer M., Killmaier T.** (2001), Uncertainty of coordinate measurements on sheet-metal parts in the automotive industry, *Journal of Materials Processing Technology,* Volume: 115, Issue: 1, 9-13.
5. **Cheung C.F., Li H.F., Lee W.B., To S., Kong L.B.** (2007), An integrated form characterization method for measuring ultra-precision freeform surfaces, *International Journal of Machine Tools and Manufacture,* Volume: 47, Issue: 1, 81-91.
6. **Li Yadong, Gu Peihua** (2004), Free-form surface inspection techniques state of the art review, *Computer-Aided Design,* Volume: 36, Issue: 13, 1395-1417.
7. **Piegl L., Tiller W.** (1997), *The NURBS Book*, 2nd ed. Springer-Verlag, New York (1997), USA.

COORDINATE MEASUREMENTS OF FREE-FORM SURFACES IN REVERSE ENGINEERING PROCESS

Andrzej WERNER[*]

[*]Faculty of Mechanical Engineering, Białystok University of Technology, ul. Wiejska 45 C, 15-351 Białystok

anwer@pb.edu.pl

Abstract: This paper presents the issues of coordinate measurements of three-dimensional objects whose shape is defined with the use of parametric surface description methods applied in CAD systems. The paper also describes a mathematical as well as a geometrical presentation of surfaces used CAD systems, and discusses coordinate measurement techniques applied in measuring objects of this class. Further in the article, a practical implementation of the methodology of reconstructing objects described with the use of free-form surface patches has been presented. The methodology includes subsequent object measurements and reconstructing the object's geometric model, and concentrates on the possibly most accurate reconstruction of the shapes and dimensions of the researched object.

1. INTRODUCTION

Nowadays, more and more emphasis is put on the quality, ergonomics and aesthetics of products. Applying coordinate measurements and CAD/CAM systems to industry opens great possibilities of integrating the two techniques, which not only greatly influences simplifying the processes of designing and manufacturing but also makes them shorter (Alan et al., 1998; Soni et al., 2009).

Today, coordinate measuring machines are widely used and they often form an integral part of the machine facilities in companies. Moreover, using the machines is not restricted to the quality control; they are also applied in reconstructing objects of complex and unknown shapes (Ainsworth et al., 2000). It happens very often at the first stage of designing that a designer creates an object, which might result in obtaining a hand-made model made of a soft material and with a shape made up of multiple surfaces of complex shapes. In order for such an object to be produced and then to undergo different analyses, it is necessary to create its virtual model. Applying coordinate measurements is the only way to obtain such a model (Yadong and Peihua, 2004; Xie et al., 2005).

2. PARAMETRIC METHODS OF SURFACE DESCRIPTION

Parametric methods of surface description are currently used in creating geometric models in CAD (computer aided design) systems. A B-spline surface (Fig. 1) is described with the use of two parameters, *u* and *v* (Piegl and Tiller, 1987, 1997; Sun et al., 2006).

A mathematical presentation of a B-spline surface is illustrated below:

$$P(u,v) = \sum_{i=0}^{m} \sum_{j=0}^{n} D_{i,j} N_{i,k}(u) N_{j,r}(v) \tag{1}$$

where: $D_{i,j}$ – apexes of the control grid on which the surface is stretched, $N_{i,k}(u)$, $N_{j,r}(v)$ – basis B-spline functions, k, r – degrees of the basis B-spline functions.
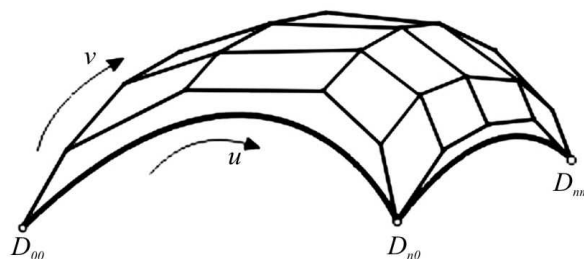

Fig. 1. B-spline surface patch

It is important to know it, since this technique is used in creating surface models on the basis of point clouds which might be created as a result of coordinate measurements. The state-of-the-art software controlling coordinate measuring machines includes, among its numerous object scanning methods, procedures of scanning surfaces of the *uv* type, i.e. according to the surface patch parameterisation directions.

3. APPLYING THE REVERSE ENGINEERING PROCESS TO AN OBJECT DESCRIBED WITH A FREE SURFACE PATCH

Coordinate measurements of complex-shape surfaces were carried out on the example of the object shown in Fig. 2. The shape of the object was described with the help of a B-spline surface patch.

Fig. 2. Reconstructed object

Performing the reverse engineering process aimed at obtaining the greatest possible accuracy of reconstructing the shape surface (Schemenauer et al., 2002). To that end, the following were performed consecutively:

− preliminary coordinate measurements with manual defining of the scanned surface,
− constructing the initial surface model of the object,
− automatic mode coordinate measurements (with the use of a previously prepared geometric model of the object),
− constructing the actual surface model,
− repeating the coordinate measurements and determining the accuracy of reconstructing the surface model.

The tests were made on a test stand comprising (Fig. 3):

− a CNC control milling centre,
− a PC-class computer integrated with a coordinate measuring machine, with the CAD/CAM (Mastercam) as well as (PC-DMIS) software installed.
− a DEA (Brown & Sharpe) Mistral 070705 coordinate measuring machine.
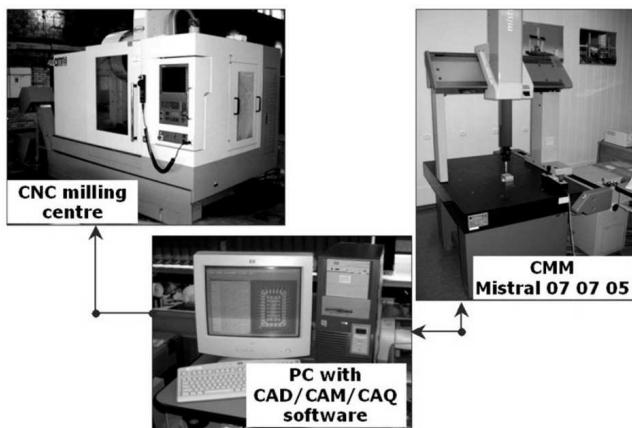

Fig. 3. Test stand

Firstly, the object described with a surface patch of complex shapes was created on this stand, and then the preliminary coordinate measurements were performed with the use of open linear scanning procedures. The object under question was scanned in successive parallel sections. The beginning, direction, and end of scanning were indicated manually. The distance between consecutive measuring points during scanning was 2 mm, while the distance between the successive scanned sections amounted to 2 mm. In that way, a point cloud of measuring points was obtained, on which a series of spline curves was stretched (Fig. 4a).

These curves were afterwards used to construct the initial surface model of the object (Fig. 4b) (Park et al., 2004).
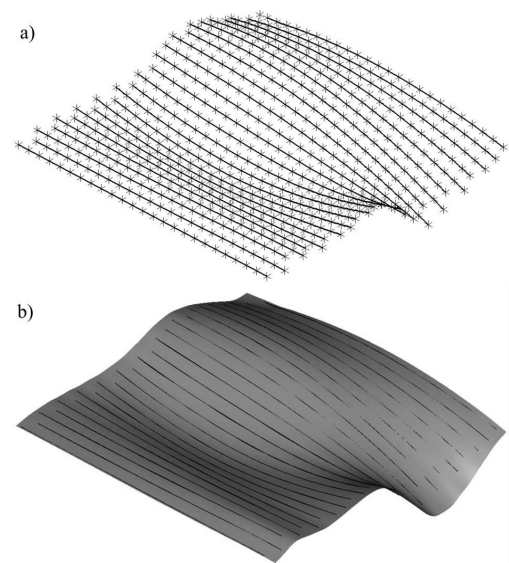
Fig. 4. Graphical presentation of measurement results
   a) measurement points and spline curves,
   b) surface patch

It has to be emphasised here that indicating the borders of scanning manually is a lengthy and troublesome process. The open linear scanning method is characterised by restrictions stemming from the very method of scanning. In this method, the initial vectors of the probe tip approach were defined by the system the moment the probe tip touched the object in the manual process. The PC-DMIS system defines the directions at which the probe tip approaches the measured surface at the consecutive measuring points on the basis of both the scanning increase pre-determined at the beginning and the last two measuring points (Fig. 5).
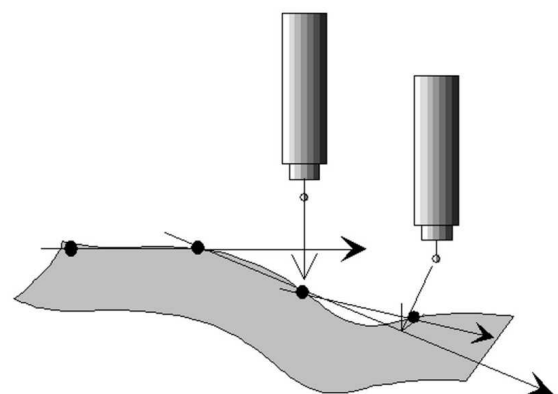
Fig. 5. Determining the direction of the measuring probe tip approach in open linear scanning

In the method presented in this paper, the measuring probe tip approach to the measured object is not located on the normal direction to the measured surface patch. This might result in inaccurate determining the compensation vector for the measuring ball tip end, which in consequence causes declining the measurement accuracy. In the light

of these facts, the measurement described above was performed mainly in order to obtain data for building the initial geometric model of the measured surface. This model in turn constitutes a basis for carrying out the actual measurement of the reconstructed object. The advantages of using a geometric model of the measured surface are as follows:

− the model includes the information concerning the borders of the scanned object,

− the measurement tip approach vectors are generated in the normal direction to the measured surface,

− it becomes possible to make use of automatic procedures of measuring the reconstructed surface.

In the following coordinate measurements, the *uv* scanning procedure was applied. This method involves scanning along the spline surface patch parameterisation directions (Fig. 1). The PC-DMIS programme window for the procedure is illustrated in Fig. 6.
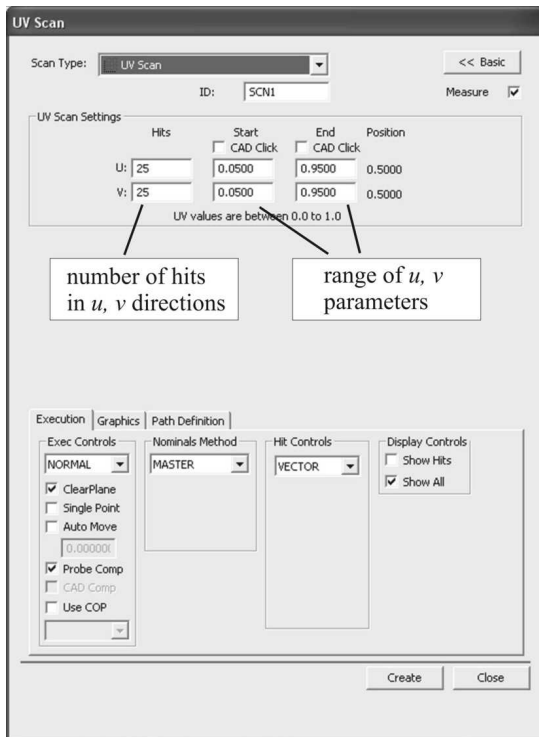

Fig. 6. UV method scanning window

The window requires the user to enter such data as:

− the scanning range through entering the *uv* parameters border values,

− the number of the measuring tip contacts in the *u* and *v* directions.

On the basis of the data listed above, the PC-DMIS system generates measuring samples on the surface patch, and the vectors of the measuring tip approach in the normal direction to the measured surface are also generated. An exemplary distribution of measuring points and the *uv* scanning directions are presented in Fig. 7. The measurement procedure in this case is performed automatically, which significantly simplifies measurements and reduces the amount of time needed to complete them.
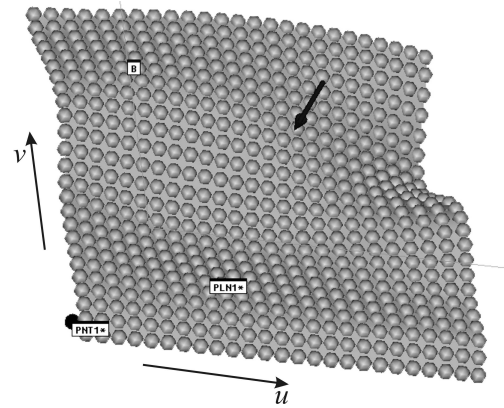
Fig. 7. Measuring points distribution and scanning directions
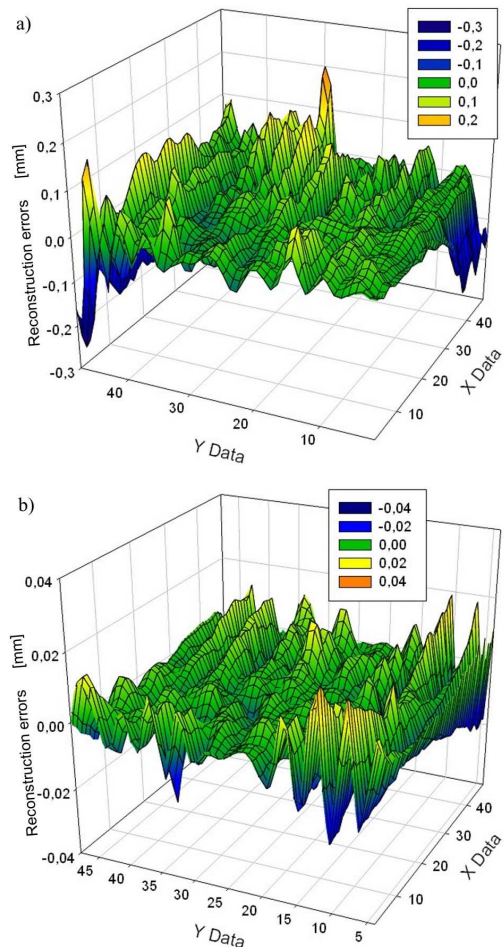

Fig. 8. Reconstruction accuracy a) after preliminary measurement, b) after subsequent measurement

Taking advantage of the *uv* scanning procedure, the measurements of the reconstructed free surface were repeated, which resulted in obtaining a cloud of 625 measuring points. On the basis of these points (in a way similar to the one in which the initial geometric model was created), the actual geometric model of the reconstructed surface was made. The model was then used to verify the suggested method of reconstructing objects described with the use of free surface patches; using this model, the control measurements of the reconstructed object were re-

programmed. Owing to making use of automatic measurement cycles, these measurements were completed in a short period of time. They constituted the basis on which the reconstruction errors of the researched shape surface were determined. The surface reconstruction errors plot are presented in Fig. 8.

The plot shows a comparison of inaccuracy in surface reconstruction on the basis of the results of the preliminary (Fig. 8a) and actual measurement results (Fig 8b). In the end, the obtained accuracy of the surface object reconstruction amounted to 0.035 mm.

4. CONCLUSIONS

Applying surface objects obtained in the two measurement stages in the reverse engineering process, greatly contributes to increasing the accuracy of the produced object's geometric model as well as to simplifying the whole procedure. Preliminary measurements are intended to define the scanned area borders and to construct a surface patch on the basis of which the second stage of measurement is performed. At this stage, having prepared a surface model of the reconstructed object, it is possible to have a greater choice of selecting the distribution and number of measurement points. In this case, the directions of the probe tip approach are generated more rationally, which contributes to increasing the measurement accuracy. It is very significant that it is possible to make use of the procedures of automatic scanning of the reconstructed surfaces, which makes the whole process last considerably shorter.

REFERENCES

1. **Ainsworth M., Ristic M., Brujic D.** (2000), Cad-Based Measurement Path Planning for Free-Form Shapes Using Contact Probes, *Advanced Manufacturing Technology*, n° 16, 23-31.
2. **Alan C. Ling, Shou-Yee Lin, Tse-Hao Fang** (1998), Automated sequence arrangement of 3D point data for surface fitting in reverse engineering. *Computers in Industry*, 38, 149-173.
3. **Park H., Jung H. B., Kim K.** (2004), A new approach for lofted B-spline surface interpolation to serial contours, *International Journal of Advanced Manufacturing Technology*, 23, 889–895.
4. **Piegl L., Tiller W.** (1987), Curve and surface constructions using rational B-splines, *CAD*, vol. 19, no. 9, 485-498.
5. **Piegl L., Tiller W.** (1997), *The NURBS Book*, 2nd ed. Springer-Verlag, New York, USA.
6. **Schemenauer L., Li N., Peng X., Zeng Y., Gu P.** (2002), A reverse engineering system for rapid manufacturing of complex objects, *Robotics and Computer Integrated Manufacturing*, vol. 18, 53–67.
7. **Soni K., Chen D., Lerch T.** (2009), Parameterization of prismatic shapes and reconstruction of free-form shapes in reverse engineering, *International Journal of Advanced Manufacturing Technology*, 41, 948–959.
8. **Sun Yuwen, Guo Dongming, Jia Zhenyuan, Liu Weijun** (2006), B-spline surface reconstruction and direct slicing from point clouds, *International Journal of Advanced Manufacturing Technology*, 27, 918–924.
9. **Xie Zexiao, Wang Jianguo, Zhang Qiumei** (2005), Complete 3D measurement in reverse engineering using a multi-probe system, *International Journal of Machine Tools & Manufacture*, 45, 1474–1486.
10. **Yadong Li, Peihua Gu** (2004), Free-form surface inspection techniques state of the art review, *Computer-Aided Design*, 36, 1395–1417

ESTIMATION OF DEFECT DEPTH IN STEEL PLATE USING LOCK-IN IR THERMOGRAPHY

Monika ZIMNOCH[*], Wiera OLIFERUK[*,**], Michał MAJ[**]

[*]Mechanical Engineering and Applied Computer Department, Bialystok Technical University,
45C Wiejska, 15-351 Bialystok, Poland
[**]Institute of Fundamental Technological Research, Polish Academy of Sciences, 5B Pawinskiego, 02-106 Warsaw, Poland

monaramona@wp.pl, wolif@ippt.gov.pl, mimaj@ippt.gov.pl

Abstract: The paper deals with the application of lock-in active infrared thermography as one of the non-contact and non-destructive techniques used for defect depth estimation. Preliminary research was done by testing a specimen made of austenitic steel plate with artificially created defects, i.e. flat-bottom holes. The obtained dependence between defect depth and phase shift was presented for different frequencies of "thermal waves" generated inside the sample. The experiment was carried out to determine the application of the lock-in thermography approach in testing materials with a high thermal diffusivity.

1. INTRODUCTION

Active infrared thermography is one of the most common methods used for nondestructive testing (NDT), and offers non-contact detection of defects occurring at a short distance below the surface. This method needs an external thermal stimulation of the tested material. The response of the material to the thermal stimulus is dependent on the existence of subsurface defects and their features. Thus, in order to obtain the information about defects, this response is studied. Depending on the external stimulus different approaches of active thermography have been developed. In recent years the most commonly used thermographic NDT technique is pulsed thermography. In this method the tested surface is flash-heated by one or more high energy flash lamps, and the temperature field on the surface during its self-cooling is recorded and analyzed. The duration of the pulse is usually very short (about a few ms). Defect presence is manifested by an increase in the surface temperature above the defective zone at the beginning of the self-cooling process after thermal stimulus (Maldague, 2001; Oliferuk, 2008).

Pulse thermography has some disadvantages, which may encourage advances in other approaches of active thermography. First of all, the tested surface should be uniform in terms of emissivity. Secondly, homogeneous heating up the surface is required. Therefore, only small parts can be inspected at the same time. Due to the above-mentioned problems the lock-in active thermography approach was taken into consideration.

The aim of this work is to find out the application of lock-in IR thermography in determining defect location under the tested surface for materials with a high thermal diffusivity.

2. LOCK-IN IR THERMOGRAPHY

The thermal stimulation in the case of lock-in thermography consists in heating the surface periodically by modulated high power lamps. A diagram of the IR thermographic system is presented in Fig. 1.
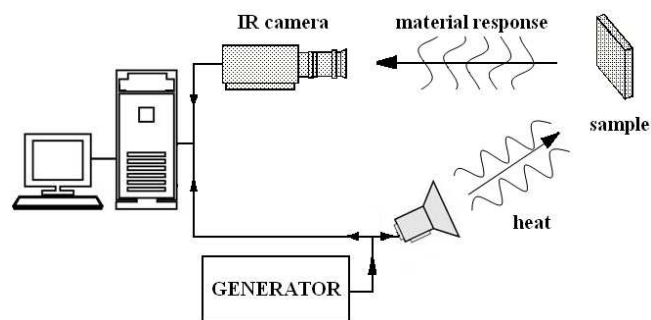

Fig. 1. Experimental setup for the lock-in IR thermography

Monitoring the exact time dependence between output and input signals, for instance thermal harmonic stimulation, it is possible to receive, on the basis of the obtained oscillating field of temperature, the amplitude and phase of the resulting "thermal wave" on the sample. Amplitude images are connected with tested material and the features of its surface, while phase images refer to wave propagation time. So lock-in thermography is based on "thermal waves" generated inside the sample. Quotation marks are used because wave equation should be the solution of the hyperbolic equation, and in this case it is the solution of the parabolic one (heat equation).

"Thermal waves" which were first studied, among other

things, by Fourier back in the XIX century, are highly attenuated (the amplitude becomes much smaller with increasing depth). Therefore, it is just possible to detect defects lying near to the tested surface. The "thermal wave" equation as a dependence of the temperature T on time t and depth z is formulated as follow (Maldague, 2001):

$$T(z,t) = T_0 e^{-\frac{z}{\mu}} \cos\left(\omega t - \frac{2\pi z}{\lambda}\right), \qquad (1)$$

where: $\lambda = 2\pi\mu$ – wave length, $\mu = \sqrt{\dfrac{2\alpha}{\omega}}$ – thermal diffusion length ($\alpha = \dfrac{k}{\rho c_p}$ – thermal diffusivity, where: k – thermal conductivity, ρ – density, c_p – specific heat capacity). Propagation velocity of "thermal wave" equals:

$$v = \lambda f = \mu\omega = \sqrt{2\alpha\omega}, \qquad (2)$$

where $f = \dfrac{\omega}{2\pi}$ – wave frequency. Presented formulas are true provided that a one-dimensional model for half space, heated up with sinusoidal changing intensity is assumed.

Thermal diffusion length means the distance after which wave amplitude becomes e-times smaller, and it is inversely proportional to $\sqrt{\omega}$, so waves with a higher frequency penetrate shallower in material than with lower frequency ones. Therefore, it is very important to employ a proper frequency, in case some of the defects are undetected. This is the main disadvantage of lock-in thermography. For each frequency it is necessary to do separate tests.

The most important advantage of lock-in thermography in many NDT applications is the fact that the φ phase is relatively independent of local optical and thermal surface features e.g. emissivity; whereas as it follows from the formula (1), directly depends on the defect depth z:

$$\varphi(z) = \frac{2\pi z}{\lambda} = \frac{z}{\mu}, \qquad (3)$$

and it is the linear dependence. Therefore, in order to determine defect depth phase shifts are investigated.

3. EXPERIMENT

For the lock-in testing the FLIR IR Thermographic System with ThermaCam Phoenix camera was used. The camera, with electrically cooled InSb detector, has a maximum frame rate of 346 Hz and temperature resolution of 20 mK (at 30°C). Other parameters are as follow: maximum frame size – 320 x 256 pixels (width x height), spectral range: 3-5 μm.

The camera was attached to halogen lamps (2,6 kW), which were used to generate harmonic heating of specimen surface with adequate heat intensity.

The specimen used in the tests (170 x 195 mm) was made of austenitic steel plate 316L, which is characterized by relatively high thermal conduction (about 15 J/kg·K). The simulated defects, i.e. flat-bottom holes were arranged

as shown in Fig. 2. The distances between the defects' centers were equal to 25 mm and 35 mm from the boundary of the sample to the centre of the nearest hole. The thickness of the plate is 3 mm.
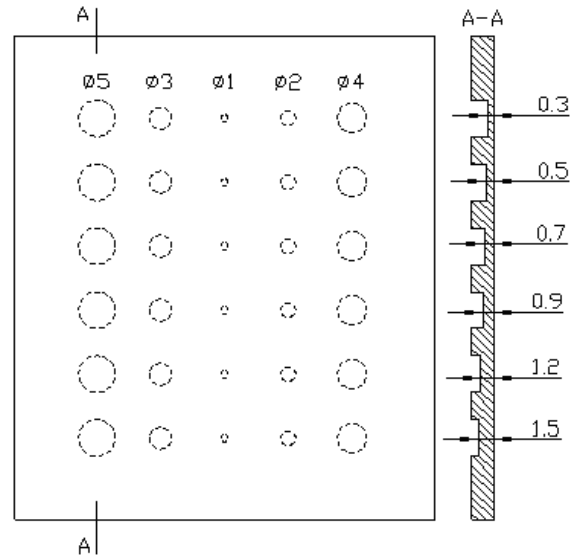

Fig. 2. Test sample

The tested surface was stimulated with halogen lamps, whose power was changed in a harmonic way. The specimen was heated up from the side where simulated defects are invisible. The following frequencies of the thermal stimulation were applied: 0.2 Hz, 0.4 Hz, 0.6 Hz; 0.8 Hz and 1 Hz. With the help of the lock-in IR thermographic system (Fig.1) the oscillating temperature field (on the tested surface) in the function of the time was measured and recorded. The response of the tested material on harmonic stimulation is not in fact a sinusoidal signal. Self-cooling of the tested specimen proceeded more slowly than the heating. Therefore the measured signal was approximated by analytic function. On the basis of this function, the "thermal waves" for each point of the surface were reconstructed. As a "thermal wave" of reference, the one on sound material surface was taken. Then the phase shift between "thermal wave" on surface above the defect and the reference "thermal wave", was determined as shown in Fig.3.
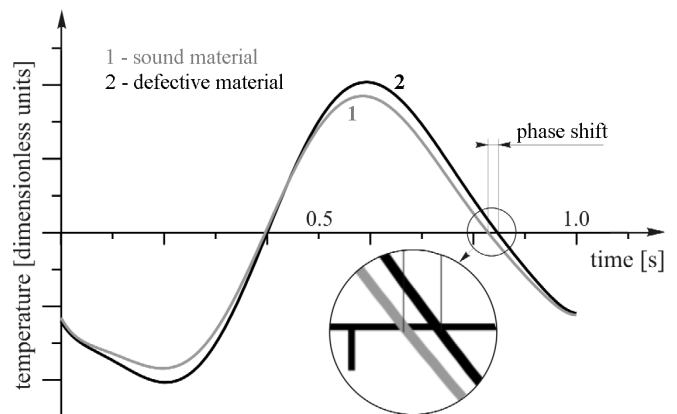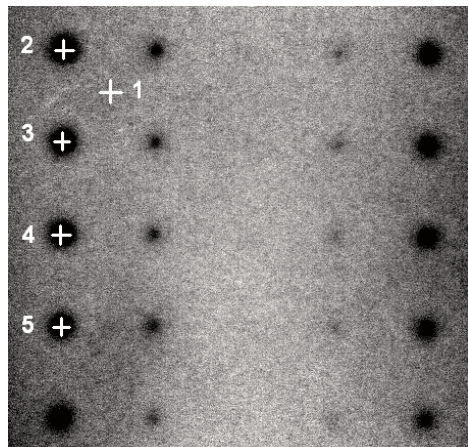

Fig. 3. Determination of phase shift

In order to identify the regions of the tested surface lying above sound material and defected one, the surface temperature distribution was used. As an example, the temperature distribution on the tested surface for thermal stimulation with frequency 0.6 Hz is shown in Fig. 4.


Fig. 4. Surface temperature distribution for 0.6 Hz stimulating signal

Analysis was made for the sixth period of the stimulation, for single pixels, corresponding to points on the tested surface, as shown in Fig. 4.

4. RESULTS

The analysis was made for the 5 mm diameter defects lying at different depth (0.3 mm, 0.5 mm, 0.7 mm and 0.9 mm) and for the stimulation frequencies 0.2 Hz and 1 Hz. The temperature of the tested surface was captured 346 times every second in the case of the 1 Hz frequency, whereas in the case of the 0.2 Hz – 172 times. The dependence between the phase shift (in relation to the sound material) and the defect depth was obtained as shown in Fig. 5.
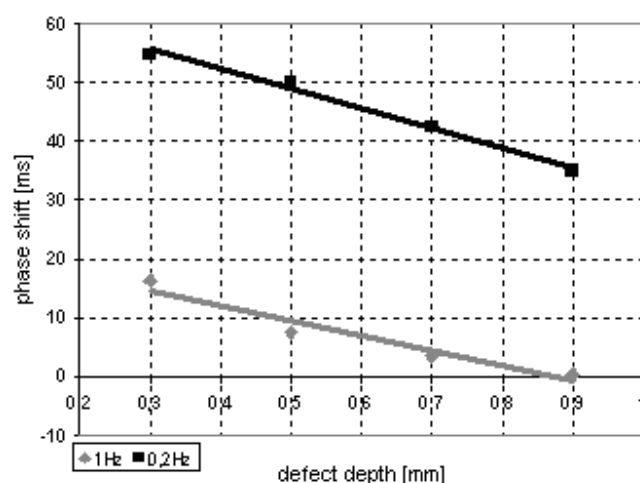

Fig. 5. Dependence of phase shift on defect depth for the defect diameter 5 mm and the frequencies of stimulation 1 Hz and 0.2 Hz

The obtained relation is linear and enables estimation of the depth of real defects. It is seen that for detecting 5 mm diameter of simulated defects (in the depth range shown in the diagram), it is better to use a lower frequency, like 0.2 Hz than a higher one, like 1 Hz. For instance, the phase shift for the 0.9 mm depth in the case of the 1 Hz stimulating signal is almost equal to zero. This means that the defect cannot be estimated using the above-mentioned frequency, which is called in this case the "blind frequency" (Manyong Ch. and others, 2008). The blind frequency exists for each specific defect lying at a certain depth.

It is seen in Fig. 5 that using lock-in IR thermography it is necessary to apply an appropriate frequency of stimulating signal in order to detect the defects lying at different depths. This is also seen in "phase diagram" (surface distribution of phase shift) available in the software operating the lock-in thermography system. Thus, there are phase shifts for each point of the tested surface (for each pixel) referring to the stimulating signal presented in that phase diagram (Fig. 6, 7).
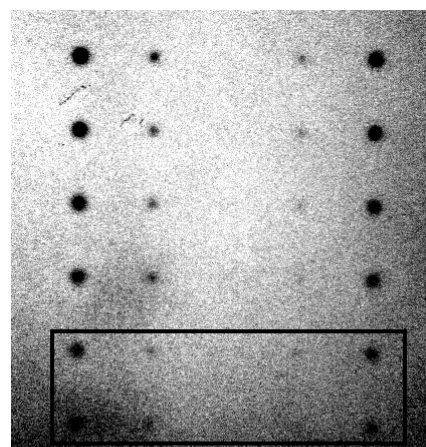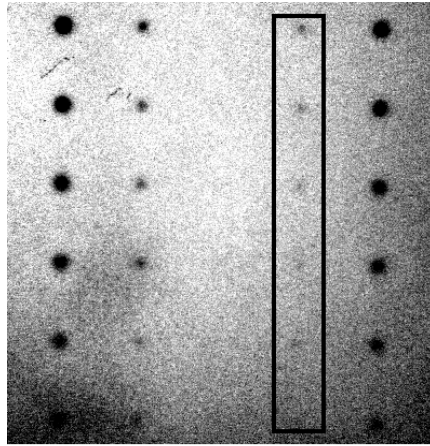

0,4 Hz
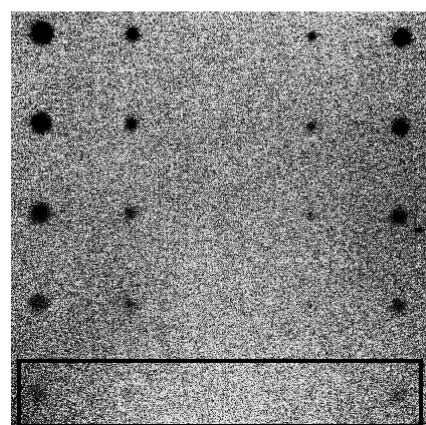
1 Hz

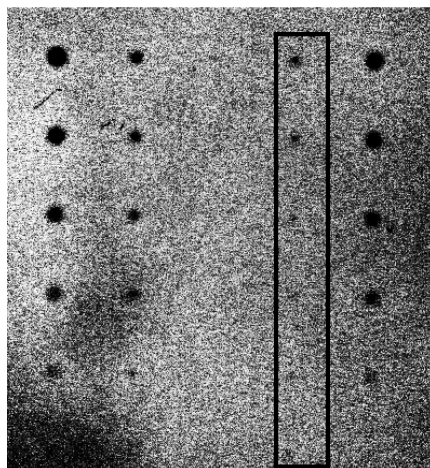**Fig. 6.** Phase shift referring to stimulating signal for 0.4 and 1 Hz

In Fig. 6 it is seen that the deeper defects, such as 1.2 mm and 1.5 mm are better perceived for the lower stimulating frequencies like 0.4 or 0.2 Hz. Whereas, in the case of the higher frequencies, like 0.8 Hz or 1 Hz, even slightly shallower defects, like 0.9 mm are not seen clearly. This

is related to a general rule, namely that lower frequencies penetrate deeper in material than higher ones.

It was also noticed that in the event of higher frequencies, like 0.8 and 1 Hz, shallower defects (in depth range shown in the diagram) with a smaller diameter (2 mm) were seen more distinctly than in the case of lower frequencies (Fig. 7).

0,4 Hz

0,8 Hz

Fig. 7. Phase shift referring to stimulating signal for 0,4 and 0,8 Hz

5. CONCLUSIONS

In this paper use of lock-in IR thermography to detect subsurface defects (0.3-0.9 mm) for materials with a high thermal diffusivity was proposed. Several of the preliminary experimental results for the defect diameter 5 mm and the frequencies of the stimulating signal 1 Hz and 0.2 Hz were presented. On the basis of the obtained results it was found that the dependence between phase shift (in reference to sound material) and defect depth is linear.

Tests done for the defects with smaller diameters showed that for estimation of their depth it is necessary to use lamps with the power higher than 2,6 kW. Further tests for different frequencies, defect locations and sizes are necessary to estimate the depth of the real defects in material.

REFERENCES

1. **Maldague X. P. V.** (2001), *Theory and practice of infrared technology for nondestructive testing*, John Wiley & sons, Inc., Canada.
2. **Manyong Ch.** and others (2008), Quantitative determination of a subsurface defect of reference specimen by lock-in infrared thermography, *NDT&E International*, No. 41, 119–124.
3. **Oliferuk W.** (2008), *Termografia podczerwieni w nieniszczących badaniach materiałów i urządzeń*, Biuro Gamma, Warszawa.
4. **Pickering S.**, **Almond D.** (2008), Matched excitation energy comparison of the pulse and lock-in thermography NDE techniques, *NDT&E International*, No. 41, 501–509.

ABSTRACTS

Sergey G. Chulkin, Aleksandr D. Breki, Irina V. Soloviova, Roman Kaczyński
Generalized methods of estimations of lubricants' influence on the tribotechnical characteristics of friction pair "steel-steel" on the four-ball machine

This article is devoted to the development of generalized methods of estimations of lubricants influence on the tribotechnical characteristics of friction pair "steel-steel" and its usage for selection of the best lubricating material out of set of materials "Litol-24"produced by different manufacturers.

Ryszard Dindorf, Paweł Łaski
Design and experimental test of a pneumatic parallel manipulator tripod type 3UPRR

The paper presents the design and experimental test of a tripod type-3UPRR pneumatic parallel manipulator. This manipulator consists of three identical kinematic chains (pneumatic axes) connecting the fixed base and the moving platform. The tool center point TCP of the moving platform is a resultant of relocation of three pneumatic rodless cylinders independently controlled by servo-valves. For simulation purposes a solid model of pneumatic tripod parallel manipulator in SolidWorks was constructed. Since the application of 3-CAD in modelling kinematics and dynamics of parallel manipulators is restricted further simulation was carried out by means of SimMechanics library and Matlab-Simulink package. The experimental research focused on determining the precision of positioning of manipulator's end-effector point of the moving platform during point-to-point control.

Józef Drewniak, Stanisław Zawiślak
Comparison of graph-based methods of kinematical analysis of planetary gears

In the paper three graph-based methods of planetary gear modeling are discussed. The following methods have been considered: Hsu's graph, contour graph and bond graphs-based methods. The theoretical ideas of the mentioned approaches were shortly revised and compared. Two of them were applied for analysis of an exemplary planetary gear. The consistency with traditional Willis method was checked. Advantages of the proposed approaches are highlighted.

Andrzej Dymarek, Tomasz Dzitkowski
Searching for the values of damping elements with required frequency spectrum

This paper concerns formulating and solving the problem of synthesis of vibrating discrete mechanical systems with two – terminal damper. In this paper a method of synthesis to determination of structure and inertial, elastical, damping parameters has been presented. Such task may be classified as a reverse problem dynamics of vibration subsystems.

Piotr Grześ
Finite element analysis of temperature distribution in axisymmetric model of disc brake

A transient thermal analysis is developed to examine temperature expansion in the disc and pad volume under simulated operation conditions of single braking process. This complex problem of frictional heating has been studied using finite element method (FEM). The Galerkin algorithm was used to discretize the parabolic heat transfer equation for the disc and pad. FE model of disc/pad system heating with respect to constant thermo-physical properties of materials and coefficient of friction was performed. The frictional heating phenomena with special reference to contact conditions was investigated. An axisymmetric model was used due to the proportional relation between the intensity of heat flux perpendicular to the contact surfaces and the rate of heat transfer. The time related temperature distributions in axial and radial directions are presented. Evolution of the angular velocity and the contact pressure during braking was assumed to be nonlinear. Presented transient finite element analysis facilitates to determine temperature expansion in special conditions of thermal contact in axisymmetric model.

Marek Jałbrzykowski, Joanna Mystkowska
Overlay dentures – constructional and research aspects

The paper presents selected issues relating to movable dentures with their general characteristics of fixings. Reference was made to the most important material-constructional aspects and the problems that arise with this type of solutions. In the work the method of durability and reliability evaluation and selection of materials for the kinematics connections of this type of structure was proposed.

Tadeusz Kaczorek
Positive switch 2D linear systems described by the general models

The positive switched 2D linear systems described by the general models are addressed. Necessary and sufficient conditions for the asymptotic stability of the positive switched system are established for any switching. The considerations are illustrated by numerical examples.

Andrzej Kaczyński, Wojciech Kozłowski
Elastostatic problem for an interface rigid inclusion in a periodic two-layer space

The article is devoted to the elastostatic three-dimensional problem of an interface sheet-like inclusion (anticrack) embedded into a periodic two-layered unbounded composite. An approximate analysis is carried out within the framework of the homogenized model with microlocal parameters. The formulation and the method of solving the general problem for an arbitrarily shaped inclusion is presented. As an example illustrating this method, the problem for a rigid circular inclusion under perpendicular tension is solved explicitly and discussed from the point of view of failure theory.

Zbigniew L. Kowalewski, Tadeusz Szymczak
A role of cyclic loading at modification of simple deformation processes of metallic materials

The paper presents experimental results of investigations carried out on the 2024 aluminium alloy and P91 steel under biaxial stress state. The loading programme comprised a monotonic tension assisted by torsion-reverse-torsion cycles. An influence of the cyclic loading and its delay with respect to uniaxial tension on the selected mechanical parameters taken on the basis of tensile characteristics was investigated. Additionally, a relative variation of the proportional limit and yield point due to the loading history applied was analyzed. A permanency of effects observed during combination of tension and cyclic torsion was experimentally assessed on the basis of an initial yield surface evolution.

Paweł Lindstedt, Rafał Grądzki
Parametrical models of working rotor machine blade diagnostics with its unmeasurable environment elimination

The paper presents the basic of the new method of rotor machine blades during their operation. The method utilizes such diagnostic models as a quotient of diagnostic signal y(t) amplification being a result of blade operation and x(t) signal of its environment as the blade tip approaches the sensor as well as amplification of these signals as the blade tip recedes from the sensor and phase shift difference of these signals as the blade tip approaches and recedes from the sensor. The adopted diagnostic models indirectly take the current blade environment x(t) into account with no necessity of measuring (Kotowski and Lindstedt, 2007; Lindstedt and Kotowski, 2004). Therefore the model is sensitive to blade technical condition changes remaining only slightly sensitive to environment changes. Suggested method may prove very important in diagnostics of rotor blades during operation of rotor machines (turbines, compressors etc.).

Bohdan Monastyrskyy, Andrzej Kaczyński
Contact strength of a system of two elastic half spaces with an axially symmetric recess under compression

Frictionless contact of two isotropic half spaces is considered one of which has a small smooth circular recess. A method of solving the corresponding boundary value problem of elasticity in axially symmetric case is presented via the function of gap height. The governing integral equation for this function is solved analytically by assuming a certain shape of the initial recess. On the basis of the closed-form solution obtained the strength analysis of a contact couple is performed and illustrated from the standpoint of fracture mechanics.

Romuald Mosdorf, Tomasz Wyszkowski
Frequency and non-linear analysis of bubble paths in bubble chain

In the paper the paths of bubbles emitted from the bras nozzle with inner diameter equal to 1.1 mm have been analyzed. The mean frequency of bubble departure was in the range from 1 to 36 Hz. Bubble paths have been recorded using a high speed camera. The image analysis technique has been used to obtain the bubble paths for different mean frequencies of bubble departures. The Fourier, wavelet analysis and recurrence plots have been used to determine the strength of interaction between bubbles in column. It has been found that the influence of previously departing bubbles on trajectory of next bubble in the column can be significant for fb > 30 Hz, in this case the bubble paths become less periodic and more instable. In this case the distance between subsequent departing bubbles (S/D) becomes close to 1. It causes that the vertical interaction between departing bubbles is enough strong to change the dynamical properties of bubble paths.

Arkadiusz Mystkowski, Leszek Ambroziak
Investigation of passive magnetic bearing with Halbach-array

The paper has described the complete design and investigation processes of permanent magnetic bearing. The passive magnetic bearing (PMB) rotor suspension rig employing no active control components was calculated, designed, constructed and tested. In order to increase the radial passive magnetic bearing stiffness, the Halbach-array configuration was used. The main purpose is to develop the nonlinear model of the PMB. Therefore, the magnetic flux circuit of the PMB was analytically calculated by using Ohm and Kirchhoff methods. The nonlinear effects of the discrete 3D model of the PMB was analyzed by using Finite Element Method (FEM). Finally, the very well matched experimental and analytical static characteristics of the passive magnetic suspension were carried out.

Arkadiusz Mystkowski
µ-Synthesis control of flexible modes of AMB rotor

In the paper the optimal robust vibration control of flexible rotor supported by the active magnetic bearings (ambs) is investigated. The purpose of the control system is stabilization of the high speed rotor and effective control of the rotor vibration due to noncollocation, gyroscopic effects and model uncertainties. The noncollocation effect is considered and frequency modal analysis of the noncollocated ambs system with gyroscopic effects is presented. The µ-Synthesis control is applied to stabilize the rigid and flexible critical frequency modes of the rotor, with emphasis structural and parametric uncertainty. The input and output signals in ambs system are limited by the weighting functions. The singular value analysis is used to obtain the robust performances of the closed-loop system. The stable operation and good stiffness of the high speed rotor supported magnetically is reached. The dynamical behaviour of the ambs rotor is evaluated in the range up to 21 000 rpm. The experimental tests show the effectiveness of the robust control system as well as good vibrations reduction and robustness of the designed controllers.

Małgorzata Poniatowska
Influence of coordinate measurement parameters on a free-form surface inspection results

Coordinate measurements are the source of digital data in the form of coordinates of the measurement points of a discrete distribution on the measured surface. The local geometric deviations of free-form surfaces are determined (at each point) as normal deviations of these points from the nominal surface (the CAD model). Obtaining discrete data is inseparably connected with losing information on the surface properties. In contact measurements, the ball tip functions as a mechanical-geometric filter. The results of coordinate measurements of geometric deviations depend not only on the grid size but also on the ball tip diameter. This article presents foundations of the influence of the ball tip diameter and the grid size on coordinate measurement results along with the experimental results of measurement of a free-form milled surface in order to determine its local geometric deviations.

Valentyn Skalsky, Pavlo Halan

Application of acoustic emission in fatigue fracture diagnostics

The most important peculiarities of the acoustic emission under fatigue loading are reviewed. Dependences of the AE signals and parameters of the growing fatigue crack on the basis of an existing literature source review are established. An essential role of the correlation for determining the crack growth rate in the relation between the AE parameters and crack parameters are shown. An energy approach for determination of cycle quantities till the initiation of a crack is proposed.

Andrzej Werner

Measuring the accuracy of producing free-form surfaces with the use of the coordinate measuring method

The present paper presents a method of determining errors in processing complex-shape surfaces produced with the use of a CNC machine tool. In order to achieve this, the whole process of making a three-dimensional object was performed, from creating a CAD model to generating a processing programme for a CNC machine tool and producing the actual object. The obtained surface was measured with a Brown & Sharpe Mistral coordinate measuring machine with the use of a Renishaw TP200 measuring probe.

Andrzej Werner

Coordinate measurements of free-form surfaces in reverse engineering process

This paper presents the issues of coordinate measurements of three-dimensional objects whose shape is defined with the use of parametric surface description methods applied in CAD systems. The paper also describes a mathematical as well as a geometrical presentation of surfaces used CAD systems, and discusses coordinate measurement techniques applied in measuring objects of this class. Further in the article, a practical implementation of the methodology of reconstructing objects described with the use of free-form surface patches has been presented. The methodology includes subsequent object measurements and reconstructing the object's geometric model, and concentrates on the possibly most accurate reconstruction of the shapes and dimensions of the researched object.

Monika Zimnoch, Wiera Oliferuk, Michał Maj

Estimation of defect depth in steel plate using lock-in IR thermography

The paper deals with the application of lock-in active infrared thermography as one of the non-contact and non-destructive techniques used for defect depth estimation. Preliminary research was done by testing a specimen made of austenitic steel plate with artificially created defects, i.e. flat-bottom holes. The obtained dependence between defect depth and phase shift was presented for different frequencies of "thermal waves" generated inside the sample. The experiment was carried out to determine the application of the lock-in thermography approach in testing materials with a high thermal diffusivity.